Hardening of Reinforced Concrete Columns Against Blast Loading by Prestressing and ECC Jacketing

Abdul Saboor Karzad

The thesis submitted to the

University of Ottawa

In partial fulfillment of the requirements for a degree of

Doctor of Philosophy

In Civil Engineering

Department of Civil Engineering

Faculty of Engineering

University of Ottawa

Abstract

The design of blast-resistant civilian structures is not a common practice in the construction industry. However, the increasing threat of terrorist attacks using vehicle bombs targeting civilian facilities has necessitated the development of innovative solutions. A key solution to prevent existing buildings from damage due to blast is to mitigate risk by providing a secured distance around the perimeter of buildings or hardening building components. Columns, being critical elements of buildings, are responsible for the overall strength and stability of the entire structure. Columns are primarily designed to carry vertical loads, with some also offering resistance to lateral loads caused by earthquakes and wind. However, their lateral capacity is limited in the event of a nearby explosion. Columns' lateral deflections must be limited to avoid localized column failure under such loadings. The loss of a column can also trigger progressive collapse, leading to partial or complete building collapse. Protecting existing building columns through blast strengthening/hardening can reduce blast risk and improve structural performance under such extreme events. This research aims to address blast risk to reinforced concrete (RC) columns and explores potential improvements in their response by developing innovative hardening techniques. It focuses on ground-floor columns, which are susceptible to external surface blasts typically triggered by vehicular or hand-carried bombs. The proposed hardening technique primarily consists of lateral support(s) provided by external prestressing strands against blast loads, which is at the forefront of innovation. The concept of prestressing against blast loading has also been extended to new columns designed to incorporate internal prestressing, thereby stabilizing column performance under blast loads. Column hardening has also been extended to include jacketing of columns by Engineered Cementitious Composites (ECC). Under blast loads, ECC's high tensile strain capacity allows it to absorb energy and reduce damage propagation in hardened columns.

The research consists of extensive experimental and analytical components. The experimental program involved designing, constructing, and testing 15 RC columns under simulated blast shock waves. Twelve of these columns were hardened either by external or internal prestressing or by ECC jacketing. The remaining three columns represent as-built columns without the implementation of any strengthening/hardening. The columns were tested against shock waves (high transient air pressures) generated by a blast simulator in the form of a shock tube while also subjected to vertical gravity loads, also known as axial loads. The test parameters included the

location of the prestressing strands (external or internal), the prestressing force and strand longitudinal profile, the amount and arrangement of column transverse reinforcement, the dosage of fibers in the ECC mix, the thickness of the ECC jacket, and the level of reflected pressure-impulse combinations. Analysis of the results obtained in the experimental phase revealed that the proposed strengthening and hardening techniques significantly enhanced the behavior of the columns subjected to combined axial and blast loading. Deployment of external post-tensioned strands noticeably reduced the displacement at the critical section created by elastic and plastic deformations, thus increasing the resistance of the column. Posttensioned columns using internal prestressing also exhibited improved blast resistance response due to additional stability and moment resistance compared to their companion reference column. Similarly, ECC jacketing proved to be an effective method to improve column resistance, resulting in reduced deformations in critical sections. ECC jacket, with its superior ductility and crack control, prevented fragmentation and spalling of concrete at the critical section. In general, the hardened columns resisted between 20% and 40 % higher blast loads as compared to their companion reference columns. When subjected to a similar blast load of their companion reference columns, the maximum and residual deflection of strengthened columns were reduced by 40 to 80 % and 76 to 100 %, respectively.

The analytical phase of the research consisted of developing resistance functions for the tested columns, which were then used to conduct nonlinear single-degree-of-freedom (SDOF) dynamic analyses. Resistance functions were developed by considering the strain rate effect (i.e., dynamic increase factor, DIF), material non-linearity, and the contributions of prestressing and ECC jacketing. The SDOF analysis also considered the effect of the P-delta moment (i.e., secondary moment). Comparisons of analytical and experimental column behavior showed that the inelastic SDOF analysis provides reasonably accurate predictions of column behavior under blast loads, making it an effective design tool. In addition, support reactions were also calculated using equations known as dynamic reactions. The research findings were used to develop economically viable and structurally sound column hardening techniques for use in engineering practice.

Acknowledgments

This journey has not been easy; alongside academic challenges, I had to overcome many nonacademic obstacles. I could not have succeeded in this journey without the help and support of people who deserve this acknowledgment.

First, I want to sincerely thank my supervisor, Prof. Murat Saatcioglu, for giving me the opportunity to pursue my Ph.D. studies in civil engineering. His patience, guidance, encouragement, and valuable ideas over the past five years have been crucial to my success. He is a true mentor and role model for many of his graduate students, including me.

I want to thank Dr. Zaid AlSadoon from the University of Sharjah and the alumni from the University of Ottawa for helping me begin this journey and supporting me along the way. I am thankful to my colleagues and mentors from the University of Sharjah and the American University of Sharjah for their encouragement during my studies.

Special thanks to my friend Dr. Wameed Al Ghazala from Carleton University for helping me settle in a new country, and to my colleagues and friends in the Department of Civil Engineering at the University of Ottawa, especially Eng. Emre Ensel and Eng. Osamah Mahmood, for their continuous support.

I appreciate the help of laboratory technical officers Dr. Muslim Majeed and Dr. Gamal Elnabelsya during the experimental work. I also thank Stephen Holder (GTi), Roberto (Utility Structures Inc.), Lafarge (ready mix company), and Minifibers for providing materials and equipment for my research.

Finally, I am deeply grateful to my family for their endless love and support. Their encouragement gave me the strength to complete this journey. I admire their patience in achieving this milestone and hope it serves us all in the best possible way.

Contents

List of Tables

Chapter 3

Chapter 4

Chapter 5

Chapter 6

List of Figures

Chapter 2

Chapter 3

Chapter 4

Chapter 5

Chapter 6

Appendix A

Appendix B

Appendix C

Chapter 1. Introduction

1.1 Background

During the past three decades, a large number of maliciously intended bomb attacks on critical infrastructure took place globally in the form of terrorist attacks. The explosions, often using a vehicle bomb, targeted not only military facilities but also civilian infrastructures, such as embassies, governmental offices, commercial centers, and even residential buildings. The hotel bombing in Mogadishu (Somalia, 2017), the bomb attack on a governmental office complex in Oslo (Norway, 2011), the car bomb attack near the neighborhood of embassies in Jakarta (Indonesia, 2004), the car bombing on the American embassies in Nairobi (Kenya, 1998)) and Dar-e-Salam (Tanzania 1998) [1], [2] are just a few examples of these incidents. Past observations indicate that non-military facilities are often soft targets that are unprotected against maliciously intended acts of terror.

Blast loads generated by explosions are in the form of short-duration intense pressures, resulting in impulsive loads. Blast events, whether due to a terrorist attack or an accidental explosion, have devastating effects on structural and non-structural elements. Therefore, developing and implementing strengthening/hardening materials and techniques for protecting civilian infrastructure against blast loads is of primary importance. Numerous researchers have addressed this need and investigated various strengthening strategies and materials to enhance the performance of existing civilian infrastructure. The methods suggested and investigated include seismic detailing for continuity and deformability, the use of ultra-high-performance fiber-reinforced cement-based composites (UHPFRC), steel jacketing or the use of concrete-filled steel tubes (CFST), externally bonded fiber-reinforced polymer (EB-FRP) materials, fiber-reinforced and steel-reinforced polyurea, and aluminum foam [3], [4].

Columns are critical building components that provide overall strength and stability to the structures. In the event of an explosion, the resulting blast load can cause significant damage to the columns, potentially triggering partial or progressive collapse of the entire building. Progressive collapse is characterized by a local failure that induces damage to adjacent members, resulting in damage to a disproportionately large part of the structure or its collapse. For instance, the truck bomb attack on the Alfred P. Murrah Federal Building in 1995 in Oklahoma City (USA) resulted in the collapse of 1/3 of the building [5], [6].

Mitigation of the blast load effect on a column can be achieved by one or a combination of three possible countermeasures. These can be classified into two categories: soft measures and hard measures. An example of a soft measure is increasing the stand-off distance between the structure (i.e., asset) and the explosives (i.e., threat). Increasing the stand-off distance is an ideal strategy for protecting the building, which can be achieved by using barriers such as roadblocks, fencing, concrete blocks, bollards, streetscape security elements, and security checkpoints. However, the type and location of the structure may limit the application of an increased stand-off distance, especially in urban areas where space is limited around the perimeter of the structure. Examples of hard measures include the use of sacrificial panels or load transfer elements to protect columns from the direct impact of blast loads. The load transfer mechanism or sacrificial panels can distribute the blast loads to slabs & beams and absorb the imparted energy, thereby reducing demands on the columns. However, the implementation of this strategy is also limited due to architectural & cost-related constraints or structural capacity limitations [4].

Another means of providing a hard measure is to increase column capacity directly (i.e., strengthening/hardening) by modifying column cross-sectional properties, which often involves the use of superior-grade materials. Adding additional mass to the existing column may have favorable effects due to increased inertia, but it may also have architectural and structural limitations. Hardening is an attractive option, but it should be designed carefully to increase the strength and ductility of the column with minimal interference to the member's functionality and aesthetics. Sometimes, combining the aforementioned protective measures may be necessary to achieve the desired protection strategy. Blast protection is a risk-based approach, not an absolute concept, aimed at minimizing damage to the column. In blast engineering, the level of protection and the potential loss should be balanced against the cost of protection.

1.2 Research Objectives

The main objective of the current research project is to develop innovative techniques of blast protection for reinforced concrete (RC) columns, either by using external or internal prestressing or by providing a column jacket that incorporates a layer (shell) of Engineered Cementitious Composite (ECC). The objective includes the development of a methodology for computing resistance functions for protected columns that is suitable for use in dynamic analysis. Finally, the

objective includes the development of design methodologies for the protection techniques investigated for use in engineering practice.

1.3 Scope

The scope of research consists of experimental and analytical phases as presented in the following bullet points:

- Design and construct a total of 15 RC columns for testing under combined simulated blast loading and axial load. The test columns share a similar geometry and material properties but have different transverse reinforcement ratios.
- Preparation and testing of three reference columns without strengthening/hardening to serve as a benchmark for the investigation of strengthened/hardened columns.
- Hardening of seven columns using externally placed 7-wire strands longitudinally and applying different levels of prestressing force and using different longitudinal profiles of strands. These columns represent existing blast-deficient columns in practice.
- Post-tensioning of two columns internally using 7-wire strands (conventional prestressing approach). These columns represent new blast-resistant columns in practice.
- Strengthening of three columns using ECC jacketing for improved blast resistance. These columns also represent blast-deficient columns in practice.
- Fabrication of a load transfer device in the form of a steel curtain to uniformly transfer and distribute the shock wave pressures generated by the shock tube to the test columns. The curtain is made of a thin/flexible steel sheet and transverse rigid steel hollow sections (HSS). The steel sheet is designed not to resist the applied pressure. The transverse rigid HSS were connected to the sheet in the transverse direction of the test columns to distribute and apply the collected pressure to the column as a uniformly distributed load.
- Conduct shock tube testing of columns by applying the desired levels of pressure-impulse combinations. Each column is subjected to multiple blast shots under incrementally increasing pressure-impulse combinations until column damage or failure is reached.
- Data acquisition, recording, and analysis to assess the performance of test columns.
- Develop a methodology to compute resistance functions for columns with due consideration given to the effects of hardening elements (prestressing and ECC jacketing), material non-linearity, strain rate effects, and presence of axial load.

- Develop analytical column models for conducting single-degree-of-freedom (SDOF) dynamic analyses of columns and validate the models by comparing the analysis results with those obtained from shock tube testing.
- Develop design procedures and recommendations for use in engineering practice for the hardening strategies developed.

1.4 Synopsis of Chapters

This thesis is organized into seven chapters and three appendices. Chapter 1 provides a general overview of the research background, objectives, scope, and significance of the current research project. Chapter 2 presents an extensive background and literature review on explosive events, blast loads, and strengthening methods proposed and applied to RC columns. Chapter 3 reports on the experimental program. It encompasses all aspects of specimen preparation and testing, including material properties, geometry, design, and preparation, as well as the strengthening methodologies employed. It also includes details of the test setup and instrumentation used to measure the required data, as well as an introduction to the specifics of the shock tube facility. Chapter 4 describes test results under blast loading. In particular, the test results, including applied pressure and impulse, measured deflections, strain data, support reactions, applied axial load, and qualitative damage stage, are presented along with photos and diagrams of each test. The presentation of test results is made in four groups: i) reference columns, ii) columns hardened by external post-tensioning, iii) internally post-tensioned columns, and iv) columns hardened by ECC jacketing. Chapter 5 presents the analysis of test data and a discussion of test results. The test results were analyzed and discussed by comparing their behavior with that of their companion reference column and with the columns that had different test parameters. Chapter 6 outlines the steps involved in generating resistance (force-displacement) curves and equivalent single-degree-of-freedom (SDOF) modeling for dynamic analysis using a nonlinear numerical integration technique. In developing the resistance curves, the effects of several factors, including dynamic material properties, the presence of prestressing strands and ECC layer, and the initial applied axial load, were considered. Chapter 7 presents the design procedure and recommendations developed for the hardening techniques researched based on test results from both prestressed and ECC jacketed columns, aiming to improve strength and ductility. The procedure includes the selection of strand profile, level of post-tensioning force, the specifics of the ECC mix with emphasis on

fiber dosage, and the thickness of the ECC layer. Moreover, Chapter 7 concludes this research project and provides recommendations for future research. Appendices are included to present additional data, such as strain data, support reactions, and SDOF analysis results.

1.5 Research Significance

This research project aims to develop blast risk mitigation strategies for reinforced concrete columns, which are critical elements responsible for the overall strength and stability of buildings. The experimental investigation of blast-resistant structural elements has challenges and difficulties due to the nature of short-duration impulsive blast loads and the required facilities to apply such loading. Conducting live field explosion tests is challenging due to high costs, a lack of control during testing, and the potential for hazardous situations. When live tests are conducted, they often involve military applications, and the resulting test results are generally classified. An alternative testing method to live testing is the use of a blast load simulator, specifically a shock tube. A shock tube facility requires relatively little operating experience and provides a safe testing environment. In this study, the test specimens are subjected to blast loads generated by a shock tube available at the University of Ottawa.

The current investigation focuses on innovative hardening methodologies for enhancing the blast resistance of existing and new reinforced concrete columns. The primary technique developed is based on the concept of prestressing RC elements using 7-wire strands. The application of prestressing strands for the blast resistance of columns is not a common construction practice. The technology developed involves generating reacting forces to blast loads along the height of the column, and as such, forms an original concept, unlike the common practice of jacketing columns for strength and ductility enhancements using steel or fiber-reinforced polymer sheets. This method is cost-effective, non-intrusive, and highly effective in resisting extreme blast loads. The second technique developed for the blast hardening of concrete columns involves the use of ECC jacketing. Previous research on the use of ECC jacketing of columns is scarce in the literature, and its application to column blast hardening is unique. Both the use of prestressing and ECC jacketing offer innovative and original methodologies for practical application, validated through a large volume of valuable test data and companion analytical studies.

Chapter 2. Background and Literature Review

2.1 History of Blast Events

This section provides brief information on documented explosions that occurred worldwide, mainly using vehicle bombs targeting civilian structures (soft targets). The statistics presented in this section demonstrate the vulnerability of soft targets in our society to militia group activity and highlight the severity of damage and destruction to structures in the event of blast loading. Vehicle bombings began at the start of the 20th century, primarily for military purposes. However, in the past three decades, due to the rise in global geopolitical conflicts, the tactic of vehicle bombing has also been used against critical infrastructure forming soft targets such as governmental buildings, embassies, commercial buildings, and even residential buildings. It is reported in the literature that in the first decade of the 21st century, there has been a 300% increase in the number of maliciously intended terrorist activities worldwide. [7]. Some examples of bombing of civilian structures, mostly reinforced concrete buildings, are provided below:

In 1989, a truck carrying 500 kg of explosives was detonated near the DAS headquarters building in Bogota (Colombia). The explosion destroyed 14 city blocks and damaged more than 300 commercial properties. In 1993, the World Trade Center Towers in New York (USA) were the target of a van bomb placed in an underground parking garage at the 2nd sub-ground basement level that generated a pressure of more than 1000 MPa. The explosion caused severe damage to the tower. Still, it did not cause partial or full collapse of the building (see Figure 2.1). In another incident in 1993, a fuel tanker carrying 500 kg of explosives targeted a mosque in Stari Vetiz village (Bosnia), damaging many nearby buildings. In 1995, a truck bomb carrying around 2500 kg of explosives was detonated in front of the Alfred P. Murrah building in Oklahoma City (USA) (see Figure 2.2). The blast pressure damaged many nearby buildings. It destroyed three columns at the front of the 9-story Alfred P. Murrah building, which were supporting a transfer beam. The explosion resulted in the loss of column load-carrying capacity, which was followed by the progressive collapse of one-third of the 9-story building. In 1996, a car bomb with a mass of 1500 kg was used to target the Manchester city center in the UK. The incident caused significant structural damage to more than ten nearby buildings; half of them were subsequently demolished. In 1996, a truck bomb attack (carrying around 10,000 kg of TNT) on Khobar Tower housing in Saudi Arabia damaged or destroyed several high-rise buildings (see Figure 2.3). In 2002, a van

bombing carrying 1020 kg of explosives targeted a bar (Sari club) on the island of Bali (Indonesia). The explosion created a one-meter-deep crater, destroying nearby buildings and shattering the windows of several farther blocks. In the span of almost a decade, from 1993 to 2005, there were 650 explosions in Pakistan, and in India, during the same period, more than 200 bomb explosions were reported. In 2011, a van bomb was detonated in front of a block in Oslo (Norway) housing many governmental offices. The blast shattered the windows on all floors of the building and those of nearby buildings. In 2015, an 8-story building was destroyed by a truck bomb in Ramadi (Iraq). In 2020, a car bomb attack was carried out in downtown Tennessee (US), causing damage to over 60 residential and commercial buildings and the collapse of one building. Figure 2.4 presents a summary of global terrorist attacks. Notably, the number of attacks peaked in 2014, followed by a decline in the subsequent years [2], [7], [8].

2.2 Properties of Blast Loads

An explosion is a rapid chemical reaction defined as a sudden release of energy. Energy is released through light, sound, heat, and changes in the volume of gases. The gas that contains most of the released energy expands violently and pushes the surrounding air out of the volume it occupies. This process forms a layer of compressed air in front of the expanding gas, known as a shock wave or blast wave. The shock wave expands and moves outward in all directions at a supersonic velocity from the explosion source (center of burst) and travels a distance known as the stand-off zone (see Figure 2.5). A blast load consists of transient high-pressure waves and high-speed wind that move like a wall of highly compressed air with a very high velocity. When the layer of compressed air is pushed outward, it causes an instant increase in incident pressure that significantly exceeds the atmospheric pressure. This pressure is known as overpressure (incident pressure), and it is enormously amplified when it encounters a surface, an object, or a structure on its path. The amplified resulting pressure is then referred to as the reflected pressure, which is multiplied by a factor (i.e., 2 to 13 times) depending on the object's type, shape, and location, as well as the blast wave's intensity and incidence angle. Typically, for design purposes, a blast load in the range of 10 kPa to 10 MPa is considered, which depends on various factors such as charge weight, standoff distance, structural properties, location, and height of the blast field, as well as urban development. [9].

Depending on how far an explosion happens from the target and the ground's surface, the waves propagate with or without a reflection. The blast is considered a free-air burst when the explosive charge is detonated adjacent to or above a structure in the air. Therefore, the initial shock wave is not amplified, and the blast wave is considered non-reflected or spherical. When the explosive charge is detonated above the ground surface, it is referred to as an airburst. During the air burst, the initial shock wave propagates away from the burst center, impacts the ground surface, and continues to propagate outward along the ground surface, forming a front known as a Mach stem or Mach front. The Mach front is the product of the interaction between the incident wave (initial wave) and the reflected wave. If the explosive charge is detonated near or on the ground surface, the initial wave is reflected and reinforced by the ground surface. At surface burst, the reflected wave merges with the incident wave and forms a single hemispherical wave at the point of detonation, as depicted in Figure 2.5 [7], [10], [11].

To calculate the time history of the blast pressure, the blast parameters should first be defined. The blast parameters include the weight of the explosives (charge), blast category, angle of incidence, and the distance between the center of the burst and the targeted object, known as the stand-off distance. Generally, the charge weight (size of the bomb) defined as a threat is expressed in Trinitrotoluene (TNT) equivalent weight. The targeted structure is labeled as an asset. The non-obstructed distance between the asset and a threat is defined as a stand-off zone (see Figure 2.5). The blast category is identified as external/unconfined (i.e., free-air, air-burst, and surface-burst) or internal/confined (i.e., fully confined, partially vented, and fully vented). The angle of incidence is a crucial factor in determining the magnitude of blast load on a structure. When the incidence angle is zero or the reflected surface is perpendicular to the blast wave, the reflected pressure reaches its peak value.

The blast pressure time history generated by an explosion is illustrated in Figure 2.6. As depicted, the pressure attenuates rapidly following an exponentially decaying function in less than a second, typically in milliseconds. Figure 2.6 also illustrates that the intensity of overpressure reduces to less than the atmospheric pressure over a short period. This decay in pressure results in a negative pressure, also called suction, which is ignored in the blast-resistant design of structures [12]. As illustrated in Figure 2.7, the intensity of overpressure (incident pressure) also decays significantly with an increase in standoff distance, and similarly to the pressure time history, the

decay follows an exponential curve. The area under the pressure-time history curve is denoted as an impulse, which indicates how long the blast load acts on the target [10], [13], [14].

Blast pressure time history can be obtained using the following methods: empirical equations proposed by various researchers, UFC (Unified Facilities Criteria) charts, and the use of software applications. It is worth mentioning that the first step in using any of the aforementioned methods is to express non-TNT explosives into a TNT equivalent charge weight using the following equation:

$$W_{P,TNT} = \left(\frac{P}{P_{TNT}}\right) \cdot W \tag{2.1}$$

where P is the peak pressure generated by the explosion of the explosive weight W, $W_{P,\,TNT}$ is the equivalent weight of TNT that will create a similar effect, and P_{TNT} is the peak pressure of TNT.

Some of the proposed equations for calculating blast load properties are briefly discussed in this section. Newmark, in 1961, suggested the following equations to calculate the peak incident pressure and peak reflected pressure from a chemical explosion at the ground surface. [8], [15].

$$P_{so} = 6784 \cdot \frac{W}{R^3} + 93 \cdot \left(\frac{W}{R^3}\right)^{1/2} \tag{2.2}$$

$$P_r = 2 \cdot P_o \cdot \frac{6}{7 \cdot P_o + P_{so}} \quad \text{when} \quad P_{so} < 10\ bar \tag{2.3a}$$

$$P_r = 4 \cdot log_{10} \cdot P_{so} + 1.5 \quad \text{when} \quad P_{so} \geq 10\ bar \tag{2.3b}$$

$$t_o = 10.23 \cdot \frac{W^{1/3}}{\sqrt{P_{so}}} \quad when \quad P_{so} < 70\ bar \tag{2.4a}$$

$$t_o = 20.77 \cdot \frac{W^{1/3}}{\sqrt{P_{so}}} \quad when \quad P_{so} \geq 70\ bar \tag{2.4b}$$

where P_{so} is the peak incident overpressure in units of bar, W is the charge weight in tons, R is the stand-off distance in meters, P_r is the peak reflected pressure in bar, and P_o is the ambient atmospheric pressure equal to 1 bar, t_o is the shock front duration.

Kinney and Graham presented the following equations to calculate the incident pressure and positive phase duration for an air-burst chemical explosion. Some computer-based applications adopted their proposed equations. [16].

$$P_{so} = P_o \cdot \frac{808 \cdot \left[1 + \left(\frac{Z}{4.5}\right)^2\right]}{\sqrt{\left[1 + \left(\frac{Z}{0.048}\right)^2\right] \cdot \left[1 + \left(\frac{Z}{0.32}\right)^2\right] \cdot \left[1 + \left(\frac{Z}{1.35}\right)^2\right]}} \tag{2.5}$$

$$t_o = W^{1/3} \cdot \frac{980 \cdot \left[1+\left(\frac{Z}{0.54}\right)^{10}\right]}{\left[1+\left(\frac{Z}{0.02}\right)^{3}\right] \cdot \left[1+\left(\frac{Z}{0.74}\right)^{6}\right] \cdot \sqrt{\left[1+\left(\frac{Z}{6.9}\right)^{2}\right]}} \ , (in\ ms) \tag{2.6}$$

$$t_a = \frac{1}{a_x} \cdot \int_{r_c}^{r} \left[\frac{1}{1+\frac{6P_{so}}{7P_o}}\right]^{1/2} \cdot dr \ , (in\ ms) \tag{2.7}$$

Where t_a is the arrival time, a_x is the speed of sound in an undisturbed atmosphere, r_c is the charge radius, r is the radial distance, and Z is the scaled distance, which can be calculated by the equation below as per Kinney:

$$Z = \frac{f_d \cdot R}{W^{1/3}} \tag{2.8}$$

$$f_d = \left(\rho/\rho_o\right)^{1/3} \tag{2.9}$$

where R is the actual distance, f_d is the transmission factor for distance, ρ is the atmosphere's density through which a shock wave passes, and ρo is the atmosphere's density for the reference explosion.

Brode presented the following equations to calculate the incident pressure [17]:

$$P_{so} = \frac{6.7}{Z^3} + 1 \quad when \quad P_{so} > 10\ bar \tag{2.10a}$$

$$P_{so} = \frac{0.975}{Z} + \frac{1.455}{Z^2} + \frac{5.85}{Z^3} - 0.019 \quad when \quad 0.1 < P_{so} < 10\ bar \tag{2.10b}$$

$$Z = \frac{R}{W^{1/3}} \tag{2.11}$$

where Z is a scaled distance that combines the two blast parameters: charge weight, W, and stand-off distance, R.

The following equation is one of many equations reported in the literature for calculating reflected pressure [8], [18]:

$$P_r = 2 \cdot P_{so} \cdot \left[\frac{7 \cdot P_o + 4 \cdot P_{so}}{7 \cdot P_o + P_{so}}\right] \tag{2.12}$$

The following expression, based on the Friedlander equation, was developed to calculate and plot the variation of positive phase pressure [18]:

$$P(t) = P_{so}\left(1 - \frac{t}{t_o}\right) \cdot e^{-\alpha \cdot \frac{t}{t_o}} \tag{2.13}$$

$$I = \int_0^{t_o} P(t) d(t) \tag{2.14}$$

where α is the waveform parameter, and it can be calculated using the table provided by Kinney and Graham [16], and I is the impulse.

The second and preferred method to predict blast load properties in the absence of readily available software applications is the use of UFC charts [19]. UFC charts (developed based on Kingery-Bulmash equations) provide all the positive phase properties of a blast pressure: incident pressure, reflected pressure, impulse, duration, and other parameters. UFC charts presented in Figure 2.8 and Figure 2.9, provide the shock wave parameters as a function of Z (scaled distance established by the US Department of Defense based on Hopkinson's proposal). The charts are prepared for a value of Z = 100 ft/(lb)$^{1/3}$ at maximum because, beyond this value, the resulting damage is superficial for most structures. The scaled distance, a combination of the two blast parameters charge weight (W) and stand-off distance (R) is established to assess the blast effect of different charge weights at varying stand-off distances. Indeed, it states that the blast pressure of a small charge weight, W_1, at a small stand-off distance, R_1, will generate the same effect as a bigger charge weight, W_2, at a greater distance, R_2, as illustrated in Figure 2.10, given that both charges have similar properties and the same atmosphere.

Figure 2.11 shows a chart that provides the coefficient when the angle between the shock front and the surface of the target (angle of incidence) is not zero. The charts are the results of the work by Baker et al. [20] & Dharaneepathy et al. [21] and are also provided in the TM5-1300 manual [11].

The third and most convenient method of obtaining blast wave properties is to use software applications developed by individuals or organizations. Some of those computer programs are listed here. ConWEP (Conventional Weapons Effects Program) is a computer program that automates the equations developed by Kingery and Bulmash to predict the air blast properties of spherical and hemispherical explosions. Kingery and Bulmash's equations can also be found in the TM5-855-1 manual [22], which provides procedures for designing and analyzing protective structures subjected to the effects of conventional weapons. Eric Jacques, a former PhD student at the University of Ottawa, developed another computer application, “Over-pressure” [23], which generates pressure-time history diagrams. The software requires the user to input the charge weight, stand-off distance, and angle of incidence, which then provides the blast wave properties. At the University of Toronto, Philip Miller [23] developed a computer program named Vector-Blast. His research study findings showed that the program could accurately calculate pressure-

time histories on the front and rear faces of the structure. A commercial computer program by Applied Research Associates (ARA) called A.T.-Blast [24] also provides blast-loading properties from a hemispherical explosion. The user can enter charge weight, minimum and maximum distance to the explosives, angle of incidence, and the calculation interval. In return, the A.T.-Blast calculates pressure (P), impulse (I), equivalent load duration (t_d), shock front velocity (V), and time of arrival (t_a).

2.3 Blast Effect on Structures and Structural Response

When an explosion occurs, the suddenly released energy is divided into two distinct phenomena: air blast overpressure and thermal radiation, and ground shock generated by the coupling of air and ground reflection. Air blasts are the leading cause of damage or collapse of a structure on the ground. Air blast or blast pressure on a structure comprises three components: i) Incident Pressure- when a shock front generated by an explosion reaches a structure, the pressure instantaneously rises from ambient conditions to a peak known as the incident pressure; ii) Reflected Pressure- as the shock wave strikes and reflects off the surface of the structure (i.e., interaction with the structure), it produces an amplified pressure known as reflected pressure, which is much higher than the incident pressure and represents the actual blast load applied to the structure; iii) Dynamic Pressure (Blast Wind)- following the initial pressure rise, a high-speed air movement known as blast wind impacts the structure, which is influenced by a drag coefficient that varies depending on the geometry and orientation of the structure relative to the blast wave. Eventually, the blast pressure decays exponentially and develops a negative pressure; however, for structural investigations and design, often only the positive pressure is considered (see Figure 2.12).

Since blast loading is a rare event typically studied within military and specialized engineering domains, comparing it to a more familiar dynamic load, such as seismic loading, can help pave the way for broader understanding. Both blast and seismic forces are dynamic in nature, meaning they involve time-dependent forces acting on a structure. However, their characteristics and the way structures respond to them differ significantly. Seismic forces are natural and originate from ground vibrations during an earthquake. These vibrations transfer energy to the structure from the foundation upward, generating internal forces as the ground shakes the building. In contrast, blast loads are man-made and result from explosions, delivering a sudden, intense pressure wave called a blast wave that impacts the structure externally, often at or above ground

level. This effect is more comparable to a shock wave or wind pressure but occurs with much greater intensity. One key difference lies in the duration of these loads: Seismic events typically last several seconds, while blast waves occur over just a few milliseconds. Additionally, a structure's mass tends to work in favor of seismic forces by increasing its inertial response, whereas in blast events, greater mass can help resist the rapid pressure by providing stability and absorbing energy.

Analysis of a structure's response to blast loading is complicated due to various factors, including the effect of high strain rates, the nonlinearity of material behavior, uncertainty in blast load calculations, and dynamic reactions. Nonetheless, to predict and investigate the resistance of a structure against blast loading, the pressure-time history of the air blast must first be generated. The second step involves computing the time history of loading (reflected pressure) acting on the structure and the structure's corresponding response. The tools for conducting such an investigation include empirical and analytical solutions, which require knowledge of dynamic analysis techniques. One of the most commonly used techniques is the equivalent single-degree-of-freedom (SDOF) model analysis. Another technique is the 3D (three-dimensional) finite element modeling, based on multi-degree-of-freedom (MDOF) nonlinear dynamic analysis, using computer applications such as LS-DYNA. In contrast to the simplified SDOF system analysis, the 3D analysis incorporates all the parameters of a structural response, providing an in-depth understanding of the behavior. However, implementing the MDOF nonlinear dynamic analysis requires advanced knowledge of sophisticated computer programs and coding languages.

Blast loading is an extreme event that causes large inelastic deformations in a structure or member. This pushes the resisting element beyond its elastic limit, resulting in an elastoplastic system. In blast-resistant design, structural members are often allowed to undergo plastic deformation to achieve a more economical and energy-absorbing response. These members are designed for the ultimate limit state, and their performance is assessed based on limiting deflections or rotations. In such cases, safety factors may be taken as unity to reflect the extreme nature of blast loading and the need to utilize full member capacity. Figure 2.13a shows a bilinear resistance function that represents the response of an RC element and illustrates the resistance versus deformation relationship. A more realistic resistance function of a flexure-dominant RC element reported in Cormie et al [25] is shown in Figure 2.13b. It can be inferred from the figure that the curve becomes flat after the yielding of the tension reinforcement and remains flat until

the concrete crushes in the compression zone. Concrete crushing usually begins when the rotation due to deflection reaches two degrees. When the member rotation exceeds two degrees, the concrete in the compression zone is thoroughly crushed, and the member will fail if no compression reinforcement is provided. For a well-designed member, when the rotation is between two and five degrees, the member will exhibit a total crushing of compression concrete and cracking of tension concrete (cover). A member may experience higher resistance under high rotational deformation due to steel strain hardening; however, eventually, it will collapse due to loss of stability or structural integrity.

2.4 Single-Degree-of-Freedom Analysis (SDOF)

The structure and loading can be replaced with equivalent systems in blast loading analysis. For the structure equivalency, the SDOF analysis is a simple method where the actual structure or member under consideration is replaced with an equivalent system of a concentrated mass and a weightless spring (see Figure 2.14). The approach assumes that the structure has only one degree of freedom (i.e., it can only move in one direction) in response to the applied loads. The structure is modeled as a mass-spring-damper system, with the mass representing the structure's weight, the spring representing the structure's stiffness/resistance, and the damper representing the energy dissipated due to damping. For loading, considering the uncertainties associated with evaluating blast loads, the blast pressure is replaced with an equivalent triangular impulsive load having a peak value of F_1 and duration of t_d, as shown in Figure 2.14. In SDOF analysis, the applied force is labeled $F(t)$, member mass or structural mass is denoted M, acceleration is $\ddot{u}$, displacement is u, and K is the spring constant. The terms are related to each other in the following form, known as the equation of motion:

$$F(t) = M\ddot{u} + Ku \tag{2.15}$$

The triangular blast pressure as a function of time and the corresponding impulse can be obtained using the following equations:

$$F(t) = F_r \cdot (1 - \frac{t}{t_d}) \tag{2.16}$$

$$I = \frac{1}{2} \cdot F_r \cdot t_d \tag{2.17}$$

The equation of motion for an undamped SDOF model for such loading will take the following form:

$$F_r \cdot (1 - \frac{t}{t_d}) = M\ddot{u} + Ku \quad (2.18)$$

The closed-form solution for the above equation can be expressed as:

$$u(t) = \frac{F_r}{K} \cdot (1 - \cos\omega \cdot t) + \frac{F_r}{K \cdot t_d} \cdot \left(\frac{\sin\omega \cdot t}{\omega} - t\right) \quad (Forced\ vibration) \quad (2.19a)$$

$$u(t) = \frac{F_r}{K \cdot \omega \cdot t_d} \cdot \left[\sin\omega \cdot t - \sin\omega \cdot (t - t_d) - \frac{F_r}{K} \cdot \cos\omega \cdot t\right] \quad (Free\ vibration) \quad (2.19b)$$

where F_r is the peak reflected force, ω is the natural frequency, and T is the natural period of vibration, and are defined using the following relationship:

$$\omega = \frac{2\pi}{T} = \sqrt{\frac{K}{M}} \quad (2.20)$$

The above solution is obtained assuming the blast load is applied statically, while in reality, a dynamic blast load is applied suddenly. To get the value under dynamic loading conditions, the solution is multiplied by a factor known as the Dynamic Load Factor (*DLF*). *DLF* is the ratio of dynamic displacement to the displacement obtained from the static application of blast load F_1. *DLF* can be computed using the following equation as a function of time; however, for simplicity, the maximum *DLF* value, denoted as $DLF_{max,}$ can be obtained and plotted against design parameters. For instance, the diagrams showing the relationship of DLF_{max} and t_d/T ratio illustrated in Figure 2.16, is a valuable design aid for design under impulsive loading [12].

$$DLF = 1 - \cos\omega \cdot t + \frac{\sin\omega \cdot t}{\omega \cdot t_d} - \frac{t}{t_d} \quad (Phase\ I, Forced\ vibration) \quad (2.21a)$$

$$DLF = \frac{1}{\omega \cdot t_d} \cdot [\sin\omega \cdot t - \sin\omega \cdot (t - t_d)] - \cos\omega \cdot t \quad (Phase\ II, Free\ vibration) \quad (2.21b)$$

It is worth mentioning that material behavior will change during the blast loading. Concrete and steel reinforcement in RC members will exhibit higher compressive and tensile strength. This is due to the high strain rate effect of the dynamic nature of blast pressure. To account for the effects of high strain rate on material behavior, a factor denoted as Dynamic Increase Factor (DIF) is developed and prescribed in design standards.

The SDOF analysis for which the equation of motion is derived is based on a concentrated mass (lumped mass) and force. However, the structural element is a multi-degree-of-freedom system with a distributed mass and load resulting from blast pressure. To generate an equivalent SDOF system (equivalent lumped mass-spring model with a concentrated load) of the actual

element, transformation factors are developed and presented in Biggs [12]. The equation of motion for the transformed system takes the following form:

$$M_e\ddot{u}(t) + k_e \cdot u(t) = F_e(t) \quad (2.22)$$

where M_e is the equivalent mass, k_e is the equivalent stiffness, and F_e is the equivalent force.

A noticeable difference between an equivalent SDOF system and the actual structure is the response of a member in terms of reaction. The reaction calculated from the equivalent SDOF model is not the same as that of an actual structure. Because the distribution of applied pressure may be uniform, however, it is not the case for the inertia force, which is a function of acceleration that varies with deflection (see Figure 2.15). In addition, when developing the equivalent SDOF system, the intent was to have the same deflection as the actual structure without considering the force characteristic to be the same. This issue has to be addressed because reactions are of interest for two reasons: the dependency of maximum shear force computations and the design of supporting structures on the reaction forces. The expressions of dynamic reactions for different cases are presented in Biggs [12], which shows that the reaction is a function of resistance and load.

Analyzing the inelastic response using the closed-form solution presented earlier is cumbersome. The alternative solution uses numerical methods such as step-by-step integration procedures, either constant or linear acceleration. However, finding the maximum strength and ductility for design is often sufficient. The US Army developed design charts (UFC charts) that can be used for analyzing the inelastic response of structural elements subjected to blast loading (see Figure 2.17). The charts are prepared based on the results of numerical analysis of the structural elements with different periods subjected to different blast loads and different ratios of ductility. Another method for inelastic analysis of a structure or an individual member is the use of software applications such as RC-Blast [26], SBEDS [27] (Single Degree of Freedom Blast Effects Design Spreadsheets), and Column Blast Analysis Retrofit Design (CBARD) [28].

Analysis of SDOF enables engineers to estimate the maximum displacements, velocities, and accelerations that the structure will experience under real-world conditions. SDOF analysis is a helpful tool for the preliminary design and assessment of structural systems and can provide valuable insights into the behavior of more complex structures. The method is well described in several dynamic analysis books and technical manuals [12], [29], [30]. The accuracy of SDOF analysis depends on selecting an appropriate SDOF system that can represent the underlying

failure mechanism of the structural element. Conventionally, most literature has depicted structural elements as possessing an elastic-perfectly plastic resistance function. However, this idealized approach has crucial limitations that must be considered during the analysis. For instance, the axial load can cause additional lateral deformation and bending in columns subjected to lateral blast pressure, indicating the well-known P-Δ effect. Simultaneously, the axial load can enhance the resistance of the column, thus mitigating the adverse P-Δ effect on the column's response in the early stage of loading. Therefore, ignoring axial-load effects while studying a structure's response to blast loads may not accurately reflect the structure's actual behavior [31].

Many researchers conducted studies to improve or modify the equivalent SDOF such that the effect of axial load, high-strain-rate effect, and material nonlinearity are considered [32], [33], [34]. For instance, Liu et al. [6] investigated the blast response of RC columns by implementing the improved SDOF, numerical approach, and experimental program. A total of 11 half-scale RC columns were tested against blast loading generated by TNT explosives. For the dynamic analysis, an improved equivalent SDOF was suggested. The SDOF analysis was developed based on the resistance function considering the complex feature of material behavior, the effect of axial load, strain rate effect, and column geometry. The maximum displacement predicted using the SDOF system was consistently in agreement with the results obtained from the experimental results.

2.5 Blast Hardening Techniques of Columns

Blast mitigation can be achieved by applying one or a combination of several protection measures (soft and hard). Increasing the stand-off distance is the most efficient measure; however, it is not always practical in urbanized neighborhoods [35]. Another measure is the use of a cladding façade (sometimes sacrificial claddings) to distribute the blast pressure and prevent severe loading of an individual member [36]. However, this may not always be possible due to architectural constraints or the structure's functionality and structural capacity limitations. The role and effectiveness of architectural planning to mitigate blast effects are also studied in the literature [37]. When the former measures cannot be implemented or are insufficient, then hardening/strengthening is the alternative measure to be implemented. In this method, the strength and ductility of the structures are enhanced by applying superior material to the existing member or using energy-absorbent materials and techniques.

Elastomeric coatings are an emerging material and technique for strengthening structural members against blast loading and ballistic protection. Polyurea is a material formed by the

reaction between isocyanate and amine, producing a heterogeneous landscape with a nano-segregated microstructure. It was initially developed for the automotive industry and has been commercially available since the 1990s in the construction industry. It was first used by a U.S. military organization, the U.S. Air Force, to retrofit walls. Polyurea's popularity is due to its ability to neutralize blast waves after capturing them and its dynamic transition from rubber to glass when subjected to high-strain-rate loading. It exhibits high strain before failure when subjected to dynamic, intense loading, such as blast and impact loads. It presents noticeable properties, including high elongation and strength, rapid curing time, and excellent tear and tensile strength, as well as flexibility, hardness, and ease of installation. Its adherence to various substrates, such as metal, timber, concrete, etc., is essential to this material. However, the disadvantages of this method are the need for rapid mixing of reactants or else it sets in seconds, strict safety requirements when spraying it on the object under consideration, and the costly application process [38], [39].

Several methods have been investigated and proposed for hardening/strengthening RC columns. For instance, Ultra High-Performance Fiber Reinforced Concrete (UHPFRC), Ultra High-Performance Concrete (UHPC), concrete-filled steel tubes (CFSTs), and well-detailed designs of transverse reinforcement (increasing the number of stirrups) are recommended for constructing or strengthening blast-resistant RC columns. The primary concern for the engineering community regarding existing buildings is the strengthening of columns that are particularly vulnerable to explosions, as these members were not originally designed to resist such extreme loads. Various materials and methods of strengthening RC columns are reported in the literature. The researchers primarily focused on using fiber-reinforced polymers (FRPs) applied externally to the columns. Additionally, the use of a steel jacket for strengthening the columns is recommended. There are also some less-studied methods for strengthening structural members against blast loading, including concrete-filled FRP tube columns, aluminum foam layers, the use of shape memory alloys (SMAs), and the application of Engineered Cementitious Composites (ECC) layers [4], [40]. The following sections present a summary of the proposed and applied retrofitting techniques to enhance the blast resistance of RC columns:

2.5.1 Seismically/Well-Detailed Columns

Protective design measures against blasts are not commonly adopted in civilian infrastructure worldwide. The alternative practical measure suggested by many researchers is implementing

seismic design and detailing to enhance the seismic and blast resistance of buildings. Seismic detailing enhances the ductility of columns and prevents progressive collapse resulting from the loss of columns. Studies reported in the literature and summarized below have shown that an increase in the ratio of transverse reinforcement enhances the impact and blast resistance of the structural member. Seismic detailing enhances the response of the column subject to blast pressure. In contrast to columns under gravity loads that are conceptually designed to undergo elastic deformations, blast columns, similar to seismic columns, undergo large inelastic deformations and crushing of the core concrete. Increasing the transverse reinforcement ratio results in better confinement of core concrete and its integrity, which can improve ductility. Improvement in ductility is conditioned by the level of axial load and whether the axial load can contain the neutral axis within the confined core [41]. Additionally, transverse reinforcement enhances the shear capacity and provides lateral support for the longitudinal reinforcement, thereby restraining it from premature buckling. Seismic detailing emphasizes the use of closely spaced ties over potential plastic-hinging or shear-critical regions. However, blast loading will not necessarily occur only at the shear critical region, and the likelihood of higher pressure at mid-height can compromise the integrity of seismically detailed columns. Additionally, well-detailed columns may have more congested reinforcement, which can pose a challenge for construction. In this section, research studies focusing on the effect of seismically/well-detailed columns improving the resistance against blast loading are summarized:

Tahzeeb et al. [42] investigated the influence of circular ties and helical/spiral transverse reinforcement on the blast resistance of RC circular columns. In addition, the study examined the role of CFRP ties and wrapping of the same columns with CFRP & steel sheets under blast loading. A total of nine axially loaded columns modeled using a FEM computer application known as ABAQUS/CAE was analysed under blast loading generated by 80 kg of TNT placed 1.5m above the ground surface and a scaled distance of 1 m/kg^3. From the nine columns tested in this study, one square column (C1) was modeled to replicate the experimental test from the literature [46], verifying the developed ABAQUS model for testing eight circular columns with a diameter of 350 mm. The tested columns had different types of transverse reinforcement, such as circular ties only in the plastic hinge regions or over the entire height (C2 and C3), spiral transverse reinforcement (C4), CFRP ties over the whole height (C5), 2mm steel sheet wrapping on the columns with circular ties or spiral over the entire height (C6 and C7), and 2mm thick CFRP wrapping on the

columns with circular ties or spiral on the whole height (C8 and C9). All the columns were loaded with 950 kN of concentric axial load during the blast loading. The test results indicated an enhancement of the column response against blast loading when extra transverse reinforcement (as required by seismic guidelines) is provided. The enhancement was more pronounced in the case of spiral reinforcement and was further improved by combining helical reinforcement with external CFRP wrapping.

Lee et al. [47] conducted an experimental and analytical investigation into the behavior of seismically designed RC columns subjected to blast and impact loading. A total of six RC columns, with dimensions of 160 x 160 x 2468 mm, were designed and built to achieve the study objectives. Out of six specimens, three were tested under a simulated blast wave generated by a shock tube testing facility at the University of Ottawa, as shown in Figure 2.18. The columns tested under blast loading were the control column (NC), seismically detailed column (SC), and UHPFRC jacket retrofitted column (UC). The generated blast pressure was transferred to the column and distributed uniformly using a load transfer device made of steel sheet and hollow structural steel (HSS) sections. A partially fixed support condition was used to restrain the rotational movement somewhat. An axial load equivalent to 40% of the column's concentric capacity was applied using a hydraulic jack. For numerical investigation, a finite element analysis (FEA) was conducted using the commercial software application LS-DYNA. LS-DYNA is a specialized application in the dynamic analysis of nonlinear transient loading as a function of time. The test results from the experiment and numerical study indicated that seismically detailed columns and columns with UHPFRC result in less maximum and residual displacement, as well as better blast load resistance. The column with combined seismic detailing and retrofitting using a UHPFRC jacket exhibited better blast load resistance compared to NC and SC columns. The study concluded that the selection of the retrofitting method depends on the expected failure mode (i.e., local or global). If local damage is expected, then UHPFRC should be considered.

Kyei and Braimah [43] numerically investigated the performance of seismically detailed RC columns with dimensions of 300 x 300 x 3000 mm subjected to blast and axial loading combined. The study was conducted on three types of columns: conventional columns (i.e., 300 mm spacing of transverse reinforcement), Seismic-1 detailed columns (i.e., reduced stirrups spacing to 75mm in the plastic hinge region), and Seismic-2 detailed columns (i.e., reduced stirrups spacing to 75mm in the plastic hinge region and mid-height region). Numerical modeling was

performed with LS-DYNA simulation of blast loading using the Load Blast Enhanced (LBE) keycard. LBE produces a blast load based on the blast load calculation code called ConWep (Conventional Weapons Effects Program). To validate the finite element numerical models of their study, the result of an experimental test from the study by Siba [44] was compared with the obtained results. The study findings showed that closely spaced transverse reinforcement resulted in less displacement at close-in explosions (i.e., small-scaled distance). The presence of axial load reduced lateral displacement due to blast loading. However, a higher applied axial load to axial resistance ratio (ALRs) resulted in concrete crushing in compression and buckling of longitudinal bars at the mid-height region.

Kadhom et al. [45] investigated the response of seismically designed and gravity-designed columns subjected to simulated blast load using a shock tube facility at the University of Ottawa. Four RC columns with dimensions of 150 x 150 x 2400 mm axially loaded to 54% of their concentric capacity were subjected to shock tube testing. The blast pressure was transferred uniformly through a load transfer element consisting of thin steel sheets and hollow structural steel (HSS) stiffeners. Two of the four columns were reinforced with transverse reinforcement spaced 37.5 mm apart to achieve seismically detailed columns that resist lateral loads. The other two columns were designed for gravity loads with transverse reinforcement with 100 mm spacing. The test results showed that the two gravity columns exhibited mid-height displacements of 125.3 mm and 157 mm at 51 kPa and 53 kPa of reflected pressure, respectively. At these displacements, the axial load dropped to 47 kN and 16.7 kN from 411 kN and 402 kN before blast loading, respectively. The columns failed due to concrete crushing at the compression face, and longitudinal bars buckled at the critical section. However, the seismic columns exhibited less mid-height displacement, equal to 114.9 mm and 130.3 mm at similar reflected pressures. The axial load measured at the instant of these displacements dropped to 140.9 kN and 80 kN from 420 kN before blast loading, respectively. The columns exhibited concrete crushing at the compression face and extensive tension cracks at the critical section. The results indicate that increasing the transverse reinforcement ratio enhances the resistance of the tested columns, thereby improving the structural performance of RC columns in the event of an explosion.

Bao and Li [46] conducted a numerical study investigating the behavior and residual axial strength of RC columns subjected to blast pressure generated by a close-in explosion (i.e., short stand-off distance). An explicit nonlinear finite element modeling (FEM) application, known as

LS-DYNA, was adopted to perform a numerical simulation. The result of their finite element model was verified against correlated experimental results reported in the literature. The study included modeling 12 columns for parametric analysis. The columns had the exact dimensions (355 x 355 mm) but varying heights of 3480, 2840, and 2130 mm, divided into groups of four columns per height. The columns were designed with varying properties to investigate the effects of axial load ratio (ALR), transverse and longitudinal reinforcement ratios, and column aspect ratio. The simulated blast pressure was modeled, assuming a stand-off distance of 5m and a charge weight of 0-1 ton of TNT, to result in different levels of damage to the tested columns. The test results showed that gravity columns or columns designed for conventional day-to-day loads exhibited more deflection than those designed according to seismic load requirements. This indicates that seismic detailing reduces blast-associated damage, thereby enhancing the response of columns in the event of an explosion. The study findings showed that columns with a low level of applied axial load exhibited more ductile behavior than those with a high axial load. It was due to the effects of the secondary moment, also known as the P-Δ effect, created by the high axial load at the instance of high mid-height displacement. The increase in longitudinal reinforcement ratio proved effective in reducing mid-height displacement, but it will not necessarily improve the blast response. This was related to the change in failure mode from flexure to shear, which occurred when the flexural capacity exceeded the shear capacity due to an excessive amount of longitudinal reinforcement. It was also found that under high, long-term axial loads, the columns exhibit a smaller ratio of residual axial strength. The study concluded with a proposed equation to predict the ratio of residual axial load capacity, considering the ratio of mid-height displacement to the column height.

Williamson et al. and Davis et al., [47], [48], [49] studied the blast response of bridge columns in an experimental program using live explosives, as shown in Figure 2.19. The study was conducted to evaluate the design parameters with a significant impact on the blast performance of bridge columns. The study consists of two phases. Phase I aimed to assess the structural loads on bridge columns from different stand-off distances and charge weights, considering both square and circular cross sections. Phase II consisted of several experimental tests focusing on small stand-off distances (close-in explosions) and contact charges. A total of 10 half-scale columns with eight different designs were tested under small stand-off blast loading to investigate the effects of five parameters: volumetric reinforcement ratio, cross-section shape, aspect ratio (L/D), transverse

reinforcement type, and splice location of longitudinal reinforcement. The cross-sectional shapes included in their study were circular (18- and 30-inch diameters) and square (30 x 30 inches); two aspect ratios were included, lower (large diameters) and higher (small diameters), representing single-column bents and multicolumn bents, respectively. Two splice configurations were considered: one near the base and one without any splice, representing typical and seismic columns, respectively. The types of transverse reinforcement considered were hoops/ties and spirals. The columns were categorized into three types according to the load demand criteria. They were denoted as gravity, seismic, and blast-resistant columns depending on the volumetric ratio of transverse reinforcement. For the blast-loaded designed columns, the volumetric ratio of transverse reinforcement was 50% higher than the seismically detailed columns. The reason for having a higher volumetric reinforcement ratio in blast design columns was the possibility of plastic hinging over the entire column height due to uncertainty associated with the location of blast loading. All the columns were cast using 28 MPa concrete and reinforced with 1% longitudinal reinforcement, having a yield strength of 420 MPa. The columns were subjected to a close-in field explosion, but the data was not shared due to confidentiality. From the analysis of the test results, it was found that the scaled stand-off distance significantly affects the performance of RC columns. Test results demonstrated that the chances of column survival increase considerably with a little increase in stand-off distance to avoid contact-charge explosion. The shape of the cross-section plays a crucial role in reducing the magnitude of reflected pressure, thereby decreasing blast pressure on a column. Therefore, the circular section was favored over the square or rectangular cross-section. The test results showed that the gravity columns with discrete ties and standard hooks had the lowest resistance against blast loading, exhibiting brittle shear failure and anchorage failure of the hooks. Shear failure was the typical failure mode; however, most tested columns had sufficient shear capacity, which minimized spalling and prevented a breach. The dominant failure mode for the tested specimens was direct shear, which can be controlled by increasing the volumetric reinforcement ratio, resulting in improved confinement, ductility, and shear capacity. Hence, the test results showed that seismically designed columns performed better than those designed for gravity. The type of transverse reinforcement significantly affected the response of the tested columns, and the results showed that continuous spirals were more effective than discrete hoops, as they provided better confinement of the core. The study concluded with proposed guidelines for designing and detailing RC bridge columns against potential blast loading. The proposed

guidelines recommend using discrete hoops with adequate anchorage or continuous spirals, increasing the ratio of transverse reinforcement that covers the entire height, and avoiding longitudinal splices to improve the blast resistance behavior of columns.

Lloyd [50] conducted experiments on fourteen half-scale reinforced concrete columns subjected to shock-wave loading induced by a shock tube. 12 of the columns were 100 x 150 mm in cross-section, and two were 150 x 150 mm. The columns were reinforced with four 10M longitudinal reinforcing bars and 6.3mm smooth round bars as transverse reinforcement. Transverse reinforcement was added in the form of closed hoops spaced at h/2 or h/4 for the entire height of the column. The columns with smaller transverse steel spacing were intended to represent seismically designed columns, while those with larger spacing represented gravity loaded columns. Axial loads ranging from 28% to 42% of the concentric capacity were applied to the columns, with concrete strengths ranging from 46.5 MPa to 58 MPa during testing. The study concluded that there was a significant variation in axial load during the dynamic response of the columns. This was due to the ends of the columns moving toward the column height with horizontal displacement. The responses of the seismic and non-seismic columns were not significantly different, which was attributed to the column's slenderness and the small area of the core concrete, making confinement effects negligible. The close spacing of the transverse ties prevented reinforcement buckling during the dynamic response for both column types. The authors also performed SDOF analysis to predict the column displacement at mid-height and then compared the predictions with actual test results. It was found that the SDOF model accurately predicted the maximum displacement of test specimens under moderate levels of response. However, for large displacement responses, the model underestimated the displacements. The SDOF model was found to perform well in predicting the displacements of columns that experienced severe damage, approaching the point of collapse. The study concluded with a recommendation to investigate the effect of increasing the cross-sectional dimensions and to monitor the degradation of axial load through the use of load sensors and time history analysis.

2.4.2 Columns Made of FRC, UHPC, and UHPFRC

UHPC and UHPFRC are cement-based composites that exhibit superior mechanical properties compared to conventional Ordinary Portland Cement (OPC) concrete. These mixes are generally obtained by using workability admixtures, lower water-cement ratio, steam curing with heat, and the incorporation of discontinuous fibers. UHPC can provide a compressive strength reaching up

to 200 MPa, a modulus of rupture around 40 MPa, and a strain-hardening response when subjected to a direct tension test [51]. It is reported in the literature that these materials can improve damage tolerance and enhance the strength, ductility, and toughness of the structural member. These improvements can enhance the resilience and performance of the structure when subjected to blast and impact loads. Whether used with fibers or without, it can dissipate higher energy compared to OPC concrete under extreme loading conditions. UHPC and UHPFRC also enable the inclusion of high-strength steel, which results in higher strength and ductility. UHPFRC is a suitable construction material for enhancing the column's performance, minimizing seismic detailing requirements, and preventing progressive collapse. In addition, UHPFRC is also used as a protective layer for existing structural members subjected to blast loading. However, despite the numerous benefits provided, the amount of fiber that can be incorporated into the mix is limited due to workability concerns. One drawback of these materials is the high cost compared to conventional OPC concrete because they need special treatment when mixing and casting [52]. In this section, previous studies of interest focusing on the blast response of columns made using UHPC and UHPFRC are summarized:

Hammoud et al. [53] conducted an experimental study investigating the response of columns made of high-strength concrete and high-strength reinforcement subjected to simulated blast loading using a shock tube. The study parameters were the type of concrete, type of longitudinal steel reinforcement, the ratio of longitudinal reinforcement, and seismic detailing. An analytical investigation was also part of the program, utilizing nonlinear SDOF and finite element modeling to predict the response of the tested columns to blast loading. A total of 10 columns, divided into two groups, were tested, where six columns were prepared using normal strength grade (400 MPa) reinforcement with either regular strength concrete (NSC) or high strength concrete (HSC). The remaining four columns were made of high-strength reinforcement (Grade 690 MPa) and high-strength concrete. The reported strength of the concrete was 35 MPa for NSC and 80 MPa for HSC. The columns' dimensions were 152 x 152 mm with a height of 2.44 m, a span of 1.98 m, and axially loaded to 30% of their concentric capacity. The longitudinal reinforcement ratio was 1.2% to 3.4%, and transverse reinforcement spacing was chosen to represent seismic and non-seismic columns. The test result illustrated that the NSC column and HSC exhibited significant damage and mid-height displacement when subjected to around 85 kPa reflected pressure. However, the maximum and residual displacements were 17% and 14% lower,

respectively, in the case of HSC columns. Both columns failed due to concrete crushing and cover spalling, with a greater extent of cover spalling for the HSC column. It was found that high-strength concrete (i.e., twice as strong as normal-strength concrete in this study) did not noticeably improve the blast response of the columns. Test results for both normal-strength bars and high-strength bar columns demonstrated that seismic detailing enhanced performance by minimizing core concrete damage and preventing bar buckling in compression. Seismic detailing reduced maximum displacement and residual deformations for both the columns with grade 400 MPa steel reinforcement and grade 690 MPa reinforcement bars. In addition, closely spaced ties in HSC columns with high-strength steel resulted in the rupture of tension reinforcement at failure. Increasing the ratio of longitudinal reinforcement reduced the maximum deformations. It improved the blast performance of columns such that columns with a higher reinforcement ratio could sustain an enormous blast load before failure. Columns with high-strength steel exhibited failure due to rupture of tension reinforcement, and the failure was delayed by using a higher ratio of steel reinforcement. This indicates that increasing the longitudinal reinforcement ratio significantly improves blast response. It was also observed that high-strength steel better controlled the maximum and residual deformation of the columns at failure, thereby reducing the damage. Moreover, high-strength steel provided better blast resistance at a lower steel ratio than conventional steel reinforcement. The analytical results showed that SDOF analysis and FEM analysis using LS-DYNA can offer a reliable and efficient prediction of column response against blast load. The accuracy of the FEM analysis was slightly better than the SDOF analysis.

Xu et al. [54] investigated the blast performance of UHPFRC and high-strength reinforced concrete (HSRC) columns subjected to actual blast loading, as shown in Figure 2.20. The tested columns had dimensions of 200 x 200 mm and a span of 2.5 m. The columns were tested at close-in explosions with a stand-off distance of 1.5 m, but with varying charge weights (1 to 35 kg of equivalent TNT). Eight columns, four made of UHPFRC and four made of HSRC, were designed to have a compressive strength of 148 MPa at 28 days. The columns were reinforced with high-strength steel having a yield and ultimate strength of 1450 MPa and 1600 MPa, respectively. Two columns from the Set of UHPFRC columns were loaded axially to 20% of their capacity, and two columns from the Set of HSRC columns were loaded with 1000 kN axial load. The test results indicated that axial load reduced the mid-height displacement under blast loading for both the UHPFRC and HSRC columns. However, it was presented that at large deflections and the

formation of plastic hinges, the axial load further increases the stress and displacement due to the P-Δ effect. Therefore, the assessment of the damage scenario revealed that a higher axial load, combined with the simultaneous application of a blast load, resulted in more severe damage to the tested HSRC columns. It was also noted that the UHPFRC columns exhibited 23% less deflection than their HSRC counterparts, indicating the effectiveness of the steel fibers.

Aoude et al. [55] investigated the response of columns made with UHPFRC subject to blast loading generated by the shock tube facility at the University of Ottawa. There were nine full-scale columns with different properties in terms of the type of concrete, dosage and properties of fibers, spacing of stirrups/transverse reinforcement, and the ratio of longitudinal reinforcement. The columns were divided into two sets; the first set comprised of four columns aimed to study the effect of fiber content and seismic detailing, and the type of concrete on the blast response of tested columns, and the second set comprised of five columns was designed to study the effect of longitudinal reinforcement ratio and properties of fibers on blast response. All the tested columns were 152 x 152 mm with a clear span of 1980 mm and were cast with conventional self-compacting concrete ($f'c$ = 52 MPa) and UHPFRC ($f'c$ = 128 to 169 MPa). The columns were tested in a partially fixed support system under a combined axial load (30% of the concentric capacity) and a simulated blast load. The columns were tested under varying degrees of blast pressure in multiple hits until they failed. The onset of failure was characterized by the simultaneous crushing of concrete in compression and the buckling or rupture of longitudinal reinforcement. A comparison of the test results with those of an earlier study by Burrell et al. [60], in which tested columns had identical properties but different concrete strengths, shows that UHPFRC columns experienced relatively minor damage. Test results indicated that using UHPFRC resulted in less maximum and residual mid-height displacement and prevented buckling of compression reinforcement at equivalent blast loads compared to normal-strength concrete. The damage tolerance was increased, and secondary blast fragments were eliminated. In addition, it was found that using UHPFRC improved confinement, as the failure was primarily due to the rupture of bars in tension. This was also evident when comparing the test results with the behavior of control columns from the Burrell et al. [60] study, which showed that UHPFRC columns with moderate transverse reinforcement performed better under higher blast loads. Increasing the fiber dosage positively affected the blast performance of the tested columns; however, this effect was negligible beyond 4% due to a volume increase in fiber content. Using fibers with higher tensile strength and aspect ratio resulted in

improved blast performance for the tested columns, which exhibited lower maximum and residual displacements. The columns with higher longitudinal reinforcement did not exhibit rupture of tension reinforcement. The blast performance of columns was further enhanced when the UHPFRC and seismic detailing effects were combined in a single column.

Burrell et al. [56] studied the response of columns cast with steel fiber reinforced concrete (SFRC) subjected to simulated blast load generated by a shock tube at the University of Ottawa, as shown in Figure 2.21. The parameter considered in the study was the volume of steel fiber content and spacing of transverse reinforcement that represents seismic and non-seismic columns. Eight self-consolidating concrete (SCC) columns were tested in two batches: two control specimens with SCC only and six columns with SCC and steel fiber content. The tested columns represent half-scale ground-floor columns, which will be the critical structural element in preventing progressive collapse and an easy target for malicious attacks. The columns' dimensions were 152 x 152 mm, and they were designed in accordance with CSA A23.3 for both seismic and non-seismic columns. The columns had the same stirrup spacing over the entire height, with 38mm and 75 mm spacing for seismic and non-seismic columns, respectively. The dosage of steel fiber used in the mix with SCC ranged from 0% to 1.5%. One column was cast with a high-strength fiber content. The columns were tested and subjected to multiple shock waves (ranging from low to high) generated by the shock tube, and were loaded axially during blast loading to 30% of their concentric capacity. The test result showed that when the blast pressure hits the column, it results in horizontal displacement that can shorten the column compared to its initial height before the blast test. This shortening results in a reduction of the column's axial load under blast loading because the rate of horizontal displacement due to the supersonic velocity of the blast load is higher than the rate at which the gravity load acts [41]. The axial load reduction momentarily recovers to its original level after the blast wave decays. The test results indicated that seismic detailing reduced the maximum displacement and residual displacement and prevented bar buckling on the compression side. The incorporation of steel fibers resulted in a reduction of both the maximum and residual displacement at mid-height. The improvement in blast performance was proportional to the amount of fiber content used in the mix. The enhancement is due to the addition of steel fibers. This can be attributed to the increase in stiffness, enhanced damage tolerance with reduced concrete fragmentation, and the development of post-cracking strength through the fiber bridging of the cracks. However, even though the SFRC columns were comparable to seismic columns in

terms of mid-height displacement, the compression bar buckling was not prevented in the case of SFRC columns. Significant blast-resistant behavior was observed in columns with SFRC and seismic detailing, characterized by closely spaced transverse reinforcement.

Astarlioglu and Krauthammer [57] conducted a numerical study to investigate the behavior of NSC and UHPFRC columns subjected to blast loading. The study parameters included concrete type, different levels of blast pressure, the effect of boundary conditions, and the axial load level. Dynamic analysis was conducted using the SDOF model, which was implemented in the computer code Dynamic Structural Analysis Suite (DSAS). DSAS is an advanced analysis program for structures that couples structural elements with a fast-running SDOF engine to the nonlinear resistance function produced by a displacement-controlled finite element solver. The tested columns had a square cross-section with dimensions of 406 mm x 406 mm and a span of 3.66 m and were designed as non-seismic columns. The columns were made using NSC of 27.6 MPa strength, UHPFRC of 164.1 MPa strength, and grade 60 steel reinforcement. The columns were tested under simply supported and fixed support conditions, with varying axial loads corresponding to the ultimate concentric capacity, yielding of the reinforcement, 10% of the concentric capacity, and no axial load. The columns were subjected to four different blast pressures generated by varying combinations of charge weights and stand-off distances. In total, 16 cases were investigated using a combination of four axial loads with four blast configurations for the NSC and UHPFRC. Test results showed that simply supported NSC columns did not fail under low blast load intensity and performed better when the axial load was increased. However, it could not survive the combination of medium-low and medium-high blast intensities with higher axial loads. In contrast, the simply supported UHPFRC exhibited a linear elastic response under blast load with lower intensity and minor plastic deformation under blast load with medium-low intensity. The UHPFRC columns exhibited significant plastic deformations under medium- to high-blast loads, and failure was observed with the high axial load case. The fixed support condition enhanced the performance of both NSC and UHPFRC. Overall, the UHPFRC columns exhibited less mid-height displacement than the NSC columns, with reductions of 27% and 30% for simply supported and fixed support conditions, respectively. Moreover, the study results showed that the UHPFRC columns subjected to blast loads resisted more than four times the load of an NSC column and could survive before failure.

2.4.3 CFSTs Columns

Concrete-filled Steel Tubes (CFSTs) are a well-known method for improving the shear resistance of columns against seismic loading. CFSTs are known as the new steel-concrete composite member, inheriting high strength and significant durability. One type of CFST is the hollow steel-concrete element constructed by pouring concrete between two steel tubes placed concentrically, which acts as a confining mechanism to the hollow core concrete. This type of CFST is known as concrete-filled double-skin tubes (CFDST). Considering the improvements provided by the CFSTs and steel jacketing, they are also adopted to enhance the blast resistance of RC columns in bridges and buildings. However, the difficulty of installation and the vulnerability to corrosion of such a method result in increased maintenance costs. In this section, previous studies investigating the effectiveness of CFSTs in improving the resistance of columns against blast loading are summarized:

Cui et al. [58] studied the behavior of concrete-filled steel tubular (CFST) columns against close-in blast loading and assessed the associated damage. The study included an experimental investigation and a numerical analysis. Their study tested two types of CFST: one was a normal solid-section (NSS), and the other was the hollow double-skin CFST, also known as CFDST. The NSS columns had a diameter of 273 mm and a steel thickness of 7 mm. They were filled with concrete with a compressive strength of 40 MPa. The CFDST columns were made of two steel pipes, with an outer diameter of 273mm and an inner diameter of 50mm, respectively, and a thickness of 7mm for the outer pipe, while the inner pipe had a thickness of 3mm. The CFDST column was also filled with 40 MPa concrete between the inner and outer pipes. The columns were subjected to a charge equivalent to 50 kg of TNT at a 0.5 m stand-off distance, placed at the mid-height of the columns. Test results showed that both columns exhibited significant plastic deformation on the surface facing the blast, resulting in the crushing of the inner concrete. The damage to the inner concrete of CFDST columns was less than that of the NSS column, while the deformation of NSS columns was less than that of the CFDST column. The mid-height deflection of the CFDST columns was 195 mm, while for the NSS columns, it was 135 mm. The results suggest that the blast response of the NSS columns was better than that of the CFDST column. For the numerical analysis, LS-DYNA software was used to establish a FEM model considering the experimental results. The numerical simulation results fell within the acceptable range, with experimental findings indicating that the mid-height deformation of the hollow section was higher

than that of the solid section. They established two damage assessment criteria: the columns are deemed safe if the mid-height deflection is less than 1/60 of the column height, and they are considered unsafe if it exceeds this ratio. The study concludes by presenting a mathematical formula to generate a pressure impulse curve for the two types of columns tested.

Li et al. [59] studied three circular CFDST columns with an internal diameter of 159 mm, an outer diameter of 325 mm, a thickness of 6 mm for both the outer and inner pipes, and a height of 2.5 m. The columns were subjected to various standoff distances (i.e., 200 and 300 cm) and charge weights of 5 and 8 kg of TNT. For numerical modeling, a commercial computer program known as LS-DYNA was used to conduct nonlinear dynamic analysis. The columns were loaded with an initial axial load of 500 kN, corresponding to 10% of column concentric capacity. In the numerical modeling, multiple tests were performed by changing the charge weight, stand-off distance, axial load ratio, and charge setup. Experimental test results indicated that the damage was primarily local denting on the blast face, resulting from the close-in explosion, without significant global deformation of the entire column. With the increase in charge weight, the steel tubes exhibited local yield in the vicinity of the explosion. Further exploration revealed severe damage to the core concrete as well, indicating plastic deformation of the concrete material around the height of the blast from the ground. The numerical results agreed with the experimental findings because they predicted similar damage patterns and deformations. The results illustrated that more than 70% of the energy from blast loading was absorbed by the core concrete, emphasizing the effectiveness of concrete fillers in CFDST columns. Meanwhile, the steel tubes provide good confinement to the core concrete, enabling the concrete to absorb more energy without spalling. The explosive charge setup, in terms of shape and dimension, proved to have a significant effect on blast loading. It was revealed that increasing the axial load enhanced the resistance of columns against blast loading. This is attributed to the fact that the P-Δ effect is not triggered because, in the close-in explosion, the columns did not experience a sizeable global deflection.

Zhang et al., [60] conducted an experimental and numerical study to investigate the behavior of a CFDST filled with steel fiber-reinforced concrete (SFRC) subjected to blast loading. The CFDST was composed of square cross-section inner and outer steel tubes filled with UHPFRC. A total of six CFDST columns were prepared using square hollow inner and outer sections filled with a UHPFRC having a compressive strength of 170 MPa. A numerical study was

performed, and a numerical model using an FEM computer (LS-DYNA) was developed. In addition, a parametric study was conducted using the numerical model, considering various parameters such as the ratio of axial load, outer and inner steel tube thickness, concrete strength, and the geometry of the outer and inner cross-sections. To investigate the effect of the mentioned parameter on blast resistance, a total of 33 numerical specimens were modeled. The tested specimens had a length of 2.5 m and dimensions of 210 mm and 100 mm with 5 mm thickness for the outer and inner sections, respectively. The tested columns were subjected to a reflected pressure generated by 35 and 50 kg of TNT at a 1.5 m stand-off distance and a simultaneous application of 1000 kN axial load, corresponding to 25% of the concentric capacity. The test result indicated that columns built with CFDSTs can sustain severe blast pressure without buckling steel tubes or crushing hollow-core concrete. Increasing the charge weight from 35 to 50 kg resulted in large mid-height displacement, which was more evident in the columns without any applied axial load. A good agreement was reported between the experimental results and the numerical modeling outcomes. The numerical study found that increasing the ratio of axial load up to a certain level reduces the mid-height displacement; however, larger axial loads affected the columns' behavior at higher mid-height displacements. Using high-strength concrete was beneficial in reducing residual displacement compared to normal-strength concrete, but it had a slight impact on maximum displacement. It was also reported that the blast resistance is improved by increasing the thickness of the outer and inner sections. However, this effect was more pronounced in the outer section thickness increment.

Wang et al., [61] studied the resistance of concrete-filled steel tubes (CFST) against blast loading and investigated the tested columns' residual strength. A total of 8 columns with varying steel tube thickness, charge weight, and cross-sectional shape were subjected to a close-in explosion in an experimental testing program. The tested columns had a tube thickness of 2.8 mm & 3.8 mm with either a square cross-section or a circular cross-section. The square columns had a dimension of 200 x 200 mm, while the diameter of the circular columns was 194 mm. The filler concrete had a compressive strength of 47.4 MPa, and the steel tube's yield strength ranged from 300 to 500 MPa, depending on the steel thickness. The columns were loaded with an axial load exceeding 500 kN and a TNT equivalence charge ranging from 25 to 50 kg, with a stand-off distance of 1.5 m. Test results showed that all the tested columns exhibited global flexural failure, with signs of local buckling failure only in columns with square cross-sections. It was evident from

the test results that increasing the charge weight resulted in increased mid-height displacement. However, the higher thickness of the steel tube resulted in less mid-height displacement. The results from the residual strength test revealed that square columns experienced concrete crushing and spalling at the core, whereas the core of circular columns was split into three pieces. Additionally, it was noted that the residual capacity of CFST-tested columns was approximately 60%. The columns with a square cross-section and higher steel tube thickness showed a better residual strength ratio.

Zhang et al. [66] numerically studied the blast response of CFDST subjected to a ConWep air blast loading model generated using LS-DYNA. In a parametric study, the effect of axial loading and charge weight was investigated, and the mode of failure was analyzed. The columns modeled had a circular cross-section with a height of 3.9 m and thicknesses of 9.3 mm and 3.18 mm for the outer tube (400 mm diameter) and inner tube (190.7 mm diameter), respectively. The columns were loaded with varying axial loads and pressure from spherical TNT charges of 400 kg, 800 kg, and 1200 kg at a stand-off distance of 2 m and 1.5 m above ground level. The results showed that a greater charge weight created the most significant displacement, with a residual displacement of 0.2 m at mid-height. At the beginning of the blast loading, the base shear force was high and then decayed with the increase in mid-height displacement, but the column lost its shear capacity at the end of the blast loading phase. The results illustrated that axial load had a limited effect on moment capacity, shear forces, and maximum displacement. However, it significantly affects the residual displacement and curvature, negatively impacting the damage to the members. The failure modes observed in this study were flexural, shear, and a combination of both damage types; however, flexural failure was more pronounced in most of the modeled columns.

Fujikura et al., [62] conducted an experimental investigation of a bridge pier system against blast and seismic loading, a so-called multi-hazard system that did not act simultaneously. In the study, a prototype multicolumn pier-bent system made of concrete-filled steel tubes CFST columns is developed and tested against blast loading. The experimental findings are compared with a simplified analysis using a SDOF dynamic analysis. The study considered the effect of blast loading from a small vehicle bomb under the bridge deck at a close distance to the piers. Initial investigation revealed that steel jacketing alone could not withstand extreme blast loads due to the large base shear forces at the location of the discontinuity between the jacket and the foundation.

Therefore, the proposed multicolumn pier-bent was designed using CFST, a continuous system integrated into the footing. The multicolumn system had a connected foundation beam and cap beam made of a concrete-embedded C-channel. The columns were made of 42 MPa concrete and had a yield strength of 254-419 MPa for the round HSS sections, respectively, but were multiplied by DIF. A 1/4-scale model of two identical multicolumn bridge pier systems, each with three circular piers of different diameters, was tested. In all cases, the columns were subjected to multiple explosions on different sides, but above ground level. The charge weight varied in each test, and the stand-off distance was also reduced, which created more significant damage to the columns. The test results showed that the multicolumn system can effectively sustain blast loads, as the initial damage was observed only in the form of denting of the steel tube and cracking of the core concrete on the tension face. With the increase in charge weight, buckling of the steel tube and fracture of both the steel tube and the core concrete were noticed at the location near the height of the explosion. Eventually, with a further increase in blast pressure due to the greater charge weight and lower stand-off distance, the column blew away from one end close to the explosion. These results indicate that the proposed multicolumn pier-bent made of CFST exhibits ductile behavior against blast loading. The results obtained from the SDOF analysis and experimental findings suggest that using a circular cross-section, compared to a flat surface, can reduce the blast pressure acting on a structural member by up to 50%.

2.4.4 Columns Retrofitted with Steel Jacketing

Steel jacketing is a well-known method for improving the shear resistance of columns against seismic loading. Researchers have studied and suggested using steel cases as jackets to provide transverse reinforcement and confine concrete in high-shear regions. The steel jacket enables the formation and development of plastic hinges near the support, thereby enhancing the strength and ductility of the columns. Retrofitted columns with steel shell jackets may appear similar to CFSTs, but their behaviors differ when subjected to blast loading. This non-similarity is due to the discontinuity of steel jackets at the top and bottom of retrofitted columns, which prevents unexpected footing or cap beam overload. This gap results in a shear failure of the column in the event of an explosion, as reported in the literature [68]. Considering the improvement provided by the steel jacketing, it is also used to enhance the blast resistance of RC columns in bridges or buildings. However, the difficulty of installation and the vulnerability to corrosion of such a method result in increased maintenance costs. Additionally, the existing structure's ability to

withstand added loads is another drawback of this method. In this section, previous studies investigating the effectiveness of steel jacketing to increase the resistance of columns against blast loading are summarized:

Thai et al. [64] conducted a numerical study to investigate the effectiveness of steel jacketing as a strengthening method for enhancing the blast resistance of columns. The study employed a parametric analysis to assess the impact of steel cover plate thickness, axial load, scaled distance, and blast loading conditions on the structural performance of columns subjected to blast loading. LS-DYNA was used to model the RC columns. The columns had a dimension of 250 mm x 250 mm and a height of 3.6 m. They were made of 30 MPa concrete and reinforced with rebars of 420 MPa yield strength. The columns were modeled as fixed boundary conditions subjected to 8 kg of TNT with varying explosive locations near the base and at mid-height. The focus of the study was a close-in explosion; therefore, the standoff distance was in the range of 0.2-0.8 m. The columns were tested under blast loading at various axial loads, ranging from 0% to 80% of the concentric capacity of the columns. Two thicknesses of steel plate, 3 mm and 6 mm, were considered to study the effect of thickness on blast response. The result indicated that when the scaled distance is less than 0.2 m/kg3, the residual axial capacity of the column is almost negligible as the column gets severely damaged during the blast loading. However, at a larger scaled distance equal to 0.3 m/kg^3 or higher, the column retained around 80% of its axial capacity. The explosion near the base of the columns resulted in local damage to the column, while the mid-height explosion caused global deflection of the columns. The results also revealed that the effect of axial loading was more severe in the case of the base charge, and the deformation increased to 90% with an increase in axial load to 80%. Furthermore, increasing the thickness of the steel plate was not particularly beneficial in preventing local damage and collapse of the column. It was suggested that a suitable thickness of steel plate jacketing be used, one that is neither too thin to be torn by blast pressure nor too thick, which would alter the retrofitted column into a CFST column.

Omran and Mollaei [65] studied various steel jacketing configurations to improve axial loading and blast resistance of RC columns in an experimental and numerical investigation, as shown in Figure 2.23. It is worth noting that the primary objective of their proposed strengthening was to increase axial resistance. The study consisted of two phases. In Phase 1, four RC columns, without any strengthening mechanism, were subjected to 18 kg of equivalent TNT explosive at a

stand-off distance of 3 m, both with and without axial load. The tested columns had a square cross-section with dimensions of 350 x 350 mm and a span of 3 m, reinforced as non-seismic columns. Two of the four experimentally tested columns were loaded axially using prestressing rods connected to the columns via top and bottom plates at both ends, with an applied axial load of 600 kN, corresponding to 16% of the concentric capacity. Due to the blast load generated by the actual explosion, the column with axial load exhibited a deflection of 3.5 mm, and the identical column without axial loading experienced 8 mm deflection. The result from Phase 1 aimed to validate the developed finite element modeling using ABAQUS in Phase 2 of the research study, which showed good agreement with the experimental results. In Phase 2, a total of six columns with exact dimensions and reinforcement were tested, but with different types of steel jacketing configurations. These columns were then modeled and tested against blast loading. The steel jacketing was applied using steel angles, channels, and connecting steel plates. The strengthening configuration consisted of two columns with four steel angles (one on each corner, but with a different number of connecting plates), two columns with two steel channels (one on each opposing face, but with a different number of connecting plates), and one column with an entire steel plate casing. The results showed that the columns with two steel channels and a higher number of connecting plates exhibited the highest axial load capacity and blast resistance enhancement. Even though the remaining jacketing configuration enhanced the axial loading capacity, the blast response was not noticeably affected. Considering the residual axial resistance after blast loading, the column with steel channels outperformed the others, followed by the column with steel plate casing.

Fouche et al., [66] proposed a modification system to improve the blast resistance of steel jacketed columns mainly retrofitted to resist seismic loading, as shown in Figure 2.24. The modified steel jacketing concept was proposed in response to reports of direct shear failure of steel jacketed columns at the discontinuity location of the steel casing when subjected to blast loading. The proposed modification involves applying a structural steel collar at the discontinuity location in the steel jacket and anchoring it to the footing or cap beam, ensuring it does not contribute to the flexural resistance of the retrofitted column. The collars were designed to transfer the column shear to adjacent members and not contribute to the flexural resistance. A non-stick filler material was used between the added steel collars and the column surface to prevent flexural contribution. This modification was intended to enhance the local shear strength while preserving the steel

jacketing's role in seismic resistance by permitting plastic hinge formation at the gap locations. To assess the effectiveness of the proposed modification, a series of actual explosive tests simulating a vehicle bomb were conducted on a ¼ scale model of a multicolumn pier-bent system. The tested columns had a height of 1.5 m and a diameter of 200 mm and were cast with a 35 MPa self-consolidating concrete. The columns were retrofitted with a steel jacket of 1.2 mm thickness and a yield strength of approximately 200 MPa. The modification collars were made of two 8 mm-thick halves of A53 steel welded together and a base plate made of steel to facilitate anchoring the collar to an adjacent member. Columns were modified at the base only or the base and top near the cap beam with varying collar heights. After multiple blast tests, signs of concrete cracking were observed at the top, near the cap beams. Additionally, several buckling waves of the steel casing appeared on the blast face near the location of the explosive material's detonation point. Test results indicated that the modification effectively prevented a direct shear failure due to blast loading. The column exhibited ductile failure, experiencing a base rotation of up to 0.15 to 0.18 radians.

Fujikura and Bruneau [63] experimentally studied the behavior of non-seismic retrofitted and seismically detailed bridge piers subjected to actual blast loading. A total of four ¼-scale RC columns were part of a bridge pier system, where two columns were seismically detailed by providing closely spaced spirals, and two columns were typical gravity columns but retrofitted with steel jacketing. It was tested in an explosion equivalent to a vehicle bombing under the bridge deck. The tested columns had a diameter of 813 mm, cast with a concrete mix having a compressive strength of 27.6 MPa and reinforced with reinforcement having a yield strength of 414 MPa. To retrofit the non-seismic columns, a steel plate with a thickness of 1.13 mm and a yield strength of 254 MPa was used as steel jacketing. The columns were tested in multiple blast tests by varying the stand-off distance in each test. The observation of test results showed that none of the four columns exhibited ductile behavior as expected. The governing mode of failure for all four columns was direct shear, as evidenced by the columns shearing off at their bases. The observation of the test result also indicated plastic hinge formation at the base of the column, as well as at the location of the explosion height, with signs of cracks and curvature before it failed in direct shear. Only one seismically detailed column did not shear off; however, spalling of concrete and shear deformation were evident, suggesting the onset of a shear failure. The study also included an analytical component, where SDOF analysis and plastic analysis were conducted

to develop a model for calculating the direct shear resistance of RC sections, considering the interaction between moment and direct shear. The proposed model predictions agreed with the experimental results because they accounted for the reduction in direct shear resistance when the section was subjected to high bending moments.

2.4.5 Columns Hardened with EB-FRP Application

As suggested by many researchers, fiber-reinforced polymer (FRP) materials are efficient in blast mitigation by improving the strength and stiffness of the structural member. FRP is a composite material composed of a polymeric resin reinforced with fibers made from various materials, including carbon, glass, and aramid, with the most recent additions being basalt and steel. FRPs were first used in the automotive and aviation industries due to their high strength, lightweight properties, non-corrosive nature, ease of installation, and durability. Since the 1990s, the use of FRPs has been introduced in the construction industry and has expanded to various applications. To name a few: strengthening of structural members (i.e., in shear, flexure, and confinement), FRP bars as reinforcement for structures (mainly supported at the ground), and the use of FRP as formwork and reinforcement of concrete-filled tubes (CFTs). However, FRP strengthening system failure occurs without much warning, and premature failure due to debonding or FRP-concrete delamination is a noticeable disadvantage of this technique. In this section, the previous studies on the use of FRPs as a strengthening technique to enhance the blast resistance of RC columns are summarized:

Hu et al. [67] conducted an extensive experimental and numerical study to investigate the behavior of retrofitted reinforced concrete columns with different configurations of Carbon Fiber Reinforced Polymer (CFRP) strengthening under blast loading. The study also considered the effect of the double-end-initiation explosion on the blast response of the retrofitted columns. The research program consisted of two phases, where columns were tested under combined axial loading and field explosion, and then the blasted specimens were tested under a compressive axial load. Four columns were subjected to a close-in explosion by initiating the explosion from both ends of the explosive cylinder. From four specimens, one served as a control, while the remaining three were retrofitted with three different strengthening configurations to determine the suitable retrofitting method for columns using CFRP sheets. The tested columns had a square cross-section with dimensions of 200 mm x 200 mm and a height of 2.5 m. The columns were made of concrete with a compressive strength of 50 MPa and reinforced with longitudinal and transverse

reinforcement, representing a non-seismic column. The retrofitted columns were wrapped with 0.167 mm thick CFRP, having a modulus of 212 GPa and a tensile strength of 4100 MPa, respectively. From the three retrofitted columns, one was wrapped with two layers of CFRP in the transverse direction; the second was strengthened with a layer in the longitudinal direction, another layer was wrapped in the transverse direction, and the third column was strengthened with segmental (i.e., middle and two ends) CFRP transverse wraps. All test specimens were loaded axially to 30% of their concentric capacity and subjected to 11.1 kg of equivalent TNT at a 1.5 m stand-off distance. Numerical modeling was conducted using the LS-DYNA computer program to perform a parametric analysis, considering the effects of axial load ratio (ALR), the explosive shape (i.e., the diameter-to-length ratio of the explosive cylinder, D/L), longitudinal reinforcement ratio, transverse reinforcement ratio, and the thickness of the CFRP layers. Field test results showed that the CFRP retrofitting prevented the compression shear failure due to concrete crushing and spalling at mid-height associated with a large diagonal crack. In addition, the maximum and residual displacements of the retrofitted columns were significantly less than those of the control column, as the CFRP layers increased the strength and stiffness of the column by providing confinement. The two retrofitted specimens exhibited different levels of flexural deformation, whereas the segmental wrapping showed diagonal cracks and concrete spalling in the un-retrofitted regions. Retrofitting the columns also increased the residual axial load-carrying capacity from 7% to 43%, depending on the different strengthening configurations. The retrofitted columns under residual axial loading suffered damage at the end parts where the CFRP wrapping was not applied. The parametric study revealed that the lateral maximum and residual displacement increase with the increase in the D/L ratio because a larger D/L ratio of the explosion cylinder generates a higher reflected overpressure. Increasing the thickness of CFRP wraps reduced the maximum and residual displacement. It was also revealed that increasing the ALR ratio improved the contribution of CFRP retrofitting. Increasing the longitudinal and transverse reinforcement ratio enhanced the blast response of the column but reduced the contribution of CFRP strengthening.

Kodham et al. [68] investigated the dynamic behavior of retrofitted columns using different types of CFRP laminates subjected to shock tube generated blast load as shown in Figure 2.25. Three half-scale columns, with dimensions of 150 x 150 x 2400mm, cast with a concrete mix reporting a compressive strength of 33 MPa at 28 days, were tested in a simply supported condition. The columns were designed as typical gravity columns, also known as non-seismic

columns. Two of the three columns were wrapped with either CFRP jackets of woven fibers in 0/90º orientation (UD.0/90) or inclined orientation to ±45 (W.0/90±45) over the entire height of the columns. The columns were loaded with an axial load of 400 kN using hydraulic jacks and then simultaneously loaded with blast pressure produced by the shock tube facility. The blast load was applied uniformly to the surface of columns using a lateral load transfer element (LLTE) made of thin steel sheets and hollow structural steel (HSS) stiffeners. All the columns were subjected to a similar blast pressure of approximately 50 kPa. The test results showed that the control column exhibited a maximum and residual displacement of 156.9 mm and 127.3 mm, respectively, when subjected to a reflected pressure of 53 kPa. The residual axial load of the control column was only 3.6 kN. The column retrofitted with a W.0/90±45 CFRP laminate was tested at a reflected pressure of 48 kPa and had a maximum and residual displacement of 53.5 mm and 20 mm, respectively. The axial load capacity after the blast loading of this column was 294 kN. Similarly, the columns with a U.0/90 CFRP jacket were subjected to a 49 kPa blast pressure, resulting in maximum and residual displacements of 51.3 mm and 20.5 mm, respectively. At the same time, its axial load resistance was 396.2 kN after blast loading. Analysis of the results suggests that the CFRP jacketing significantly reduced mid-height displacement and prevented associated damage in the critical zone. The results also indicated that the CFRP laminate with the W±45 design had better ductility performance than the CFRP laminate with only unidirectional laminates.

Beger et al. [69] studied the effect of strengthening using Steel-Reinforced Polymer (SRP) and CFRP on the blast performance of RC columns. A total of 18 specimens with varying strengthening methods and scaled distances were subjected to actual blast load using C4 explosives. The specimens were 150 x 150 mm square cross-sections with a height of 2,100 mm and a span of 1,500 mm, made of 44 MPa concrete and reinforced with 450 MPa steel reinforcement. The columns were loaded with a 300 kN axial load and maintained this load during the blast loading. The charge weight for blast pressure ranged from 49 kg to 100 kg, and two different stand-off distances were applied: 4 m and 5.25 m. The test results showed that the control columns could resist lower charge weights with signs of cracks or concrete spalling until complete damage occurred when exposed to 100 kg of C4 at a 4 m stand-off distance. The test result on SRP-strengthened columns revealed that with the same applied load that completely damaged the control columns, there were significant deformations on the SRP columns. The deformations were in terms of longitudinal SRP rupture. However, the load-carrying capacity was still substantial.

The deformations in the columns strengthened with only longitudinal SRP were permanent cracks, delamination, and spalling. There was a distributed curvature along the full height of the SRP-strengthened columns. However, the CFRP-strengthened columns mostly remained straight outside the plastic hinge location. In addition, the CFRP columns exhibited fewer and localized deformations, primarily at the location of plastic hinges. This is attributed to the CFRP's higher stiffness compared to the SRP used in the study. It was also evident that the ductility of CFRP columns was less than that of the SRP columns, and SRP columns better resisted small projectile impacts due to blasts.

Elsanadedy et al. [70] numerically studied the effect of stand-off distance and charge weight on the blast response of RC columns without strengthening and with the CFRP strengthening technique. The tested columns were modeled using LS-DYNA and represented the exterior RC columns of an existing typical building in Riyadh. The columns modeled had circular cross-sections with a diameter of 600 mm and a height of 4 m, made of 30 MPa concrete and reinforced in both longitudinal and transverse directions. The specimens were retrofitted in both transverse and longitudinal directions using two layers of 1 mm thick CFRP sheets. The CFRP strengthening was applied to increase the area and the moment of inertia of the cross-section. In addition, the strengthening provides confinement to prevent the spalling of the concrete cover during blast loading, thereby increasing the cracked moment of inertia. The columns were assumed to have fixed conditions at both ends and were subjected to axial loading and blast loads. To generate blast pressure, different charge weights of TNT explosives (i.e., 100, 200, 500, and 1000 kg) at varying stand-off distances (1, 2, 4, and 15 m) and at 1 m above the ground were modeled using the numerical software LS-DYNA. The test result showed that strengthening the columns reduced the initial period of vibration by 11.7%. The effect of stand-off distance was increasing exponentially on maximum lateral and residual displacements. It was reported that a 2 m stand-off distance, with applied charge weights of 500 kg and 1000 kg, destroyed both strengthened and un-strengthened columns, and a similar result can be expected at a 1 m stand-off distance. In contrast, the strengthened and un-strengthened columns did not sustain any damage when subjected to 100 kg of explosives at a 15 m stand-off distance. The analysis of the results illustrated that the retrofitting prevented damage to the column against blast loads generated by charges of 200 and 500 kg at a 4 m stand-off distance. Strengthening the columns reduced the maximum lateral displacement by 8% and 79% when applying 100 kg and 500 kg of charge weight at a 4 m stand-off distance. The

study suggested that retrofitting enhances the behavior of the columns, which can provide noticeable blast resistance and prevent progressive collapse in the event of a moderate explosion.

Rodriquez-Nikl et al., [71] experimentally investigated the protection of RC columns from blast loading using CFRP jackets. A total of ten columns were tested against simulated blast loading using a blast simulator facility at the University of California, San Diego. The blast simulator utilizes hydraulics to accelerate large masses toward the target, imparting a controllable impulse to the test specimen and applying a repeatable blast-type pressure to the specimen. The applied impulse level on the specimens ranged from 6.8 MPa-ms to 15.7 MPa-ms. The specimens were designed to resist gravity loads in so-called non-seismic columns. Some of the columns were wrapped with CFRP jackets of different thicknesses. Test results showed that the control columns exhibited brittle shear failure at a low level of blast loading. However, the CFRP-hardened columns exhibited a ductile flexural hinging failure, which resulted in lower deflections. The study's findings indicated a significant enhancement in blast response due to the hardening of columns using CFRP jacketing.

Crawford et al., [72] modeled the blast performance of first-story columns retrofitted with Carbon Fiber Reinforced Polymer (CFRP) or carbon wraps subject to blast loading and simultaneous axial loading using DYNA3D finite element code. The studied columns were designed to match the specifications of UBC seismic zone 1 (gravity columns) and UBC seismic zone 4 (seismic columns). The columns' dimensions were 30-inch square cross-sections with a height of 14.5 ft, made of grade 60 steel reinforcement and concrete with a compressive strength of 5,000 psi. Carbon wraps were used to increase axial and flexural capacity while mainly mitigating direct shear failure. The six layers of carbon wrap used for retrofitting had a thickness of 0.019 inches per layer, a strength of 54 ksi, and a stiffness of 7600 ksi. Two shapes of carbon wrapping were applied: direct application and a circular wrapping, which was provided by injecting grout between the square column surface and the carbon wrap. Various charge weights (i.e., 1500 lb and 3000 lb) and stand-off distances (i.e., 10, 20, and 40 feet) were considered in the study. The study results illustrated that the significant potential collapse mechanism for the building is the direct shear failure of the ground floor columns. The blast performance of the unwrapped seismic columns was better than that of the gravity columns at combinations of 20 feet stand-off distance & 1500 lb charge weight and 40 feet stand-off distance with both 1500 lb & 3000 lb charge weights. It was evident from the results that wrapping the columns in a circular

shape significantly enhanced the columns' blast resistance and prevented them from collapsing. However, the improvement in the direct composite wrap in a square shape in the blast response of columns was not the same as that of the circular wrapping method.

2.4.6 Other Strategies and Techniques to Improve Column Blast Response

Wang et al. [73] numerically studied the blast performance of RC columns strengthened with a layer of UHPFRC. Their study included four parts; the first part investigated the effectiveness of UHPFRC as a protective layer for columns subjected to blast loading using a commercial FEM computer application known as ANSYS/LS-DAYNA, the second part is focused on sensitivity analysis using Tornado diagram (TD) and first-order second moment (FOSM) methods to identify controlling design variables, in part three different length and location of UHPFRC layer is investigated to find the effective required length of UHPFRC, part four discusses the response surface model (RSM) to quantify the dynamic response of strengthened columns by measuring the residual capacity. For quantifying the residual capacity of columns subjected to blast loading, a displacement-control load was applied in the axial direction using the restart analysis module. The columns established for FEM using ANSYS/LS-DYNA had dimensions of 400 x 400 mm and a height of 4 m reinforced as a typical gravity column. For comparison, two models were established: a normal RC column and an RC column strengthened with an 80 mm thick UHPFRC layer around the perimeter of the entire column height. Conventional concrete was modeled as C40 grade, and the UHPFRC layer was modeled to have a compressive strength of 160 MPa and a steel fiber content of 2% by volume. The axial load considered during the test resulted in a stress of 18 MPa on the columns. To study the effectiveness of the UHPFRC layer, the RC column and strengthened columns were subjected to 10 kg of TNT and different stand-off distances of 0.25, 0.375, 0.5, 0.75, 1, 1.5, 2, and 3 m. The test results showed that the conventional RC columns exhibited severe damage compared to strengthened columns under the same loading conditions, especially in small stand-off distances of less than 2 m. The restart analysis module showed that the residual capacity of the UHPFRC-strengthened column is 2 to 4 times higher than that of the conventional RC columns. At some point, the damage index was the same for both columns. However, the residual capacity of strengthened columns was always higher than that of conventional columns. For the sensitivity analysis, four parameters were considered: thickness & strength of the UHPFRC layer and ratio of transverse & longitudinal reinforcement. The results indicated that the UHPFRC layer thickness is the governing factor in terms of the residual capacity of the columns. At the same

time, the ratio of longitudinal reinforcement was the most influential factor in determining the maximum displacement and elemental peak stress. Two different strengthening configurations were applied to determine the most effective length and location of UHPFRC: symmetrically mirrored at mid-height and a one-ended application from the bottom of the column to the total height. It was shown that the longer the layer, the higher the strength, and when the entire column's height was covered, the column achieved the best result. Moreover, the established model using RSM provided accurate predictions of UHPFRC residual capacity and was in good agreement with the results achieved from FEM simulations.

Vavilala et al. [40] numerically studied the effect of polymeric foam on blast mitigation of RC columns. The blast loading and blast response were modeled using the Coupled Eulerian-Lagrangian (CEL) method provided by the software known as ABAQUS/Explicit. The modeled columns had square cross-sections of 355 x 355 mm and a height of 3.48 m, reinforced in both longitudinal and transverse directions using eight #25M and 10 # M@350 mm, respectively. This study proposes the use of polymeric foam, which is also used as a mitigation and packaging material for impact loading. The columns were jacketed with varying thicknesses of polymeric foam (i.e., 5, 8, and 10 mm) and sandwiched with a 1 mm steel sheet for uniform load distribution. Various TNT explosives (i.e., 10, 25, and 50 kg) and stand-off distances are considered in their study to perform a parametric analysis. Numerical results and analysis illustrated that the displacement was reduced when the thickness of polymeric foam was increased. Increasing the stand-off distance had a significant effect on the response of columns. The best result was obtained for 10mm polymeric foam subjected to 10 kg of TNT explosive.

Codina et al., [74] investigated two strengthening methods to enhance the blast response of RC columns subjected to field blast testing. There were three samples: one serving as a control, one retrofitted with typical steel jacketing, and one using a sacrificial polyurethane brick layer. The test columns had a square cross-section with dimensions of 230 mm x 230 mm and a height of 2.44 m. The columns were made of concrete with a compressive strength of 30 MPa and reinforced with steel rebars of 420 MPa yield strength. The transverse reinforcement was placed so that the spacing detailing matched seismic demand detailing at both ends. A steel jacket, 3.25 mm thick, was made from a mild steel plate and wrapped around one column. On the blast face of another column, polyurethane bricks were placed first, and then a very thin layer of 0.89 mm steel sheet was used to restrict them in their location. The columns were subjected to a blast load

generated by 8 kg of equivalent TNT at a stand-off distance of 60cm placed near the bottom of the columns to replicate the vehicle bomb on the ground. It should be noted that no axial load was applied to the tested column during or before the blast testing. The test result showed that the control column exhibited significant damage at the plastic hinge close to the location of the explosive. In contrast, the steel jacketed column was the least damaged specimen. The sacrificial polyurethane bricks were also efficient in absorbing the blast energy, resulting in less damage and residual displacement compared to the control column. The steel jacketed column had 60% less residual deflection, and the polyurethane brick column had around 20% less residual deflection than the control column. The study suggested that higher-density polyurethane bricks could further improve the energy absorption of RC columns in the event of an explosion.

Qasrawi et al. [75] studied the blast performance of concrete-filled FRP tubes (CFFTs) subjected to an actual close-in explosion. CFFTs are used to strengthen and confine reinforced concrete, thereby improving the resistance of members subjected to conventional loads. In addition, CFFTs in the form of glass fiber-reinforced polymer (GFRP) tubes are used as stay-in-place formwork and reinforcement, which not only expedite the construction process but also improve the structural behavior of a member. Their study tested eight full-scale circular RC columns with and without GFRP tubes under monotonic static and blast loading. The parameters investigated were the effect of the GFRP tube, the longitudinal reinforcement ratio, and the scaled distance on the behavior of CFFTs subjected to close-in blast loading. The columns were 4m long and 220mm in diameter, made of 34 MPa concrete and reinforced with longitudinal reinforcement having a yield strength of 430 MPa. Two longitudinal reinforcement ratios were used in the tested specimens, which were 1.2% and 2.4%, representing the minimum and maximum recommended ratios. The GFRP tubes encasing the columns had a hoop tensile strength of 128 MPa, a hoop modulus of 21.6 GPa, a tensile strength of 48.3 MPa, and a modulus of 10.1 GPa. The outer diameter of the tubes was 220 mm, and the thickness was 5.5 mm. Six of the eight columns were tested under blast loading generated by incremental charge weights of 15, 30, 50, and 100 kg of C4 explosives, placed at a 2 m standoff distance. It was evident from the test results that the CFFT columns did not exhibit visible signs of damage, whereas the RC columns without GFRP tubes showed crushing of the compression concrete and spalling of the concrete on the tension face. All the RC columns had higher residual displacement than their counterparts, but with GFRP tubes. The comparison of results indicates that the presence of GFRP tubes provides blast resistance and

protects the core concrete by confining it. The residual displacement of CFFT columns with a 2.4% longitudinal reinforcement ratio was reported to be zero for higher-scaled distance blast loading. However, for the smaller scaled distance, it was reduced significantly by 29% compared to control specimens. The findings suggested that CFFT columns outperformed the control columns by reducing the localized damage and residual displacement under blast loading.

Lloyd [9] conducted an extensive experimental and analytical study to investigate different materials and strengthening techniques to retrofit RC columns against blast loading, as shown in Figure 2.26. The data obtained in the experimental phase of the study were then used for validation of SDOF analysis to model the behavior of the column when subjected to blast loading. Sixteen half-scale columns were prepared in addition to two from a previous study. Of the 18 columns, 12 were designed for gravity loads (non-seismic), and six were seismic columns; 13 columns were retrofitted using different mechanisms. The columns were square (150 mm x 150 mm) and rectangular (100 mm x 150 mm) in cross-section, with a height of 2.4 m. The columns were made of concrete mixes with different compressive strengths but reinforced with the same diameter of longitudinal rebar (10M). Four columns were strengthened with a single layer of CFRP jacketing over the entire height of the columns. Two columns were reinforced with longitudinal CFRP strips on the loaded and unloaded faces of the column. Two columns were strengthened with a combination of longitudinal CFRP strips and wrapped with a single layer of CFRP jacketing. One column was strengthened using a confinement retrofitting technique that comprised fiber-reinforced concrete (FRC) wedges placed externally around the column and then wrapped with high-strength prestressed steel straps over the wedges. One column was retrofitted with an innovative compression steel brace placed externally to the blast face of the column and then combined with FRC wedges and external hoop prestressing. Three columns were retrofitted using innovative tension steel braces placed externally, which braced the columns at two points over their height. All the columns were axially loaded using hydraulic jacks with a load level ranging from 11.6% to 36.7% of their concentric capacities. The columns were subjected to simulated incremental blast loading ranging from 45 kPa to 99 kPa generated by the shock tube facility. The blast load was transferred uniformly to the column using a load-transferring device (LTD) composed of a thin steel sheet and a hollow structural steel (HSS) section. The LTD was designed because the shock tube opening had a square cross-section that could not be fully covered with a column, and the shock wave could escape from the open sides of the columns on the shock tube if

the LTD were not used. The test results showed that all the retrofit methods used in the study improved the blast response of the RC column, with varying levels of enhancement. The control columns failed due to concrete crushing and buckling of the compression bar in the compression face of the columns. The seismic columns with small hoop spacing prevented the buckling of compression bars at failure. The seismic detailing in their study did not result in a significant enhancement because the axial load level was significantly dropped during the dynamic response to blast loading. The columns retrofitted with the combined application of longitudinal CFRP and transverse jacketing CFRP had the highest improvement in the CFRP retrofitted category. Lateral bracing, either compression or tension brace that developed restoring forces during blast loading, provided a better dynamic response than all the control and retrofitted columns. The columns with tension bracing were the most efficient retrofitting techniques among all the retrofitting options studied in their research program. It was also found that the prediction by equivalent SDOF system analysis was comparable to the experimental results. The study concluded with recommendations for retrofitting RC columns against blast loading.

2.6 Summary

A comprehensive review of the literature, primarily focusing on the strengthening of reinforced concrete (RC) columns against blast loading, is presented in this chapter. An overview of the existing knowledge on the behavior of reinforced concrete (RC) columns and the effects of various strengthening methods is reported. The benefits and shortcomings of the methods reported in this chapter are also highlighted. A deep investigation of the literature revealed that the concept of prestressing to strengthen columns against blast loading has not yet been explored. In particular, external prestressing, an innovative hardening method, is not documented in the literature to the author's knowledge. Additionally, the application of ECC (an emerging construction material) for blast-loading strengthening has not yet been thoroughly studied. The current study aims to introduce and investigate these innovative strengthening methods, not only to enrich the existing literature database but also to provide a new alternative method for blast hardening.

Figure 2.1 – Inside the parking garage of the World Trade Center in New York after the bombing in 1993.

Figure 2.2– Alfred P. Murrah Building in Oklahoma City 1995 before and after the blast.

Figure 2.3 – Khobar Towers in Saudi Arabia 1996 before and after the blast.

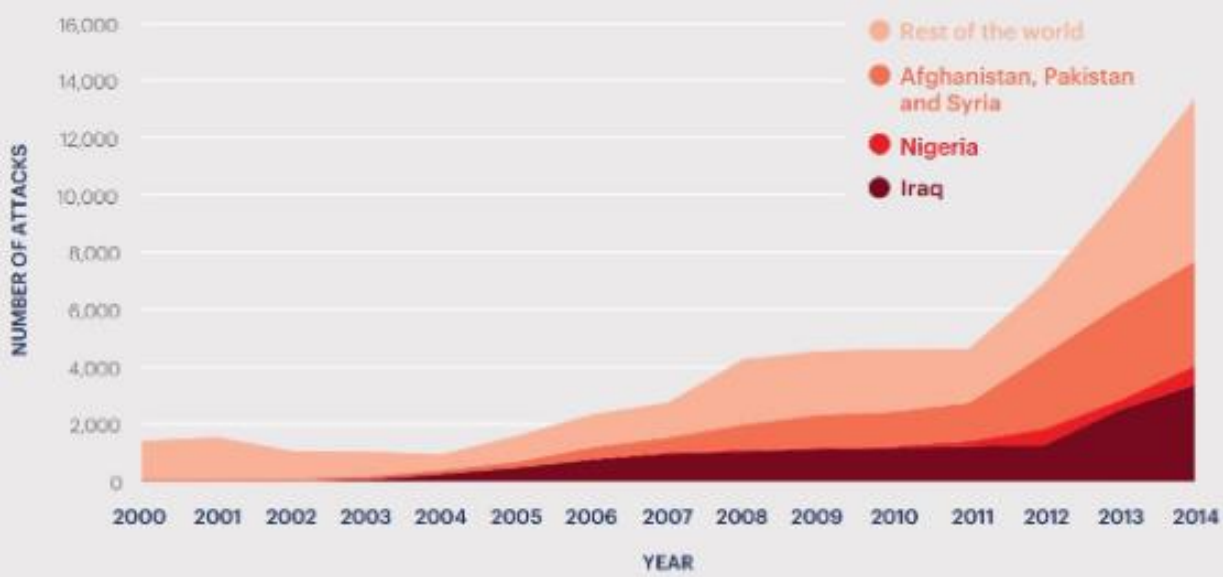

(a)

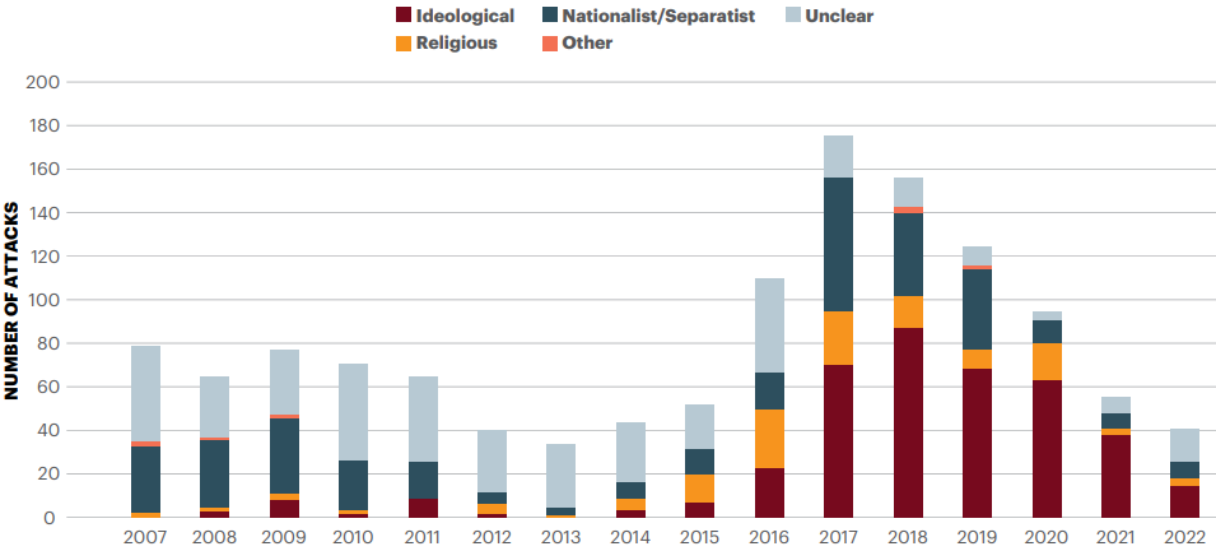

(b)

Figure 2.4 – a) Number of explosive events between years 2000 and 2014, b) Terror attacks in the West by motivation, 2007–2022 (source: [76]).

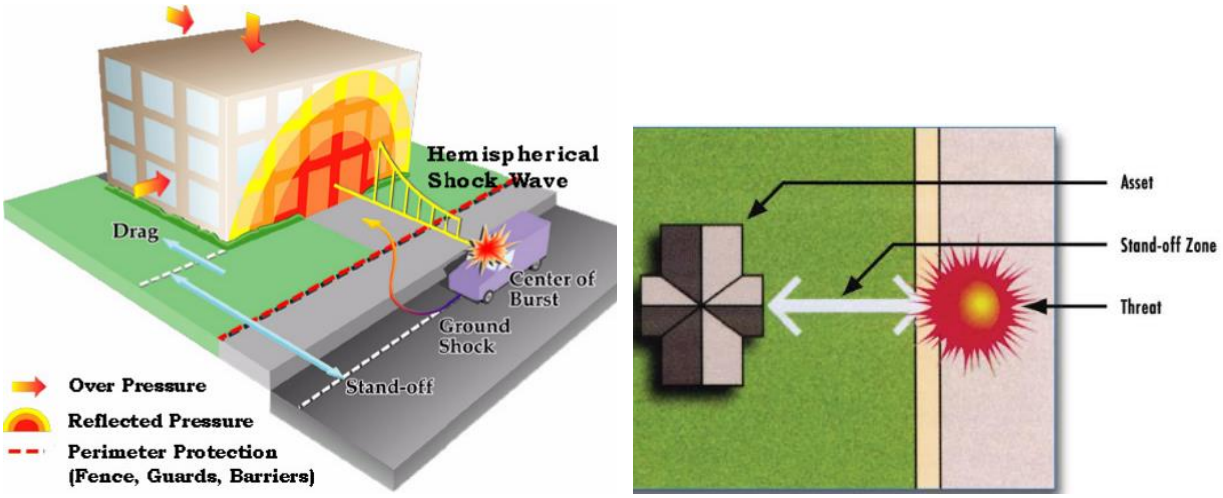

Figure 2.5 – Blast load properties and parameters (source : [10]).

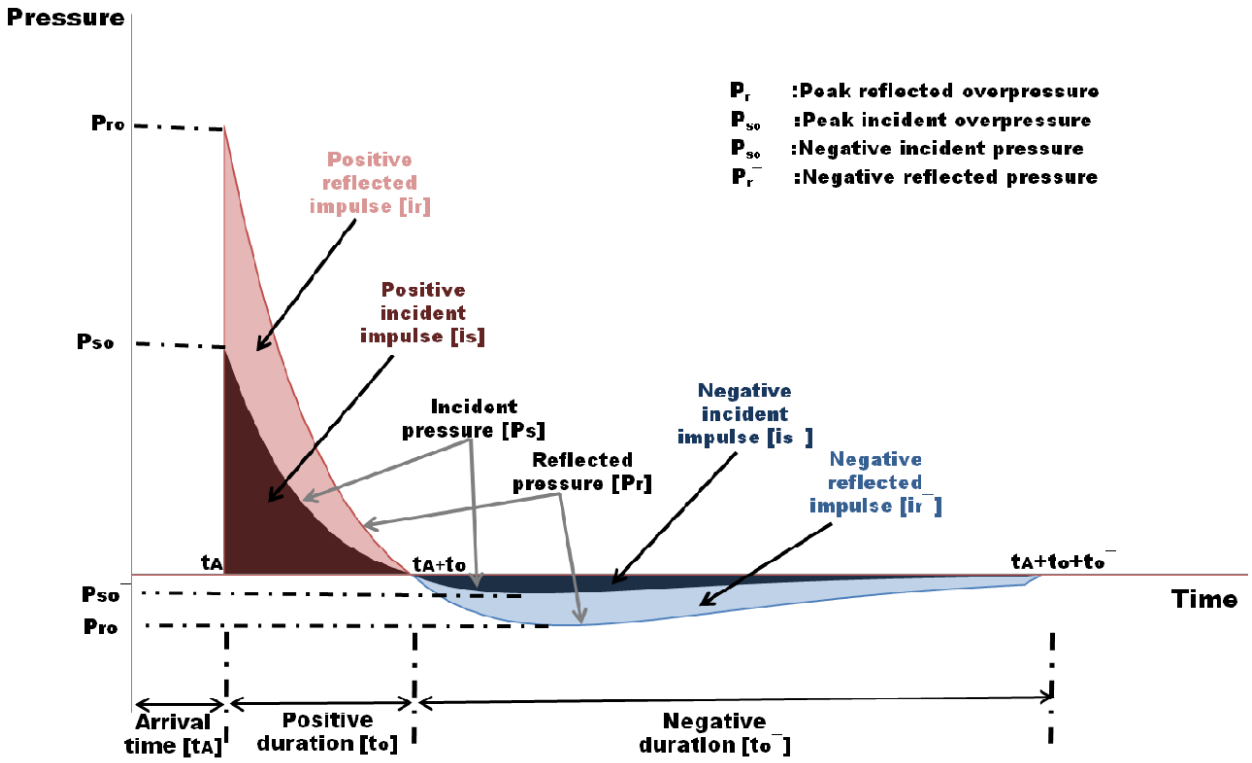

Figure 2.6 – Incident and reflected pressure versus time (Source: [77]).

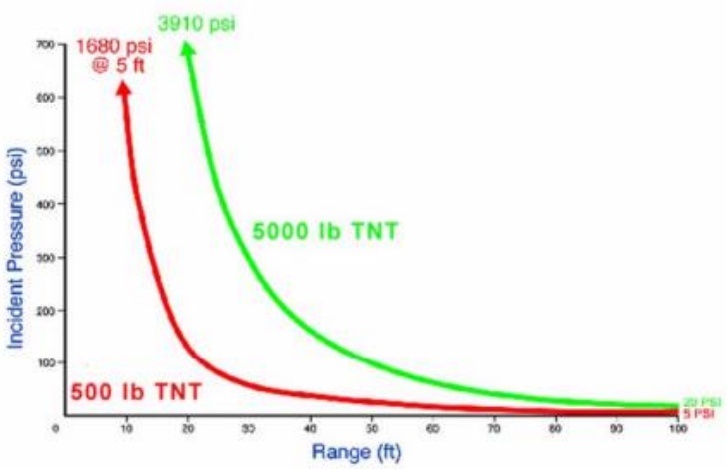

Figure 2.7 – Pressure decay with an increase in standoff distance (Source: [10]).

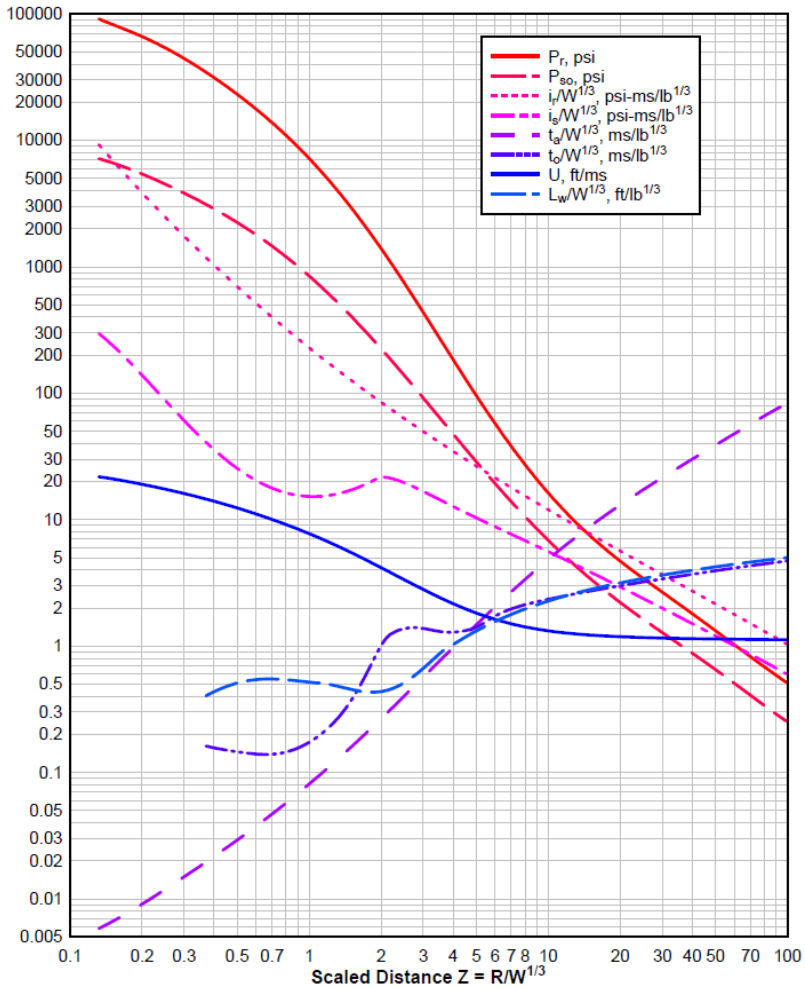

Figure 2.8 – Positive phase parameters of shock wave for a free air (spherical) TNT explosion at sea level (source: [19]).

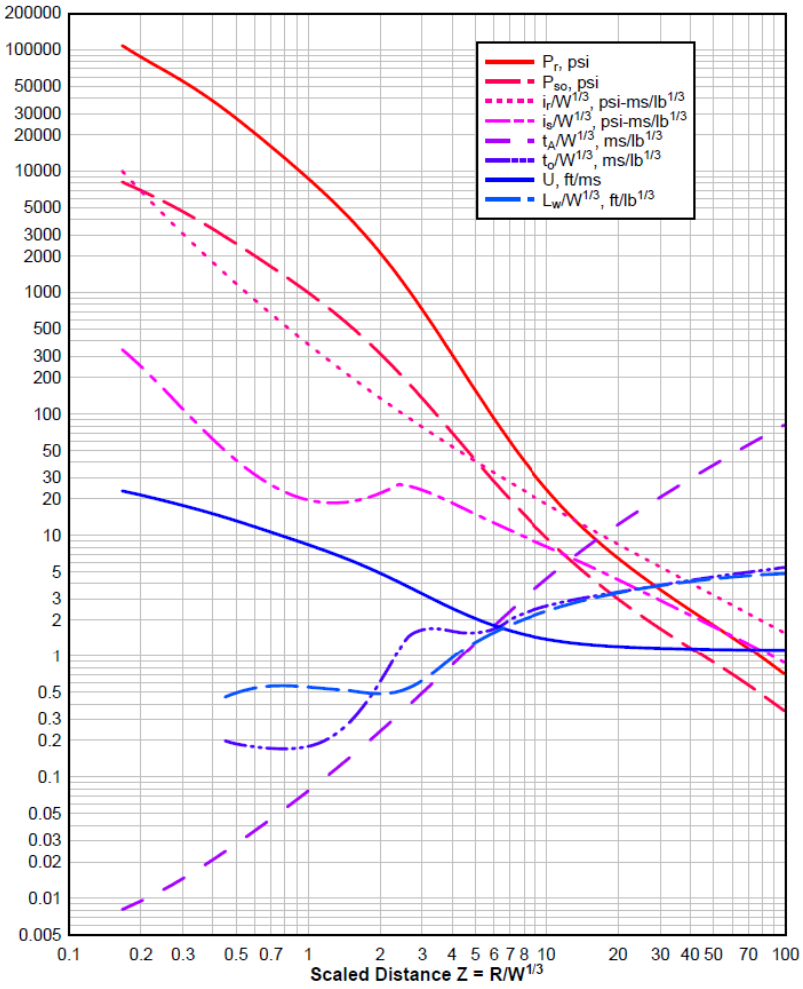

Figure 2.9 – Positive phase parameters of shock wave for a surface (hemispherical) TNT explosion at sea level (source: [19]).

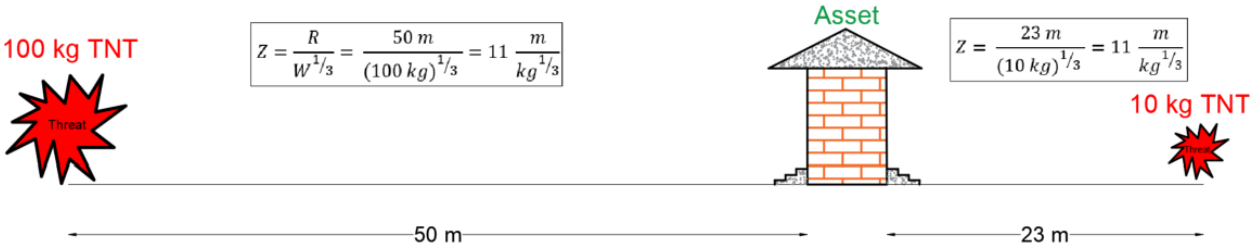

Figure 2.10 – Illustration of scaled distance concept.

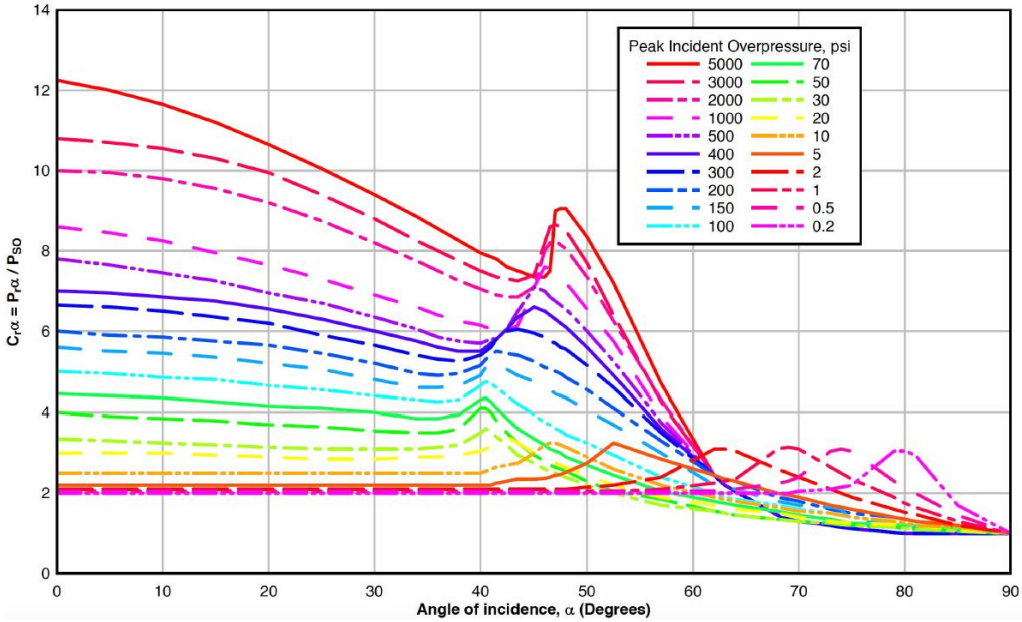

Figure 2.11 – Variation of reflected pressure vs angle of incidence (source: [19]).

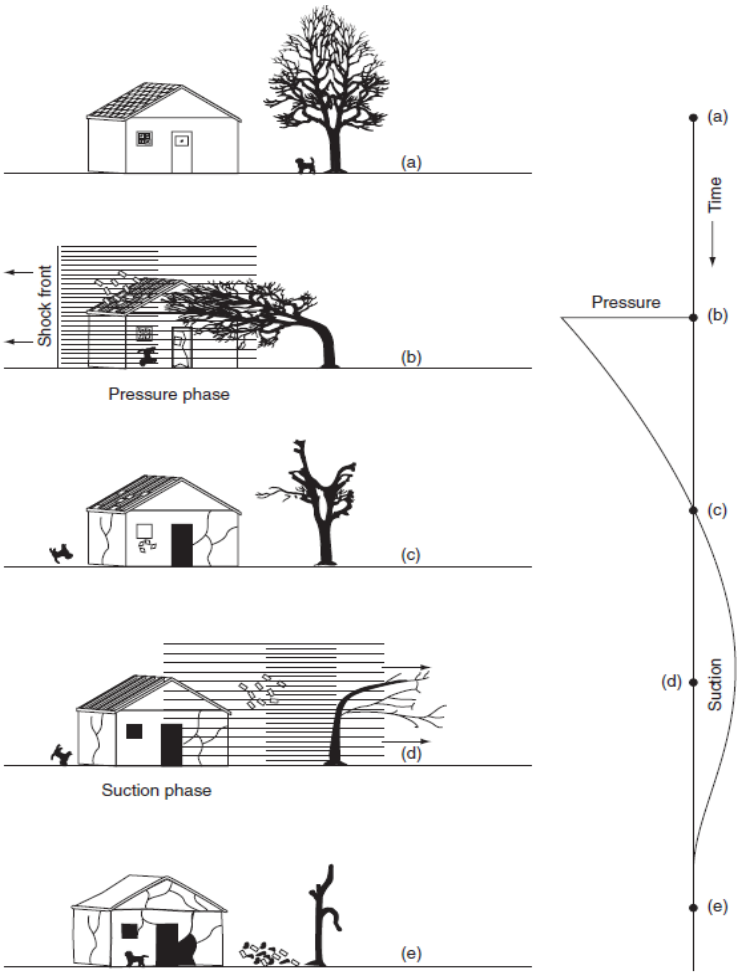

Figure 2.12 – Effect of blast load positive and negative phase on target (source : [25]).

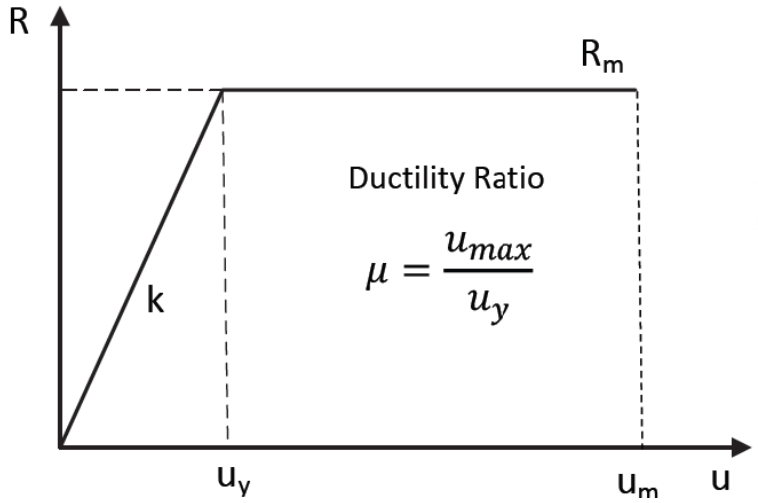

(a)

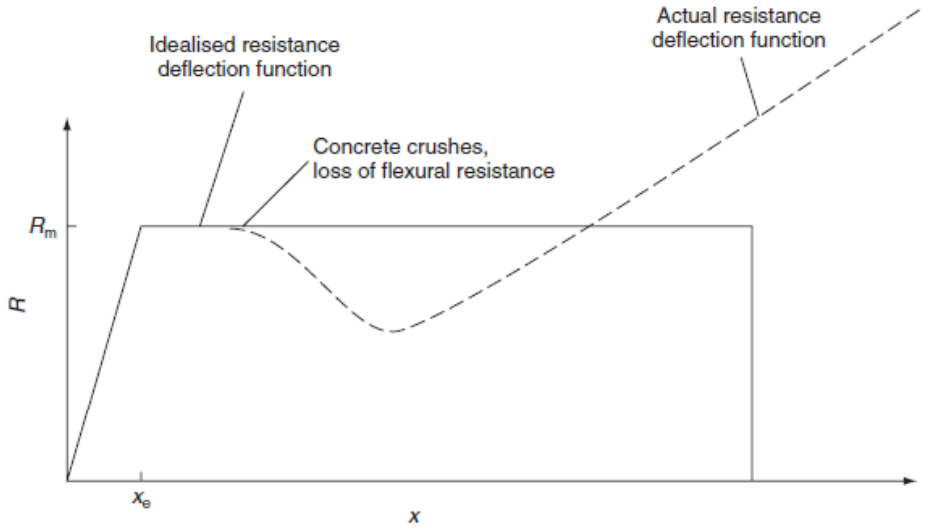

(b)

Figure 2.13 – a) bilinear resistance function, b) resistance function for RC with large deflections (source: [25]).

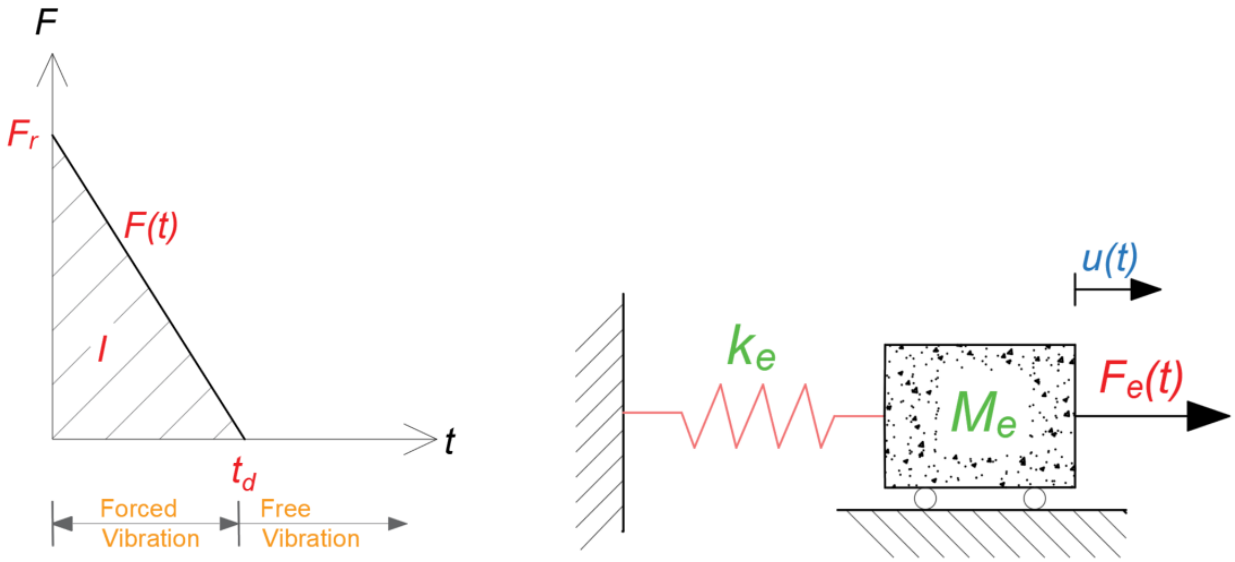

Figure 2.14 – Idealization of blast load and equivalency of structure to SDOF system.

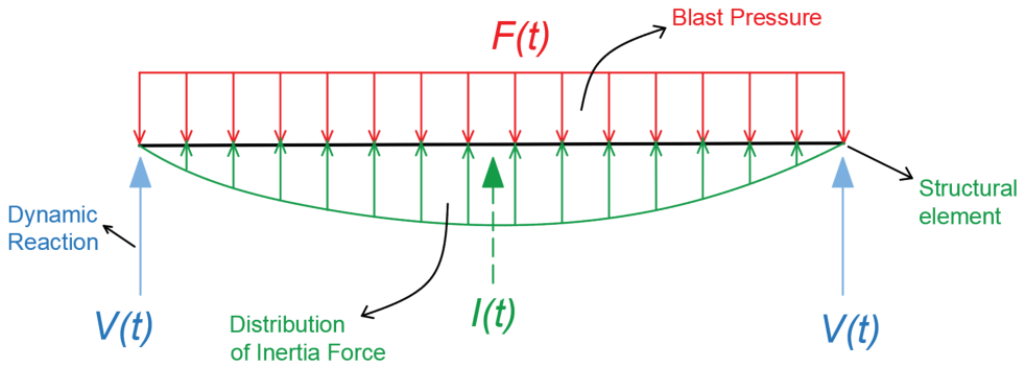

Figure 2.15 – A member's response in terms of reaction and inertia.

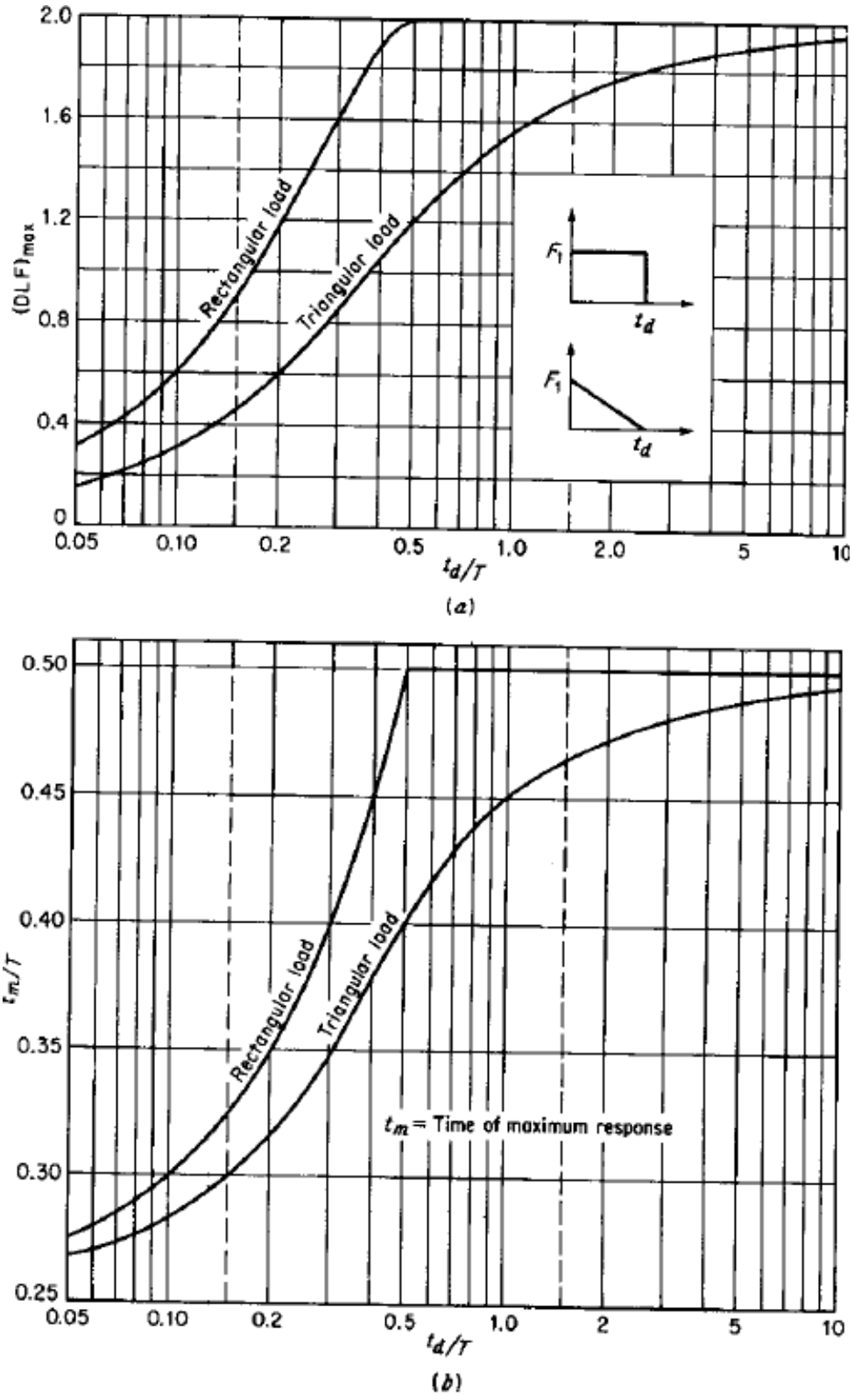

Figure 2.16 – Relationship of DLF maximum and time to maximum response with the ratio of blast duration over the natural period of a structure (source: [12]).

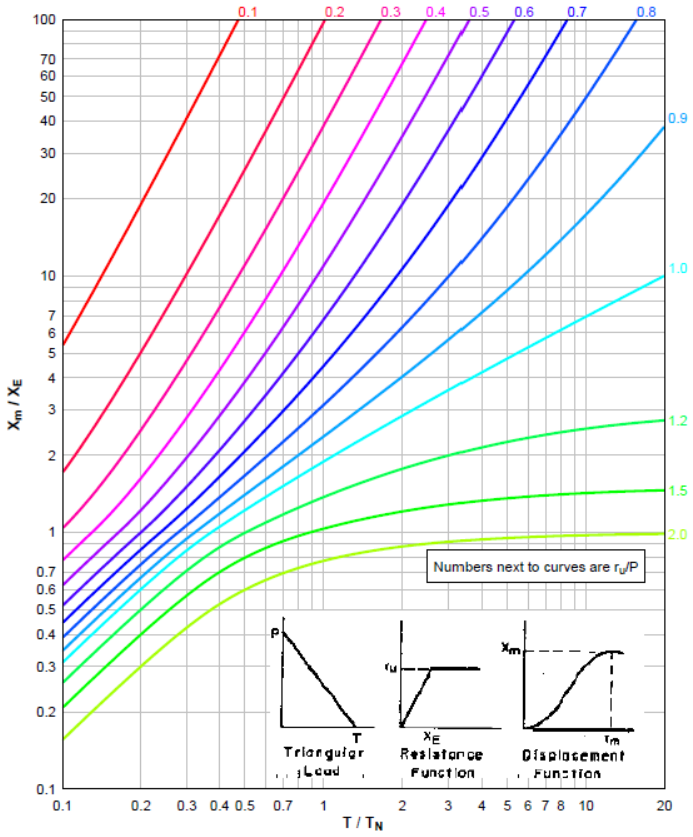

Figure 2.17 – UFC charts showing the relationship of ductility (Xm/Xe) with ratio of blast duration and period (T/TN) (source: [19]).

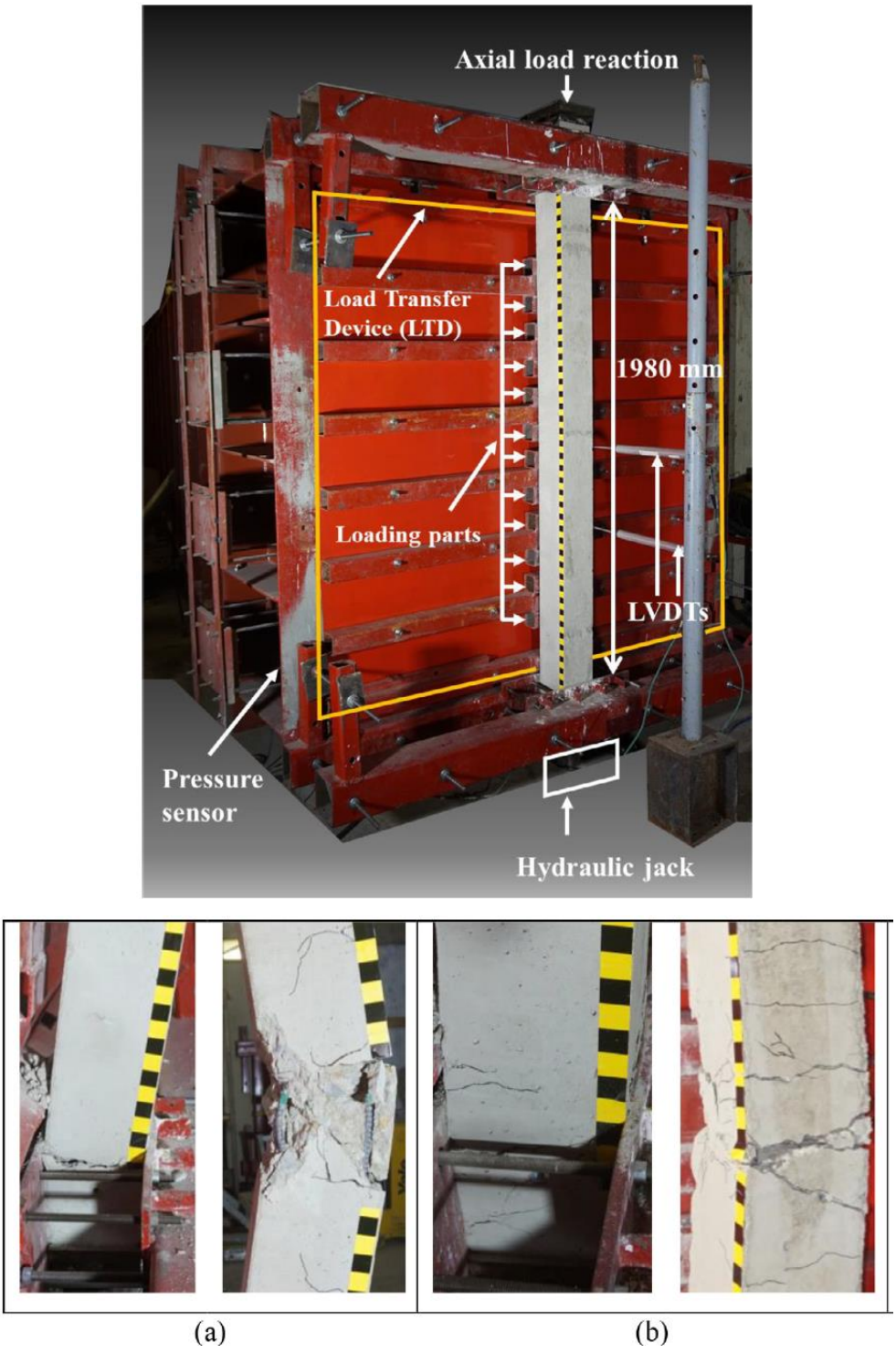

Figure 2.18 – Test setup and failure at the bottom and mid-height of non-seismic column (a) and seismic column (b) after three blast shots generated by shock tube (source:[78]).

Figure 2.19 – Photo of the test setup and test result focusing on scaled standoff distance; a) large distance, b) small distance (source:[47], [48], [49]).

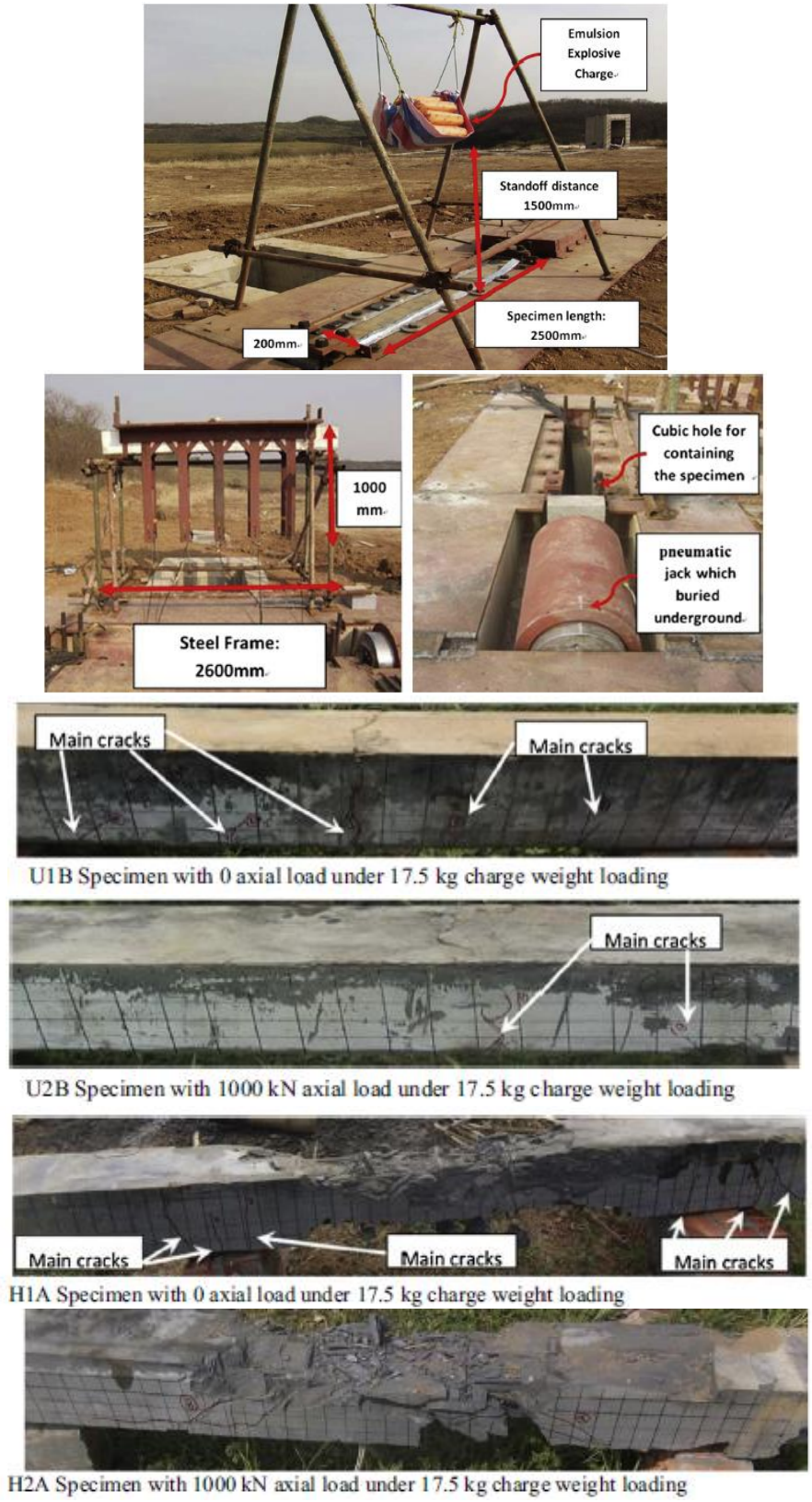

Figure 2.20 – Test setup and the result of different columns with UHPFRC (U1B and U2B) and HSRC (H1A and H2A) (source: [54]).

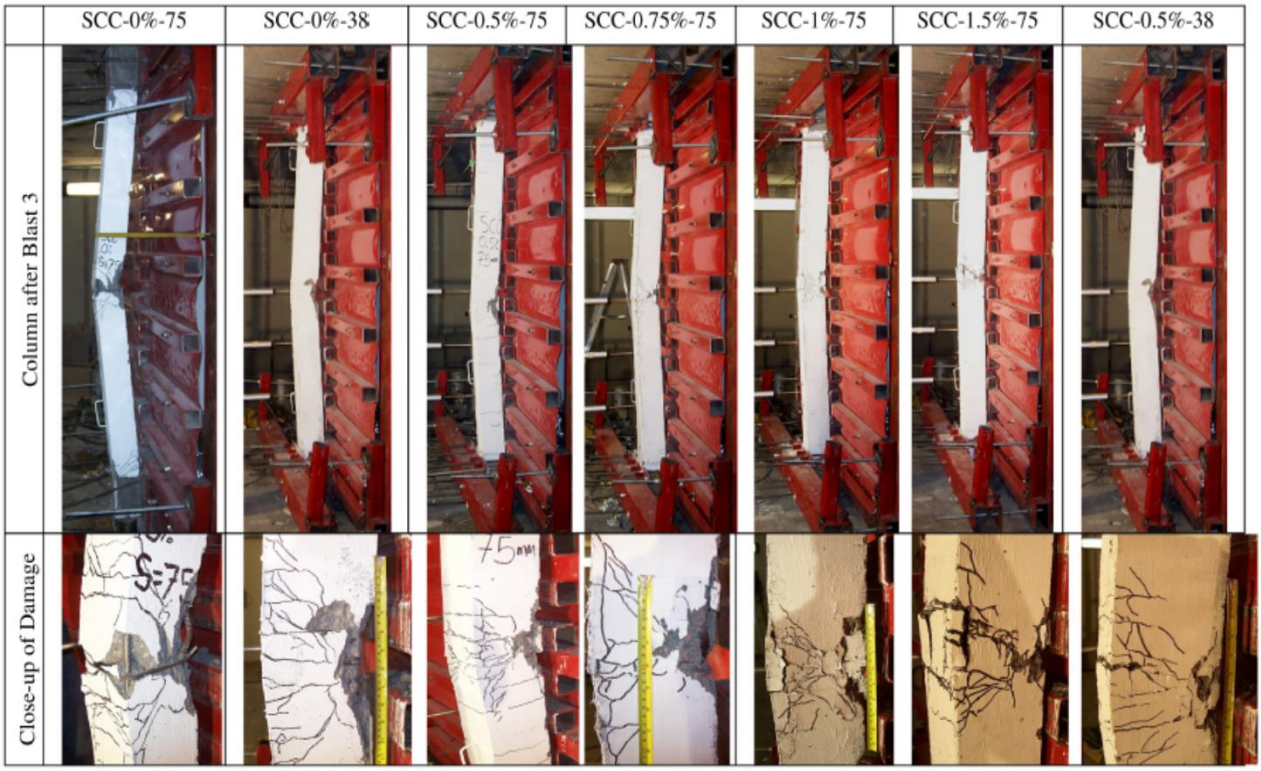

Figure 2.21 – Column failure after 3rd blast shot for different columns having different stirrups spacing and percentage of discrete steel fibers in concrete (source:[56]).

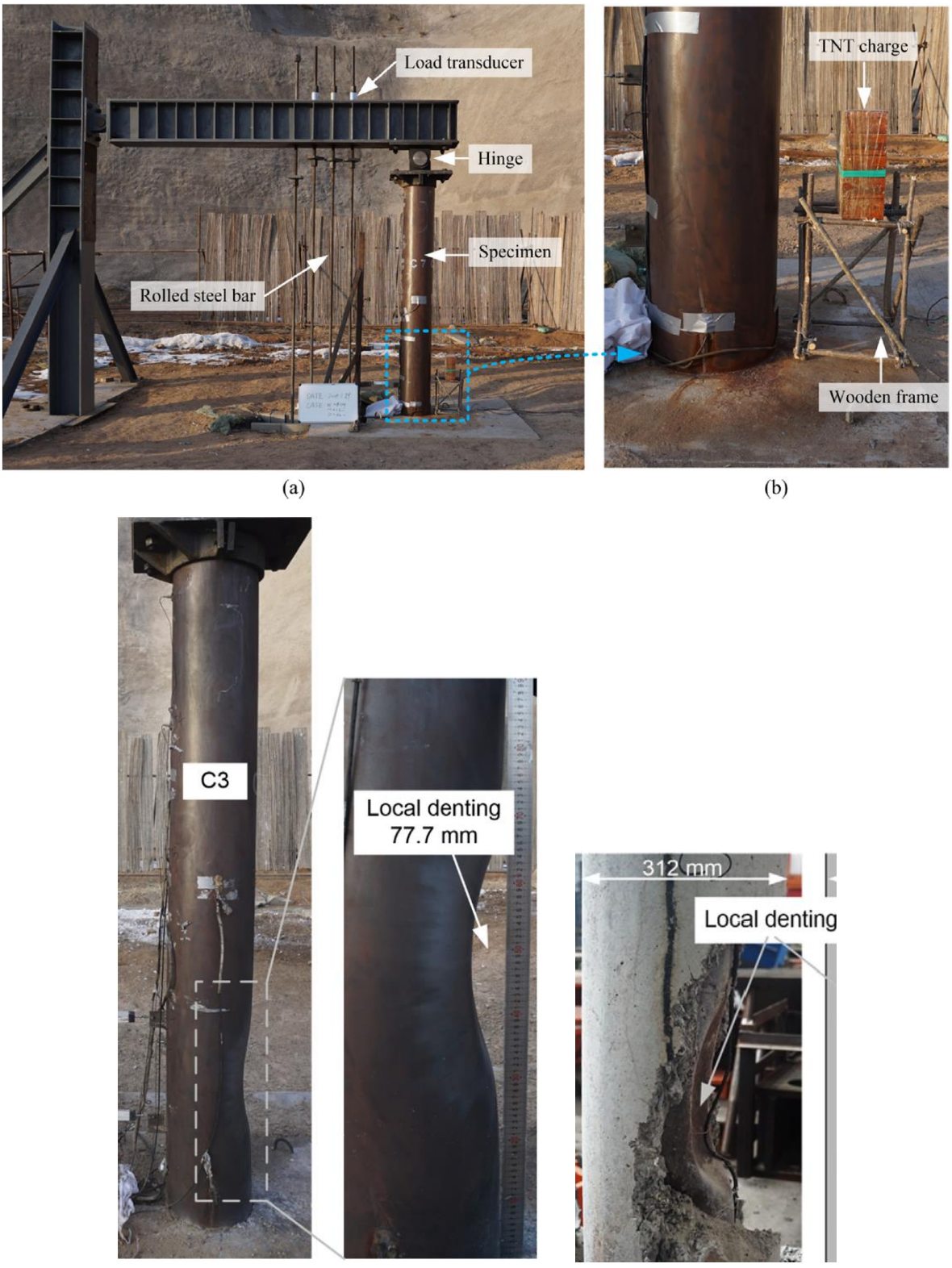

Figure 2.22 – (a) blast testing setup, (b) detail of TNT explosive charge setup, and (c) test results of specimen C3 (source: [59]).

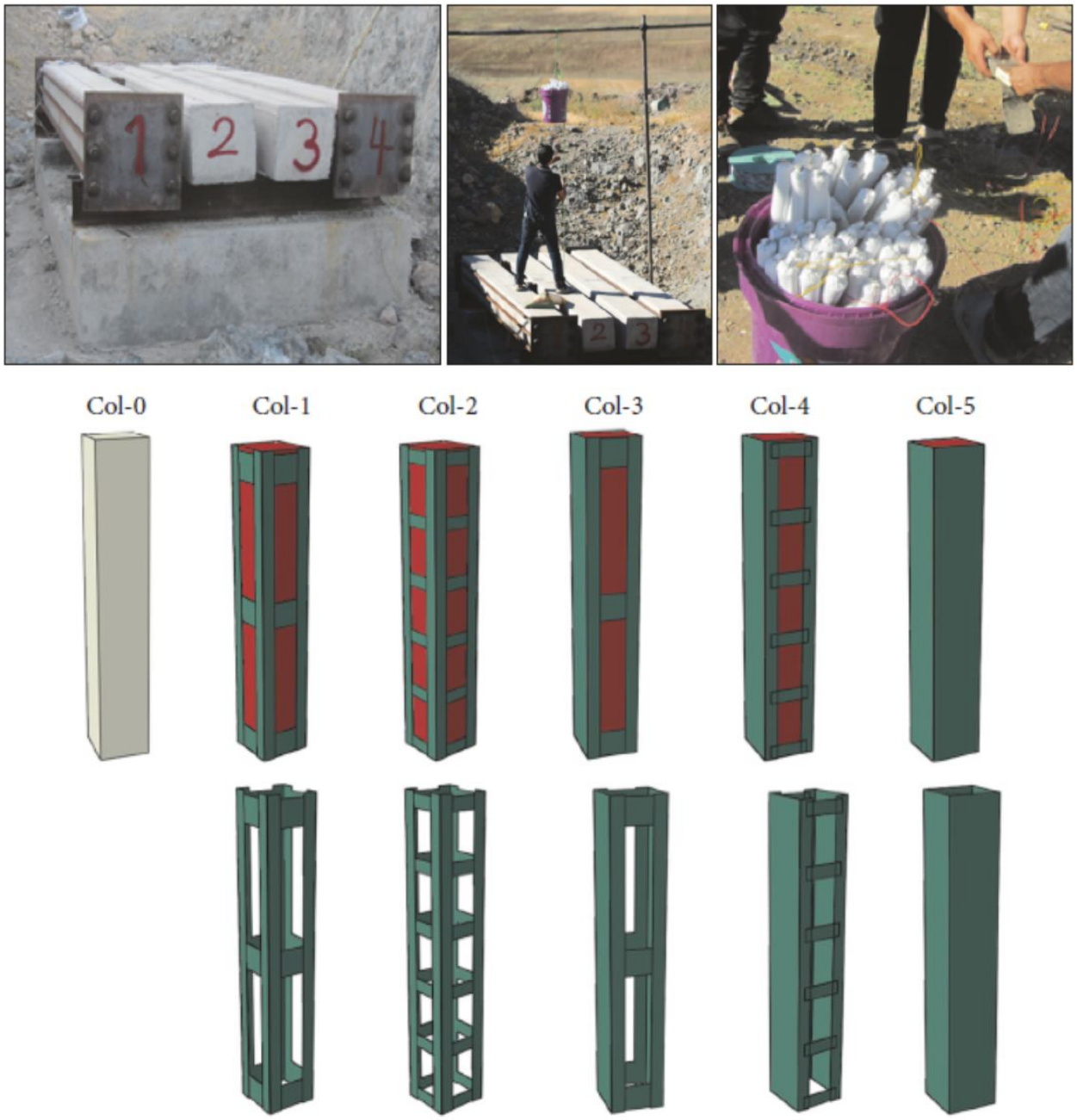

Figure 2.23 – Test specimen and setup and finite element modeling samples (source:[65]).

Figure 2.24 – Failure of test specimen labeled MSJC4 (global view and close up of base (source: [66])).

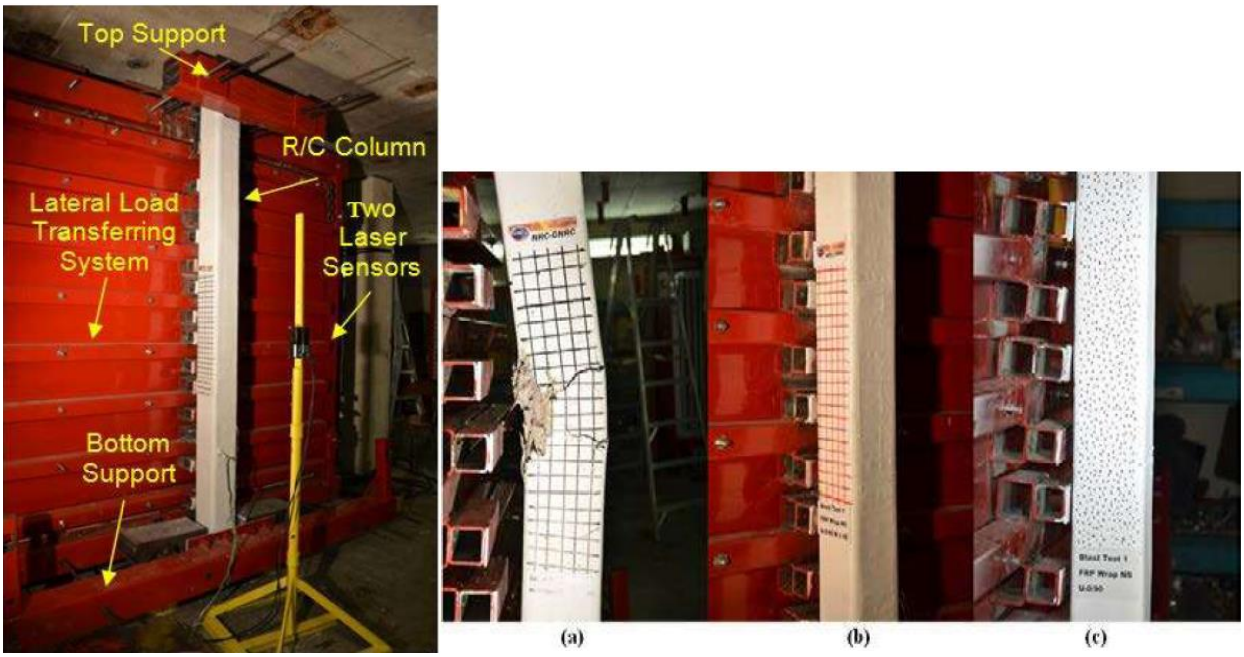

Figure 2.25 – Test setup and damage at critical section after the test (a) Col.1, b) Col.2, (c) Col.3 (source:[68]).

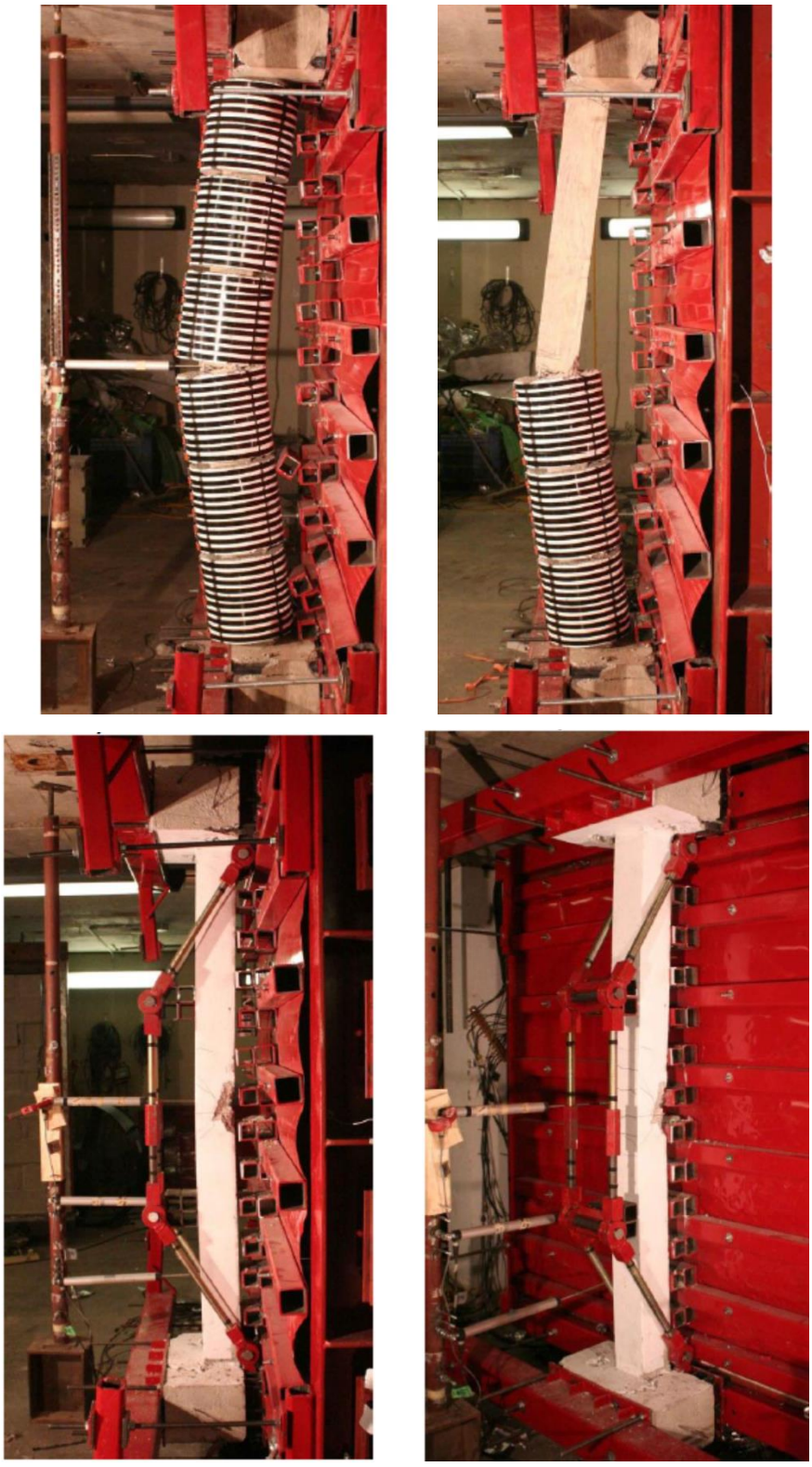

Figure 2.26 – Test result of two retrofitting methods after 4th blast shot: a) hoop prestressed column, b) tension braced column (source: [9]).

Chapter 3. Experimental Program

A comprehensive experimental investigation was conducted to generate test data for achieving the study objectives. The experimental program involves preparing, strengthening, and testing specimens using the shock tube facility at the University of Ottawa. The test specimens were tested under combined axial load and blast load. A total of 15 columns were constructed and tested. The columns were grouped into two main categories (i.e., with and without seismic/blast detailing) and then divided into four sub-groups: a group of reference columns and three groups of hardened/strengthened columns according to the strengthening method proposed and used, as follows:

a) Hardening by external post-tensioning using prestressing strands.
b) Post-tensioning by conventional prestressing using internal prestressing strands.
c) Hardening by jacketing using an Engineered Cementitious Composite (ECC) shell covering.

This chapter describes the test specimens, material properties, instrumentation and test setup, and the loading regime.

3.1 Test Specimens

Fifteen reinforced concrete (RC) columns were designed and constructed. The columns are representative of the ground floor exterior columns of a building. The columns had a square cross-section with dimensions of 152 x 152 mm and a height of 2400 mm. The concrete cover was 10 mm to outside of the longitudinal reinforcement. Four 10M longitudinal reinforcements were distributed in each corner of the cross-section, providing a reinforcement ratio of 1.7%. The longitudinal reinforcement had hooks with a 90-degree bend extending more than 50 mm into the core concrete to provide better anchorage. 12 of the 15 constructed columns represent typical gravity columns (non-seismic) having transverse reinforcement (ties) spaced at a distance of h/2 (i.e., 75 mm). The remaining three columns had reduced spacing of ties to h/4 (i.e., 37 mm) spacing, representing a seismic/blast resistant column. The column ties were square closed hoops with a 135-degree bend at the ends, extending 40 mm into the core concrete. Two gravity-designed columns were tested as reference columns, representatives of non-seismic columns without hardening, and one column with closely spaced ties was tested as a reference column, representative of seismic/blast detailed columns. Figure 3.1 shows the geometry and reinforcement

details of test specimens. Figures 3.2 to 3.4 show the stages of column preparation, including the assembly of the reinforcement cage, as well as the casting and curing of concrete.

3.2 Materials Properties

3.2.1. Concrete

The columns were made of Ordinary Portland Cement (OPC) concrete mix with a compressive strength of 45 MPa and 50 MPa on the test date. Some columns were made of self-consolidating concrete (SCC), also called self-compacting concrete, supplied by a local ready-mix company, having a compressive strength of 45 MPa at 28 days. The SCC mix had a w/c ratio of 0.4, a slump of 650 mm, and a maximum aggregate size of 14 mm. The remaining columns were cast using an in-house batched regular concrete mix as per the mix proportions reported in Table 3.1. This concrete mix had a w/c ratio of 0.5, a slump of 125 mm, and a maximum aggregate size of 14 mm. Standard cylinder tests were conducted as per ASTM C39, which resulted in a 28-strength of 50 MPa. The column tests were conducted at or shortly after 28 days, with concrete strength remaining approximately the same as reported.

3.2.2. Steel Reinforcement

The longitudinal column reinforcement consisted of deformed rebars, while transverse reinforcement was in the form of smooth wire. Coupon tests were conducted according to ASTM E8 standards to obtain the yield and ultimate strength of steel reinforcement. The longitudinal and transverse reinforcement had an actual yield strength of 480 MPa and 455 MPa, respectively. Mechanical properties of the deformed and smooth reinforcement are given in Table 3.2.

3.2.3. Seven-wire Strands

Two of the hardening methods investigated in this study involved the use of prestressing strands. The strands consisted of 7-wire steel strands. The 7-wire strands had a diameter of 13 mm and 15 mm. These strands are generally reported to have an ultimate strength of 1860 MPa without a specific yielding point. It is noted in the literature that these strands typically have a yield strength of 1650 MPa, corresponding to a tensile strain of 1%. To verify the actual strength of the materials supplied, coupon tests were conducted according to ASTM A1061. When tested at the University of Ottawa Structures Laboratory, the ultimate strength of strands was observed to reach

approximately 2200 MPa. The mechanical properties of the prestressing strands are given in Table 3.2.

3.2.4. Steel Parts and Fasteners

The hardening techniques used as external post-tensioning required rigid spacers, called deviators, and an anchorage mechanism, called end fixtures. The deviators and the end fixtures were made of mild steel plates and angles. The steel plates were welded or fastened using grade 3 and 6 steel bolts and nuts.

3.2.5. Engineered Cementitious Composite (ECC)

Table 3.3 presents the mix proportions of the ECC mixes used to cast the shell covering all sides of the column. The mixes had 2% and 1.5% of UHMWPE (ultra-high molecular weight polyethylene) fibers with properties given in Table 3.4. ECC batching was performed in-house using a regular pan mixer. The mixing steps differ from the traditional concrete (OPCC) and fiber-reinforced concrete (FRC) mixes because there is no coarse aggregate in the ECC mix used in this study. The batching process of the ECC mix is shown in Figure 3.5. When batching the ECC, the water plus the superplasticizer and cement plus silica fume are mixed first, forming a cement slurry. Fiber is added to the mix gradually to prevent agglomeration (known as balling effect). Before adding the fibers to the water-cement slurry, the fibers were dispersed inside a bucket using air pressure. It is essential to disperse the fibers for at least a minute in small portions using a bucket and air pressure, without which the fibers cannot be easily distributed during mixing. The ECC mix used for jacketing of the columns had a compressive strength of 70 MPa, cracking strength of around 3 MPa, an ultimate tensile strength of 5 MPa, and young modulus of 23,000 MPa, at testing age. The mechanical properties of the ECC mix are presented in Table 3.5. Figure 3.6 to Figure 3.10 show photos of coupon tests and the stress-strain behavior of the tested coupons. The compressive stress-strain diagram of the ECC cylinder was obtained under force-controlled monotonic loading conditions that does not capture the post peak behavior in compression.

3.3 Hardening/Strengthening Methodology

This study presents and investigates three methods of hardening/strengthening RC columns. The methods proposed aim to enhance column strength and ductility. Two of the methods are designed to harden the existing columns of a structure, while the third method is suggested for designing

newly built blast-resistant columns. Figure 3.11 shows the test matrix presenting the category of specimens tested for each suggested strengthening/hardening method.

3.4 Strengthening Procedure

3.4.1. Hardening by External Posttensioning

The first hardening method proposed is external post-tensioning using prestressing strands based on the conventional prestressing concept. In this method, seven non-seismic (gravity-designed) columns were hardened with different longitudinal profiles of the external post-tensioning strands. These are shown in Figure 3.12 to Figure 3.19. The strands were installed in such a way that they created an active negative moment to act against the positive moment generated by blast loads. In addition, a reserve (passive) moment capacity was presumed to be activated when the column develops large enough deflections under blast loads to further tension the strands. The post-tensioning was done against rigid end fixtures provided at the ends, designed to anchor the strands without any possible slippage. End fixtures were designed to provide end anchorage without having to drill through columns for passing the strands through the member. Drilling the concrete column is an option that can be used in practice. However, this approach has two disadvantages: first, it is difficult to drill long distance through a large size column, and second, the presence of column reinforcement may create challenges while drilling. It is worth noting that securing the end fixtures is crucial since the stress concentration at the anchorage location can result in movement or failure of the anchorage system, resulting in prestressing losses.

Four longitudinal strand profiles were designed to investigate the most effective post-tensioning profile for blast hardening of columns. One column was hardened with single-harped profile strands, two with a double-harped profile, two with a triple-harped (semi-parabola) profile, and two with a parabolic profile (i.e., five deviators). The strands were prestressed to a low level of tension compared to conventional prestressing. The intent was not to impose excessive compression on the column due to post-tensioning so that the level of compression, when combined with the effects of gravity loads would not reach critical levels (i.e. exceeding 55% of concentric capacity). In addition, the initially low level of prestressing would permit further stress development capacity of strands during blast loading. Therefore, single-harped strands were prestressed to 15% of their ultimate tensile capacity (f_{pu}), where f_{pu} = 1860 MPa. Double-harped strands were prestressed to 13% (first column) and 16% (second column) of their ultimate tensile

capacity. The triple-harped (semi-parabolic) profiles were prestressed to 10% (first column) and 15% (second column) of their ultimate tensile capacity. Parabolic strands were prestressed to 9% (first column) and 16% (second column) of the strand ultimate tensile capacity. An important consideration for the level of prestressing was not to exceed service load stress limits specified in CSA A23.3 [79]. Accordingly, the service load stress limits of $0.5\sqrt{f_c'}$ and $0.6f_c'$ for tension and compression were considered in establishing the initial stress levels. Table 3.6 shows the details of the pre-blast design of each prestressing profile investigated in this study based on the resisting forces illustrated in Table 3.7. The single-harped and double-harped strands are identical to the first two profiles shown in Table 3.7. The other two profiles investigated, i.e., triple-harped and assumed parabolic profiles, correspond to the third profile given in the same table (Table 3.7).

In the experimental program, the hardening procedure can be implemented either when the column is lying on the laboratory floor (as shown in Figure 3.20a) or when the column is in an upright position mounted on the shock tube (as shown in Figure 3.21). The latter position represents the actual condition of a column in a structure under load. In this study the strands were snag tighten on the ground however actual prestressing of the column was implemented in an upright position when mounted in the test setup under axial load . The presence of axial load increases the column moment capacity, which in turn prevents cracking due to initial post-tensioning of the proposed hardening technique.

The following procedure was followed in the experimental program to prepare columns for blast testing:

- The end fixtures (L-shape steel angles) were secured to top and bottom ends of the column using two rods connected to a thick steel plate attached to the protected side of the column opposite the threat side also called blast side. The L-shape angle was also connected using three ½ inch bolts to the steel plate placed on top and bottom of the column mainly designed for axial load application, as shown in Figure 3.20b. The end fixtures were made of 75 mm x 75 mm with 10 mm thick steel angles, and were designed to provide a rigid anchorage platform. The angles had slot holes on both ends aligned on either side of the column with at least one-inch clearance to enable not only the passage of the strands but also to ensure free rotation of the pinned-support top and bottom load plates during blast loading. In addition, thick steel shims were attached to the inner side of the angles (positioning under the chucks of prestressing strands) to achieve the required angle for each strand profile with

respect to first deviator along the column height, and also prevent kinking of the strands during blast loading. Figure 3.20c shows a photo of the disassembled past of described end fixture.

- To obtain the desired strand profiles, deviators were placed between the strand and the face of the column (protected side) opposite to the blast face (loading side). Deviators (in the form of half-moons and thick steel plates) were attached to the columns using two rods connected to another thick plate placed on the blast face of the column, as shown in Figure 3.20. Deviators were sufficiently rigid and appropriately secured not to move from their designed location during blast loading. Deviators were made of thick steel plates and welded notched arc-shaped steel parts, so-called half-moon guides (see Figure 3.20c). The half-moons not only provided the specified deviation for the strands but also acted as a guide to keep the strands in their track during the strengthening and loading stages. Half-moon guides were designed to sink in the strand to prevent misalignment during blast loading. The friction between the half-moons and the strands is assumed to be negligible.
- Deviators were placed at various locations along the height depending on the strand profile (see Figure 3.12 to Figure 3.19). The desired strand profile dictated the deviator dimension. For instance, the dimension of the mid-height deviator for parabolic shape lies between the single-harped profile and the triple-harped deviation at mid-height. This was required to ensure a similar slope at each deviation point to create an almost perfect parabolic shape. In some cases where a small deviation was needed, a deviator with a round surface (made of one piece long steel plate) on one side was used instead of the half-moon deviators setup. The number of deviators differed according to the longitudinal strand profiles as follows:
    I. The single-harped profile strand had only one 55 mm deviator at the mid-height of the column.
    II. Double-harped had two 55 mm deviators at 1/3 and 2/3 of the column height.
    III. The column with a triple-harped strand profile had a 95 mm maximum deviator at mid-height with two small deviators of 15 mm located closer to each column end.
    IV. The columns with parabolic profile strands had five deviators: a maximum 75 mm deviation at mid-height, two deviators 45 mm above and below the mid-height, and two deviators 15 mm close to each end of the column.

- Two #13M seven-wire strands were longitudinally installed along the height of the column by first anchoring them to the blast face. The strands were aligned such that they ran on two sides of the column (i.e., faces parallel to the shock wave), were anchored on both ends, and then passed over the fastened deviator on the protected side.
- The strands were anchored at either the top or bottom of the column using conventional chucks (wedge and ring) secured to the end fixtures, as shown in Figure 3.20b. At the other end, a splice chuck (also called tensioner) was used to anchor the strand and also to facilitate post-tensioning of the strands, similar to a turnbuckle. To obtain an equivalent torque force to create the desired tension force in the cable, torque wrenches were calibrated using a digital torque meter. The calibration was done by applying torque force using a torque wrench with attached torque meter and measuring the resultant tensile force using a 500 kN tensile testing machine setup. In the calibration process, a one-meter-long strand was hooked to a servo-electric tension testing machine, anchored using a regular chuck from one end and a splice tensioner chuck from the other. The torque meter was attached to the torque wrench stem, and the force was applied by fastening the splice nut, while the tensile force was measured using the load cell embedded in the setup.
- Post-tensioning was applied using the splice chuck and tensioner but without any conventional jacking method of post-tensioning. Conventional prestressing using hydraulic jacks may become challenging in an existing build environment. A heavy-duty tensioner in the prestressing industry can be used with commonly used torque wrenches to apply the desired tensioning force instead of jacking particularly in repair of deteriorated strands of bridge girders. The tensioner also called splice chuck can be fastened to coupling nuts (used for current tests) or secured to a female-anchored nut embedded into a hard surface. The splice chuck, as shown in Figure 3.22 is mainly designed for barrier cables used in vehicle parking floors above the ground level. To obtain maximum strength of tensioner used in this study, it was tested under tension while anchored to a 7-wire strand using a 500 kN servo-electric machine in the structural laboratory at the University of Ottawa. The test was terminated due to strand rupturing without any visible deformation of the splice chuck.

3.4.2. Posttensioning using Internal Prestressing Strands

The strengthening method investigated in current research, hereafter called post-tensioning, is the conventional post-tensioning of columns using internally placed 7-wire strands, as shown in Figure

3.23 and Figure 3.24. Two seismic/blast columns were post-tensioned with straight profile (constant eccentricity) strands placed inside the column through a duct provided when casting the column. The first column had only one #15M strand placed internally on ¾ of column breadth (b) longitudinally over the protected face. The strand with a straight profile on the protected face could also be another choice of external post-tensioning discussed in the hardened columns section above. However, using an external straight longitudinal profile would be more challenging in implementing and also maybe less effective. A larger strand size and higher prestressing force (35% of ultimate tensile capacity of strand) were designed to make a comparable effect to the externally placed strands method. The higher prestressing force would compensate for the smaller eccentricity when using straight profile strands. In the case of the hardening method using external prestressing, the prestressing force was low because the role of the deviator was significant in creating a reacting moment before and during blast loading.

The second posttensioned column had two internally placed #15M strands running at ¼ and ¾ of column breadth (b) longitudinally on both faces of the column (Blast face and protected face). Both strands were straight in profile and prestressed to 40% of their ultimate tensile capacity. In this case, the prestressing level was slightly higher than the column with a single straight strand. This is because of the absence of a reacting moment created by the eccentricity of a single strand. Even though double strands do not provide any active moment to act against blast loading, it offers several advantages compared to non-prestressed columns. The prestressing provides stability and rigidity to the column and improves the column's shear resistance. In addition, in the case of an explosion from inside or outside the structure, the column with strands on both sides provides an attractive choice for the mitigation of blast damage from either side.

To implement post-tensiong of these columns, the following procedure was followed:

- During the assembly of column reinforcement cage, a PVC (polyvinyl chloride) pipe with an internal diameter of 17 mm was provided to create a duct inside the cage (so called sheath in prestressing construction). The pipe was adequately secured with wires to maintain its longitudinal straight profile during concrete pouring. One duct was provided for the column with a single strand, and two ducts were provided for the column with double strands.

- After the column was cast and the concrete was cured, the 7-wire strand (either one or two strands) was inserted through the duct. The strands remained unbonded inside the duct without grease or any other protective material.
- A stress-bearing thin plate with holes to accommodate the strands was also placed on each column end to prevent stress concentration at anchorage locations.
- The strands were locked from one end and pulled from the other end using hollow cylindrical jacks, as shown in Figure 3.25. Since post-tensioning was performed before the axial load was applied, the prestressing force was slightly increased to account for column shortening due to the application of axial load during testing.
- As seen in Figure 3.25b, the chucks (ring and the wedge) on both ends of the columns are projected up, which would prevent the application of axial load through pinned support plates. To resolve this limitation, a rigid thick steel plate with holes larger than the outside diameter of the chuck was fabricated. The rigid plates were then placed on both ends of the column between the column and axial load-hydraulic jack and column and axial load-cell, as can be seen in Figure 3.25b

A seismic/blast column with built in duct was also prepared and tested without putting any strands in the duct pipe (see Figure 3.26) to investigate the effect of concrete removal from the compression zone of the column with a double strand. The column was also built to serve as a reference column to the post-tensioned columns. In addition, this column can be used to study the effect of closely spaced ties on the behavior of a column in the event of a blast load compared to the gravity-designed column (i.e. companion reference to hardened columns).

3.4.3. Hardening by ECC Jacketing

The second hardening technique investigated was jacketing with Engineered Cementitious Composite (ECC). The ECC jacket acted like a shell over the column core and developed full composite action with the existing column. ECC is known as a strain-hardening material with multi-cracking behavior under tension. When subjected to compression, it behaves a bit softer than traditional concrete because of its relatively low rigidity. It provides a ductile behavior with energy absorption capacity. The columns considered for this method included non-seismic columns with h/2 spacing of column ties. Three columns were built and jacketed with ECC to investigate the effectiveness of ECC, The columns were tested under constant axial load and blast shock wave.

Two columns were retrofitted with two different thicknesses (i.e., 30 mm and 20 mm) of ECC layer with 2% fiber content, and one column was jacketed with a 25 mm thick layer having 1.5% fibers (see Figure 3.27 to Figure 3.31). The following procedure was employed to first jacket the columns and prepare them for testing under blast loading.

- The core concrete surface was roughened prior to casting ECC around the column. Roughening was done with a bushing tool intended for this purpose. The bushing tool was used with rotary hammers in machine hammering mode. The goal was to achieve a surface roughness of a minimum of concrete surface profile index of 6 (CSP6) as per the International Concrete Repair Institute [83]. All four side surfaces were roughened to a CSP of at least six and then air-blown and water-washed to remove any loose debris and dust resulting from the roughening process. The roughening process removed the cover concrete entirely, leaving only column core concrete.
- Wooden formwork was prepared with dimensions matching the jacketed column size. The ECC mix was poured on the bottom layer before placing the core column inside the formwork. The core column was placed inside the wooden formwork with proper spacers to ensure the required spacing on all sides. The approach successfully assured homogeneous casting of the bottom layer and prevented possible gaps. However, in practice this would not be necessary as all sides would be exposed and easily accessible for placing the ECC layer.
- The remaining three sides were poured after the column was already inside the formwork and resting on the bottom layer. The time to place the column above the bottom layer was less than 10 minutes, so there was no bonding problems or cold joints between the remaining three sides and the bottom layer.
- The jacketed columns were cured using wet burlaps and covered with polyethylene sheets for at least seven days.

3.5 Test Matrix

Table 3.8 presents the geometry of columns and the details of the strengthening methodology. The table also shows the column categories considered (non-seismic with a tie spacing of h/2 or seismic/blast with a tie spacing of h/4). In addition, the table presents the level of axial load as a percentage of the column concentric capacity based on CSA A23.3. The columns were labeled

with acronyms and numbers stating the type and the parameters of hardening method. For instance, columns Ref-N1 and Ref-S represent the reference columns designed as a non-seismic and seismic column, respectively, cast during the first phase with a concrete compressive strength of 45 MPa. Column SH-207e-0.15f_{pu}-N1 represents a non-seismic column with an external single-harped prestressing 7-wire strand with 207 mm eccentricity and prestressed to 15% of strand ultimate tensile capacity. Similarly, DH, TH, and P stand for double-harped, triple-harped, and parabolic longitudinal profiles of hardened columns post-tensioned with external 7-wire strands. The column labels from the post-tensioned group with internal 7-wire strands start with the letters PT. For example, PT-SS-0.35fpu-S presents the post-tensioned seismic column with an internal single strand (SS) prestressed by a prestressing force equal to 35% of strand tensile capacity. Similarly, column PT-DS-0.40fpu-S represents the post-tensioned seismic column with an internal double strand (DS) prestressed by a prestressing force equal to 40% of strand capacity. The jacketed columns were also given specific labels such as ECC-2.0%v_f-t30-N1, represented non-seismic column from the first phase jacketed with a 30 mm thick ECC layer made from ECC mix containing 2% dosage polyethylene fibers. The last two columns jacketed with ECC differ from the first ECC column in fiber dosage or thickness as reflected in their labels. The suffix N2 in the column labels presents the columns cast in the second phase with a concrete compressive strength of 50 MPa at 28 days.

3.6 Instrumentation and Test Setup

All the columns were instrumented with electrical resistance strain gauges to monitor the state of strain at selected stages of loading (see Figure 3.32). Electrical resistance strain gauges embedded inside the specimens were used for longitudinal and transverse reinforcements. Strain gauges were glued on to the longitudinal reinforcement at column mid-height (critical section). A strain gauge was glued at 1/3 of the column height on the transverse reinforcement. In addition, external strain gauges were attached to prestressing strands and the ECC surface. For internally post-tensioned columns a strain gauge was glued to the strand before inserting it inside the duct, and then the strand was carefully placed in. However, during the jacking process of the strands the strain gauges stopped working, possibly either the gauge or the wiring being damaged between the duct and the strand surface because of the very tight confined space around the strand and the duct wall.

A high-sensitivity LVDT (Linear Variable Displacement Transducer) was deployed at mid-height with a customized protection steel frame, as shown in Figure 3.33. The protection steel frame is designed to protect the LVDT in case of total collapse of the specimen. The LVDT and the protection frame were mounted to a rigid steel pipe secured between the laboratory floor and ceiling. The other end of LVDT was bolted to the surface of the column, which was tested to measure the deflection and rebound of the column during blast loading. All the instrumentation was monitored using a high-speed data acquisition system that can record up to 100,000 samples per second. In addition, the high-speed cameras (Phantom VL420 with a recording capability of 2000 frames per second) were used to measure positive and negative (rebound) deflections during blast loading and used as backup in case of LVDT malfunctioning. Two cameras were used in the process, one capturing the side view and the second capturing the front view. The cameras were set up with a triggering mechanism programmed in the data acquisition system to initiate the recording of the column time history response. The triggering was important in synchronizing video time history to the data time history of the tested column.

The columns were mounted vertically between the hydraulic jack used to apply the axial load and the load cell that was placed above the column and under the laboratory ceiling. Before mounting the column, a custom-made Load Transfer Device (LTD), described in Section 3.9 was installed on the shock tube, covering the end frame. The column was placed between the flanges of the shock tube frame and supported by roller-pinned supports, as shown in Figure 3.33. The roller-pinned supports were attached to a rigid hollow structural steel (HSS) tied to the shock tube opening flanges using threaded rods at the top and bottom of the shock tube opening. In addition, the HSS section was supported with two steel pipes to maintain its location along the height in the vertical direction. Columns were resting on roller-supported plates to restrict lateral translation but allow free rotation and longitudinal translation. Longitudinal translation is expected because of column shortening due to axial compression and blast-induced lateral deflection.

The pressure generated by the shock tube (described in Section 3.8) was uniformly transferred to the columns using the LTD. The built-in Piezotronics pressure sensors (at the side and bottom) located inside the shock tube near the reflecting surface of LTD were used to measure the reflected pressure-time history. The axial load time history was monitored using a load cell placed between the top of the column and the laboratory ceiling, which was a 910 mm thick reinforced concrete slab as shown in Figure 3.33. The pressure generated by the hydraulic pump

for the jack that used to apply the axial load was also monitored using a pressure gauge to ensure the application of the designed axial load. In addition, two load cells were placed at the bottom and top supports between the rigid HSS section and column to measure the support reactions in the direction of blast loading (see Figure 3.33).

3.7 Loading Protocol

Columns were subjected to combined axial load applied by hydraulic jack and blast load generated by the shock tube. The columns were first loaded with axial load prior to applying blast pressure. The axial load was equal to 35% of the column concentric capacity. It was applied using a 500 kN capacity hydraulic jack placed at the bottom of the column (see Figure 3.34). To facilitate axial rotation during blast loading, grooved plates with smooth round bars were used at the top and bottom of the column between the column and the hydraulic jack (sandwiched), as well as between the column and the load cell.

The columns were subjected to multiple incremental blast shots to assess their elastic and inelastic responses. The axial load was adjusted to the initial level after each blast shot when needed and it could be resisted by the test column. Occasionally it was observed that the load dropped not due to the column strength reduction, but rather due to the movement of the overall setup. The adjustment of axial load was also done during the prestressing application prior to blast testing because it was being reduced. The vertical force component of post-tensioned strands resulted in the shortening of the column, thus releasing a portion of the pressure exerted by the hydraulic jack. Similarly, reapplying the lost portion of the axial load caused some loss of tension in the strands. Therefore, the prestressing force and the axial load were adjusted periodically to achieve the desired levels of forces.

3.8 Blast Simulator

Performing live blast tests (field testing) using explosive materials is costly and strictly controlled due to safety and security concerns. Blast simulators provide an alternative to field testing that can generate a similar effect of blast load. A commonly used blast simulator is a shock tube. The shock tube generates a blast load by driving air to hit the test specimen at a high velocity. The shock tube at the University of Ottawa can generate blast loading with high strain rates, simulating blast loading conditions observed during far-field explosions. To generate a blast load with a desired reflected pressure and impulse, a combination of driver length and pressure need to be considered.

Shock tubes consist of two major sections: a driver and an expansion section, as shown in Figure 3.35. The driver section can have a spool section added for double diaphragm shock tubes for improved control of shock waves. The pressure in the spool is used to balance driver pressure until the desired pressure level is attained prior to releasing the spool pressure to trigger the blast shot. The driver section has an adjustable length, consisting of steel pipes to generate the required pressure and impulse (duration). The driver length of the shock tube used in the current research project can be adjusted in increments of 305 mm based on the required pressure-impulse combination. The driver section is filled with compressed air which is contained inside the driver section by an aluminum diaphragm at the location of the spool (see Figure 3.35). The spool section facilitates the controlled firing mechanism as previously indicated using an air pressure control device shown in Figure 3.35e. The testing mechanism at the University of Ottawa shock tube is called a double firing mechanism, where the three sections are separated using aluminum foils. To achieve the desired pressure, diaphragms are placed on both ends of the spool section (a diaphragm before the expansion section and on the side of the driver section (as shown in Figure 3.35c), creating a gap. When the driver section is filled with targeted pressure, the spool section is also filled with approximately half the targeted air pressure to balance some of the driver pressure and prevent the rupturing the diaphragms prematurely (Figure 3.35d shows the hoses connected to the spool and driver sections). Therefore, the thickness of the diaphragm used on the spool side is adjusted according to the difference in pressures considered. Diaphragms are usually made of aluminum foils with varying thicknesses according to the desired pressure in the driver section. The aluminum foil thickness and quantity are selected based on the predetermined pressure-impulse combination. The aluminum foils used were supplied in square shapes and had to be drilled with holes matching the diameter of the fastener (steel bolts) on the shock tube spool section (see Figure 3.36). The blast load is generated when the diaphragms rupture and the air pressure rush towards the expansion section (end frame) at supersonic velocities. The driver pressure determines the reflected pressure, while the driver length controls the duration of load (impulse).

The expansion section is equipped with vents on the sides and top of the rigid frame that are closed before the shock wave is released. The presence of vents releases the pressure after it hits the test sample to minimize secondary pressures that result from the returning air pressure after hitting the back of the shock tube. The expansion section of the shock tube at the University of Ottawa has a rectangular opening (end frame) of 2032 x 2032 mm. If test specimens are larger

than the existing opening, the expansion section can be modified, but not for the current study. For nonplanar test specimens (i.e., columns, beams, window parts, etc.), a carefully designed load transfer device (LTD) is used to uniformly distribute the load without providing additional resistance. In addition, the LTD can also simulate a cladding façade in an actual building. The combination of driver air pressure and driver length generates a unique combination of pressure and impulse. Table 3.9 presents the combinations of driver length and air pressure used in the current test program to simulate blast loads generated by a specific charge weight and stand-off distance combination.

3.9 Load Transfer Device (LTD)

Since columns are nonplanar test specimens, LTD is required to uniformly distribute the blast pressure to the surface of the column without venting the pressure generated through the openings around the column (if not LTD), while also providing ability to increase blast loads over and above the shock tube capacity by collecting the pressure over the entire test area and transferring it to the surface of the column (i.e. maximizing the available capacity). In this study, LTD is made of a thin steel sheet having a thickness of 0.71 mm and dimensions of 2083 mm x 2083mm (see Figure 3.37 to Figure 3.39). The LTD was slightly bigger than the shock tube opening (2032 x 2032 mm) to prevent pressure loss during blast loading and stop the curtain from penetrating in the shock tube opening at rebound (negative phase). The steel sheet is bolted to eight long hollow structural steel (HSS) stiffeners (2083 mm long). Six of the eight stiffeners each carry two short HSS (203 mm long and 6 mm indented on the column side) sections welded in the middle of the stiffeners. In total, 14 contact surfaces (i.e., top and bottom HSS beams and 12 short HSS sections welded to the long HSS beams) were created between the curtain and the test specimen, as shown in Figure 3.39. The total mass of the LTD used is 250 kg. LTD is attached only from the top side to the flange of the shock tube opening (swivel joint), so it acts like a curtain that freely moves laterally while collecting the shock wave from the shock tube and transferring it to the column without contributing to resistance.

Table 3.1 – Mix proportions of OPC concrete.

Materials	Quantity (kg)
Cement (GUL)	360
Sand (0-5 mm)	862
Coarse Aggregates (14 mm)	1075
Water (L)	180
Superplasticizer (L)	4

Table 3.2 – Mechanical properties of longitudinal & transverse reinforcement and prestressing strands.

Property	6.35 mm smooth bar	10M deformed rebar	13M seven-wire strand	15M seven-wire strand
Yield strength (MPa)	455	480	1650	1650
Ultimate strength (MPa)	600	670	2200	2200
Yield strain	0.002	0.002	0.1	0.1

Table 3.3 – Mix proportions of ECC mix.

Materials	2% fiber	1.5% fiber
Cement (kg)	1326.6	1333.3
Silica Fume (kg)	132.7	133.3
Fibers (kg)	19.6	14.7
Water (L)	437.7	440
Superplasticizer (L)	26.5	26.7

Table 3.4 – Mechanical Properties of UHMWPE fibers.

Diameter (microns)	**18**
Length (mm)	13
Tenacity (GPa)	3
Modulus (GPa)	114
Specific gravity (g/cm^3)	0.97

Table 3.5 – Mechanical properties of ECC mixes obtained experimentally.

Property	2% fiber	1.5% fiber
Ultimate Compressive Strength (MPa)	70	75
Compressive Strain at Maximum Strength	0.007	0.007
Tensile Cracking Strength (MPa)	3	3
Ultimate Tensile Strength (MPa)	6	5
Tensile Cracking Strain	0.00015	0.00016
Tensile Maximum Strain	0.02	0.015

Table 3.6 – Calculation of pre-blast reactive moment and stresses.

Strand Profile	**Single-harped**	**Double-harped**		**Triple-harped**		**Parabolic**		**Single-Straight**	**Double-Straight**
Column ID, short name	**SH**	**DH1**	**DH2**	**TH1**	**TH2**	**P1**	**P2**	**SS**	**DS**
Total Strand Area, mm^2	198	198	198	198	198	198	198	140	280
Total Prestressing Force, kN	55.2	47.9	58.9	36.8	55.2	33.1	58.9	91.1	208.3
Eccentricity, mm (tension)	207	207	207	247	247	227	227	37	37
Eccentricity, mm (Compression)	76	76	76	76	76	76	76	0.0	37
Strand Angle, degrees	78.8	75.2	75.2	NA	NA	NA	NA	0.0	0.0
Resultant Reactive Moment, kN.m	8.7	7.5	9.2	6.3	9.4	5	8.9	3.4	0.0
Resultant Compressive Force, kN	54.2	46.3	57.0	36.8	55.2	33.1	58.9	91.1	208.3
Initial Axial Load, kN	300	300	300	300	300	300	300	300	300
Stress, MPa (on tension side)	-0.4	-2.3	0.2	-3.8	0.8	-5.9	-0.3	-11.2	-22.0
Stress, MPa (on compression side)	-30	-28	-31	25	-31	-23	-31	-23	-22
Camber, mm	2.4	2.6	3.2	2.6	3.6	2.0	3.4	2.6	0.0

Table 3.7 – Taken from Table 8.1 of CPCI design manual 5th edition [81].

TENDON PROFILE	EQUIVALENT MOMENT OR LOAD	EQUIVALENT LOADING	CAMBER	END ROTATION	
			+ ↑	+ ↻	+ ↻
(4) 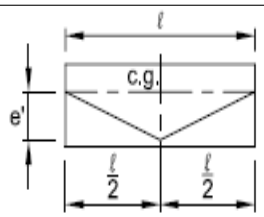	$N=\frac{4Pe'}{\ell}$	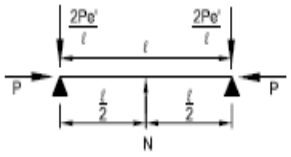	$\frac{N\ell^3}{48EI}$	$\frac{N\ell^2}{16EI}$	$-\frac{N\ell^2}{16EI}$
(5) 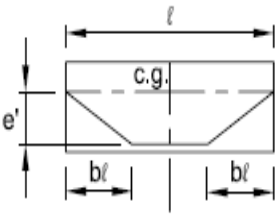	$N=\frac{Pe'}{b\ell}$	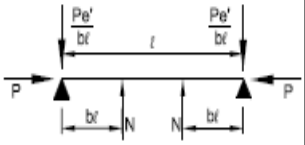	$\frac{b(3-4b^2)N\ell^3}{24EI}$	$\frac{b(1-b)N\ell^2}{2EI}$	$-\frac{b(1-b)N\ell^2}{2EI}$
(6) 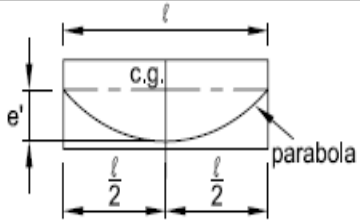	$w=\frac{8Pe'}{\ell^2}$	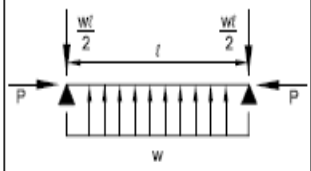	$\frac{5w\ell^4}{384EI}$	$\frac{w\ell^3}{24EI}$	$-\frac{w\ell^3}{24EI}$

Note: 1. The tabulated values apply to the effects of prestressing. In all cases, prestressing force is denoted as "P". By adjusting the directional notation, they may also be used for the effects of loads.

2. In cases where P is not applied at the c.g., total cambers will be the sum of the effects of pattern (3) plus those of (4), (5) or (6).

Table 3.8 – Test Matrix of current research study.

#	Specimen ID	Qty	Category	Cross-section Dimensions (mm)	Initial Axial Load (%)	Prestressing
1	Ref-N1	1	Non-seismic	152x152	35	None
2	Ref-N2	1	Non-seismic	152x152	35	None
3	Ref-S	1	Seismic/Blast	152x152	35	None
4	SH-207e-0.15f_{pu}-N1	1	Non-seismic	152x152	35	55mm deviator, 15% of f_{pu}
5	DH1-207e-0.13f_{pu}-N1	1	Non-seismic	152x152	35	55mm deviator, 13% of f_{pu}
6	DH2-207e-0.16f_{pu}-N1	1	Non-seismic	152x152	35	55mm deviator, 16% of f_{pu}
7	TH1-247e-0.1f_{pu}-N1	1	Non-seismic	152x152	35	95mm deviator, 10% of f_{pu}
8	TH2-247e-0.15f_{pu}-N2	1	Non-seismic	152x152	35	95mm deviator, 15% of f_{pu}
9	P1-227e-0.09f_{pu}-N1	1	Non-seismic	152x152	35	75mm deviator, 9% of f_{pu}
10	P2-227e-0.16f_{pu}-N2	1	Non-seismic	152x152	35	75mm deviator, 16% of f_{pu}
11	PT-SS-0.35f_{pu}-S	1	Seismic/Blast	152x152	35	35% of f_{pu}
12	PT-DS-0.40f_{pu}-S	1	Seismic/Blast	152x152	35	40% of f_{pu}
13	ECC-2.0%v_f-t30-N1	1	Non-seismic	152x152	35	None
14	ECC-2.0%v_f-t20-N2	1	Non-seismic	152x152	35	None
15	ECC-1.5%v_f-t25-N2	1	Non-seismic	152x152	35	None
	Total number of samples	**15**				

Table 3.9 – Combinations of driver length and air pressure to generate blast loading.

Driver Length (m)	Driver pressure (kPa)	Reflected pressure (kPa)	Impulse (kPa-ms)	Equivalent TNT charge weight (kg)	Equivalent stand-off distance (m)
2.75	150	32	264	136	49
2.75	300	64	461	191	36
2.75	375	81	560	231	34
1.83	150	32	194	71	31
1.83	375	77	437	116	27
1.83	525	108	598	186	27

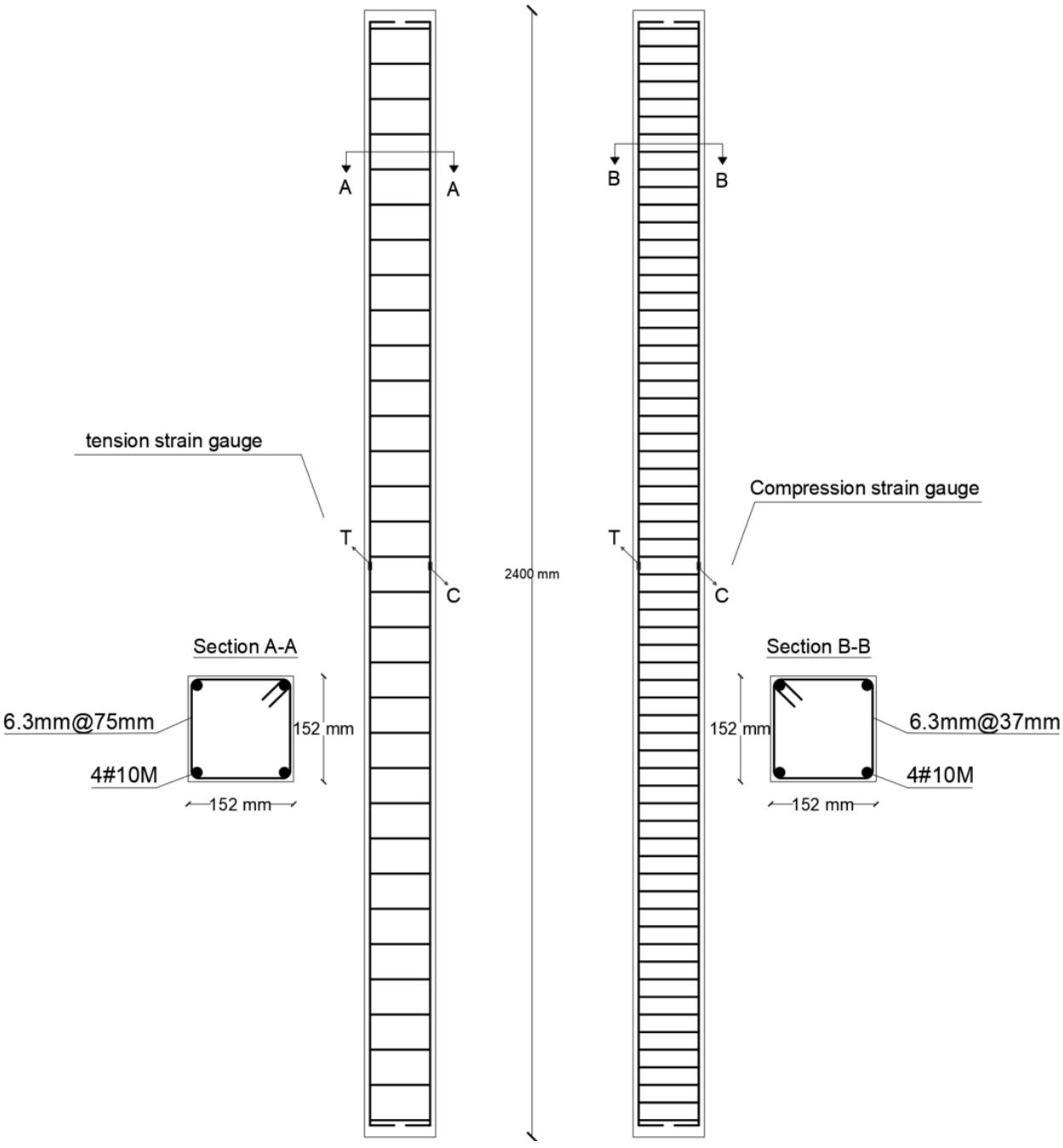

Figure 3.1 – Geometry and reinforcement details of the columns.

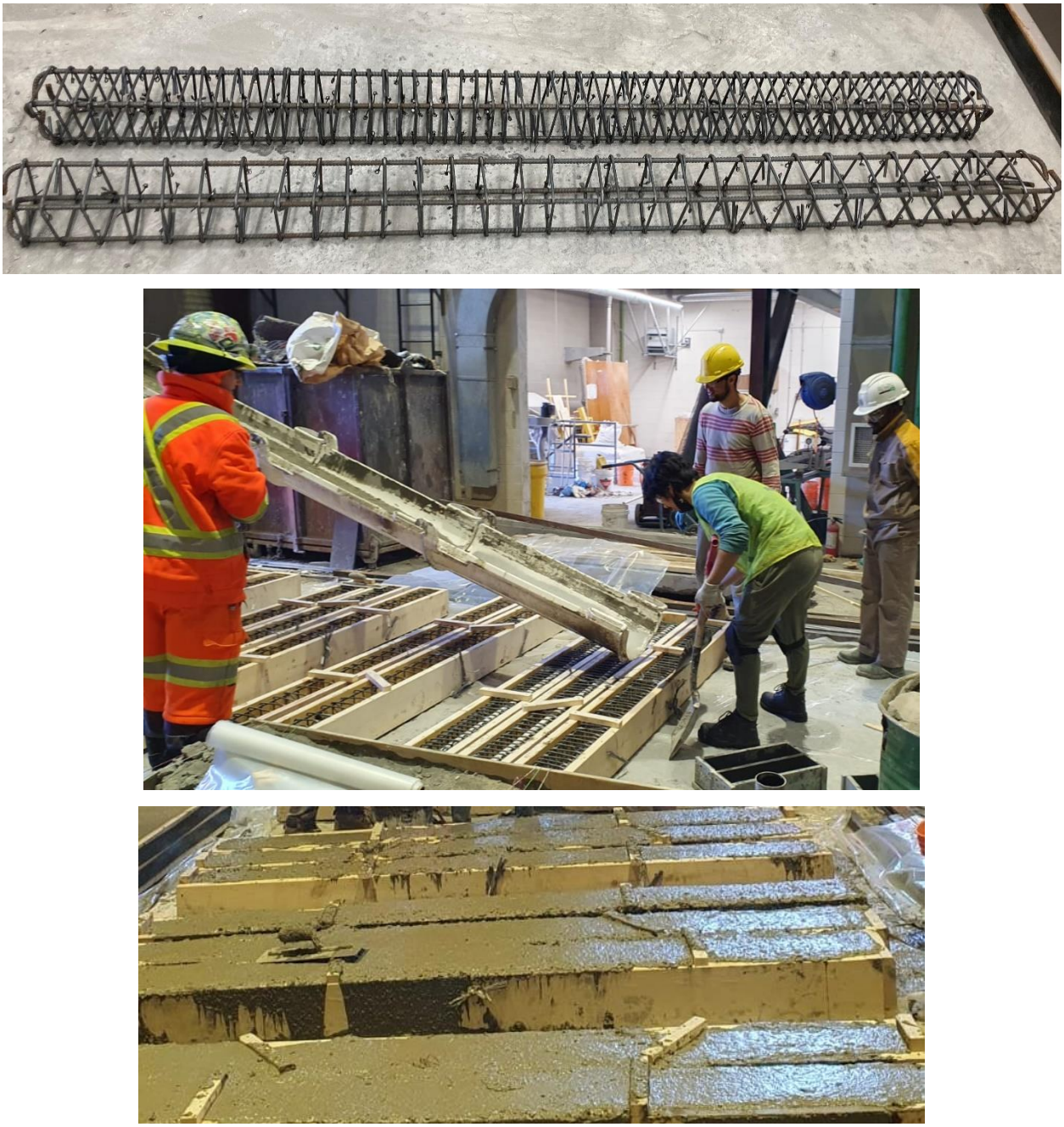

Figure 3.2 – Assembly of reinforcement cage and casting concrete.

Figure 3.3 – Curing of columns with wet burlaps and polyethylene sheets.

Figure 3.4 – Columns after curing; ready for strengthening/hardening and testing.

Figure 3.5 – Batching process of ECC mix.

Figure 3.6 – ECC dog-bone coupon test setup and a close-up photo of a coupon with 2% polyethylene fibers.

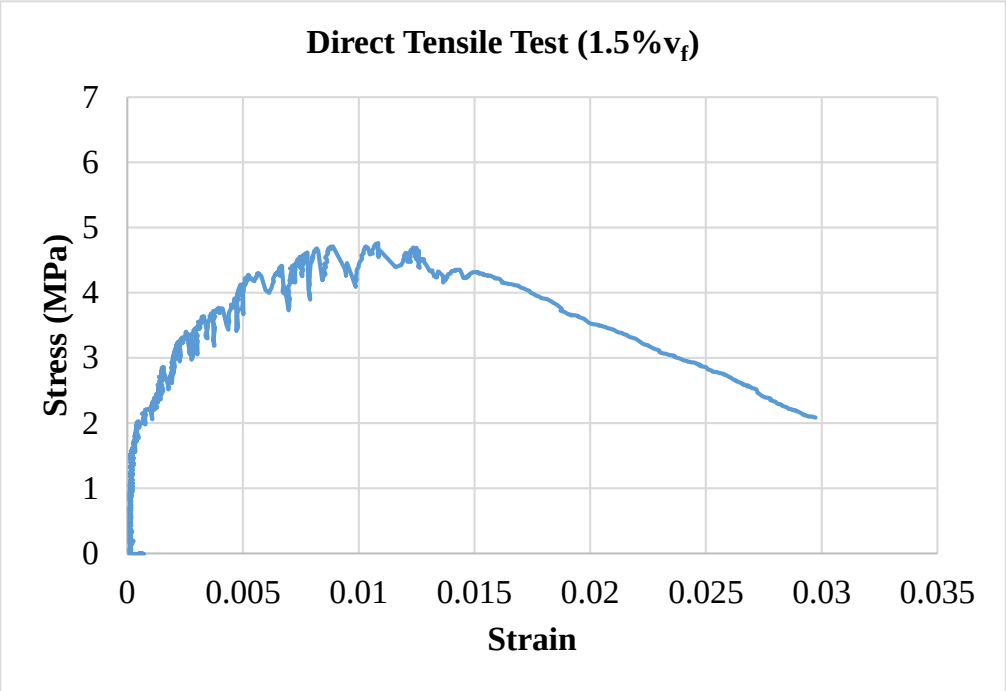

Figure 3.7 – Stress-strain relationship of ECC mix with 1.5% fibers.

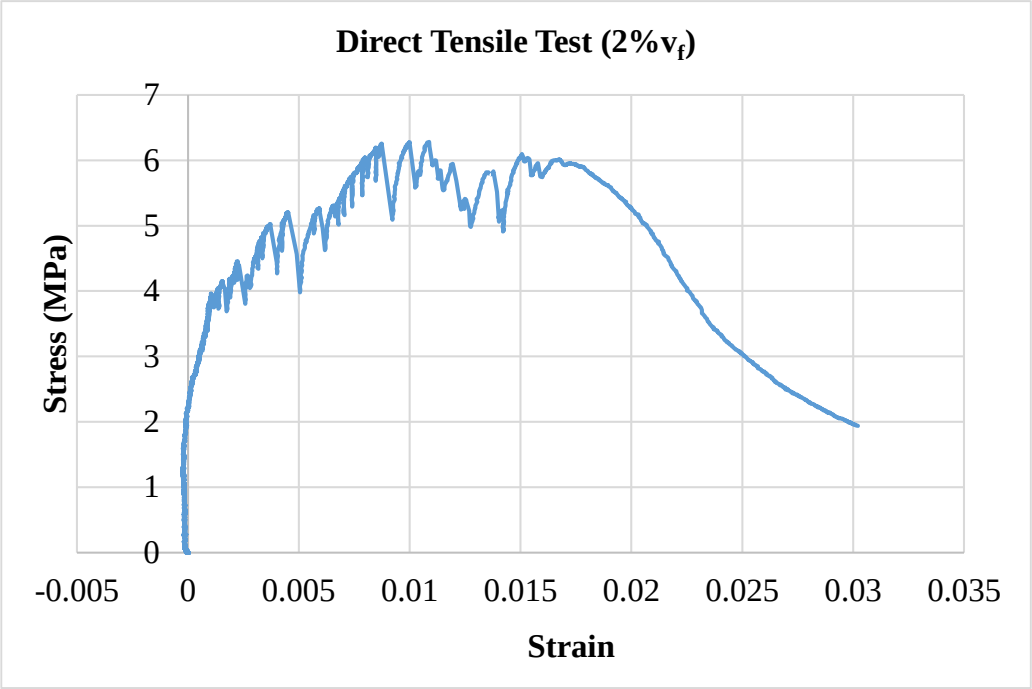

Figure 3.8 – Stress-strain relationship of ECC mix with 2.0% fibers.

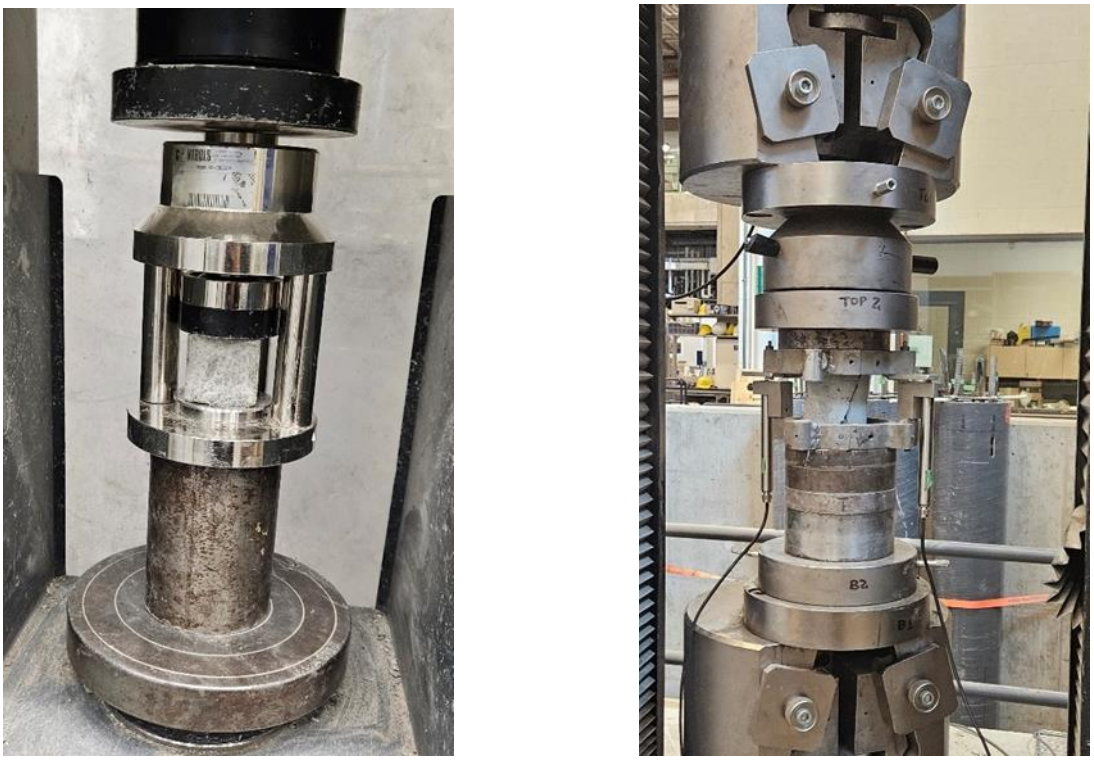

Figure 3.9 – ECC cube tests.

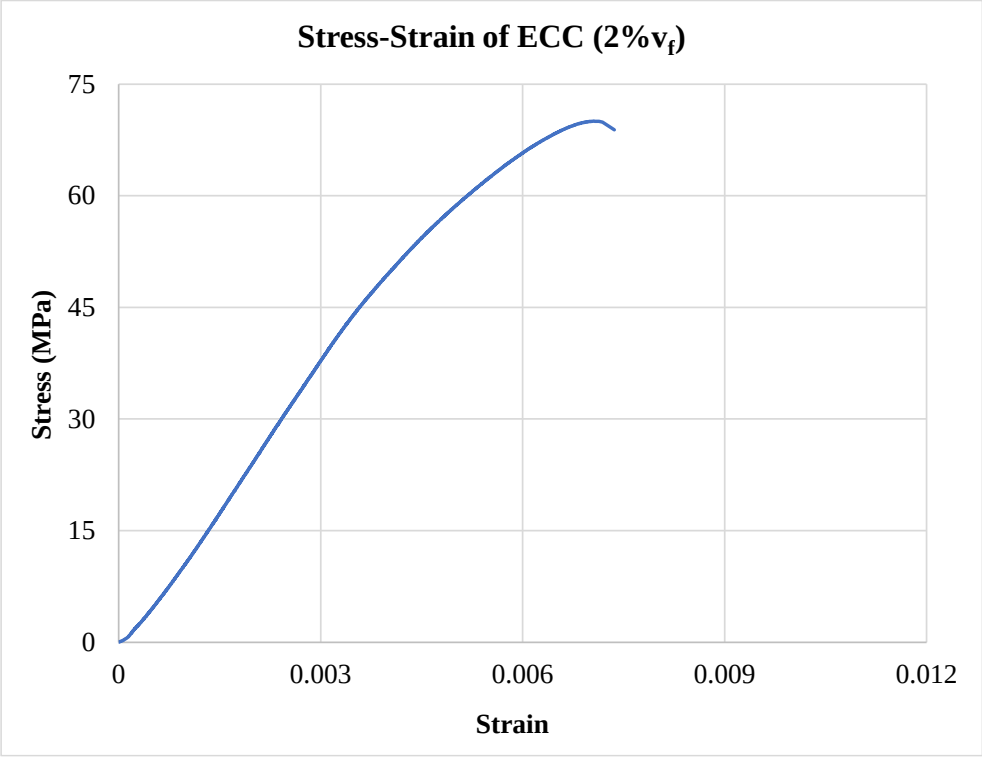

Figure 3.10 – Stress-strain relationship of ECC with 2% of polyethylene fibers under compression.

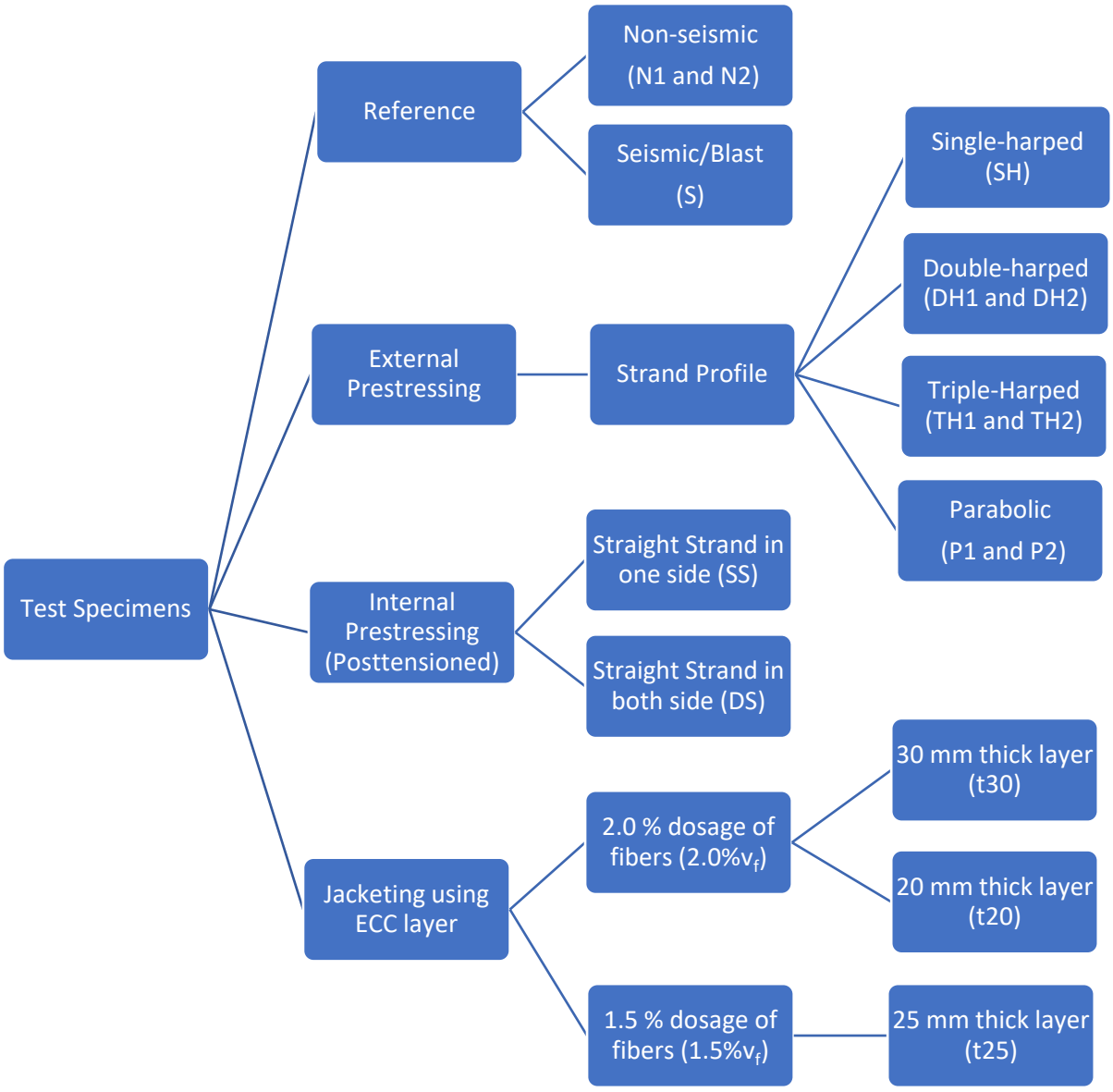

Figure 3.11 – Test matrix of current research study.

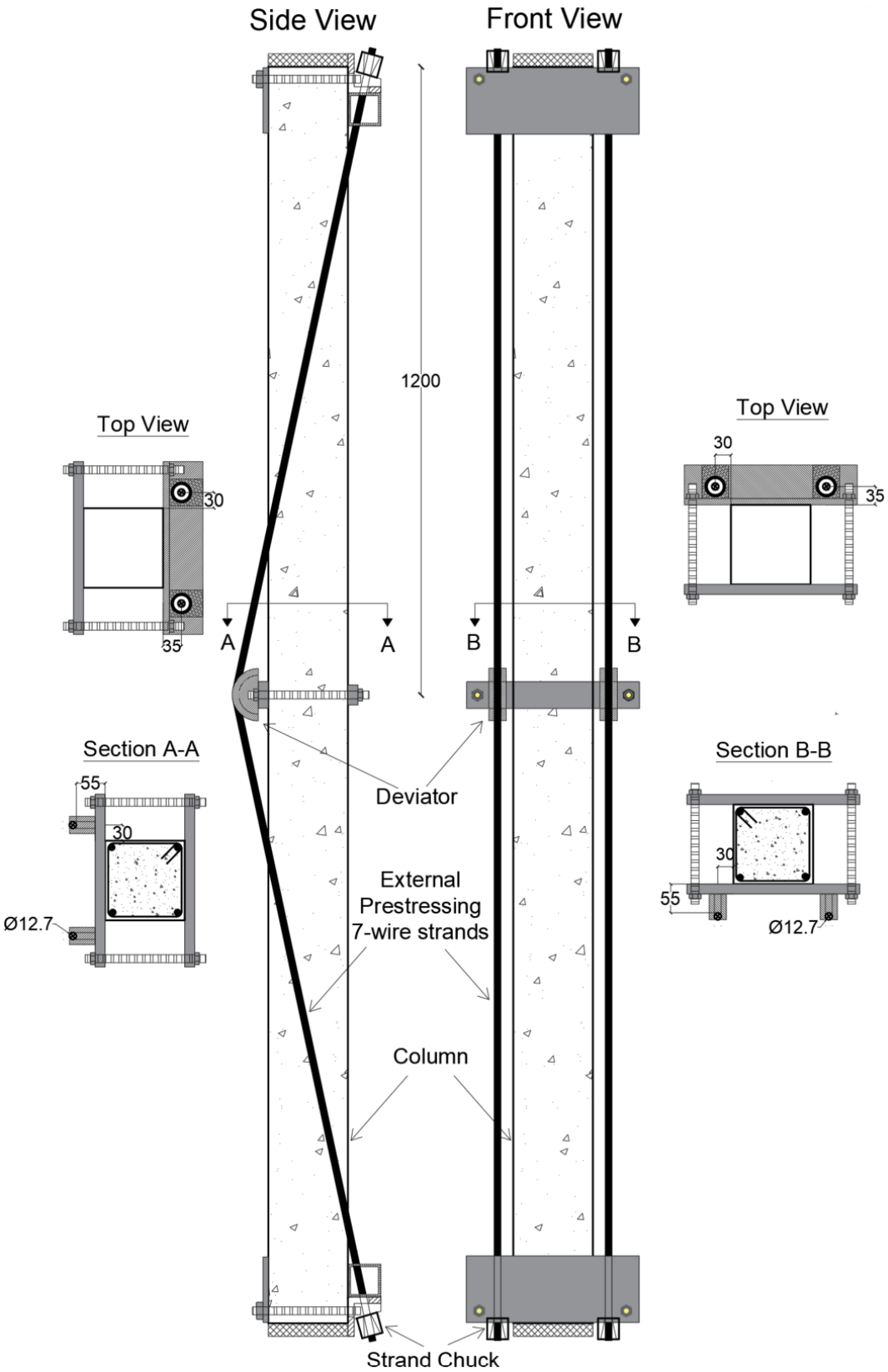

Figure 3.12 – The column with two external prestressing strands having a single-harped profile.

Figure 3.13 – A photo of a column with single-harped profile prior to testing.

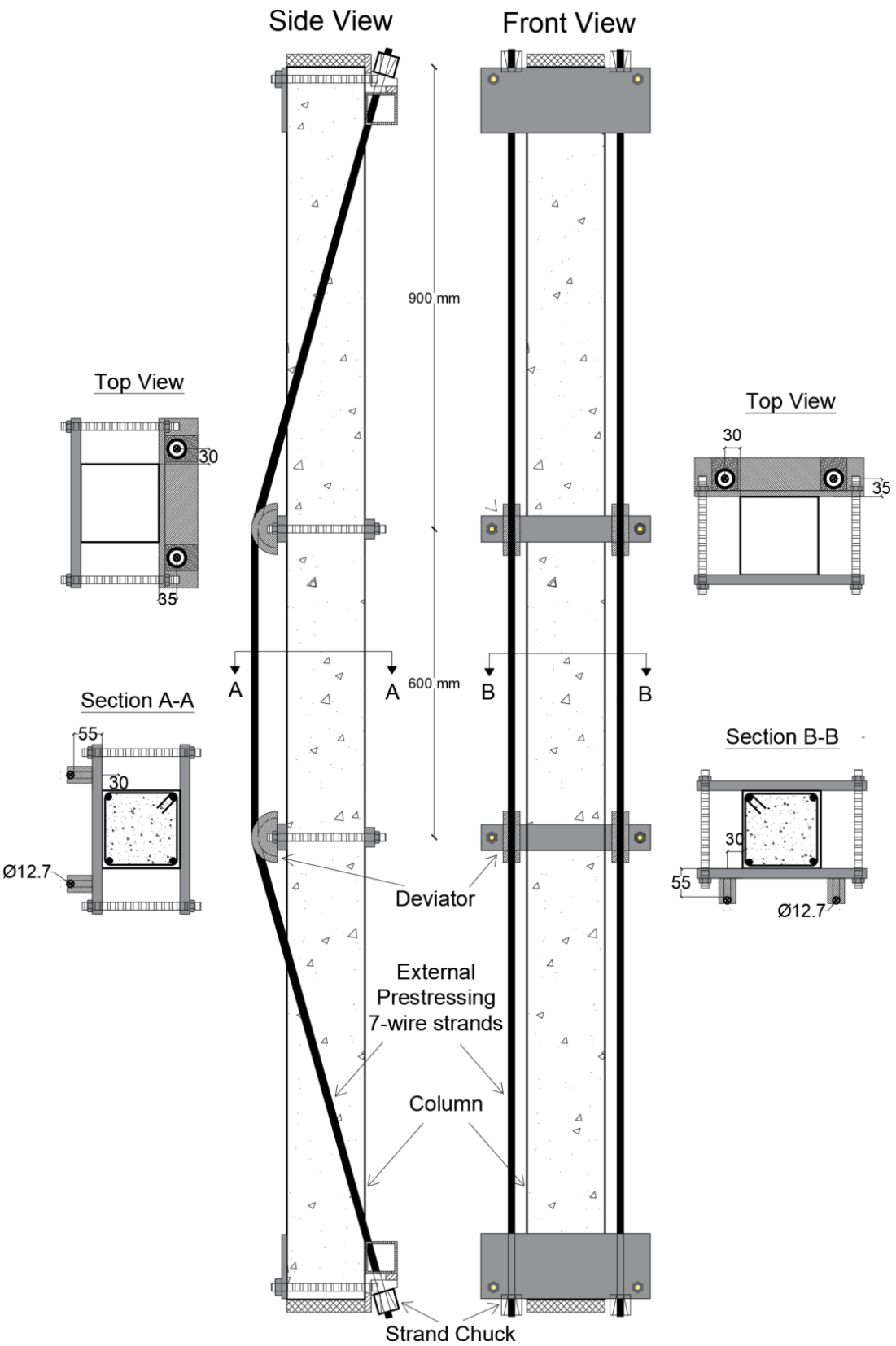

Figure 3.14 – Column with two external prestressing strands having a double-harped profile.

Figure 3.15 – A photo of a column with double-harped profile prior to testing.

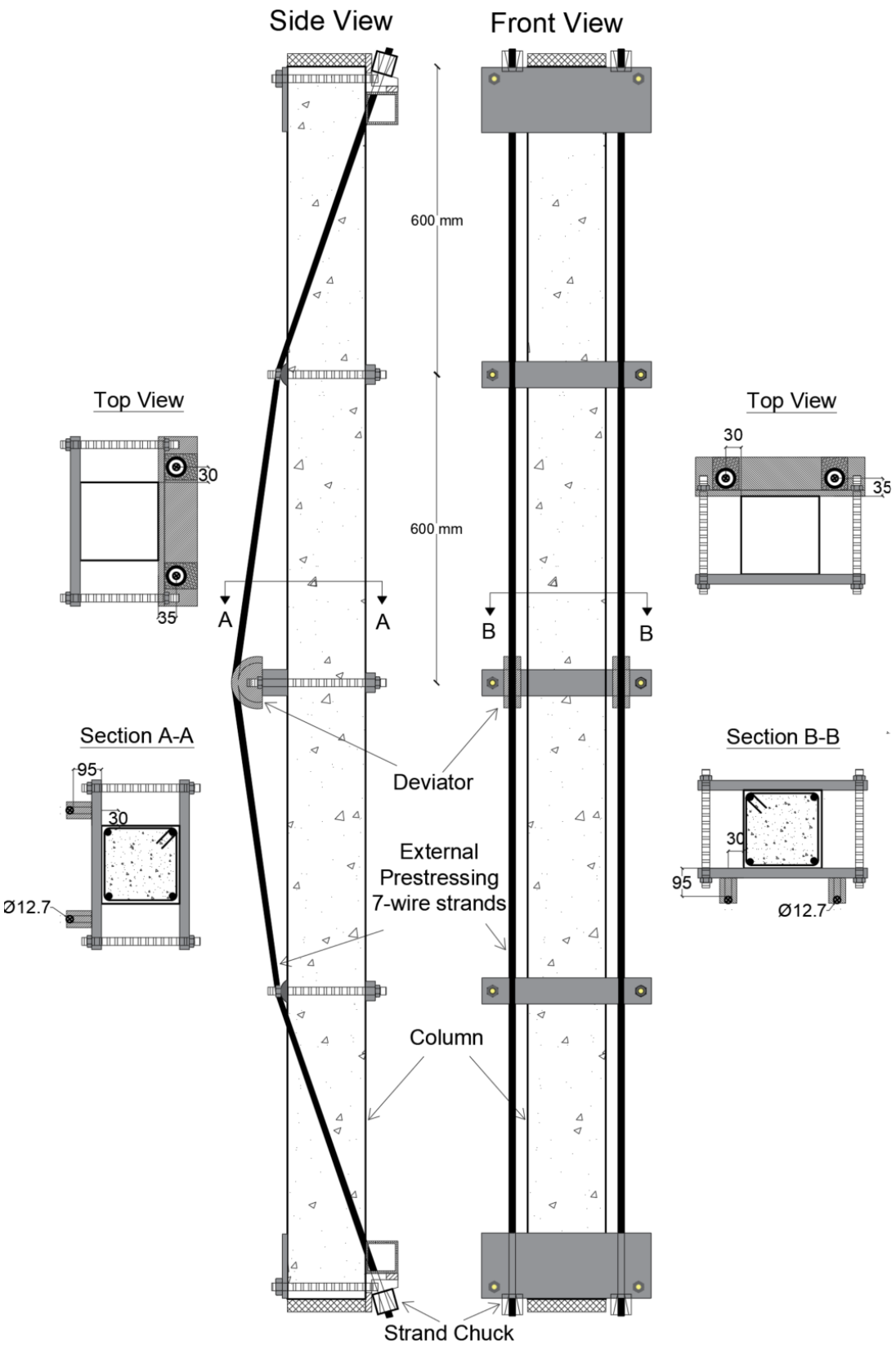

Figure 3.16 –Column with two external prestressing strands having a triple-harped (semi-parabolic) profile.

Figure 3.17 – Photo of a column with triple-harped profile prior to testing.

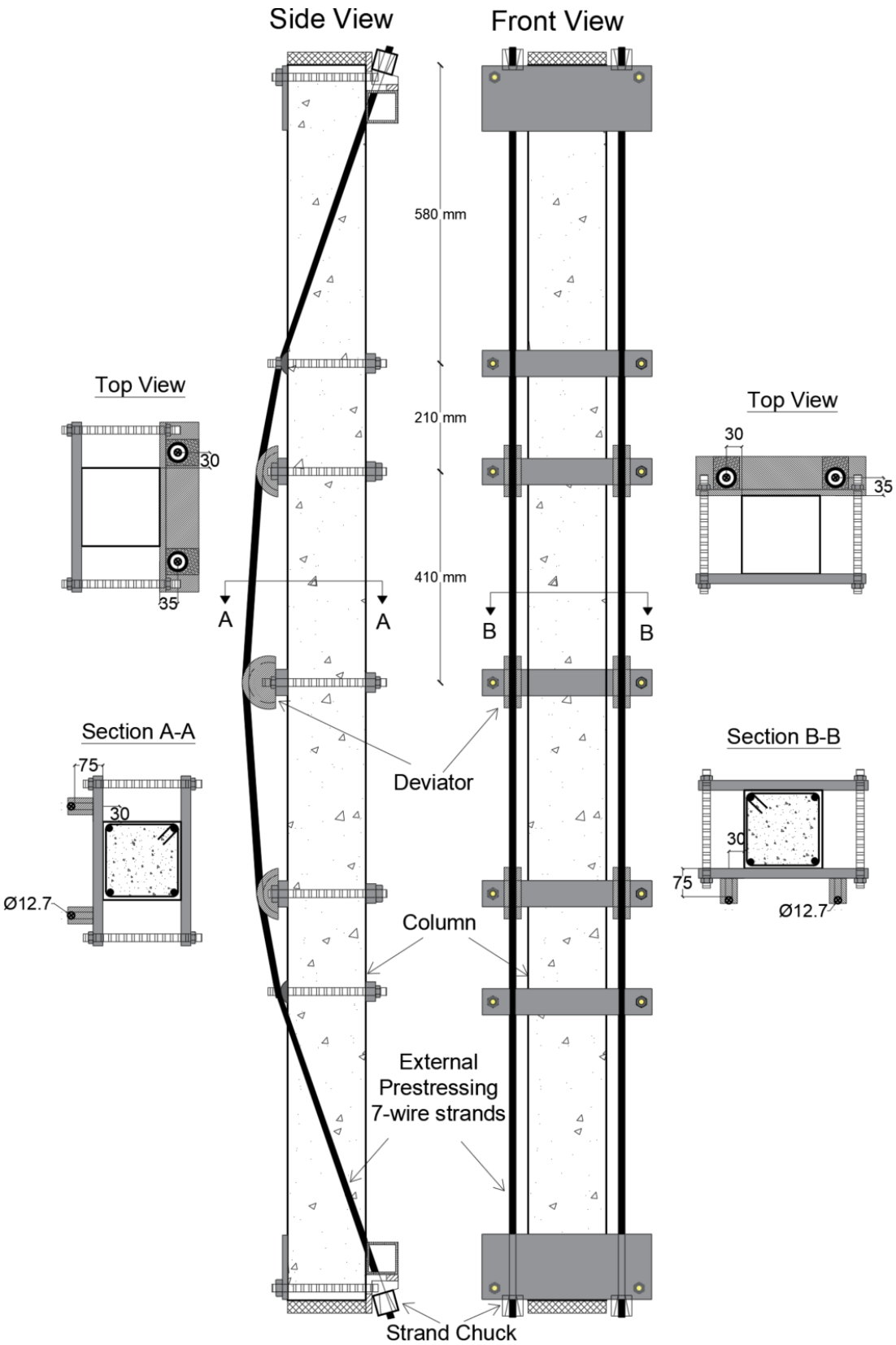

Figure 3.18 – Column with two external prestressing strands having a parabolic profile.

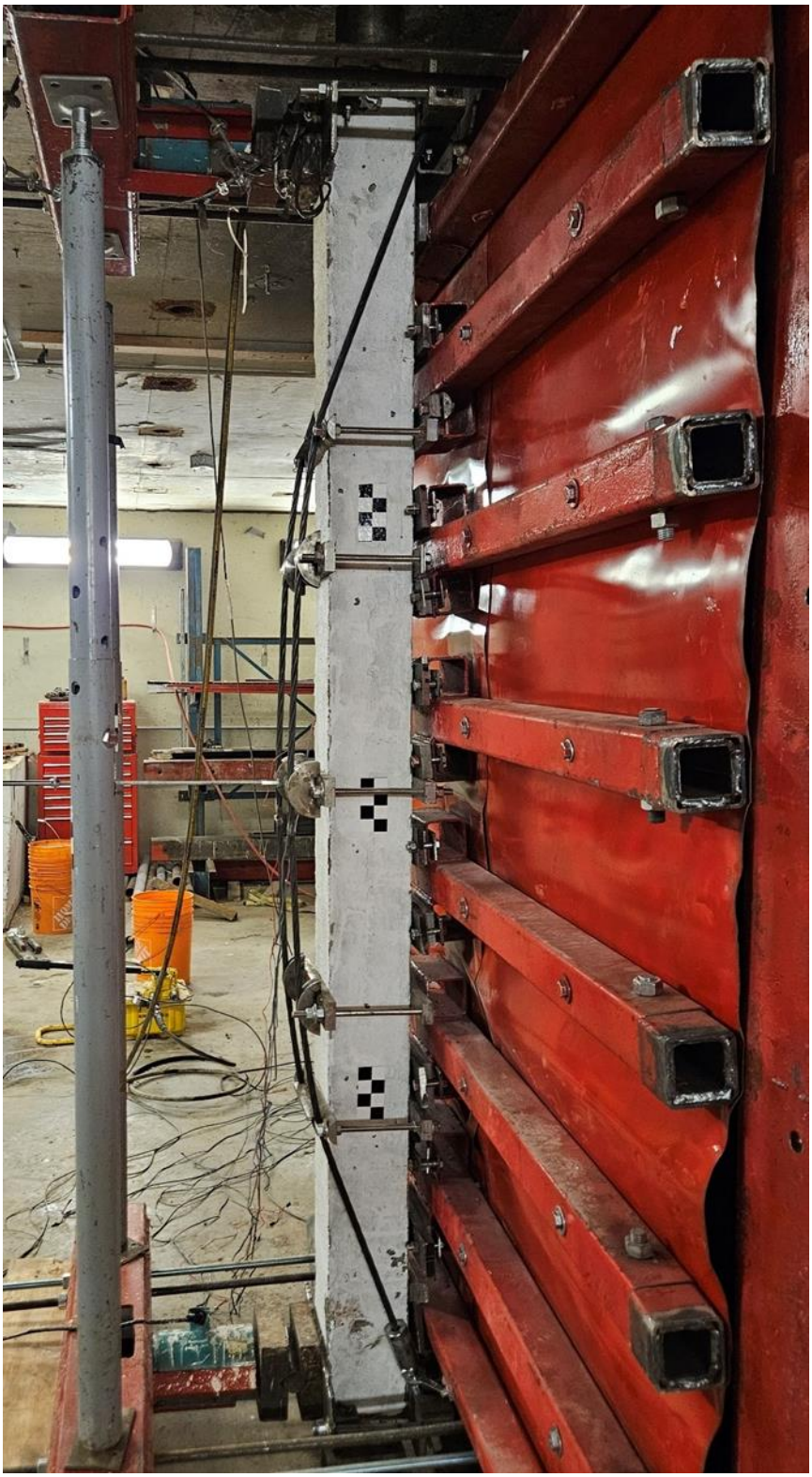

Figure 3.19 – Photo of a column with parabolic profile prior to testing.

(a)

(b)

(c)

Figure 3.20 – Photos showing process of hardening columns using external prestressing strands; a) parabolic-profile strands, b) top and bottom end of the column with end fixtures showing regular chucks and tensioner chucks, and c) disassembled parts of the end fixtures and deviators .

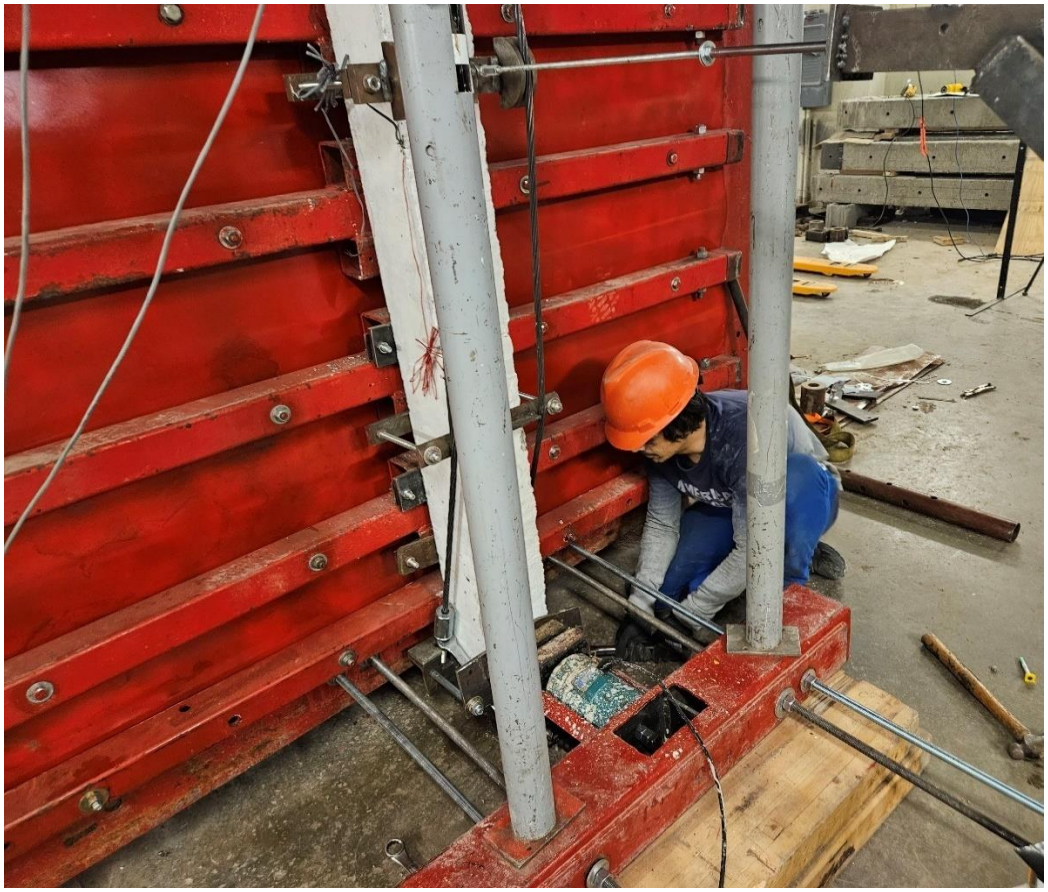

(a)

(b)

(c)

Figure 3.21 – Photos showing the process of tensing external prestressing strands by applying torque force on the tensioner splice chuck using a torque wrench and a torquemeter; a) full view, b) close-up view from left side, c) close-up view from right side.

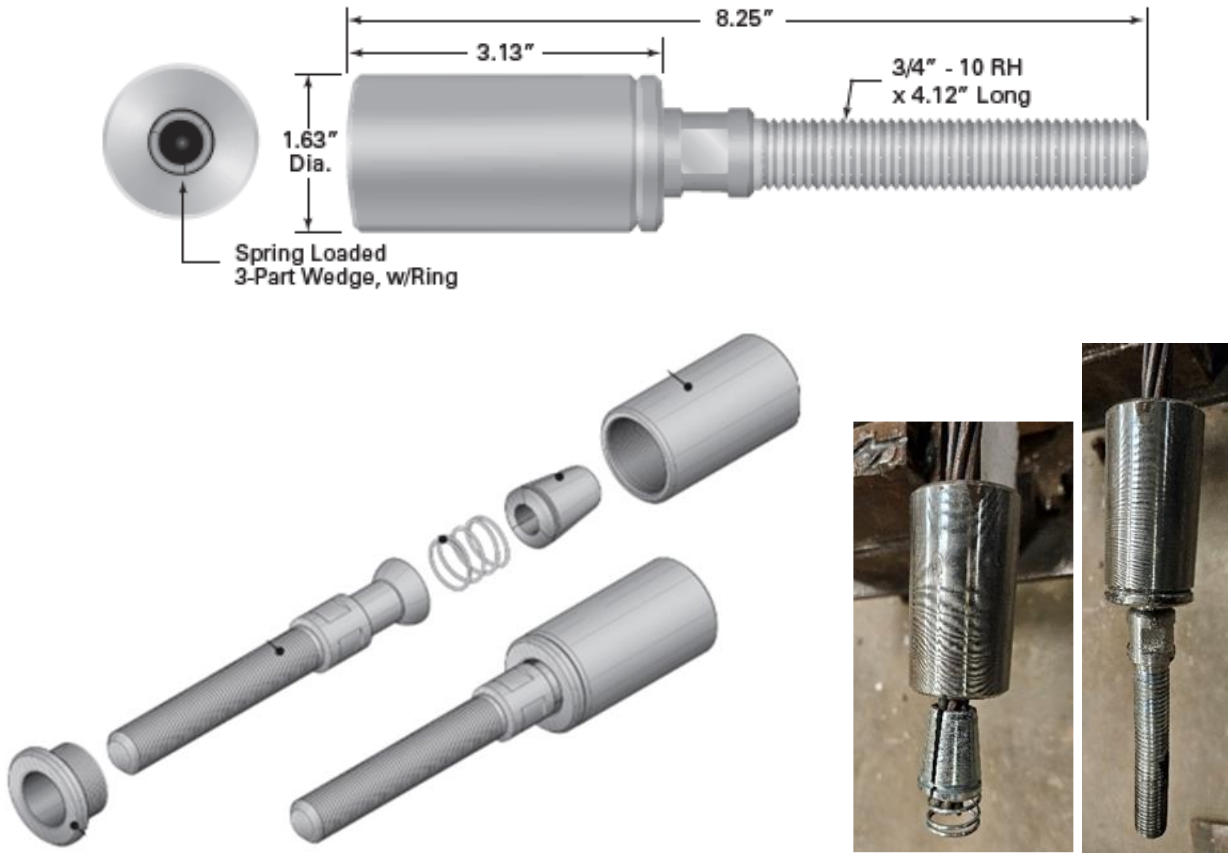

Figure 3.22 – Photo and details of the male tensioner splice chuck supplied by General Technologies Incorporation.

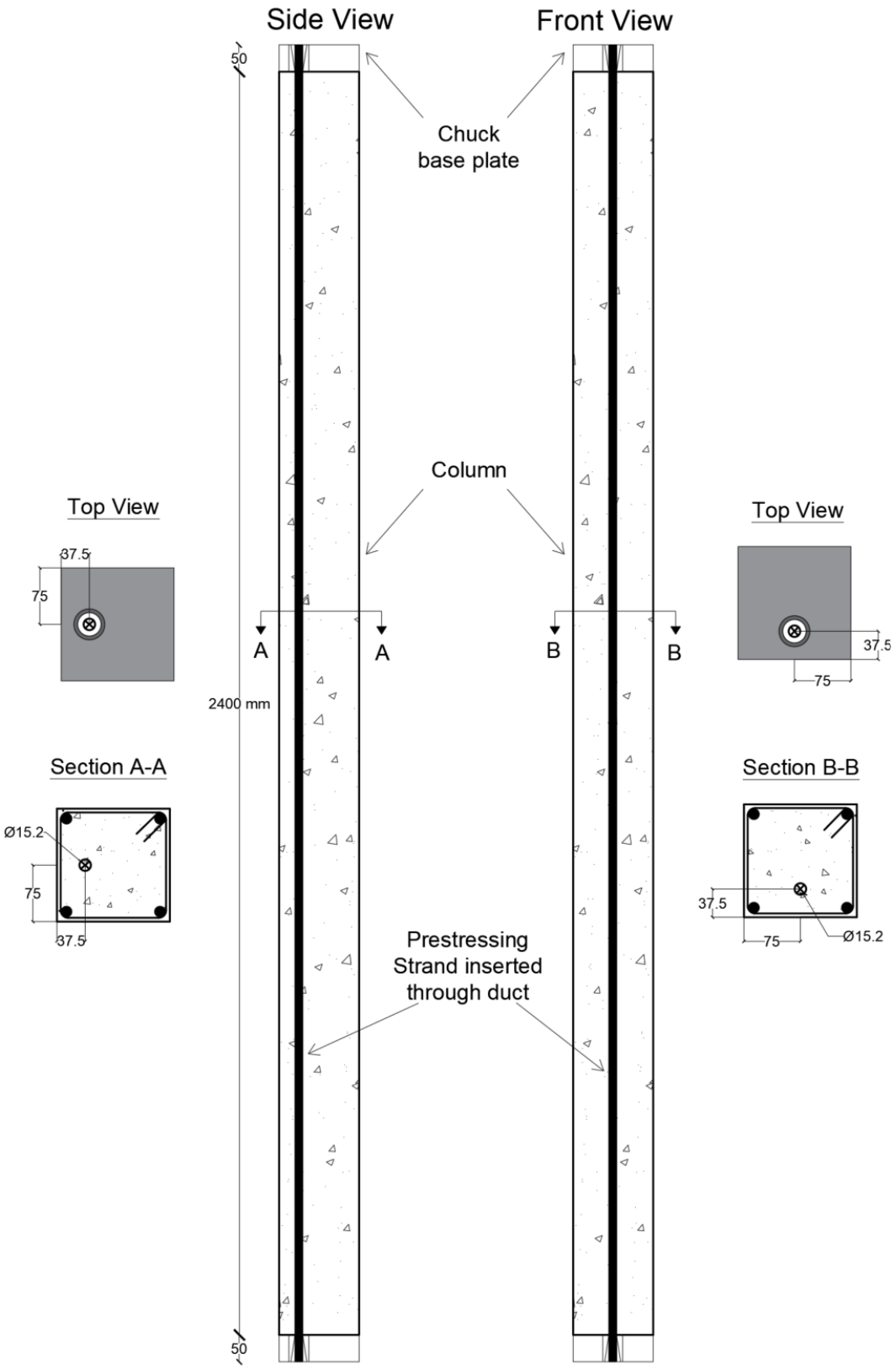

Figure 3.23 – Column strengthened with single internal prestressing strands having a straight profile (constant eccentricity).

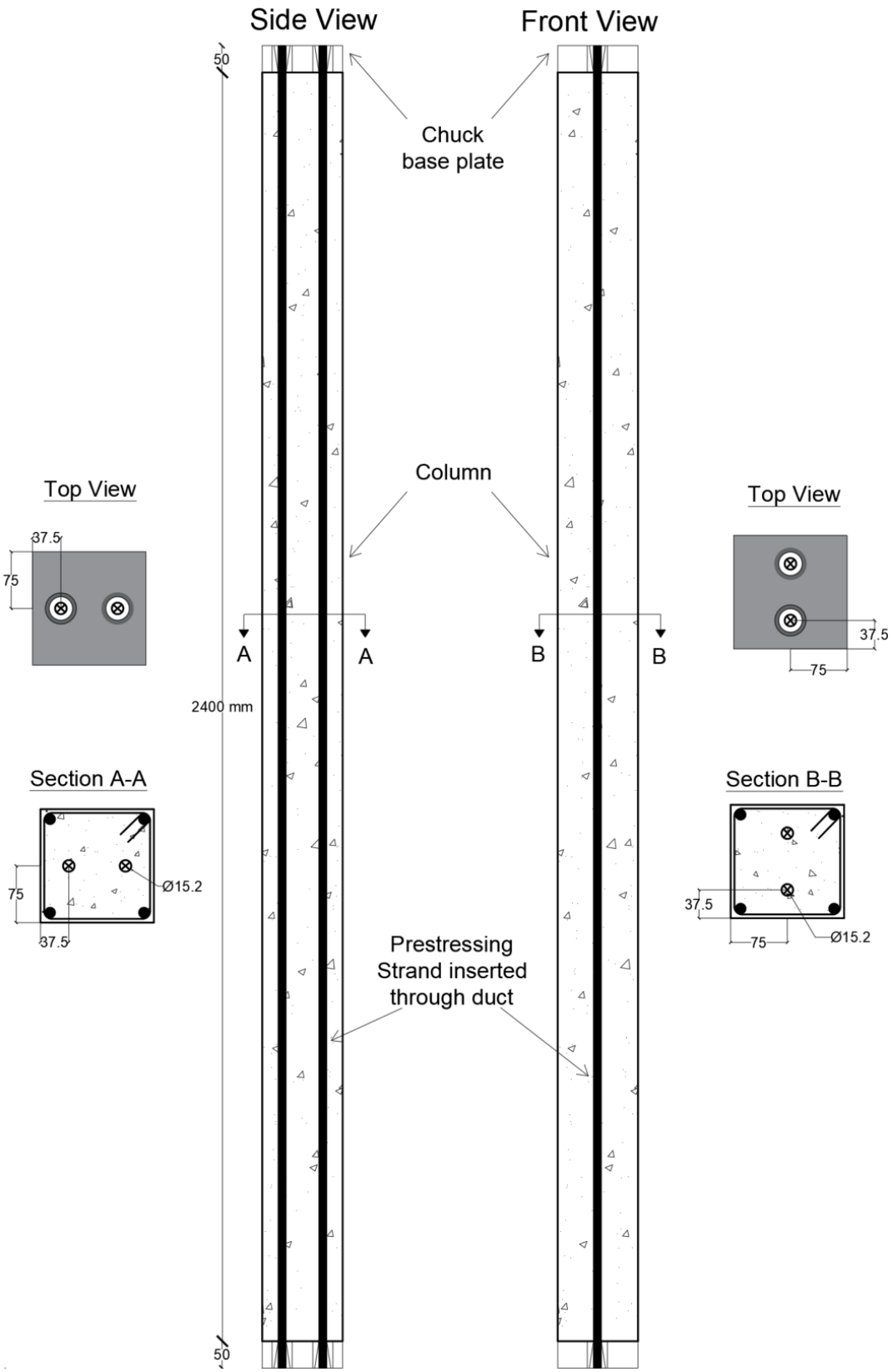

Figure 3.24 – Column strengthened with two internal prestressing strands having a straight profile (constant eccentricity).

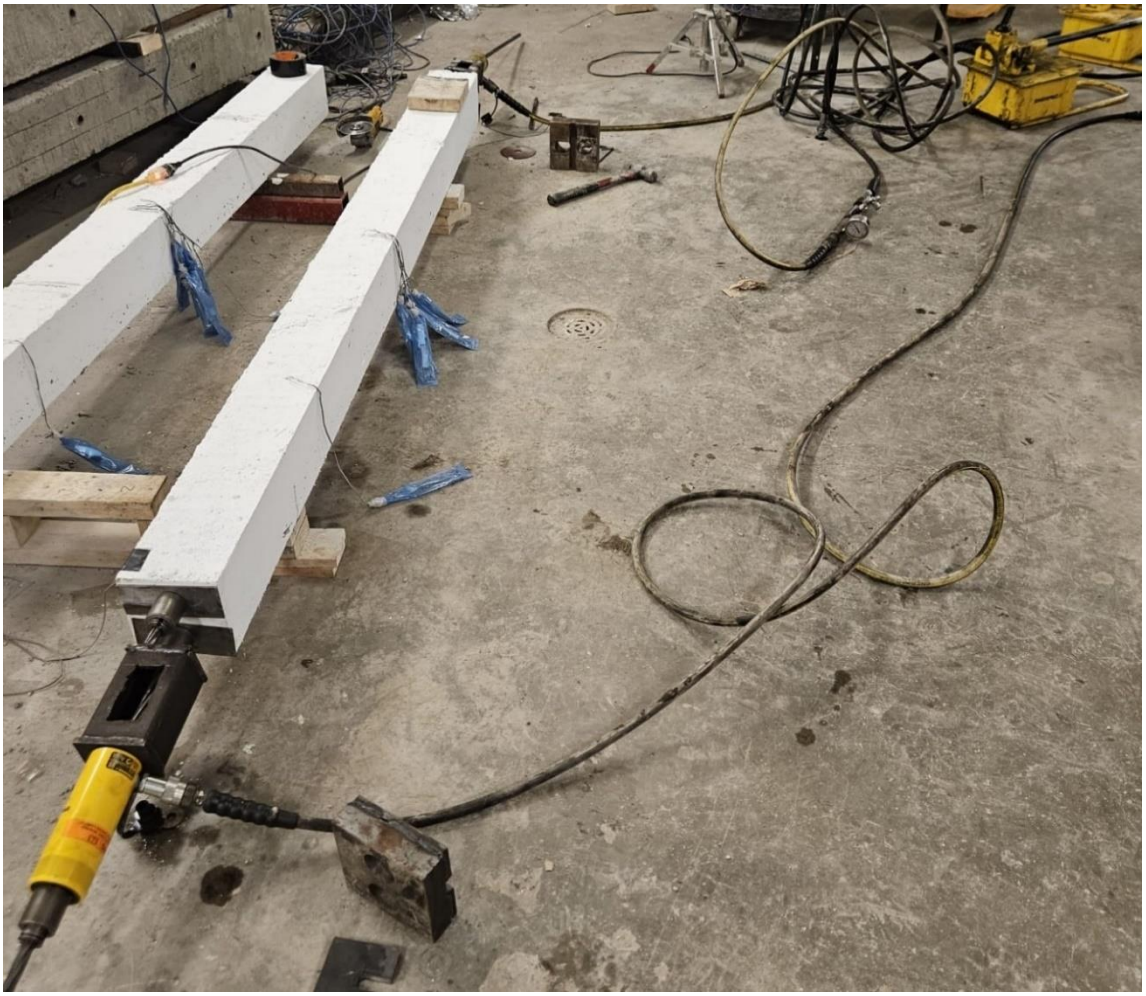

(a)

(b)

Figure 3.25 – Photos of post-tensioning of columns with internal prestressing strands: a) column with double strands during jacking, b) end of the columns with one and two strands and a thick hollow cap to facilitate axial load application during testing.

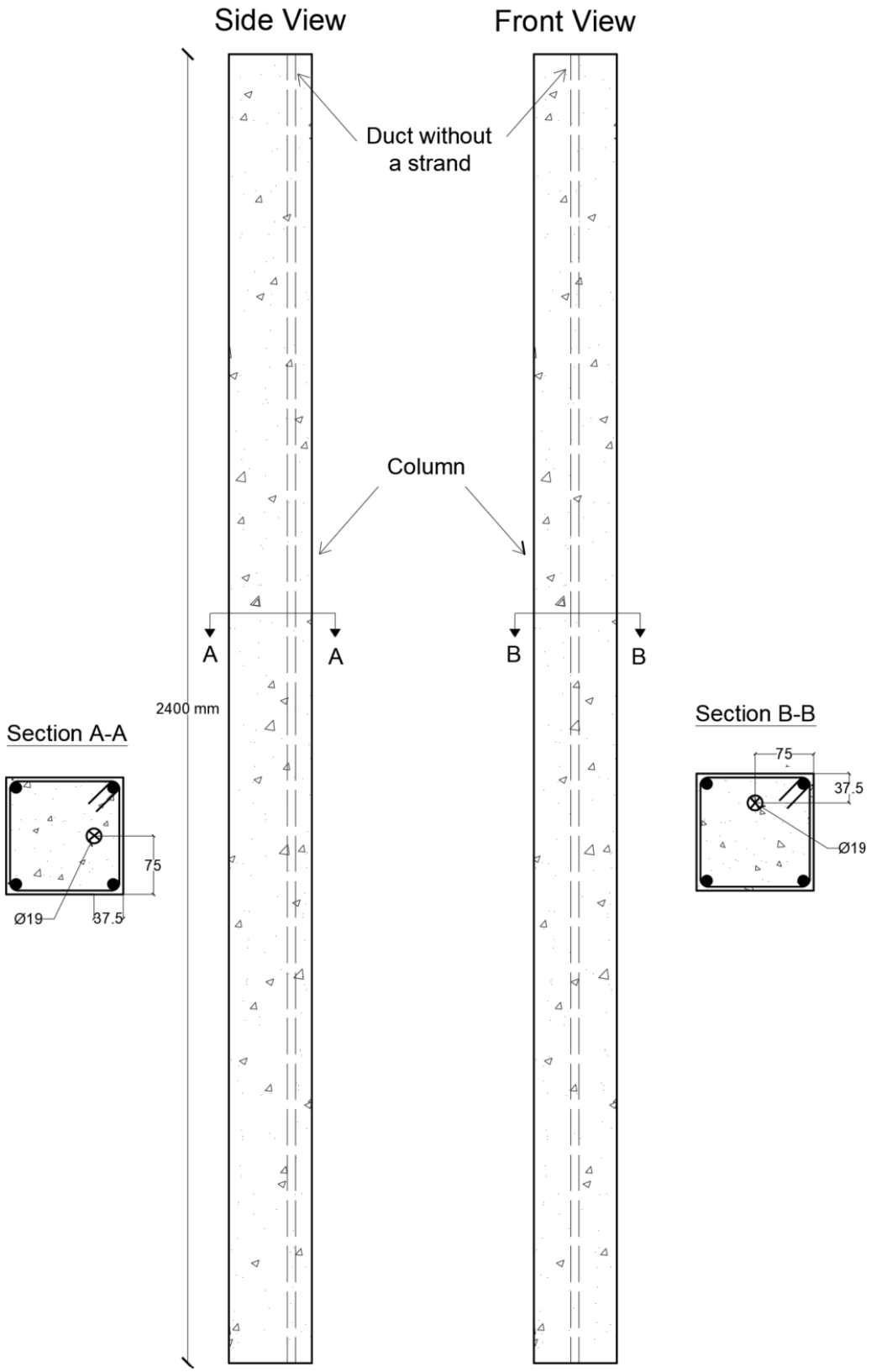

Figure 3.26 – Reference column with a longitudinal duct serving as a control for internally post-tensioned columns.

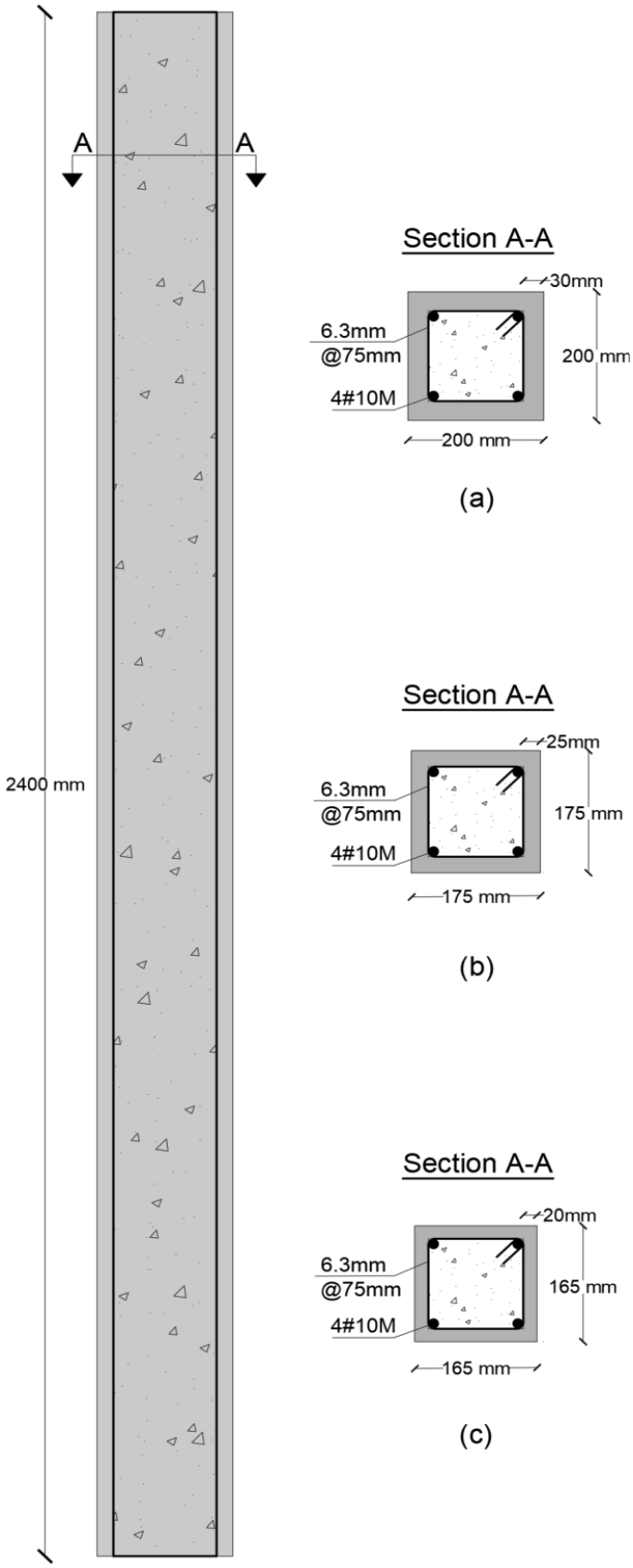

Figure 3.27 – ECC jacketed column with three different thicknesses and two percentages of polyethylene fibers: a) ECC-2.0%v_f-t30-N1, b) ECC-1.5%v_f-t25-N2, and c) ECC-2.0%v_f-t20-N2.

Figure 3.28 – Photo of a column prior to testing, representative of internally post-tensioned and jacketed columns.

Figure 3.29 – Photos showing the process of roughening the surface of the column on all four sides prior to pouring ECC jacket.

Figure 3.30 – A photo taken while pouring the ECC layer on all surfaces of the column core for ECC jacketed columns.

Figure 3.31 – Photos of ECC jacketed columns ready for testing.

Figure 3.32 – A photo illustrating strain gauges on longitudinal and transverse reinforcement.

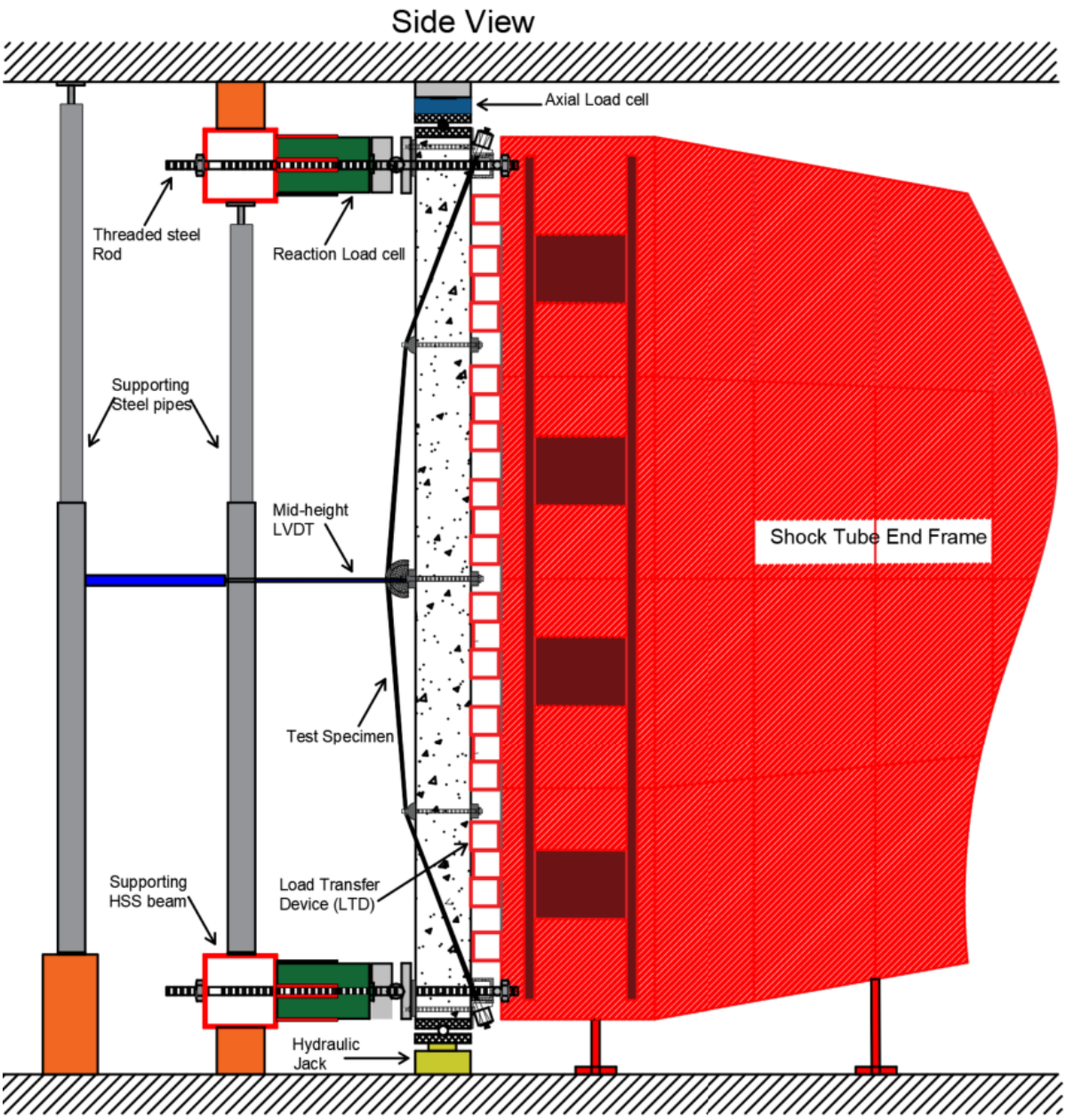

Figure 3.33 – The test setup showing shock tube model and instrumentations.

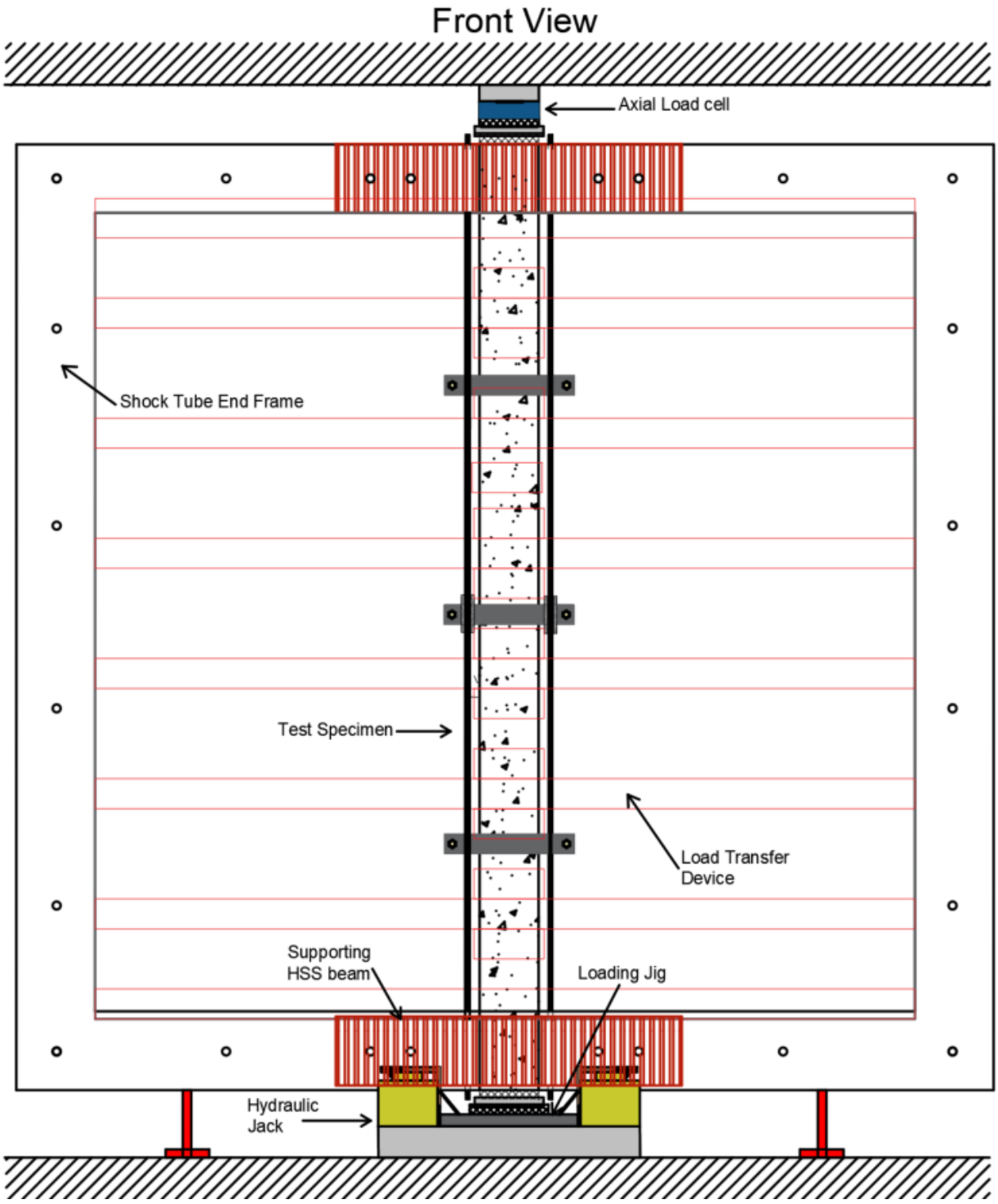

Figure 3.34 – Test setup - front view.

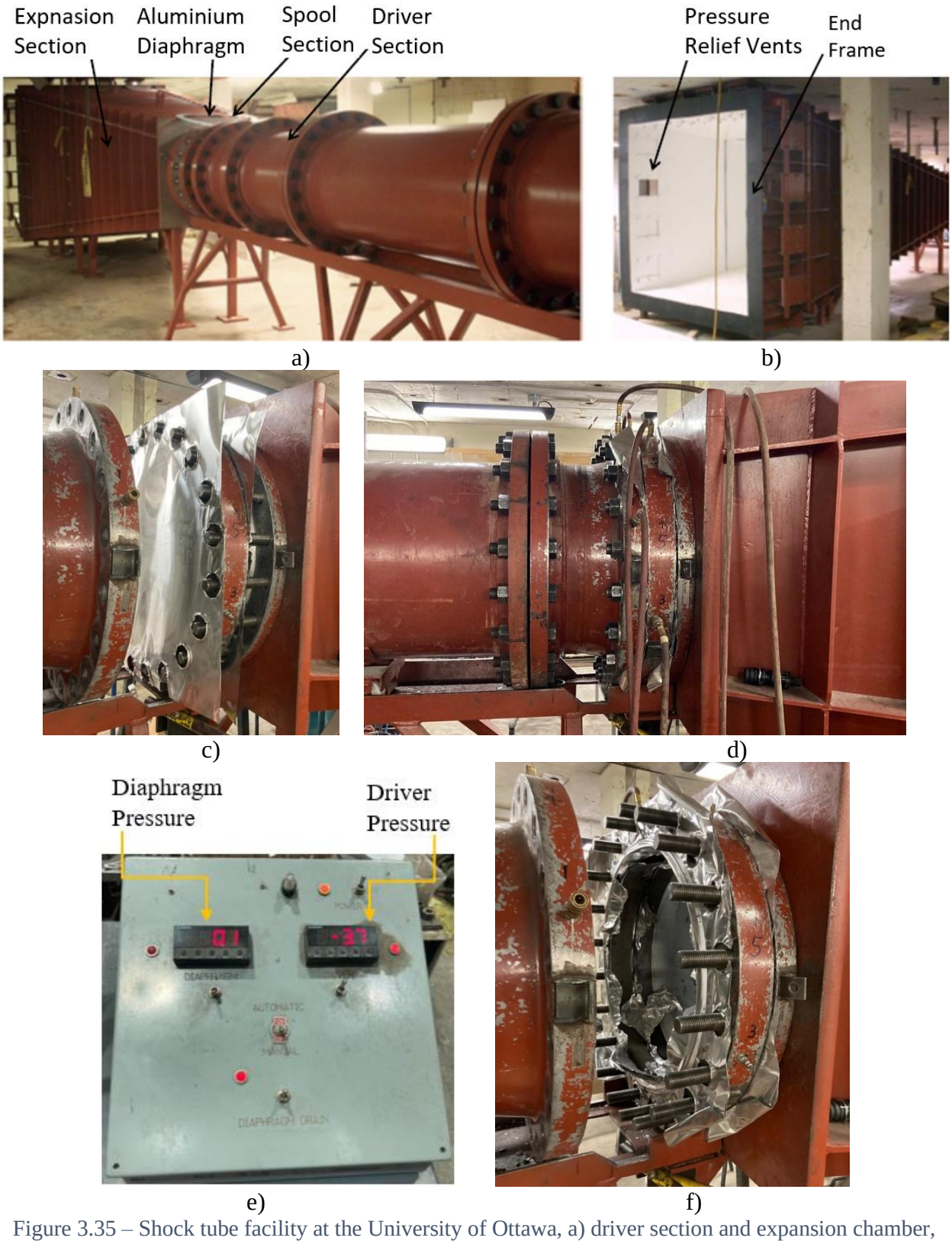

Figure 3.35 – Shock tube facility at the University of Ottawa, a) driver section and expansion chamber, b) end frame, c) aluminum foil of the driver section, d) Spool section with connected air hoses, e) air pressure control device, f) ruptured aluminum diaphragm after the test.

Figure 3.36 – Photos from the process of preparing diaphragms from aluminum foils.

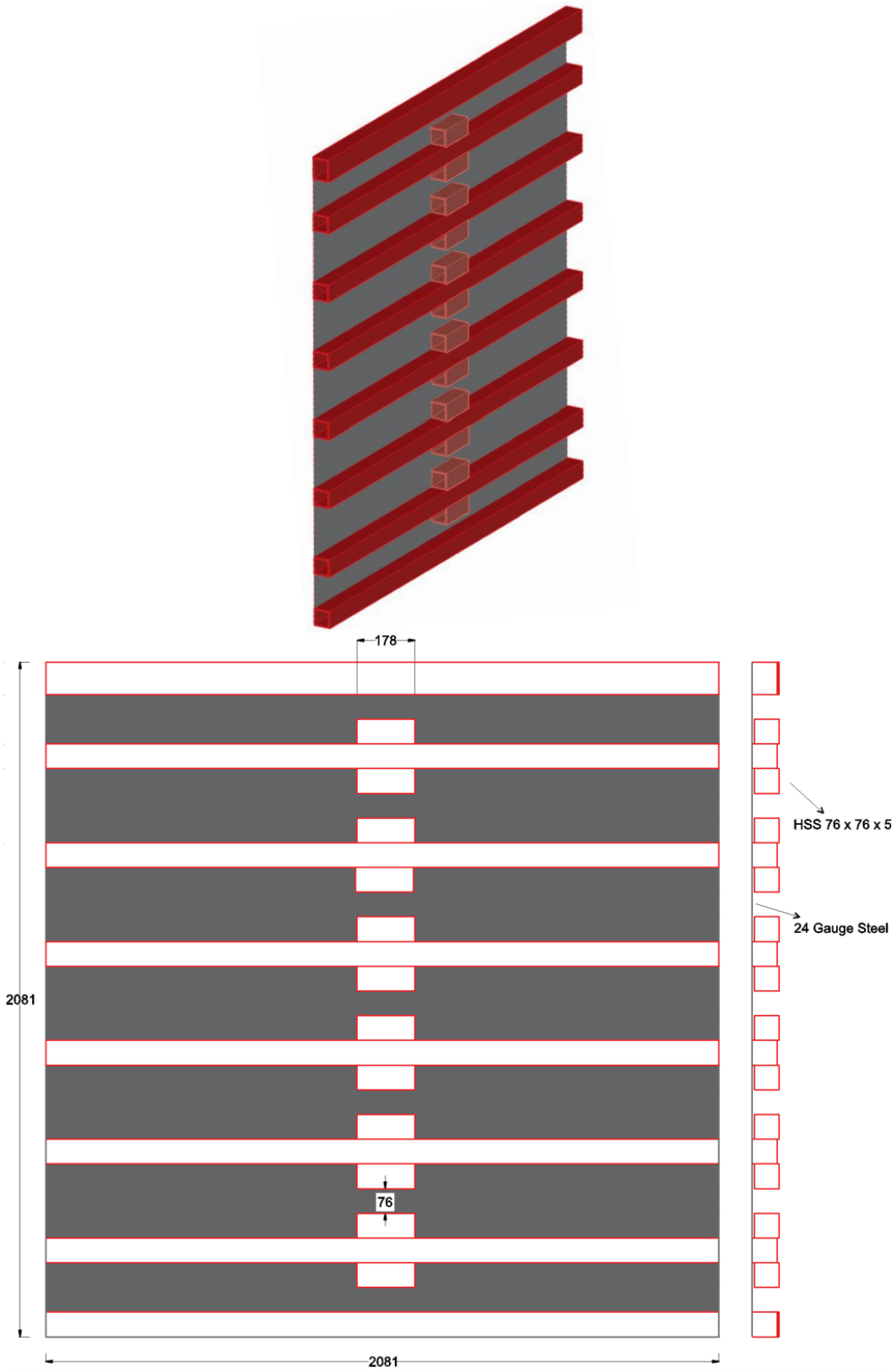

Figure 3.37 – 3D layout and Front view of LTD.

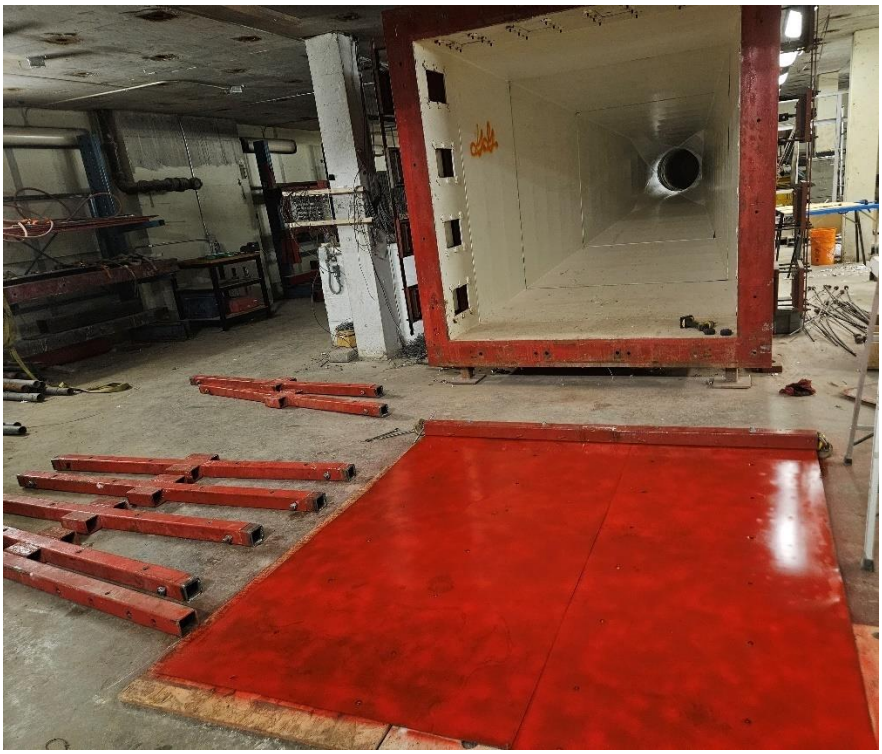

Figure 3.38 – Photos from the process of preparing LTD.

Figure 3.39 – Photos from the process of installing LTD and its stiffeners in the form of HSS.

Chapter 4. Experimental Results

This chapter presents the results of blast loading on 15 reinforced concrete columns. The columns were subjected to a series of progressively increasing shock waves (blast shots) until the collapse or significant deterioration of the test specimens. The results presented include reflected pressure, mid-height maximum and residual deflections, drop in axial load during testing, reaction force at support locations, strain measurements of internal reinforcement and external 7-wire strands when applicable, and an assessment of visual qualitative level of damage after each shot. The plots of applied reflected pressure, displacement, axial load, and reaction force time histories are presented at the end of this chapter. The graphs are plotted for each shot; however, if there was any residual deflection in the previous shot, the result of the subsequent shot begins from the same residual deflection and not necessarily from zero, except in the first shot. All the columns are tested under a combined loading configuration comprised of initial axial and applied blast loads. Therefore, the columns undergo an initial compressive strain, which is considered when calculating true/net strain. True strain is the sum of the initial axial strain, the residual strain from the previous shot, if applicable, and the relative maximum/residual strain.

The result of each column is reported and discussed, referring to the label predefined in Chapter 3. A summary of the applied shock wave parameters and the corresponding test results is presented in Table 4.1 to 4.4. The reported parameters in these tables include driver length (L_D), driver pressure (P_D), reflected pressure (P_r), reflected impulse (I_r), idealized duration of positive phase (t_d), maximum mid-height region deflection (d_{max}), residual and accumulated residual mid-height deflections (d_{rs} and d_{rs_acm}), and residual and maximum support rotations (θ_{rs} and θ_{max}). The measured strain values (residual strain and true strain) are presented in Table 4.5 to 4.8. The following subsections describe the test results for all the tested columns and report their behavior after each shot.

4.1 Reference columns

Reference columns, also called control columns, were tested as built without any hardening/strengthening. Two columns from the non-seismic columns category were tested to serve as reference columns to compare with columns hardened by externally placed prestressing strands and ECC jackets. One column from the seismic/blast columns category was tested to serve as a reference to the internally post-tensioned columns. The columns were loaded axially to 300

kN before the application of blast loads. The axial load level was kept constant through periodic adjustments if allowed by the column residual capacity and when necessary to maintain the combined loading configuration.

4.1.1 Ref-N1

The non-seismic reference column was tested by applying two blast shots with two different driver pressures. The first shot was generated by applying a driver pressure of 186 kPa and a diver length of 2.7 m. The second shot was generated by applying a driver pressure of 276 kPa with the same driver length. During the first shot, the columns were under 300 kN axial load, while the axial load during the second shot decreased and was maintained at 200 kN due to the damage created from the first shot. The reflected pressure on the column due to the first blast shot was 35 kPa, and the impulse was 303 kPa-ms, resulting in a maximum deflection of 66 mm and a residual deflection of 55 mm. The reflected pressure due to the second shot was 42 kPa, and the impulse was 395 kPa-ms, associated with maximum and residual deflections of 148 mm and 116 mm, respectively (see Figure 4.1).

Visual observations of the column showed that after the first shot, there were signs of concrete crushing on the compression side and multiple major cracks on the tension side at the critical section (i.e., mid-height), as shown in Figure 4.2. The axial load capacity of the column dropped to less than 200 kN. The second shot induced a total collapse of the columns, as illustrated in Figure 4.3, resulting in the complete loss of its axial load resistance. The support reaction was measured to be 53 kN during the first shot, and it was around 24 kN.

Measurement of strain gauges (reported in Appendix A, Figure A.1a) revealed that the tension reinforcement was significantly strained, almost ten times the yield strain. At the end of the second shot, the residual strain for tension reinforcement was more than 2%. The strain gauges reached their maximum reading capacity during this shot. The strain gauge attached to the compression steel did not provide meaningful data.

4.1.2 Ref-N2

The second non-seismic reference column with a 5 MPa higher concrete strength than the first column was tested at different pressure-impulse combinations. It was subjected to three blast shots with varying driver pressures but a fixed driver length of 1.8 m for all the shots. The first shot was generated using a driver pressure of 138 kPa. The second and third shots had 221 kPa and 372 kPa

driver pressures, respectively. The maximum reflected pressure on the column during the first shot was 29 kPa, and the impulse was 198 kPa-ms, resulting in a maximum mid-height deflection of 21 mm and a residual deflection of 2 mm. The reflected pressure and impulse due to the second shot were 37 kPa and 290 kPa-ms, respectively. This shot generated maximum and residual deflections of 42 mm and 25 mm, respectively. The third shot increased the reflected pressure and impulse to 55 kPa and 384 kPa-ms, respectively, resulting in a maximum deflection of 144 mm and a residual deflection of 97 mm (see Figure 4.4).

Visual observations of the column showed no signs of concrete crushing and cracking at the end of the first shot (see Figure 4.5). However, after the second shot, there was concrete crushing on the compression side and major cracks on the tension side at a location below the critical section (i.e., mid-height), as depicted in Figure 4.6. After the third shot, the column was completely damaged, with a chunk of concrete spalling from both the compression and tension sides, as illustrated in Figure 4.7. The column axial load capacity did not drop during the first and second shots. However, it totally lost its axial load capacity during the third shot. The support reactions were measured to be 29, 47, and 53 kN during the first, second, and third shots, respectively.

Measurements of strain gauges (presented in Appendix A, Figure A.1b) revealed that the compression steel was below the yield strain during the first shot, with tension reinforcement exceeding yield. However, the residual strains for compression and tension reinforcements were close to 0 %. During the second shot, the compression steel experienced nearly yield strain (i.e., 0.2 %) while the tension steel strain gauges were reading 1.1 % strain at the time of maximum pressure. The residual strain value of compression steel was around 0.07 %, while the tension steel indicated 0.6 % strain. During the third shot, the strain in the compression steel was unstable and lower than that recorded during the second shot. However, the strain gauges attached to the tension reinforcement reached their maximum capacity and stopped reading. The discrepancy in the strain measurement of the compression steel can be justified by the location of the plastic hinge, which did not occur at exactly mid-height where strain gauges were installed.

4.1.3 Ref-S

The seismic/blast designed control column was also tested by applying two blast shots with different driver pressures. The first shot was generated by a driver pressure of 138 kPa and a diver length of 2.7m. The second shot was generated by a higher driver pressure of 276 kPa, using the same driver length. The column was subjected to a reflected pressure of 26 kPa and an impulse of

272 kPa-ms) during the first blast shot, resulting in a maximum deflection of 37 mm and a residual deflection of 13 mm. The reflected pressure during the second shot was 43 kPa, and the impulse was 415 kPa-ms, resulting in a maximum deflection of 166 mm and a residual deflection of 140 mm (see Figure 4.8).

Visual observations of the column showed that after the first shot, there were signs of concrete crushing on the compression side. Multiple visible cracks were observed on the tension side within the critical section region near mid-height. This is shown in Figure 4.9. The axial load capacity of the column exhibited a slight drop after the first shot; however, after the second shot, the column lost its axial load capacity. The second shot induced a total collapse of the column, as illustrated in Figure 4.10. The maximum measured support reaction during the first and second shots was 43 kN and 72 kN, respectively.

Measurement of strain gauges (presented in Appendix A, Figure A.1c) revealed that both compression and tension bars exceeded the yield point (1.3 % in compression and 2.3% in tension). The residual steel strains for compression and tension were 1% and 1.3%, respectively. During the second shot, both compression and tension reinforcement experienced a maximum strain of 2 % and a residual strain of around 2 %. Strain data showed that the seismic/blast detailed column developed higher strains than the non-seismic column at a similar load level. The difference in strains is attributed to the effect of concrete confinement in the seismically detailed column. The increase in concrete internal forces resulting from confinement provides greater elongation of longitudinal reinforcement, thus resulting in higher strain values.

4.2 Columns Hardened by External Post-tensioning

The test program presented in Chapter 3 included two techniques of column hardening, as illustrated and described in Section 3.3. The first technique involved external post-tensioning of columns using prestressing strands, and the second was based on ECC jacketing of columns. All the hardened columns represented non-seismic columns of existing buildings. They were loaded with an axial load of 300 kN before post-tensioning and tested under combined blast and axial loading. The test results of hardened columns by external post-tensioning are presented in the following subsections:

4.2.1 SH-207e-0.15fpu-N1

The first hardened column was post-tensioned with two external strands having a single-harped longitudinal profile. The column was subjected to three incrementally increasing blast shots with driver pressures of 159 kPa, 276 kPa, and 362 kPa, respectively. The driver length for all three shots was kept at 2.7 m. During the first shot, the column was subjected to a reflected pressure of 32 kPa and the resulting impulse of 308 kPa-ms, which led to elastic behavior. The maximum deflection at this stage of loading was 30 mm, with a rebound deflection of 12 mm and a small residual deflection of 3 mm. The second shot generated a reflected pressure of 45 kPa and an impulse of 420 kPa-ms, resulting in a maximum deflection of 60 mm and a residual deflection of 45 mm. The reflected pressure impulse combination during the third shot was 75 kPa / 511 kPa-ms, which generated a maximum deflection of 207 mm and a residual deflection of 160 mm (see Figure 4.11).

There were no signs of crushing and cracking observed at the end of the first shot, as seen in Figure 4.12 There was a negligible drop in the level of axial load. However, after the second shot, there were visible concrete crushing signs on the compression side, as well as cracks on the tension side, as shown in Figure 4.13. The axial load during the second shot was dropped by about 50 kN but adjusted back to the initial load level for the next shot. The third shot caused complete damage to the column, as illustrated in Figure 4.14. The axial load was completely lost at the end of this shot. It was observed that the location of the plastic hinge was not at or close to the mid-height. The shift in the location of the plastic hinge was due to the presence of the deviator for the prestressing strand. Since the reactive force in this case resulted in peak resisting moment at mid-height, the column failed at a section with the highest resultant moment below the mid-height section, as illustrated in Figure 4.14c. The maximum support reactions were recorded as 53 kN, 88 kN, and 78 kN for the first, second, and third shots.

The strain gauge measurements (presented in Appendix A, Figure A.2) showed that during the first shot, the compression steel was less than the yield strain, and the residual strain was almost zero. While the tension reinforcement already yielded at the time of maximum pressure, its residual strain was nearly zero. However, during the second shot, the compression and tension reinforcements were strained beyond yielding. During the third shot, the compression steel was less strained than in the second shot and exhibited tensile strains. Similarly, the tension steel was less strained during the third shot at maximum, and the residual strain was zero. The strain

measurements on the 7-wire strands showed a strain of 0.08 % during the first shot, almost 0.2 % during the second shot, and stayed at 0.2 % during the third shot. The observed damage locations were consistent with the strain measurements. The column mid-height locations of the strain gauges were away from the plastic hinge location.

4.2.2 DH1-207e-0.13fpu-N1

The column hardened with two double-harped shape strands was subjected to three blast shots. The driver length for all three shots was kept at 2.7 m. The driver pressures were 165 kPa, 276 kPa, and 365 kPa for the first, second, and third shots, respectively. The maximum reflected pressure of 33 kPa and impulse of 310 kPa-ms during the first shot resulted in an elastic response. The maximum deflection from the first shot was 35 mm, with a rebound deflection of 15 mm, but there was no residual deflection. The second shot generated a reflected pressure of 43 kPa and an impulse of 418 kPa-ms, resulting in a maximum deflection of 59 mm and a residual deflection of 32 mm. The reflected pressure impulse combination increased to 55 kPa and 540 ka-ms during the third shot, resulting in a maximum deflection of 123 mm and a residual deflection of 79 mm, as shown in Figure 4.15.

Visual inspection of the column revealed no signs of crushing and cracking after the first shot (see Figure 4.16). The drop in axial load was minimal. However, after the second shot, there was visible concrete crushing and cracking in the critical mid-height region, as shown in Figure 4.17. The axial load during the second shot dropped by 50 kN, but it was adjusted back to the initial load before the next shot. After the third shot, the column was fully damaged, with the loss of its total axial load-carrying capacity (see Figure 4.18). The maximum reaction forces at the supports were 51 kN, 83 kN, and 85 kN during the first, second, and third blast shots, respectively.

The strain gauge measurements reported in Appendix A, FigureFigure A.3a and A.3b) showed that during the first shot, the compression steel was almost at yield when pressure was maximum, but the residual strain was nearly zero. Meanwhile, tension reinforcement yielded at the time of maximum pressure, and its residual strain showed negative readings. However, during the second shot, the compression and tension reinforcement were strained beyond the yielding strain, reaching 1 % and 2.5 %, respectively. Their residual strains were measured to be 2.5 % for tension and 0.15% for compression reinforcement. During the third shot, tension and compression reinforcement stopped recording readings as they reached their maximum capacity. The strains in the 7-wire strands showed a gradual increase, from 0.16% during the first blast shot to 0.34% during the

second shot and almost 0.4 % during the third shot. Their residual strains varied between 0 % and 0.05 % during the three consecutive blast shots.

4.2.3 DH2-207e-0.16fpu-N1

This column is similar to the previous double-harped column except that the prestressing force applied to the strands was higher, and it was also subjected to three blast shots. The driver length for the three shots was kept at 2.7 m. The diver pressures for the three shots were 159 kPa, 255 kPa, and 393 kPa. The reflected pressure from the first shot was 36 kPa, and the corresponding impulse was 337 kPa-ms, which was resisted elastically by the column. The maximum deflection from the first shot was 41 mm, with a rebound of 8 mm and a small residual deflection of 4 mm. The second shot generated a reflected pressure of 42 kPa and an impulse of 435 kPa-ms, which resulted in a maximum deflection of 62 mm and a residual deflection of 23 mm. The reflected pressure due to the third shot was 80 kPa, and the impulse was 543 kPa-ms, resulting in a maximum deflection of 105 mm and residual deflection of 60 mm, as can be inferred from Figure 4.19.

There were no signs of crushing or cracking after the first shot, as seen in Figure 4.20. There was also no drop in the applied axial load, as expected. However, the second shot produced visible signs of concrete crushing and cracking near the critical section in the mid-height region. This is depicted in Figure 4.21. The axial load during the second shot dropped by 25 kN, but it was subsequently adjusted back to the initial applied load level before the following shot. After the third shot, the column was fully damaged, with the loss of its total axial load capacity (see Figure 4.22). Contrary to the single-harped column, the plastic hinge location of this column was not shifted from the expected mid-height location. Figure 4.20c illustrates that the resultant highest moment is still at the mid-height, as no deviator is placed there. The maximum support reactions were measured to be 61 kN, 85 kN, and 87 kN, respectively, during the first, second, and third shots.

The strain gauge readings plotted in Appendix A, Figure A.3c and A.3d, showed that the tension steel started yielding during the first shot and remained in the post-yield range thereafter. The compression reinforcement data was not recorded due to technical problems. The strain measurements on the 7-wire strands showed maximum strains of 0.15 %, 0.35 %, and 0.4 % during the first, second, and third shots, respectively. The residual strand strains varied between -0.08 % and 0.08%.

4.2.4 TH1-247e-0.10fpu-N1

This column was hardened with two external post-tensioned strands having a semi-parabolic longitudinal profile with three-point deviators. It was subjected to three incrementally increasing blast shots with driver pressures of 207 kPa, 310 kPa, and 379 kPa as shots 1, 2, and 3. The driver length for all three shots was kept constant at 2.7 m. The reflected pressure from the first shot was 40 kPa, and the impulse was 361 kPa-ms, resulting in a maximum deflection of 57 mm and a residual deflection of 13 mm. The second shot generated a reflected pressure of 45 kPa and an impulse of 435 kPa-ms, resulting in a maximum deflection of 70 mm and a residual deflection of 30 mm. The reflected pressure due to the third shot was 55 kPa with an impulse of 543 kPa-ms, resulting in a maximum deflection of 230 mm and a residual deflection of 200 mm below the mid-height section (see Figure 4.23).

There were no signs of crushing and cracking after the first shot (see Figure 4.24). The drop in axial load was negligible. However, after the second shot, there were visible signs of concrete crushing and cracking below the critical section, as shown in Figure 4.25. The axial load during the second shot dropped by 100 kN but adjusted back to the initial load level prior to the next blast shot. After the third shot, the column was fully damaged (see Figure 4.26) with a total loss of axial load. The maximum support reactions recorded from the load cells were 59 kN, 89 kN, and 76 kN during the first, second, and third shots, respectively.

The strain gauge measurements reported in Appendix A, Figure A.4a and A.4b, showed that the compression steel yielded at maximum pressure during the first shot and exhibited a residual strain of around 0.05 %. The tension reinforcement also strained to yield strain. The compression reinforcement was strained less than the yielding strain during the second shot and less than the strain recorded during the first shot. The residual strain of compression steel during the second shot was almost 0 %, but the tension steel gauge reached its capacity at the residual load stage. During the third shot, the compression steel was strained less than the strain values at the second shot and exhibited tensile strains. The strain measurement on the 7-wire strands showed a strain of around 0.2% during the first shot and a strain of around 0.35 % during the second and third shots. The location of induced damage, which was not where the strain gauges were located, justifies the discrepancy in the level of measured strains from the second and third shots.

4.2.5 TH2-247e-0.15fpu-N2

This column is similar to column TH-247e-0.10Fpu-N1 except for the level of initial prestressing force in post-tensioned cables and the concrete strength. The prestressing force was 15% of the ultimate strength of high-strength 7-wire strands, and the compressive strength of concrete was 50 MPa at 28 days. The column was subjected to three blast shots with driver pressures of 207 kPa, 345 kPa, and 517 kPa, respectively, for blast shots 1, 2, and 3. The driver length of all three shots was kept at 1.8 m. The reflected pressure from the first shot was 36 kPa, and the impulse was 278 kPa-ms, generating a maximum deflection of 23 mm without a residual deflection. The second shot generated a reflected pressure of 58 kPa and an impulse of 413 kPa-ms, resulting in a maximum deflection of 37 mm and almost no residual deflection. The reflected pressure due to the third shot was 75 kPa, and the impulse was 562 kPa-ms, resulting in a maximum deflection of 133 mm and a residual deflection of 120 mm. This can be seen in Figure 4.27.

The first shot did not cause any concrete crushing or cracking, as can be seen in Figure 4.28. After the second shot, a localized concrete crushing was observed on the compression side at a section below the critical section (i.e., mid-height) between the two deviators (mid-height deviator and deviator at 1/3 of height). This is illustrated in Figure 4.29. There were no cracks observed on the tension side anywhere along the column height. In addition, there was no drop in axial load after the first and second shots. During the third shot, however, the column was fully damaged (see Figure 4.30), and there was a 70% loss in the applied axial load. Similar to the single-harped column, the presence of a deviator at the mid-height caused a shift in the location of the plastic hinge. This behavior is again related to the reactive moment from strands that changed the location of the highest resultant moment during blast loading. During the third shot, the post-tensioning system experienced a failure at one of the end connections (see Figure 4.31) due to the shear failure of the steel bolts connecting the top steel plate to the side steel angle. The maximum support reactions were recorded to be 33 kN, 68 kN, and 96 kN during the first, second, and third shots, respectively.

The strain gauge measurements (presented in Appendix A, Figure A.4c and A.4d) showed that the compression steel was below the yield strain during the first shot and did not exhibit any residual strain. The tension reinforcement slightly exceeded the yield strain and rebounded afterwards, showing a strain of around 0 %. However, during the second shot, the compression reinforcement was strained slightly above the yield strain, and the tension reinforcement was reading a strain of 0.5 %. The residual strain of compression and tension steel during the second

shot was around 0.02%. During the third shot, the compression steel was less strained than in the second shot, and the tension reinforcement read 1.5 % strain at maximum pressure. The residual strain of compression steel during the third shot was around 0.05 %, and tension steel was around 0.6 %. The drop in strain level during the third shot is attributed to the location of plastic deformation below the mid-height region where strain gauges were installed. The strain measurement of the 7-wire strands showed a strain value of 0.13 % during the first shot and a residual strain of 0.05 %, but with the opposite sign. Similarly, a strain of around 0.33 % was recorded during the second blast shot, and a residual strain of 0.06 %. During the third shot, the strain gauge on the right-side cable stopped reading while the left cable strain gauge measured a strain value of almost 0.2 % and a residual strain of 0.1 %.

4.2.6 P1-227e-0.09fpu-N1

This column was hardened with two post-tensioned external strands in a draped longitudinal profile (parabolic profile with five-point deviators). It was subjected to five incremental blast shots with a driver length of 2.7 m for each shot. The driver pressures were 138 kPa, 165 kPa, 310 kPa, 345 kPa, and 379 kPa, respectively, for the first through fifth shots. The reflected pressure–impulse combination of the first shot was 29 kPa and 270 kPa-ms. The maximum deflection generated by this shot was 31 mm, and no residual deflection was produced. The second shot generated a reflected pressure–reflected impulse combination of 32 kPa-301 kPa-ms, resulting in a maximum deflection of 40 mm and a residual deflection of 2 mm. The reflected pressure data from the third shot was not recorded due to technical problems. However, assessing the first two shots (observing the driver pressure in psi and corresponding reflected pressure in kPa) and comparing the reflected pressure of a triple-harped column fired with similar driver pressure, an estimated reflected pressure of 50 kPa and an impulse of 450 kPa-ms were assumed. The maximum deflection during shot#3 was 60 mm, and the residual deflection was 18 mm. The reflected pressure from shot#4 was 60 kPa, and the impulse was 612, resulting in a maximum deflection of 73 mm and residual deflection of 45 mm. The fifth blast shot resulted in a reflected pressure of 55 kPa and an impulse of 569 kPa-ms, causing a maximum deflection of 120 mm and a residual deflection of 70 mm (see Figure 4.32).

Visual inspection of the column revealed that after the first and second shots, the column exhibited elastic behavior and did not lead to a drop in axial load. During the first and second blast shots, there were no signs of concrete crushing and cracking (see Figure 4.33 and Figure 4.34).

However, the third shot led to visible concrete crushing and cracking at the critical section (i.e., mid-height). This can be seen in Figure 4.35. The fourth shot resulted in significant damage to the column (see Figure 4.36), accompanied by a drop in axial load to 150 kN. The axial load was adjusted, but could not be increased above 200 kN for the fifth shot because of the damage caused from the fourth shot. The axial load dropped to zero after the fifth shot, and the column failed as shown in Figure 4.37. The support reactions measured during the first four blast shots were 50 kN, 67 kN, 107 kN, and 75 kN, respectively.

The strain gauge measurements reported in Appendix A, Figure A.5a and A.5b showed that during the first shot, the tension steel yielded with zero residual strain. The strain measurement recorded during shot #2 was not recorded due to technical problems. During shot #3, tension steel developed 0.75 % strain at maximum pressure, which dropped to yield strain afterwards. Similar strain values recorded during shot #3 were also recorded during shot #4. It is worth mentioning that the compression steel strain data were not measured in this column. The strain measurements on 7-wire strands during the first shot showed values of up to 0.13 %. Similar strain values were recorded during shot #2. During shot#3, higher strains were recorded with a strain value of around 0.4 %. The residual strain in the 7-wire strands after shot #4 was almost zero, indicating unloading of prestressing strands that remained in the elastic region even after multiple shots.

4.2.7 P2-227e-0.16fpu-N2

This column was similar to column P-227e-0.09f_{pu}-N1 except for having a higher level of prestressing and higher concrete strength. The initial prestressing force in the strands was 16% of the ultimate tensile strength, and the compressive strength of concrete was 50 MPa. It was subjected to three progressively increasing blast shots with a driver length of 1.8 m for each shot. The driver pressures during these three shots were 221 kPa, 365 kPa, and 510 kPa for the first, second, and third shots, respectively. The reflected pressure-impulse combination for the first shot was 37 kPa-292 kPa-ms and resulted in 23 mm, without developing any residual deflection. The second shot resulted in a reflected pressure-impulse combination of 60 kPa-473 kPa-ms and a maximum deflection of 43 mm and a residual deflection of 6 mm. The third shot had an increased reflected pressure combination of 75 kPa - 576 kPa-ms with a higher maximum deflection of 80 mm and an increased residual deflection of 65 mm (see Figure 4.38).

Visual inspection of the column after the first shot revealed an elastic response without any drop in applied axial load. At this stage of loading, there were no signs of concrete crushing and

cracking (see Figure 4.39). However, after the second shot, there were visible localized concrete crushing on the compression side and hairline cracks on the tension side at a location slightly above the critical section, as illustrated in Figure 4.40. The third shot resulted in significant damage to the column (see Figure 4.41), and the axial load dropped to below 150 kN. During the third shot, the post-tensioning system experienced failure at one of the end connections (see Figure 4.42) due to the shear failure of the steel bolts connecting the top steel plate to the side steel angle. The maximum support reactions measured during blast shots #1, #2, and #3 were 48 kN, 79 kN, and 92 kN, respectively.

The strain gauge measurements reported in Appendix A, Figure A.5c and A.5d indicated tension steel yielding at maximum deflection without any residual strain. The compression reinforcement remained below yield. During the second shot, both tension and compression reinforcement strained beyond yield, showing strains that varied around 0.75%. The compression reinforcement showed 0.3 % residual strain. No residual strain was recorded in the tension reinforcement. The strain gauges reached their limits during the third shot and stopped working. The strain measurement on the 7-wire strands showed a strain of around 0.14 % during the first shot but dropped back to 0.05 % with an opposite sign at the end of the shot. During the second shot, at the time of maximum deflection, the strain was measured to be 0.4 %, but the residual strain was as low as 0.05 %. Higher prestressing strains were recorded during the third shot, reaching 0.5 %, but dropped to zero strain at the end of the shot.

4.3 Posttensioned Columns using Internally Prestressing Strands

The seismic/blast resistant columns designed according to the respective CSA standards for newly built columns were strengthened by unbonded internal 7-wire post-tensioning strands. The columns were subjected to 300 kN of axial load prior to blast loading. The 300 kN axial load was applied after the prestressing strand was inserted through the duct and prestressed. Application of axial load develops shortening of the column, thus may result in loss of prestressing force. Therefore, the initial post-tensioning force was intentionally increased slightly higher than what was required to account for the loss due to axial loading. The following subsections present the test results of two internally post-tensioned columns:

4.3.1 PT-SS-0.35fpu-S

This column was built with closely spaced ties along its entire height and post-tensioned with a single 7-wire unbonded prestressing strand. The column was subjected to three progressively increasing blast shots with a constant driver length of 2.7m for each shot. The driver pressures during the first, second, and third shots were 138 kPa, 276 kPa, and 414 kPa, respectively. The first shot resulted in a reflected pressure-impulse combination of 29 kPa-268 kPa-ms, generating a maximum deflection of 26 mm with a residual deflection of 2 mm. The reflected pressure due to the second shot was 44 kPa with an impulse of 415 kPa-ms, causing a maximum deflection of 85 mm and a residual deflection of 52 mm. Reflected pressure from the third shot increased to 60 kPa with an impulse of 614 kPa-ms, resulting in a maximum deflection of 152 mm and a residual deflection of 89 mm. These results are shown in Figure 4.43.

Visual inspection of the column revealed that after the first shot, the column exhibited elastic behavior with a negligible drop in axial load. No visible signs of concrete crushing and cracking observed (see Figure 4.44). However, there were signs of concrete crushing and cracking at the critical mid-height section after the second shot. This is illustrated in Figure 4.45. In addition, the axial load dropped to below 200 kN, but it was readjusted to 300 kN before applying the third shot. The third shot significantly damaged the column, as shown in Figure 4.46 and the axial load dropped to zero. The support reactions measured by the load cell indicated maximum reactions of 55 kN, 78 kN, and 66 kN during the first, second, and third shots, respectively.

The strain measurements (reported in Appendix A, Figure A.6a) indicated post-yield strains on compression and tension steels with strains of 0.5 % and 0.9 %, respectively. The reason for the much higher strain values compared to the externally post-tensioned hardened non-seismic columns is the effect of confinement in the current column with seismic/blast detailing, as explained earlier in Section 4.1.3. The residual strain in compression steel was at the yield strain level, while it was below the yield strain for tension steel. The strain recovery in tension reinforcement is attributed to the presence of the unbonded strand over the tension side and its role in the rebound of the column that relaxed the tension steel. During the second shot, the maximum tension and compression reinforcement developed approximately 2% strains, while the compression steel had a higher residual strain (1.75%) than the tension (0.8%) steel. During the third shot, the strain gauges reached their maximum reading capacity (i.e., 20000 to 25000 micro-

strain) and stopped giving meaningful results. The strain measurement of the prestressing strand was not successful because of the loss of connection of the strain gauge wire during post-tensioning.

4.3.2 PT-DS-0.40fpu-S

Similar to column PT-SS-0.35fpu-S, this column was built with closely spaced ties along its entire height. However, this column was post-tensioned with two 7-wire unbonded strands. The column was subjected to three blast shots with a constant driver length of 2.7m for each shot. The driver pressure during the first, second, and third shots was 138 kPa, 276 kPa, and 365 kPa, respectively. The reflected pressure-impulse combination was 29 kPa-267 kPa-ms during the first shot. The maximum deflection at this stage of loading was 37 mm, and the residual deflection was 10 mm. The second shot produced a reflected pressure of 44 kPa with an impulse of 407 kPa-ms. The maximum deflection increased to 90 mm with a residual deflection of 60 mm. Reflected pressure from the third shot was recorded to be 55 kPa with an impulse of 539 kPa-ms, resulting in a maximum deflection of 140 mm and a residual deflection of 70 mm (see Figure 4.47).

Visual inspection of the column revealed that after the first shot, the column exhibited elastic behavior with a negligible drop in axial load. There were no signs of concrete crushing and cracking (see Figure 4.48). However, there were visible signs of concrete crushing on the compression side and cracking on the tension side at the critical section (i.e., mid-height) after the second shot. This is depicted in Figure 4.49. In addition, the axial load dropped to about 150 kN. It was adjusted to 280 kN before the third shot was applied. The third shot resulted in significant damage to the column as can be seen in Figure 4.50, causing the axial load to drop to zero. The load cell at the location of supports measured maximum reactions as 56 kN, 79 kN, and 53 kN during the first, second, and third shots.

The strain gauge data (reported in Appendix A, Figure A.6b and A.6c) showed that the compression and tension steels were well beyond their yield strain with 1% and 1.8% strains, respectively. Once again, the high strain values attained can be explained by the confinement of core concrete having seismic/blast detailing, as also explained in Section 4.1.3. The residual strain during the first shot in each longitudinal reinforcement was measured to be higher than 0.5%. During the second and third shots, the strain gauges reached their capacity, showing 20000 to 25000 micro-strains (2% to 2.5%). The strain measurement of the prestressing strand on the compression side recorded strains of approximately 0.08%, 0.35%, and in excess of 0.8 % during the first, second, and third shots, respectively.

4.4 Columns Hardened using ECC Jacketing

The second method of hardening investigated in this research study is applying Engineered Cementitious Composite (ECC) shell to jacket the columns as described in Section 4.2. Three columns were jacketed with an ECC shell for blast loading. The ECC shell was cast on all four sides of columns (i.e., jacketing or complete wrapping) and tested under blast loads while simultaneously subjected to axial loads. The following three subsections describe the performance of ECC jacketed columns.

4.4.1 ECC-2.0%v_f-t30-N1

This ECC jacketed column was hardened with a 30 mm thick ECC layer containing 2% polyethylene high modulus fibers in the mix. The column was subjected to four progressively increasing blast shots with a constant driver length of 2.7 m for each shot. The first three shots were generated by driver pressures of 159 kPa; 276 kPa, and 414 kPa. The axial load was kept approximately constant at 350 kN during these shots. The fourth shot was applied with a slightly reduced driver pressure relative to the third shot (i.e., 345 kPa) and a lower axial load. This was done because of the extensive damage imposed on the column during the third shot. The reflected pressure-impulse combination generated during the first shot was 32 kPa-315 kP-ms. This level of blast load produced a maximum deflection of 13 mm without any residual deflection. The 2nd blast shot created a reflected pressure of 47 kPa and an impulse of 441 kPa-ms, causing a maximum deflection of 36 mm without any residual deflection. The reflected pressure from the third shot was 63 kPa with an impulse of 610 kPa-ms, resulting in a maximum deflection of 115 mm and a residual deflection of 104 mm (see Figure 4.51). The reflected pressure-impulse combination for the fourth and the last shot was 48 kPa-510 kPa-ms, causing full collapse of the column (blowout).

Visual observations during the column tests indicated no visible concrete crushing or cracking (see Figure 4.52) at the end of the first shot. Similarly, there were no signs of any crushing or cracking after the second shot (see Figure 4.53) except for hardly visible small hairline cracks on the tension side. The applied axial load remained constant during these two shots, without any drop. After the third shot, there was a wide crack opening on the tension side and the beginning of concrete crushing on the compression side, as seen in Figure 4.54. The applied axial load dropped below 200 kN at the end of the shot. The fourth blast shot was applied to observe the inevitable collapse of the column. Indeed, this shot resulted in a catastrophic failure of the column, and the column bounced out of the supporting frames, freeing itself from the supports as illustrated in

Figure 4.55. The maximum support reactions were recorded to be 42 kN, 71 kN, and 95 kN during the first, second, and third shots, respectively.

The strain gauges on internal reinforcement were mostly damaged during the surface roughening process for ECC jacking, except for one strain gauge reported in Appendix A, Figure A.7a. During the first shot, tension reinforcement exhibited yielding at the time of maximum deflection but remained at almost 0 % strain afterwards. In the second shot, the highest strain reading was 1.1%, which returned to 0 % at the end of the shot. During the third shot, the strain gauges stopped reading after reaching their capacity (i.e., 25000 micro-strain or 2.5%).

4.4.1 ECC-2.0%v_f-t20-N2

This column was similar to the previous column tested except for having a jacket thickness of 20 mm ECC but containing the same 2.0% polyethylene high-modulus fibers. The column was subjected to three blast shots with a constant driver length of 1.8 m for each shot. The driver pressures increased from 207 kPa for the first shot to 366 kPa, and 448 kPa for the second and third shots. The applied axial load was 300 kN for the first two shots. However, for the third shot, the column could not carry the 300 kN intended axial load because of the damage induced during the second shot. The axial load was adjusted to a maximum of 270 kN before the third shot was applied. The reflected pressure-impulse combinations generated from the first shot was 39 kPa-272 kPa-ms, resulting in a maximum deflection of 32 mm and a residual deflection of 3 mm. The 2nd blast shot created a reflected pressure of 54 kPa with an impulse of 394 kPa-ms, causing a maximum deflection of 78 mm and a residual deflection of 70 mm. The reflected pressure-impulse combination applied on the column during the third shot was 60 kPa-486 kPa-ms, causing the column to develop a maximum deflection of 265 mm and an estimated residual deflection of 230 mm (see Figure 4.56). During the third shot, the column completely collapsed (blowout), so the LVDT could not measure the actual deflection.

After the first shot, there were no visible crushing or cracking observed (see Figure 4.57). However, after the second shot, there was concrete crushing on the compression side and multiple distributed cracks over the middle third of the column on the tension side as shown in Figure 4.58. The third shot resulted in a catastrophic collapse of the column, as seen in Figure 4.59. After the first shot, there was no drop in the applied axial load; however, the axial load dropped to 250 kN after the second shot. The column lost its full axial load after the third shot and was dragged out of the test setup upon failure as depicted in Figure 4.59. The maximum support reactions during the

three shots were recorded as 53 kN during the first shot, 77 kN during the second shot, and 32 kN during the third shot. The strain gauges were damaged when the column was jacketed with ECC layer, hence, no strain data were collected for this column.

4.4.1 ECC-1.5%v_f-t25-N2

The third ECC jacketed column had a 25 mm thickness. The ECC mix had 1.5% polyethylene high-modulus fibers. The column was subjected to three progressively increasing blast shots with a constant driver length of 1.8m for each shot. The driver pressure increased from 207 kPa for the first shot to 372 kPa for the second shot, and to 517 kPa for the third shot. Like all the previous columns tested, this column was also loaded with an axial load of 300 kN before blast loading. The reflected pressure-impulse combinations and the deflections generated were recorded as 38 kPa-266 kP-ms, resulting in a maximum deflection of 30 mm without any residual deflection; 56 kPa-410 kPa-ms, resulting in a maximum deflection of 57 mm and a residual deflection of 6 mm; and 71 kPa-536 kPa-ms, causing a maximum deflection of 143 mm and a residual deflection of 129 mm for the first, second and third shots, respectively (see Figure 4.60).

Observations made after the first and the second shots indicated no concrete crushing or cracking (see Figure 4.61 and Figure 4.62). The column did exhibit a drop in applied axial load. However, after the third shot, there was significant damage within the mid-height region (see Figure 4. *63*). As a result, the applied axial load dropped below 100 kN. The maximum support reactions were measured to be 43 kN, 75 kN, and 87 kN during the first, second, and third shots, respectively.

The strain gauges developed strains of 0.18 % and 1.15 % for compression and tension reinforcement, respectively, during the first shot (reported in Appendix A, Figure A.7b and A.7c). The residual strain of compression steel was almost zero, while the tension reinforcement exhibited a residual strain of 0.5 %. The strain gauges attached to the surface of the ECC layer on the tension side recorded a strain of 0.7 % at the maximum deflection during the first shot. At the time of maximum deflection during the second shot, the compression steel was below yield, and the tension steel experienced a significant strain of 1.65 %. The residual strain of compression steel was around 0.02 %, and tension steel was around 0.35 %. The ECC strain gauge showed a strain of 1.5 % and a residual strain of 0.35 %. During the third shot, the compression steel significantly measured a strain value of 0.85 %. The residual strain of the compression steel was around 0.7 %. During the third shot, the strain gauges reached their maximum reading capacity and stopped working.

Table 4.1 – Blast load parameters and response quantities of reference columns.

Column ID	Short name	Shot#	D_L (m)	P_d (kPa)	P_r (kPa)	t_d (ms)	I_r (kPa-ms)	d_{max} (mm)	d_{max_acm} (mm)	d_{rs} (mm)	d_{rs_acm} (mm)	θ_{max_acm} (°)	θ_{rs_acm} (°)
Ref-N1	RN1	1	2.7	186	35	17.3	303	66	66	55	55	3.2	2.6
		2	2.7	276	42	18.3	395	148	203	116	171	9.6	8.1
Ref-N2	RN2	1	1.8	138	29	13.5	198	21	21	2	2	1.0	0.1
		2	1.8	221	37	15.7	290	42	44	25	27	2.0	1.3
		3	1.8	372	55	13.8	384	144	171	97	124	8.1	5.9
Ref-S	RS	1	2.7	138	26	21	272	37	37	13	13	1.8	0.6
		2	2.7	276	43	19.4	415	166	179	140	153	8.5	7.3

Table 4.2 – Blast load parameters and response quantities of columns hardened with external prestressing strands.

Column ID	Short name	Shot #	D_L (m)	P_d (kPa)	P_r (kPa)	t_d (ms)	I_r (kPa-ms)	d_{max} (mm)	$d_{max,acm}$ (mm)	d_{rs} (mm)	$d_{rs,acm}$ (mm)	θ_{max_acm} (°)	$\theta_{rs,acm}$ (°)
SH-207e-0.15fpu-N1	SH	1	2.7	159	32	18.9	308	30	30	3	3	1.4	0.1
		2	2.7	276	45	18.8	420	60	63	45	48	3.0	2.3
		3	2.7	362	55	18.8	511	207	255	160	208	12.0	9.8
DH1-207e-0.13fpu-N1	DH1	1	2.7	165	33	18.8	310	35	35	0	0	1.7	0.0
		2	2.7	276	43	19.7	418	59	59	32	32	2.8	1.5
		3	2.7	365	55	19.6	540	123	155	79	111	7.36	5.3

Column ID	Short name	Shot #	D_L (m)	P_d (kPa)	P_r (kPa)	t_d (ms)	I_r (kPa-ms)	d_{max} (mm)	$d_{max,acm}$ (mm)	d_{rs} (mm)	$d_{rs,acm}$ (mm)	θ_{max_acm} (°)	$\theta_{rs,acm}$ (°)
DH2-235e-0.16fpu-N1	DH2	1	2.7	159	33	20.7	335	41	41	4	4	2.0	0.2
		2	2.7	255	43	20.3	435	62	66	23	27	3.2	1.3
		3	2.7	393	60	21.1	633	105	132	60	87	6.3	4.2
TH1-247e-0.10fpu-N1	TH1	1	2.7	207	40	18.3	361	57	57	13	13	2.7	0.6
		2	2.7	310	45	19	434	70	83	30	43	4.0	2.0
		3	2.7	379	55	19.7	543	230	273	200	243	12.8	11.5
TH2-247e-0.15fpu-N2	TH2	1	1.8	207	36	15	278	23	23	0	0	1.1	0.0
		2	1.8	345	58	14.3	413	37	37	2	2	1.8	0.1
		3	1.8	517	75	15	562	133	135	120	122	6.4	5.8
P1-227e-0.09fpu-N1	P1	0	2.7	138	29	18.3	270	31	31	0	0	1.5	0.0
		1	2.7	165	32	19.4	301	40	40	2	2	1.9	0.1
		2	2.7	310	50	18	450	60	62	18	20	3.0	1.0
		3	2.7	345	60	20.4	612	73	93	45	65	4.4	3.1
		4	2.7	379	55	20.2	569	120	185	70	135	8.8	6.4
P2-227e-0.16fpu-N2	P2	1	1.8	221	37	15.8	292	23	23	2	2	1.1	0.1
		2	1.8	365	60	15	450	42	44	6	8	2.1	0.4
		3	1.8	510	75	15.3	576	80	88	65	73	4.2	3.5

Table 4.3 – Blast load parameters and response quantities of internally post-tensioned columns.

Column ID	Short name	Shot #	D_L (m)	P_d (kPa)	P_r (kPa)	t_d (ms)	I_r (kPa-ms)	d_{max} (mm)	d_{max_acm} (mm)	d_{rs} (mm)	d_{rs_acm} (mm)	θ_{max_acm} (°)	θ_{rs_acm} (°)
PT-SS-0.35fpu-S	SS	1	2.7	138	29	18.4	268	26	26	2	2	1.2	0.1
		2	2.7	276	44	18.6	415	85	87	52	54	4.2	2.6
		3	2.7	414	60	20.1	614	152	206	89	143	9.7	6.8
PT-DS-0.40fpu-S	DS	1	2.7	138	29	18.5	267	37	37	0	0	1.8	0.5
		2	2.7	276	44	18.5	407	90	90	60	60	4.8	3.3
		3	2.7	365	55	19.5	539	140	210	70	140	9.9	6.7

Table 4. 4 – Blast load parameters and response of hardened columns by ECC-jacketing.

Column ID	Short name	Shot #	D_L (m)	P_d (kPa)	P_r (kPa)	t_d (ms)	I_r (kPa-ms)	d_{max} (mm)	d_{max_acm} (mm)	d_{rs} (mm)	d_{rs_acm} (mm)	θ_{max_acm} (°)	θ_{rs_acm} (°)
ECC-2.0%v_f-t30-N1	E30	1	2.7	159	32	19.8	315	13	13	0	0	0.6	0.0
		2	2.7	276	47	18.8	441	36	36	2	2	1.7	0.1
		3	2.7	414	63	19.6	610	117	119	108	110	5.7	5.2
		4	2.7	345	48	21.2	510	335	445	NA	NA	20.4	NA
ECC-2.0%v_f-t20-N2	E20	1	1.8	207	39	14.1	272	32	32	3	3	1.5	0.1
		2	1.8	365.5	54	14.6	394	78	81	70	73	3.9	3.5
		3	1.8	448	60	15.6	468	265	338	NA	NA	15.7	NA
ECC-1.5%v_f-t25-N2	E25	1	1.8	207	38	14	266	30	30	0	0	1.4	0.0
		2	1.8	372	56	14.6	410	57	57	6	6	2.7	0.3
		3	1.8	517	71	15.1	536	143	149	129	135	7.1	6.4

Table 4.5 – Strain measurements of flexural longitudinal reinforcement of reference columns.

Column ID	Shot #	$\varepsilon_{C\text{-}i}$ (%)	$\varepsilon_{C\text{-}max/net}$ (%)	$\varepsilon_{C\text{-}rs/net}$ (%)	$\varepsilon_{T\text{-}i}$ (%)	$\varepsilon_{T\text{-}max/net}$ (%)	$\varepsilon_{T\text{-}rs/net}$ (%)	Damage Level
Ref-N1	1	-0.038	NR	NR	-0.038	2.5	2.5	Heavy
	2	-0.034	NR	NR	-0.034	SR	SR	Hazardous
Ref-N2	1	-0.038	-0.17	-0.053	-0.038	0.29	-0.0055	Superficial
	2	-0.038	-0.23	-0.1	-0.038	1.05	0.56	Heavy
	3	-0.038	Fl	Fl	-0.038	SR	SR	Hazardous
Ref-S	1	-0.038	-1.37	-1.038	-0.038	2.34	1.14	Moderate
	2	-0.038	-2.4	-1.9	-0.038	SR	SR	Heavy

Note: NR = not recorded, SR = stopped recording, Fl = started fluctuating in tension and compression

Table 4.6 – Strain measurements of flexural longitudinal reinforcement and prestressing strands of columns hardened by external post-tensioning.

Column ID	Sh #	$\varepsilon_{C\text{-}i}$ (%)	$\varepsilon_{C\text{-}max/net}$ (%)	$\varepsilon_{C\text{-}rs/net}$ (%)	$\varepsilon_{T\text{-}i}$ (%)	$\varepsilon_{T\text{-}max/net}$ (%)	$\varepsilon_{T\text{-}rs/net}$ (%)	$\varepsilon_{p\text{-}i}$ (%)	$\varepsilon_{p\text{-}max/net}$ (%)	$\varepsilon_{p\text{-}rs/net}$ (%)	Damage Level
SH-207e-0.15fpu-N1	1	-0.045	-0.21	-0.07	-0.045	0.33	-0.045	0.14	0.22	0.14	Superficial
	2	-0.045	-0.22	-0.07	-0.045	0.30	0.015	0.14	0.33	0.15	Moderate
	3	-0.045	Fl	Fl	-0.045	Fl	Fl	0.14	Fl	Fl	Hazardous
DH1-207e-0.13fpu-N1	1	-0.043	-0.200	-0.043	-0.043	0.39	-0.14	0.12	0.29	0.12	Superficial
	2	-0.043	-0.914	-0.289	-0.043	2.42	1.73	0.12	0.48	0.18	Moderate
	3	-0.043	SR	SR	-0.043	SR	SR	0.12	0.55	0.18	Heavy
DH2-207e-0.16fpu-N1	1	-0.045	NR	NR	-0.045	0.615	0.325	0.15	0.32	0.15	Superficial
	2	-0.045	NR	NR	-0.045	2.155	1.415	0.15	0.51	0.21	Moderate
	3	-0.045	NR	NR	-0.045	SR	SR	0.15	0.57	0.15	Heavy
TH1-247e-0.10fpu-N1	1	-0.041	-0.29	-0.1	-0.041	1.75	0.13	0.093	0.27	0.10	Superficial
	2	-0.041	-0.20	-0.05	-0.041	2.63	2.63	0.093	0.46	0.15	Moderate
	3	-0.041	Fl	Fl	-0.041	SR	SR	0.093	0.45	0.1	Hazardous

Column ID	Sh #	$\varepsilon_{C\text{-}i}$ (%)	$\varepsilon_{C\text{-}max/net}$ (%)	$\varepsilon_{C\text{-}rs/net}$ (%)	$\varepsilon_{T\text{-}i}$ (%)	$\varepsilon_{T\text{-}max/net}$ (%)	$\varepsilon_{T\text{-}rs/net}$ (%)	$\varepsilon_{p\text{-}i}$ (%)	$\varepsilon_{p\text{-}max/net}$ (%)	$\varepsilon_{p\text{-}rs/net}$ (%)	Damage Level
TH2-247e-0.15fpu-N2	1	-0.045	-0.212	-0.045	-0.045	0.228	-0.045	0.15	0.30	0.15	Superficial
	2	-0.045	-0.271	-0.087	-0.045	0.455	-0.045	0.15	0.49	0.23	Moderate
	3	-0.045	-0.235	-0.102	-0.045	1.376	0.700	0.15	Fl	Fl	Heavy
P1-227e-0.09fpu-N1	0	-0.041	NR	NR	-0.041	0.259	-0.041	0.084	0.19	0.08	Superficial
	1	-0.041	NR	NR	-0.041	0.308	-0.041	0.084	0.27	0.08	Superficial
	2	-0.041	NR	NR	-0.041	NR	0.090	0.084	NR	0.13	Moderate
	3	-0.041	NR	NR	-0.041	0.696	0.260	0.084	0.47	0.20	Heavy
	4	-0.034	NR	NR	-0.034	Fl	Fl	0.084	Fl	Fl	Hazardous
P2-227e-0.16fpu-N2	1	-0.045	-0.225	-0.082	-0.045	0.240	-0.045	0.15	0.28	0.15	Superficial
	2	-0.045	-0.765	-0.379	-0.045	0.655	-0.045	0.15	0.51	0.17	Moderate
	3	-0.045	-2.045	-2.045	-0.045	1.273	1.273	0.15	0.65	0	Heavy

Note: NR = not recorded, SR = stopped recording, Fl = started fluctuating in tension and compression

Table 4.7 – Strain measurements of flexural longitudinal reinforcement and prestressing strands of internally post-tensioned columns.

Column ID	Shot #	$\varepsilon_{C\text{-}i}$ (%)	$\varepsilon_{C\text{-}max/net}$ (%)	$\varepsilon_{C\text{-}rs/net}$ (%)	$\varepsilon_{T\text{-}i}$ (%)	$\varepsilon_{T\text{-}max/net}$ (%)	$\varepsilon_{T\text{-}rs/net}$ (%)	$\varepsilon_{p\text{-}i}$ (%)	$\varepsilon_{p\text{-}max/net}$ (%)	$\varepsilon_{p\text{-}rs/net}$ (%)	Damage Level
PT-SS-0.35fpu-S	1	-0.049	-0.549	-0.337	-0.049	0.751	0.051	0.33	NR	NR	Superficial
	2	-0.049	-1.763	-1.599	-0.049	1.751	0.751	0.33	NR	NR	Heavy
	3	-0.049	SR	SR	-0.049	SR	SR	0.33	NR	NR	Hazardous
PT-DS-0.40fpu-S	1	-0.063	-1.063	-0.683	-0.063	1.694	0.444	0.37	0.404	0.38	Superficial
	2	-0.063	-2.678	2.063	-0.063	2.457	2.450	0.37	0.67	0.65	Heavy
	3	-0.063	SR	SR	-0.063	SR	SR	0.37	1.16	0.83	Hazardous

Note: NR = not recorded, SR = stopped recording

Table 4.8 – Strain measurements of flexural longitudinal reinforcements of hardened columns by ECC jacketing.

Column ID	Shot #	$\varepsilon_{C\text{-}i}$ (%)	$\varepsilon_{C\text{-}max/net}$ (%)	$\varepsilon_{C\text{-}rs/net}$ (%)	$\varepsilon_{T\text{-}i}$ (%)	$\varepsilon_{T\text{-}max/net}$ (%)	$\varepsilon_{T\text{-}rs/net}$ (%)	$\varepsilon_{T\text{-}max/net\text{-}ECC}$ (%)	$\varepsilon_{T\text{-}rs/net\text{-}ECC}$ (%)	Damage Level
ECC-2.0%v_f-t30-N1	1	-0.045	NR	NR	-0.045	0.245	-0.045	NR	NR	Superficial
	2	-0.045	NR	NR	-0.045	1.06	-0.045	NR	NR	Superficial
	3	-0.045	NR	NR	-0.045	2.63	2.63	NR	NR	Hazardous
	4	NR	NR	NR	NR	NR	NR	NR	NR	Blowout
ECC-2.0%v_f-t20-N2	1	-0.038	NR	NR	-0.038	NR	NR	NR	NR	Superficial
	2	-0.038	NR	NR	-0.038	NR	NR	NR	NR	Heavy
	3	-0.038	NR	NR	-0.038	NR	NR	NR	NR	Blowout
ECC-1.5%v_f-t25-N2	1	-0.038	-0.189	-0.038	-0.038	1.09	0.96	0.66	0.002	Superficial
	2	-0.038	-0.23	-0.072	-0.038	1.6	0.32	1.39	0.31	Superficial
	3	-0.034	-0.87	-0.71	-0.034	1.6	1.6	1.39	1.39	Hazardous

Note: NR = not recorded

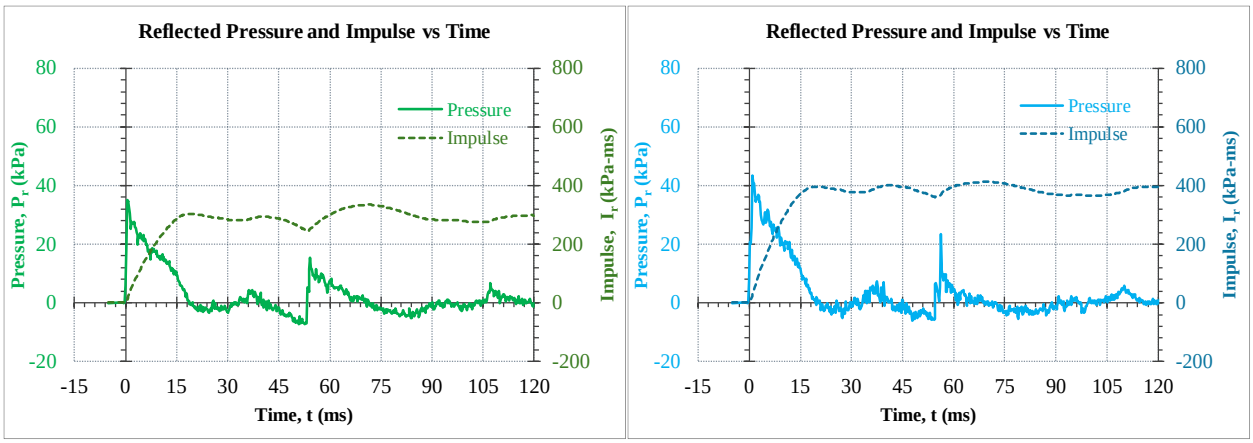

(a) (b)

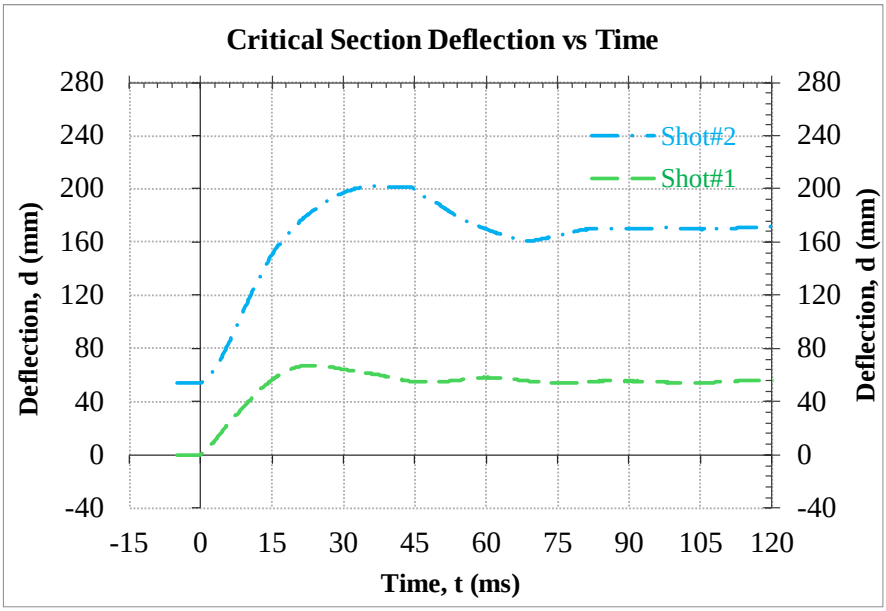

(c)

Figure 4.1 – Reflected pressure, impulse, and displacement time histories of column Ref-N1 a) blast shot#1, b) blast shot#2, and c) deflection at the mid-height region.

(a) (b)

Figure 4.2 – Photos of column Ref-N1 after blast shot#1: a) side view, b) front view.

Figure 4.3 – Photo of column Ref-N1 after blast shot#2.

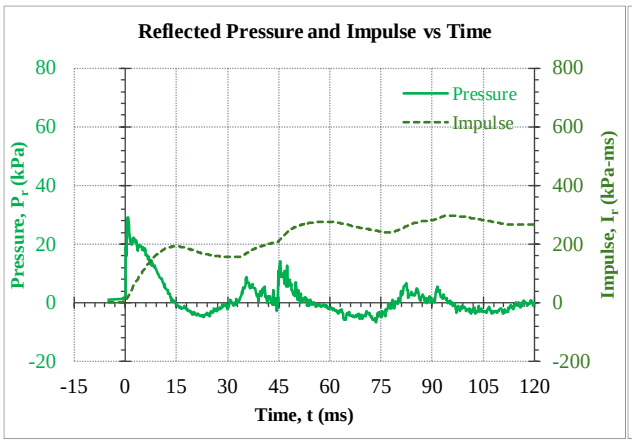

(a)

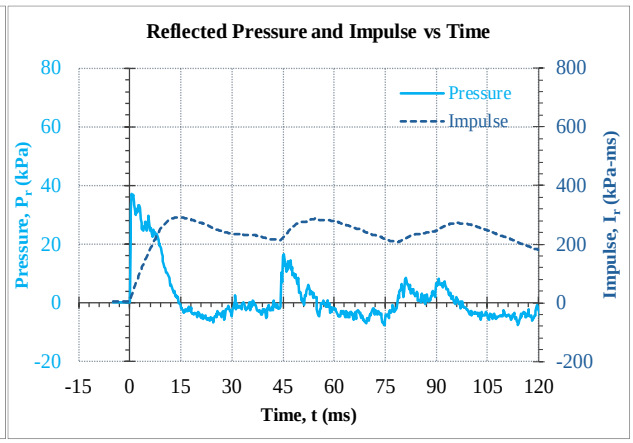

(b)

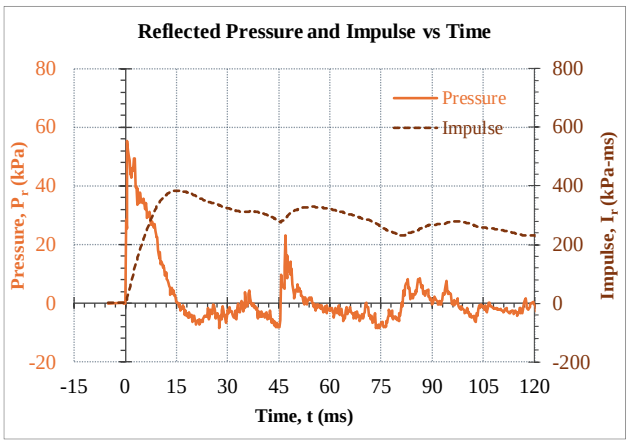

(c)

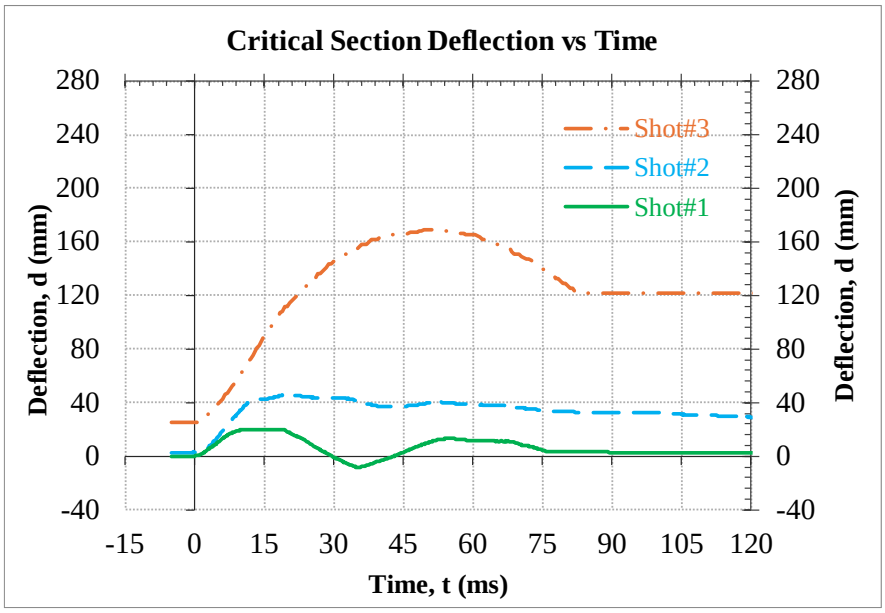

(d)

Figure 4.4 – Reflected pressure, impulse, and displacement time histories of column Ref-N2: a) blast shot#1, b) blast shot#2, c) blast shot#3, and d) deflection at mid-height region.

(a) (b)

Figure 4.5 – Photos of column Ref-N2 after blast shot#1: a) side view, b) front view.

(a) (b)

Figure 4.6 – Photos of column Ref-N2 after blast shot#2: a) side view, b) front view.

(a) (b)

Figure 4.7 – Photos of column Ref-N2 after blast shot#3; a) side view, b) front view.

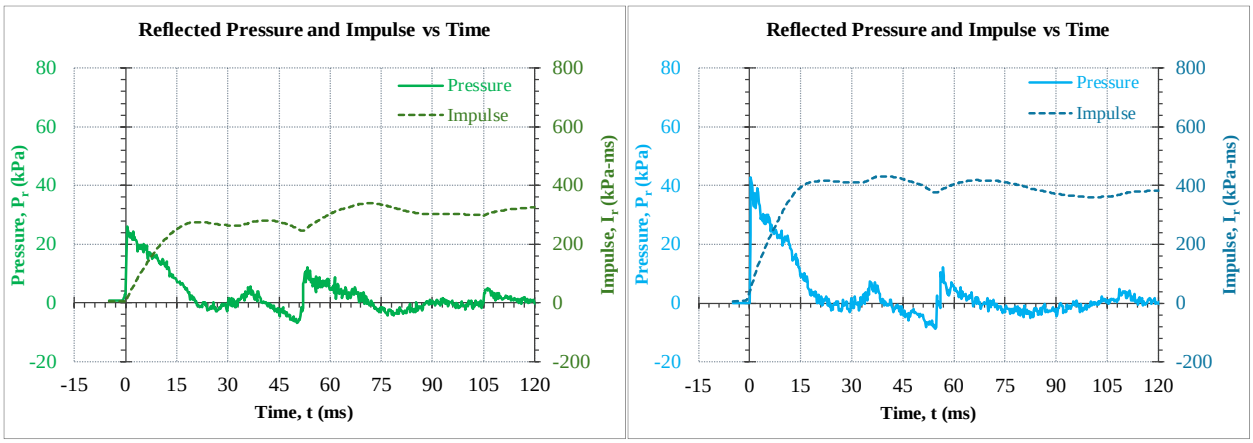

(a) (b)

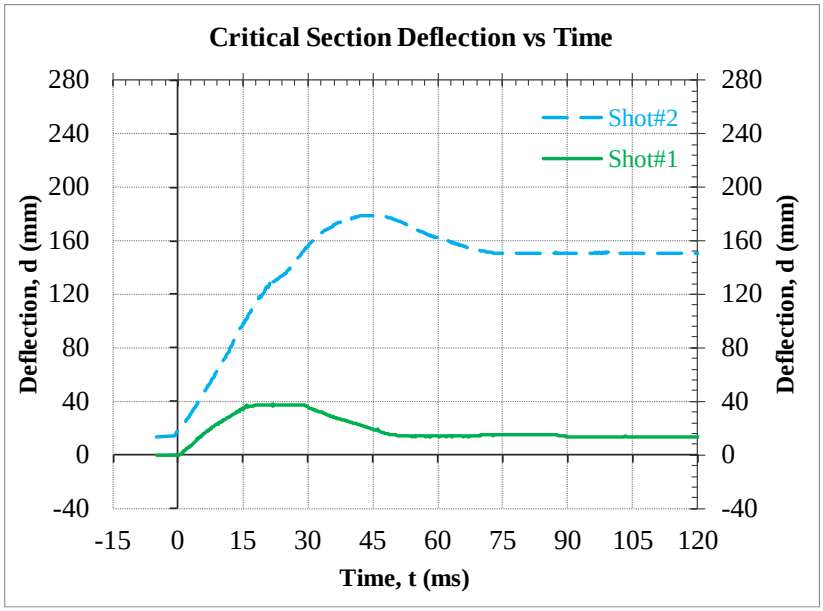

(c)

Figure 4.8 – Reflected pressure, impulse, and displacement time histories of column Ref-S: a) blast shot#1, b) blast shot#2, and c) deflection at the mid-height region .

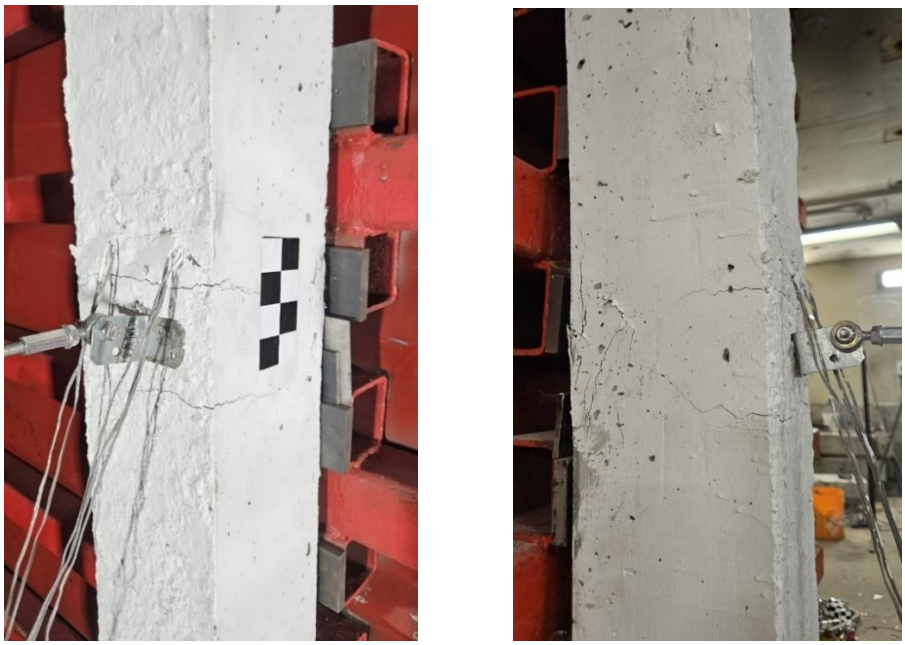

(a) (b)

Figure 4.9 – Photos of column Ref-S after blast shot#1: a) side view, b) front view.

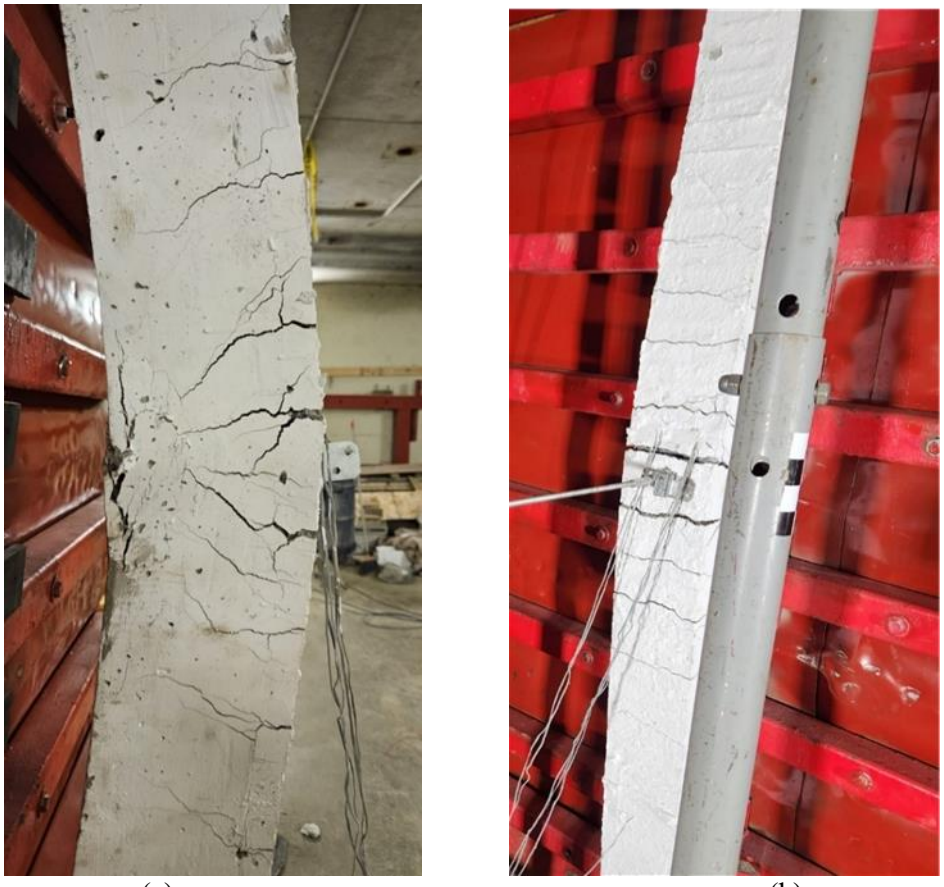

(a) (b)

Figure 4.10 – Photos of column Ref-S after blast shot#2: a) side view, b) front view.

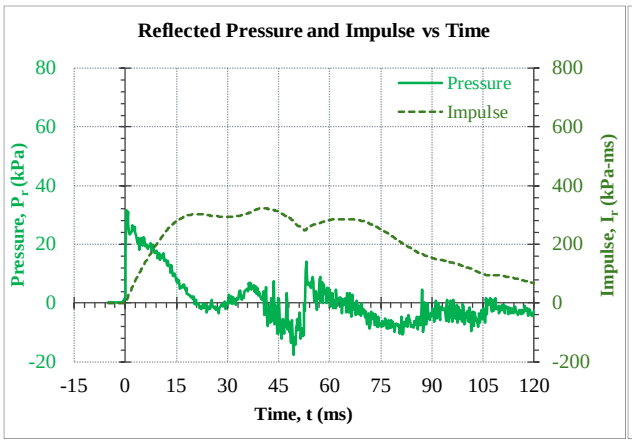

(a)

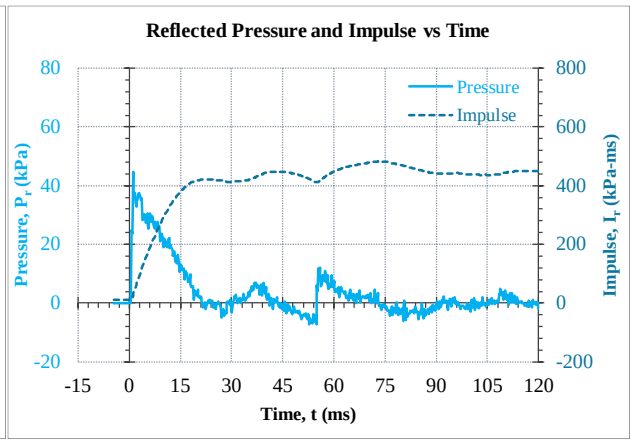

(b)

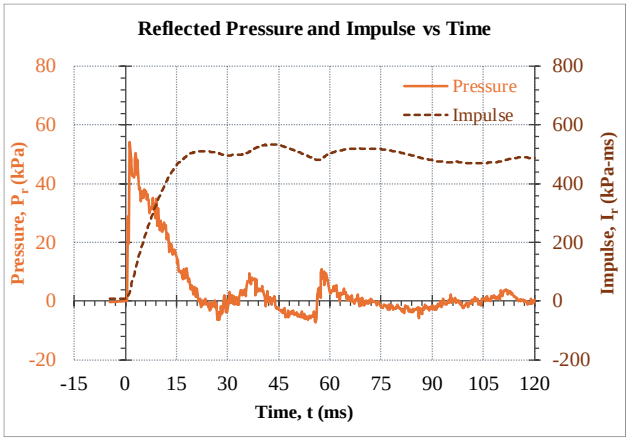

(c)

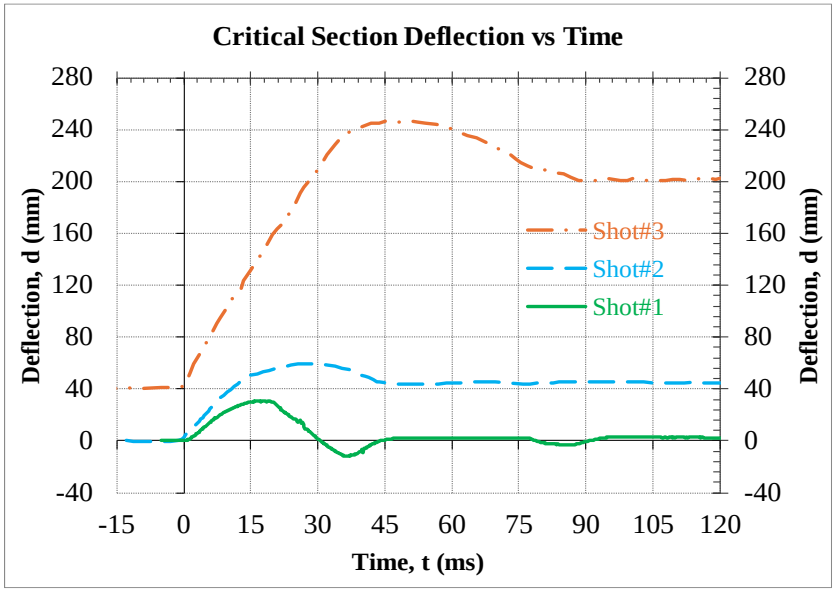

(d)

Figure 4.11 – Reflected pressure, impulse, and displacement time histories of column SH-207e-0.15fpu-N1; a) blast shot#1, b) blast shot#2, c) blast shot#3, and d) deflection at the mid-height region.

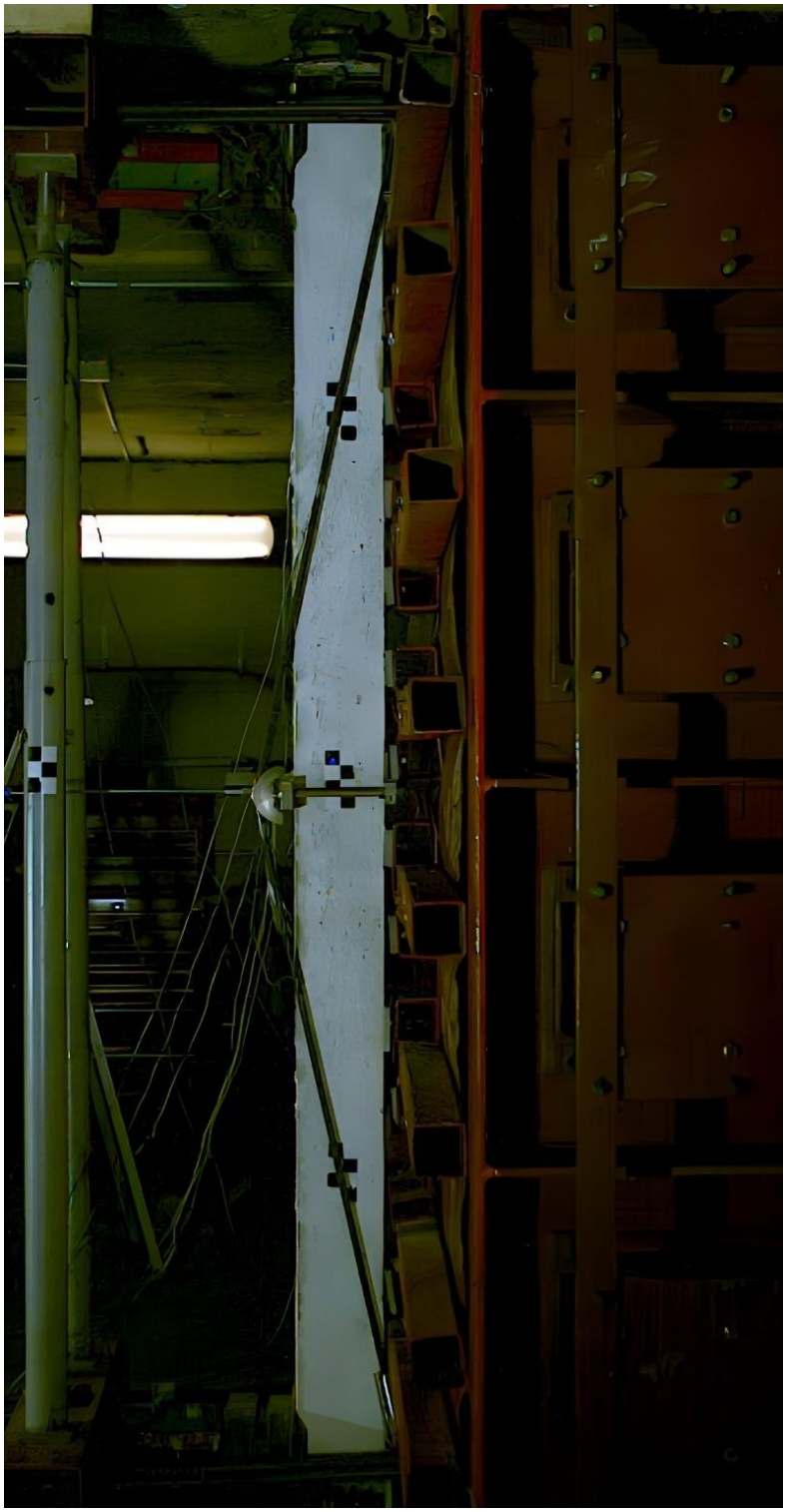

Figure 4.12 – Photos of column SH-207e-0.15fpu-N1 after blast shot#1.

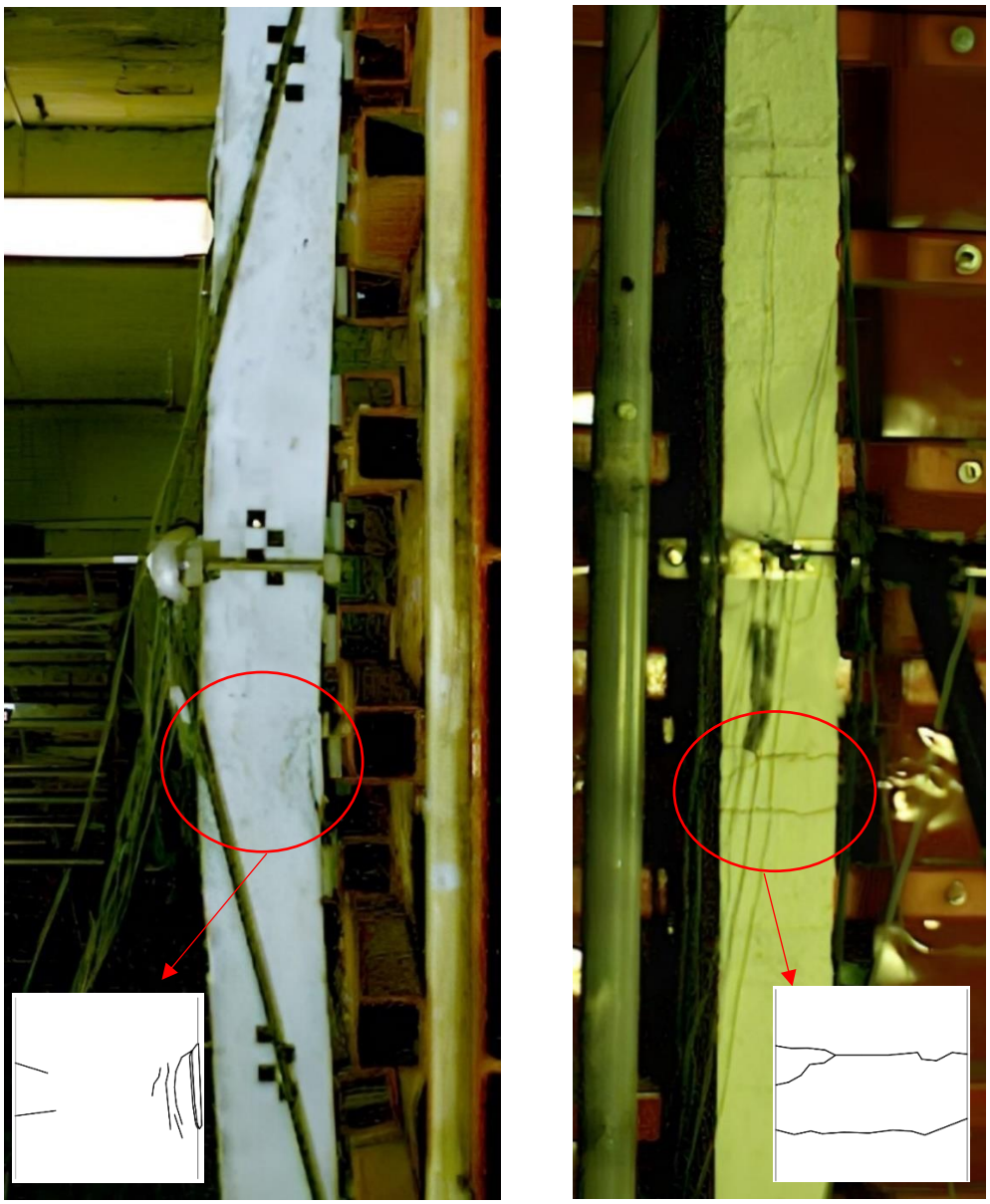

(a) (b)

Figure 4.13 – Photos of column SH-207e-0.15fpu-N1 with a sketch at the location of damage after blast shot#2: a) side view, b) front view.

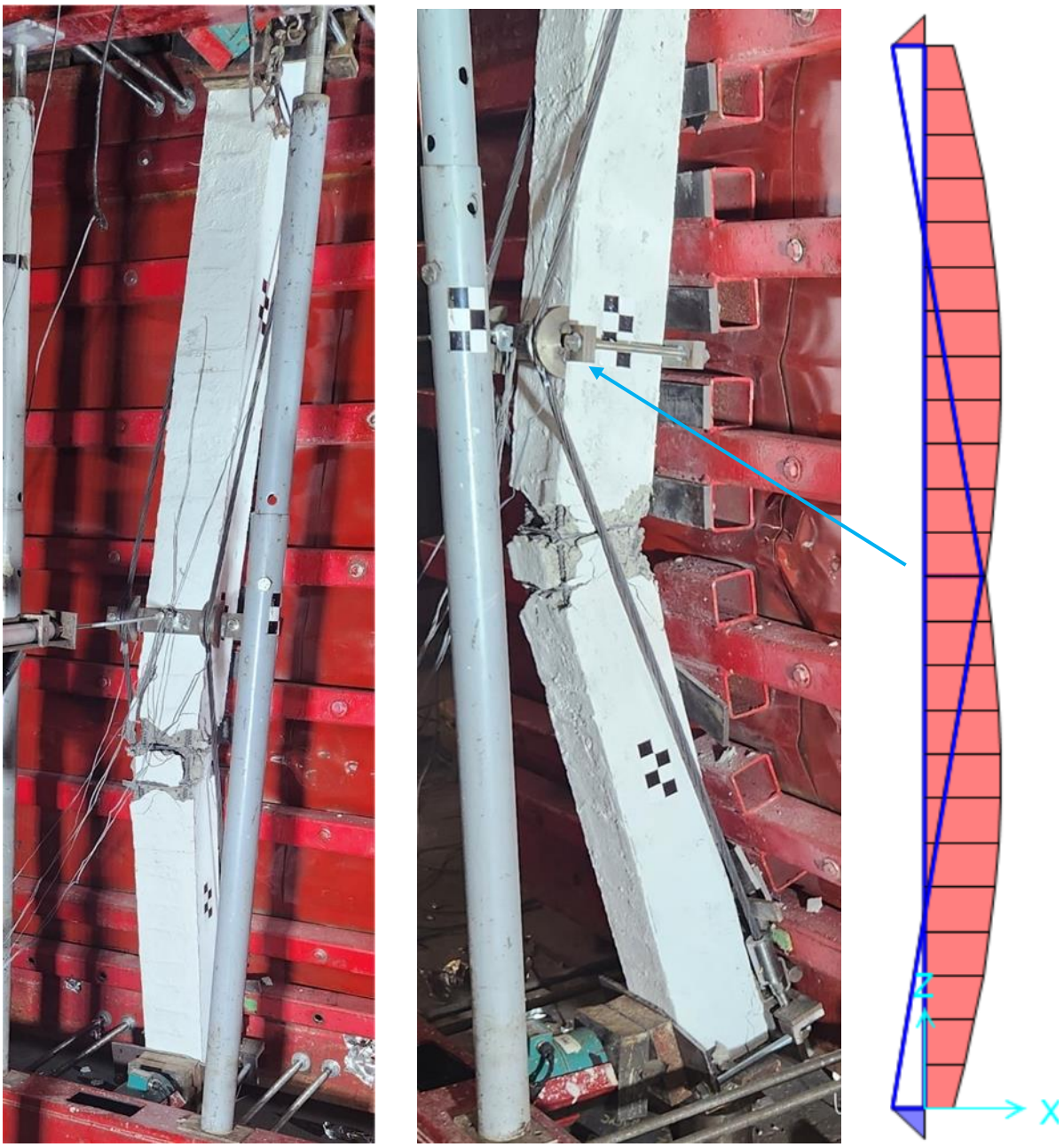

(a) (b) (c)

Figure 4.14 – Photos of column SH-207e-0.15fpu-N1 after blast shot#3; a) side view, b) front view, c) resultant moment diagram.

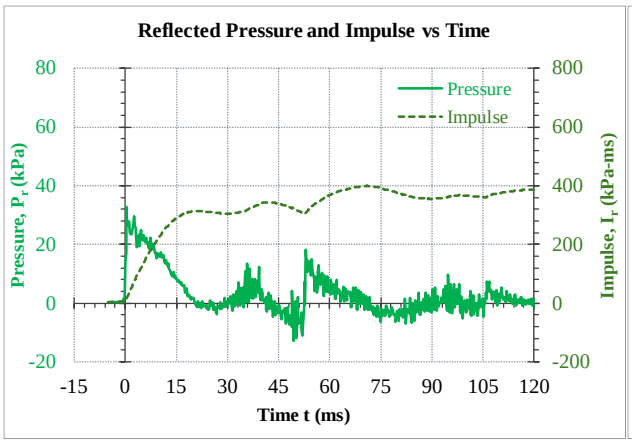

(a)

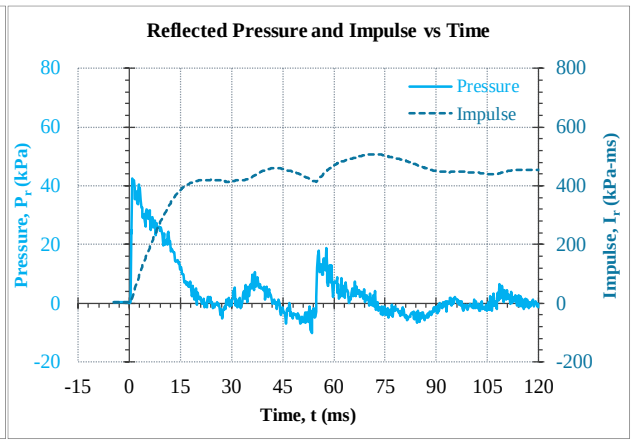

(b)

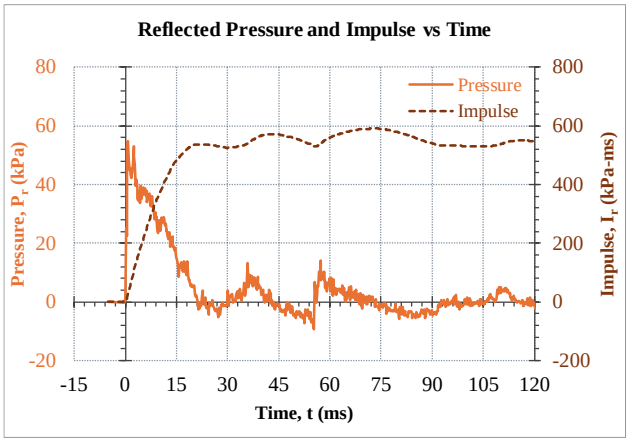

(c)

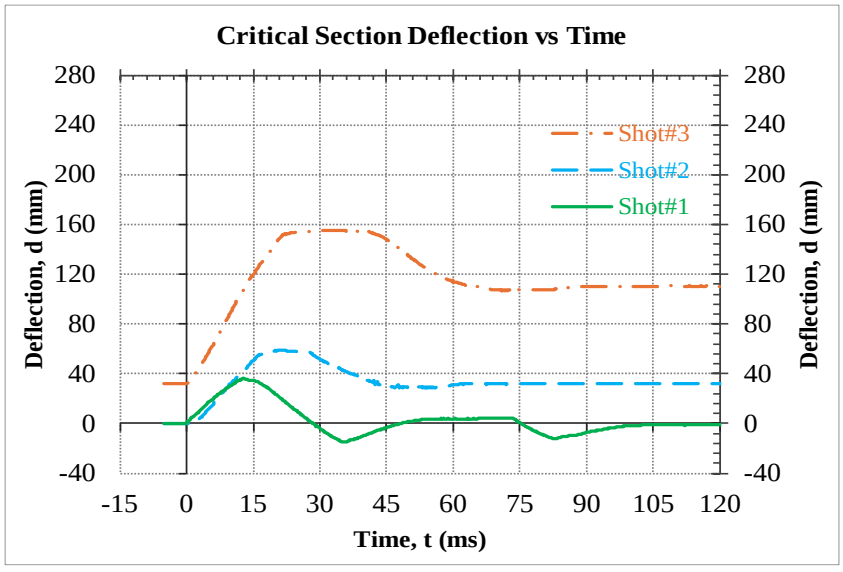

(d)

Figure 4.15 – Reflected pressure, impulse, and displacement time histories of column DH1-207e-0.13fpu-N1; a) blast shot#1, b) blast shot#2, c) blast shot#3, and d) deflection at mid-height region.

(a) (b)

Figure 4.16 – Photos of column DH1-207e-0.13fpu-N1 after blast shot#1: a) side view, b) front view.

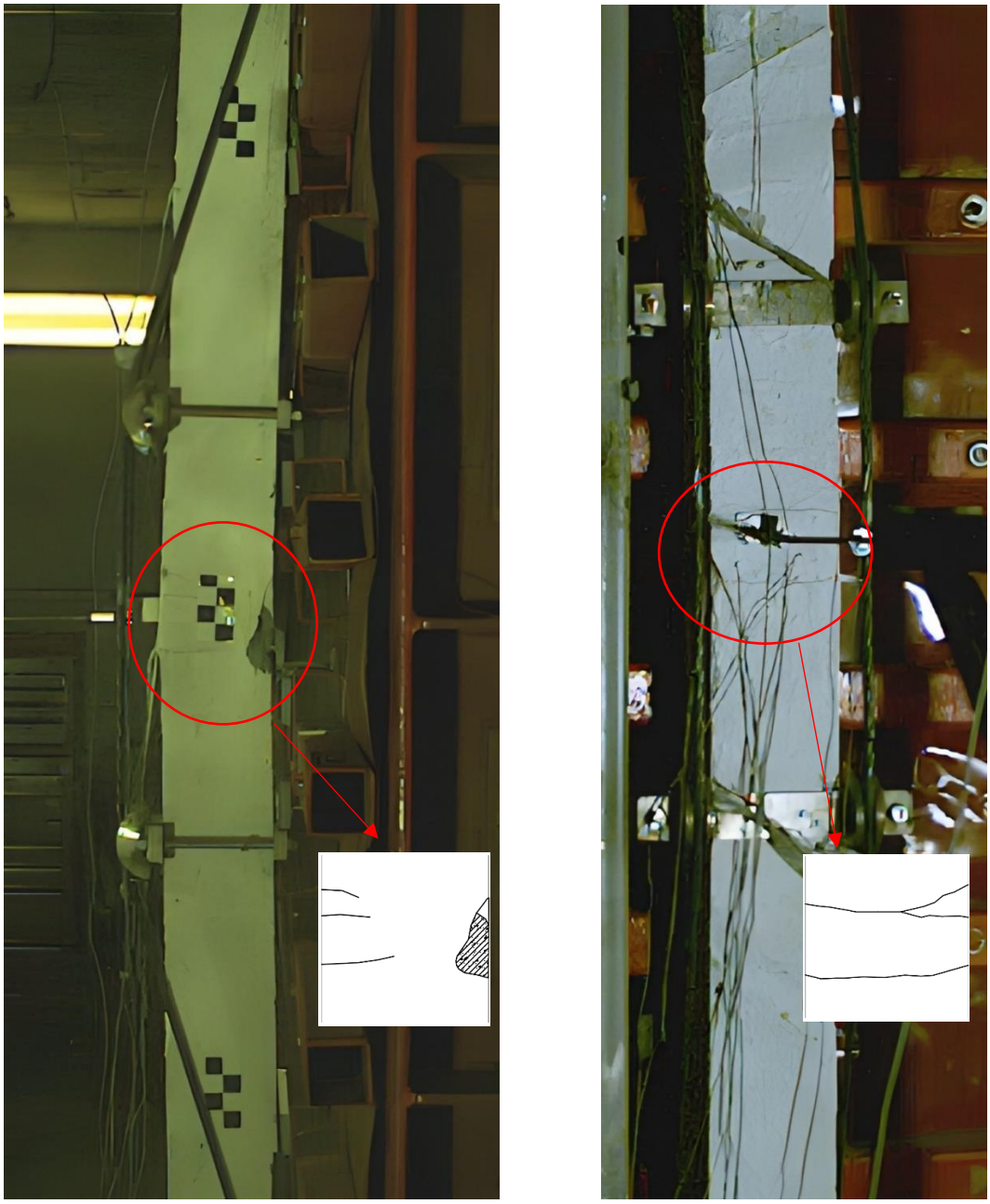

(a) (b)

Figure 4.17 – Photos of column DH1-207e-0.13fpu-N1 with a sketch at the location of damage after blast shot#2; a) side view, b) front view.

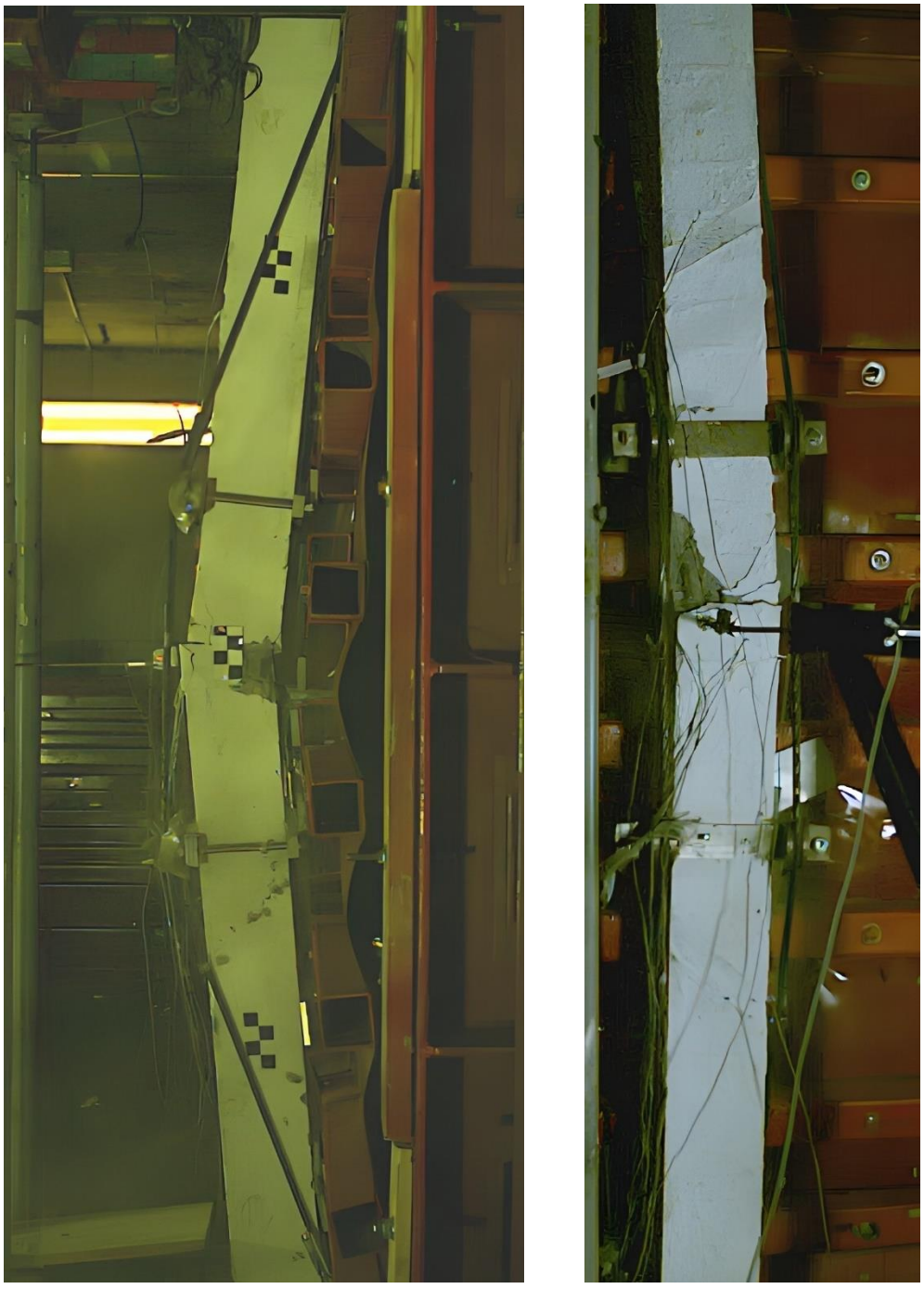

(a) (b)

Figure 4.18 – Photos of column DH1-207e-0.13fpu-N1 after blast shot#3: a) side view, b) front view.

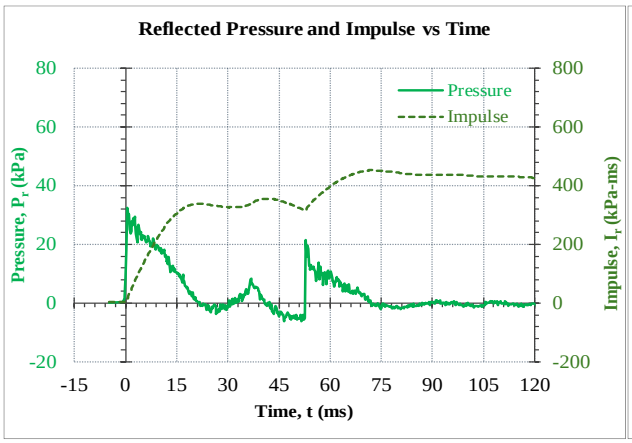

(a)

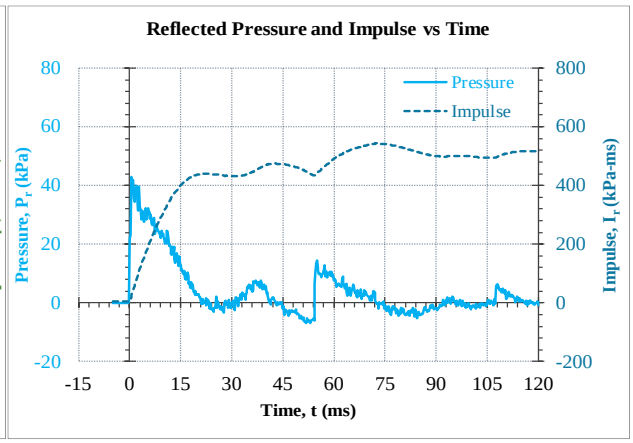

(b)

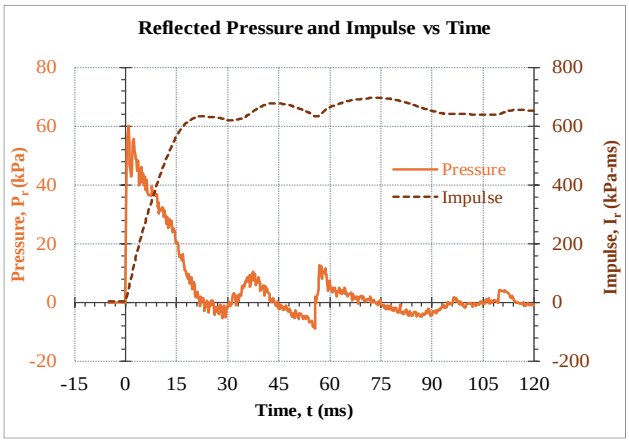

(c)

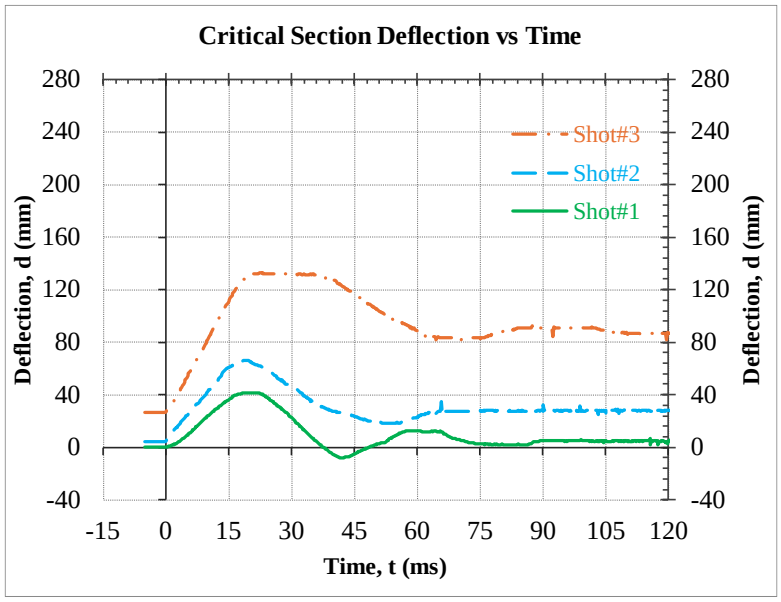

(d)

Figure 4.19 – Reflected pressure, impulse, and displacement time histories of column DH2-207e-0.16fpu-N1; a) blast shot#1, b) blast shot#2, c) blast shot#3, and d) deflection at mid-height region.

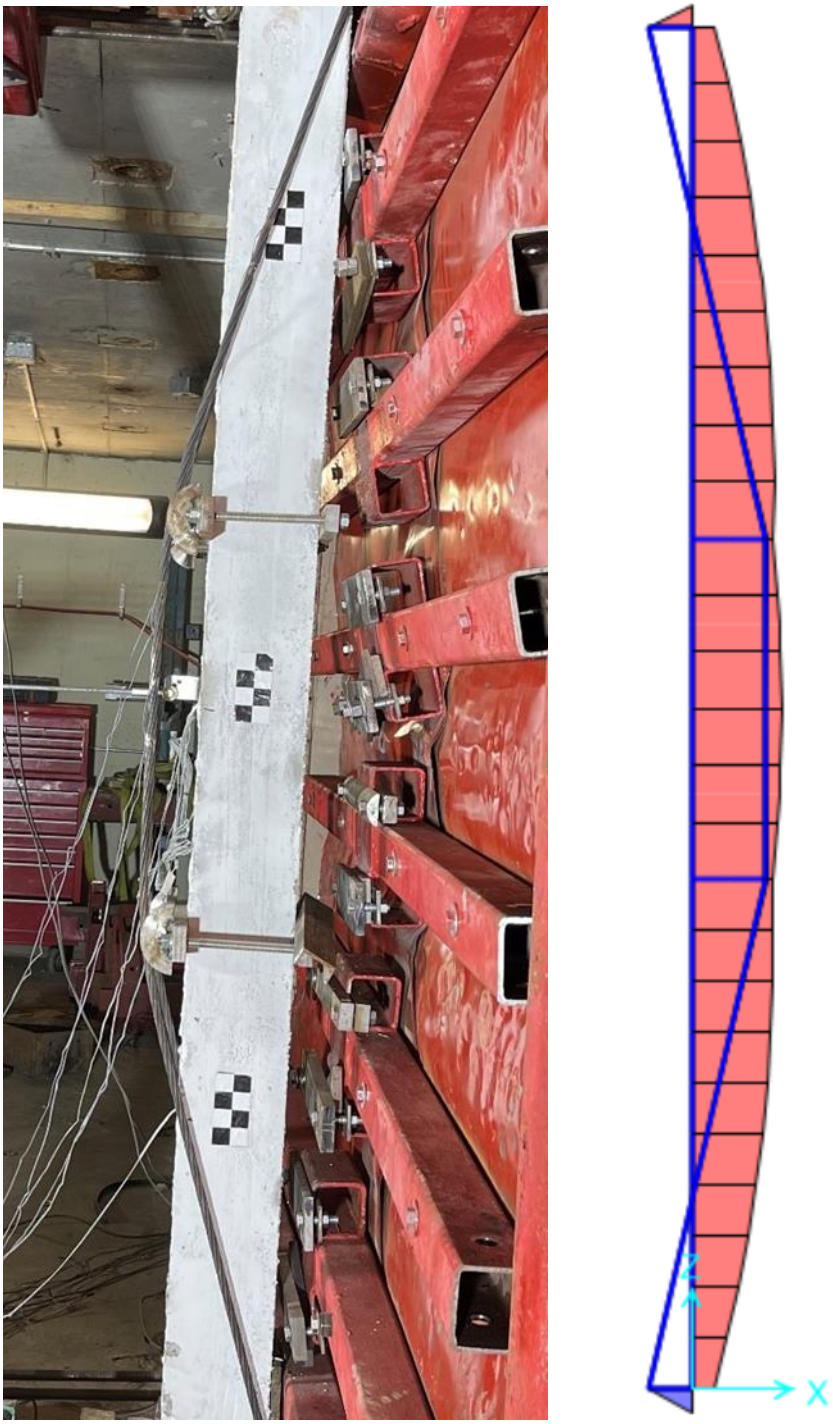

(a) (b)

Figure 4.20 – Photos of column DH2-207e-0.16fpu-N1 after blast shot#1; a) side view, and b) resultant moment diagram .

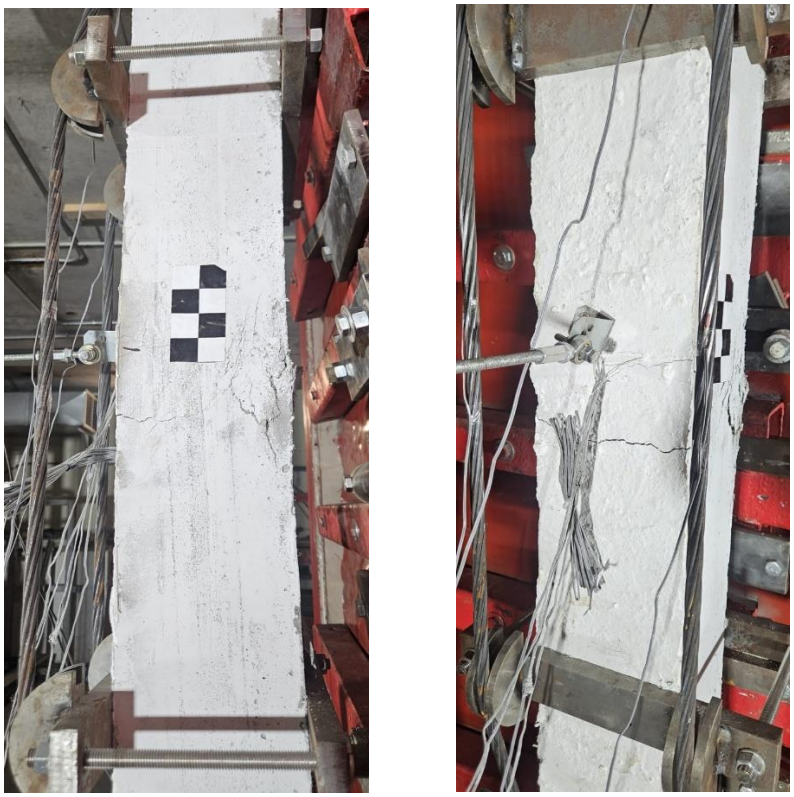

(a) (b)

Figure 4.21 – Photos of column DH2-207e-0.16fpu-N1 after blast shot#2: a) side view, b) front view.

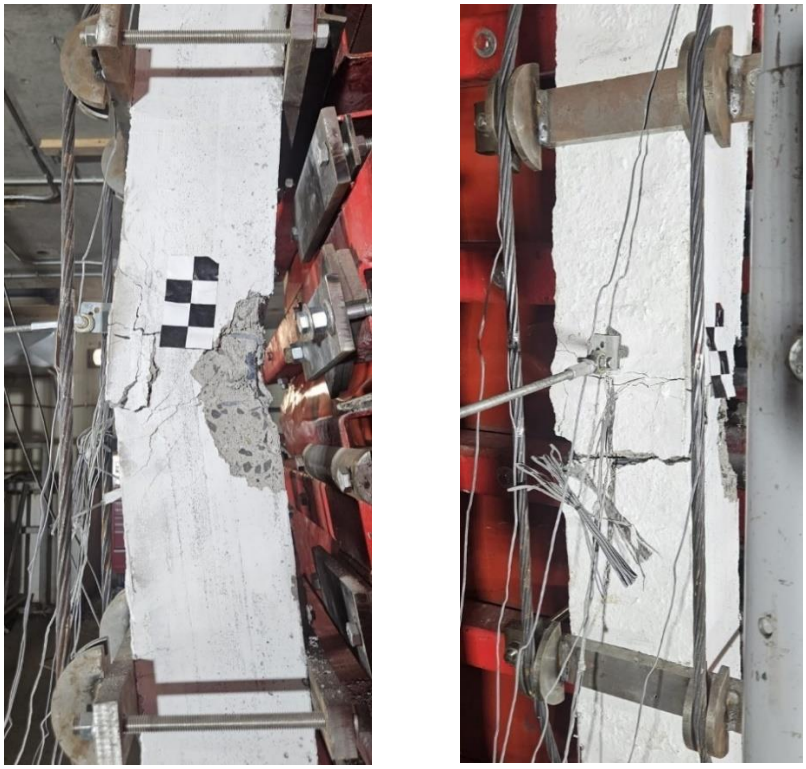

(a) (b)

Figure 4.22 – Photos of column DH2-207e-0.16fpu-N1 after blast shot#3: a) side view, b) front view.

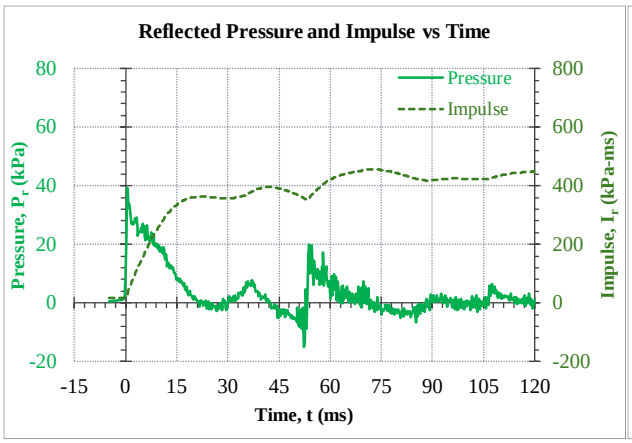

(a)

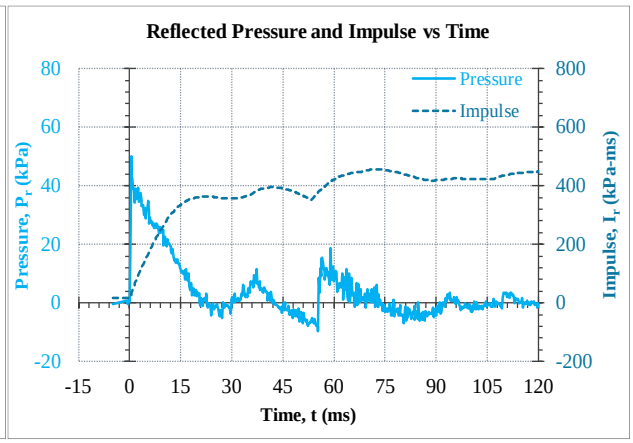

(b)

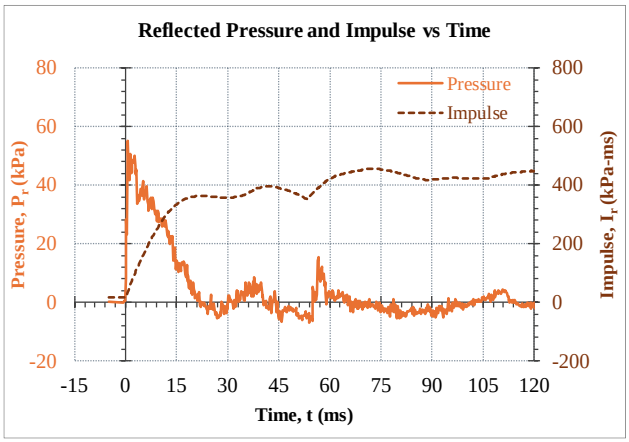

(c)

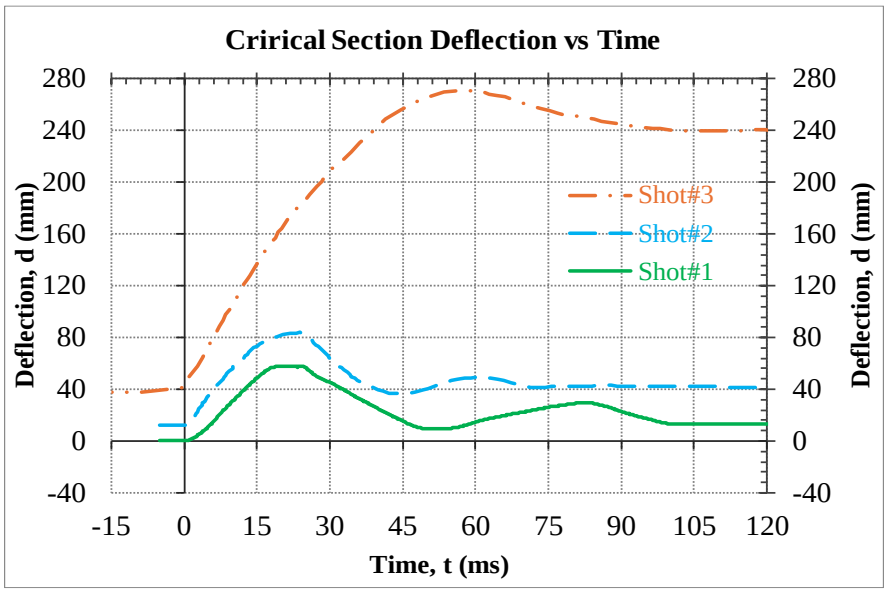

(d)

Figure 4.23 – Reflected pressure, impulse, and displacement time histories of column TH1-247e-0.10fpu-N1; a) blast shot#1, b) blast shot#2, c) blast shot#3, and d) deflection at mid-height region.

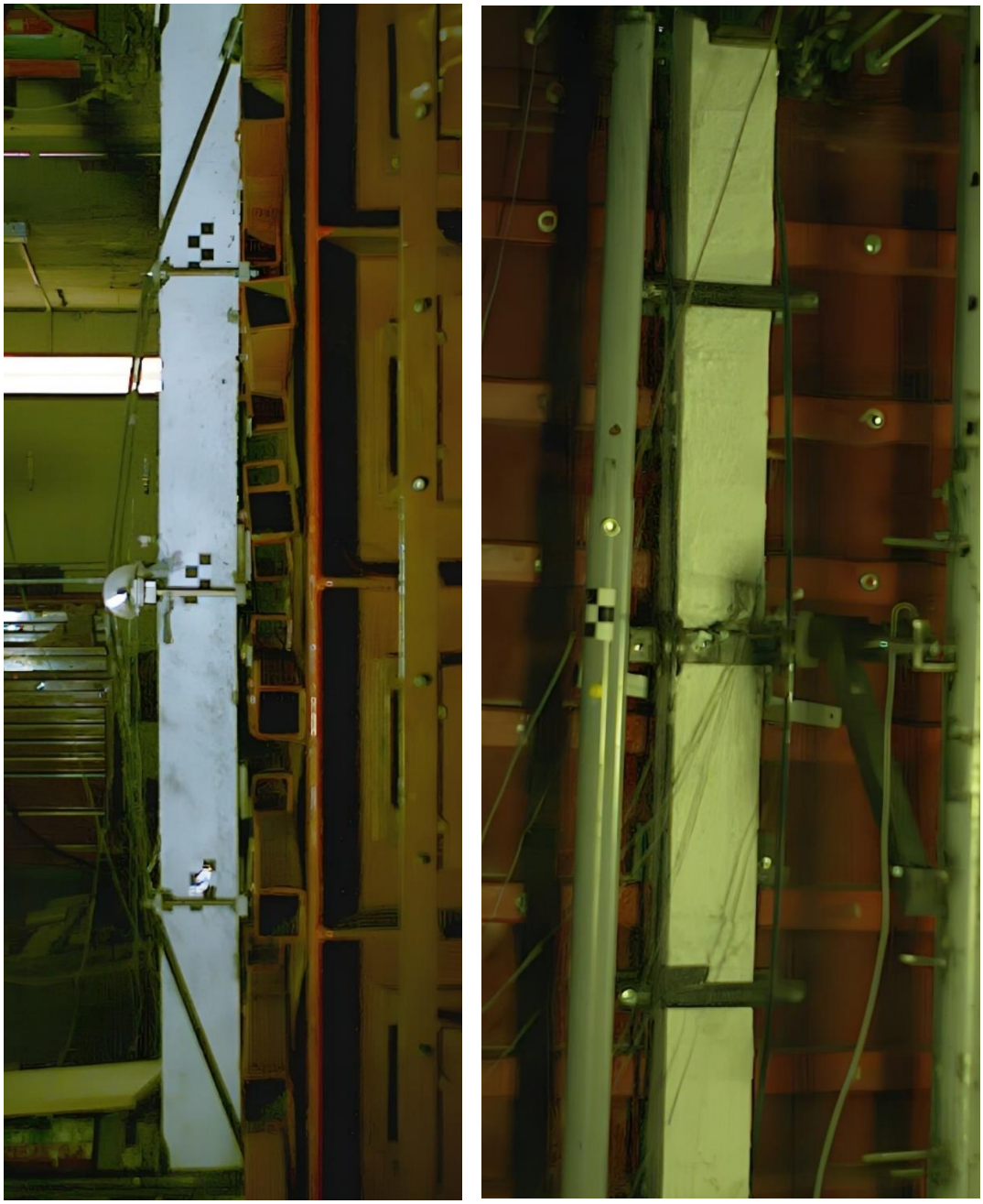

(a) (b)

Figure 4.24 – Photo of column TH1-247e-0.10fpu-N1 after blast shot#1; a) side view, b) front view.

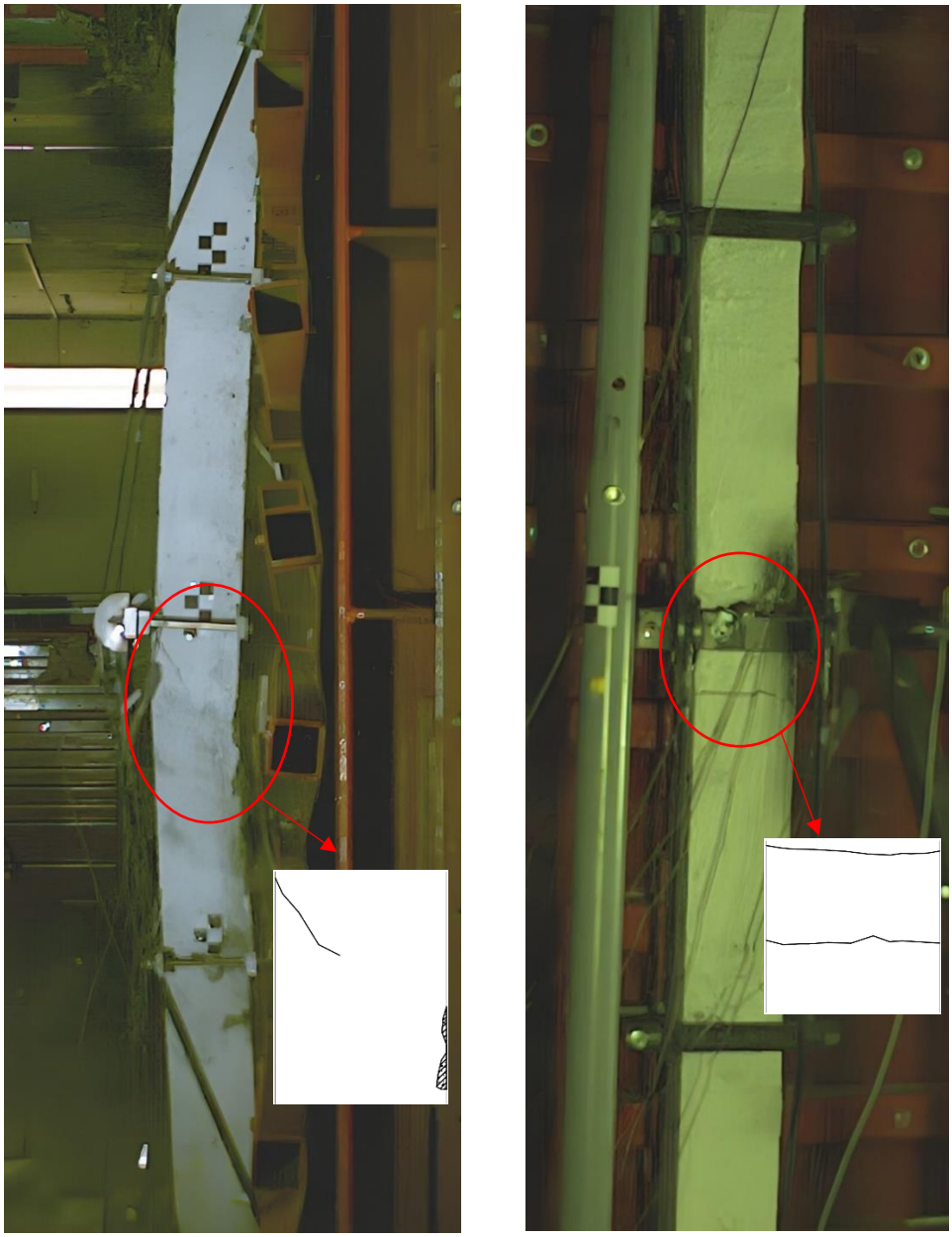

(a) (b)

Figure 4.25 – Photos of column TH1-247e-0.10fpu-N1 with a sketch at the location of damage after blast shot#2; a) side view, b) front view.

Figure 4.26 – Photos of column TH1-247e-0.10fpu-N1 after blast shot#3.

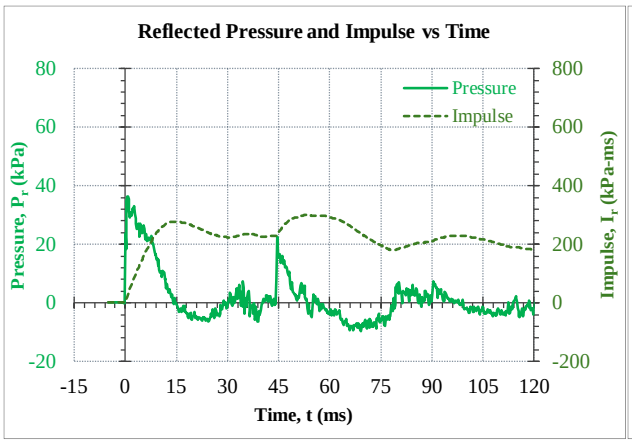

(a)

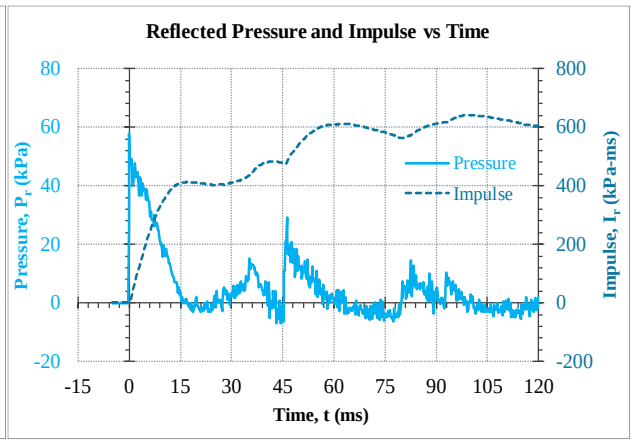

(b)

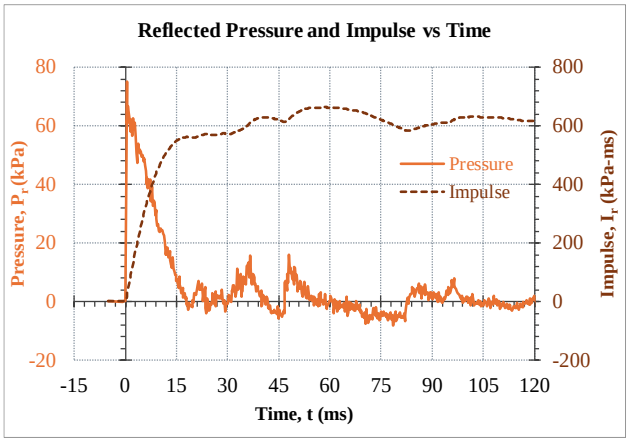

(c)

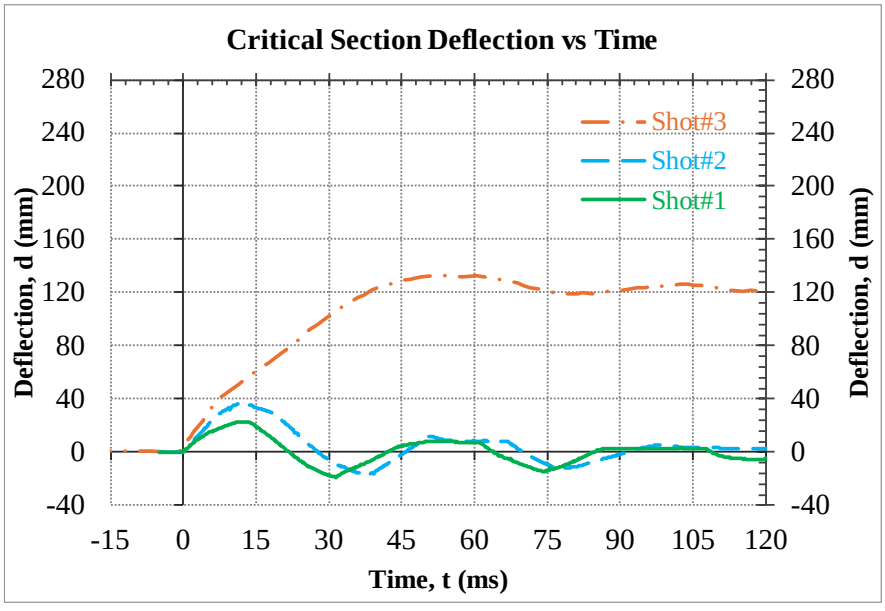

(d)

Figure 4.27 – Reflected pressure, impulse, and displacement time histories of column TH2-247e-0.15fpu-N2; a) blast shot#1, b) blast shot#2, c) blast shot#3, and d) deflection at mid-height region.

(a) (b)

Figure 4.28 – Photos of column TH2-247e-0.15fpu-N2 after blast shot#1: a) side view, b) front view.

(a) (b)

Figure 4.29 – Photos of column TH2-247e-0.15fpu-N2 after blast shot#2: a) side view, b) front view.

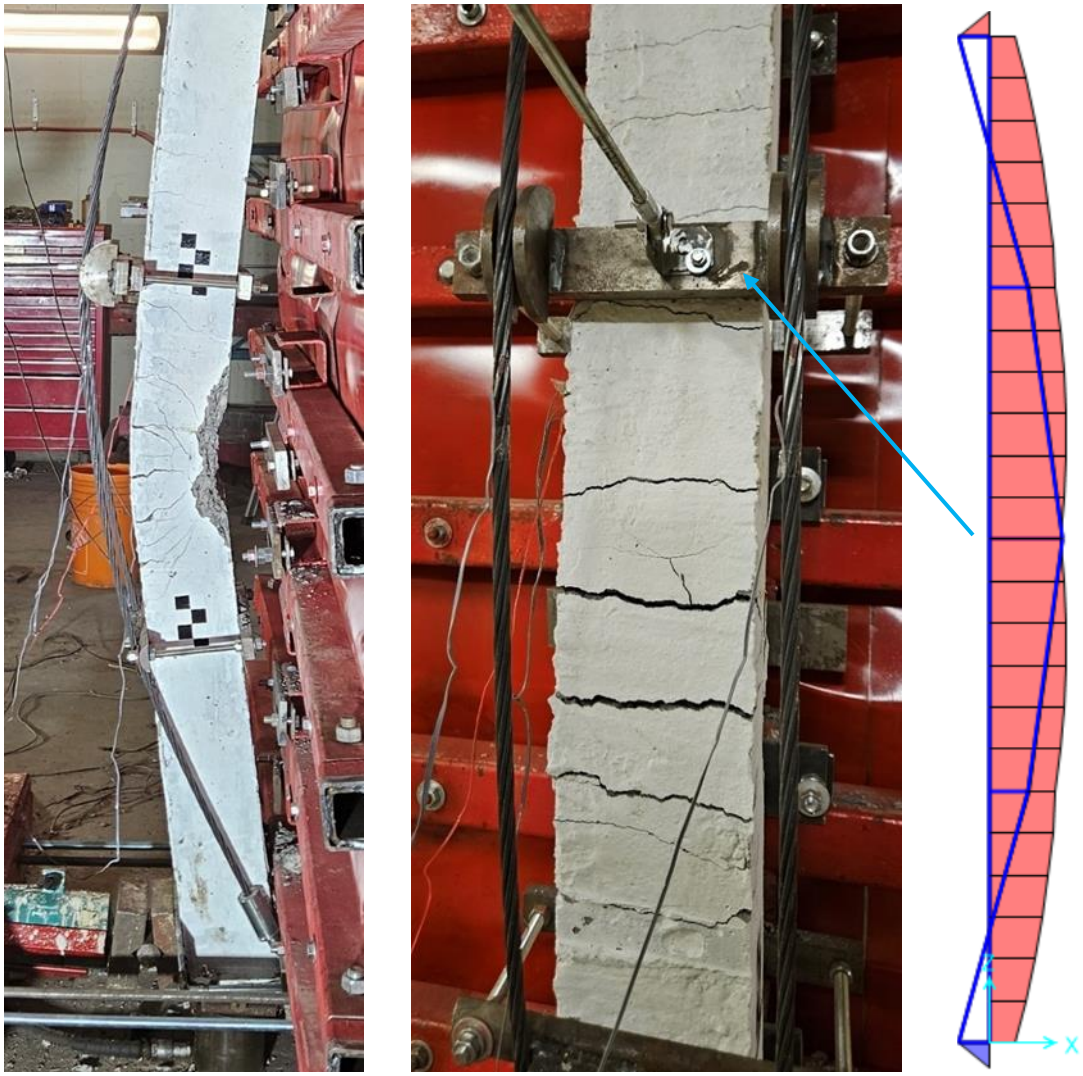

(a) (b) (c)

Figure 4.30 – Photos of column TH2-247e-0.15fpu-N2 after blast shot#3: a) side view, b) front view, and c) resultant moment diagram.

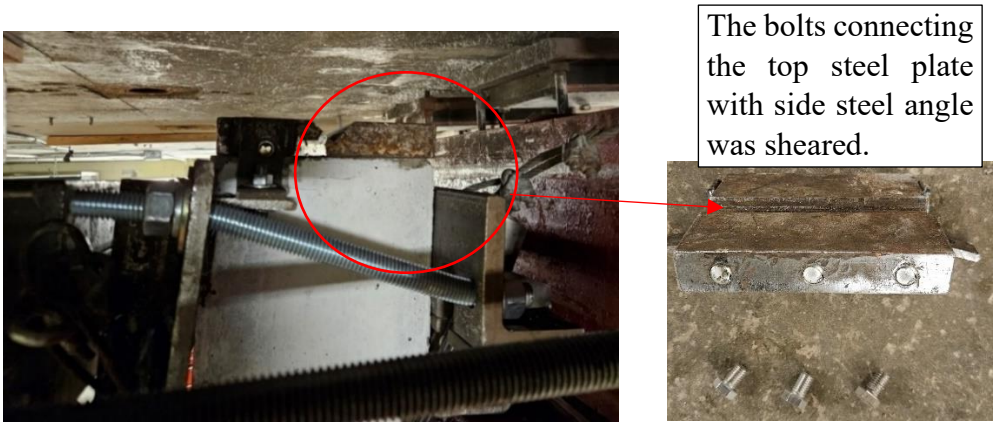

Figure 4.31 – A close-up photo of connection failure during the third blast shot of column TH2-247e-0.15fpu-N2.

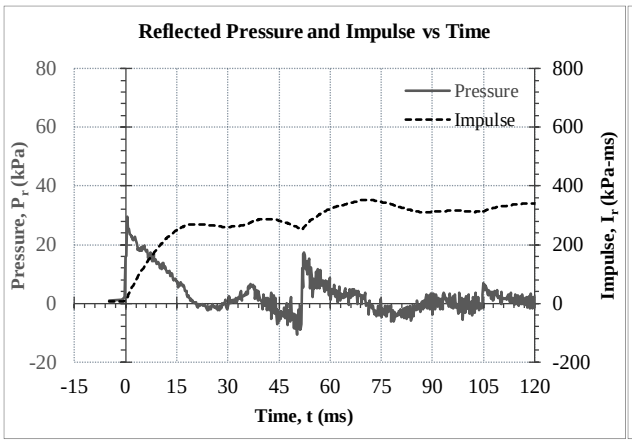

(a)

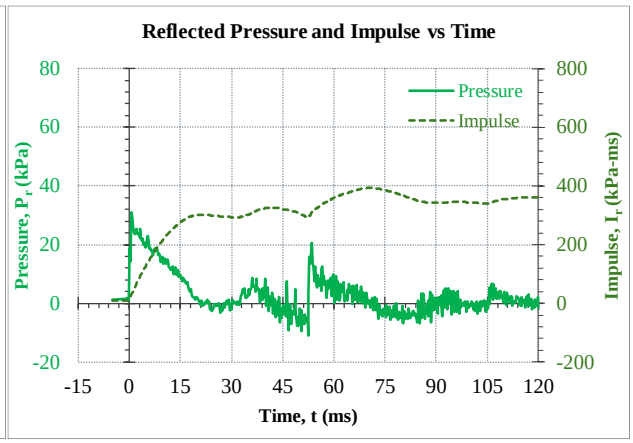

(b)

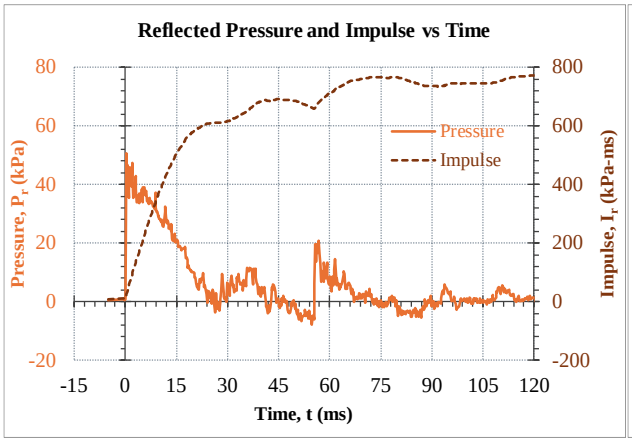

(c)

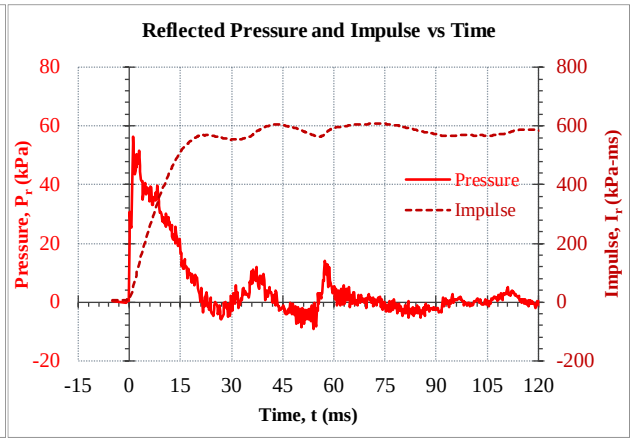

(d)

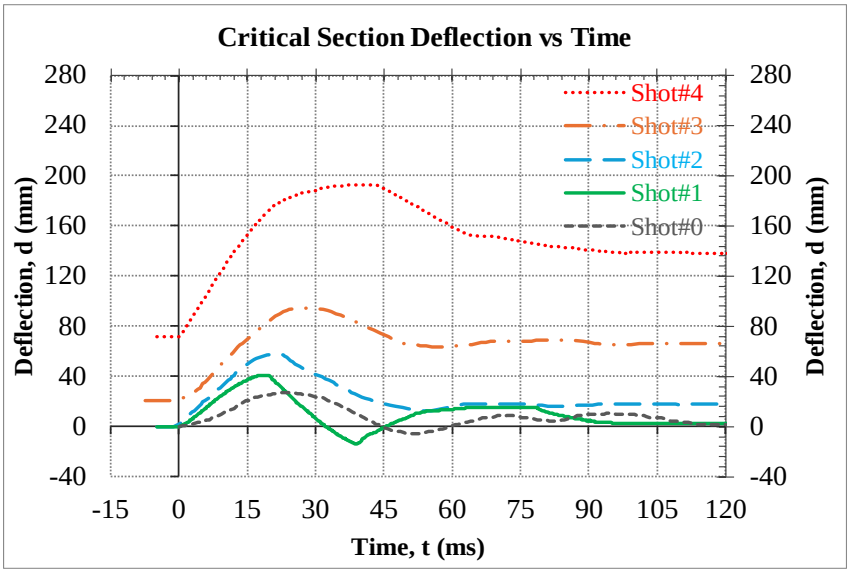

(e)

Figure 4.32 – Reflected pressure, impulse, and displacement time histories of column P1-227e-0.09fpu-N1; a) blast shot#1, b) blast shot#2, c) blast shot#3, d) blast shot #5, e) deflection at mid-height region.

(a) (b)

Figure 4.33 – Photos of column P1-227e-0.09fpu-N1 after blast shot#1: a) side view, b) front view.

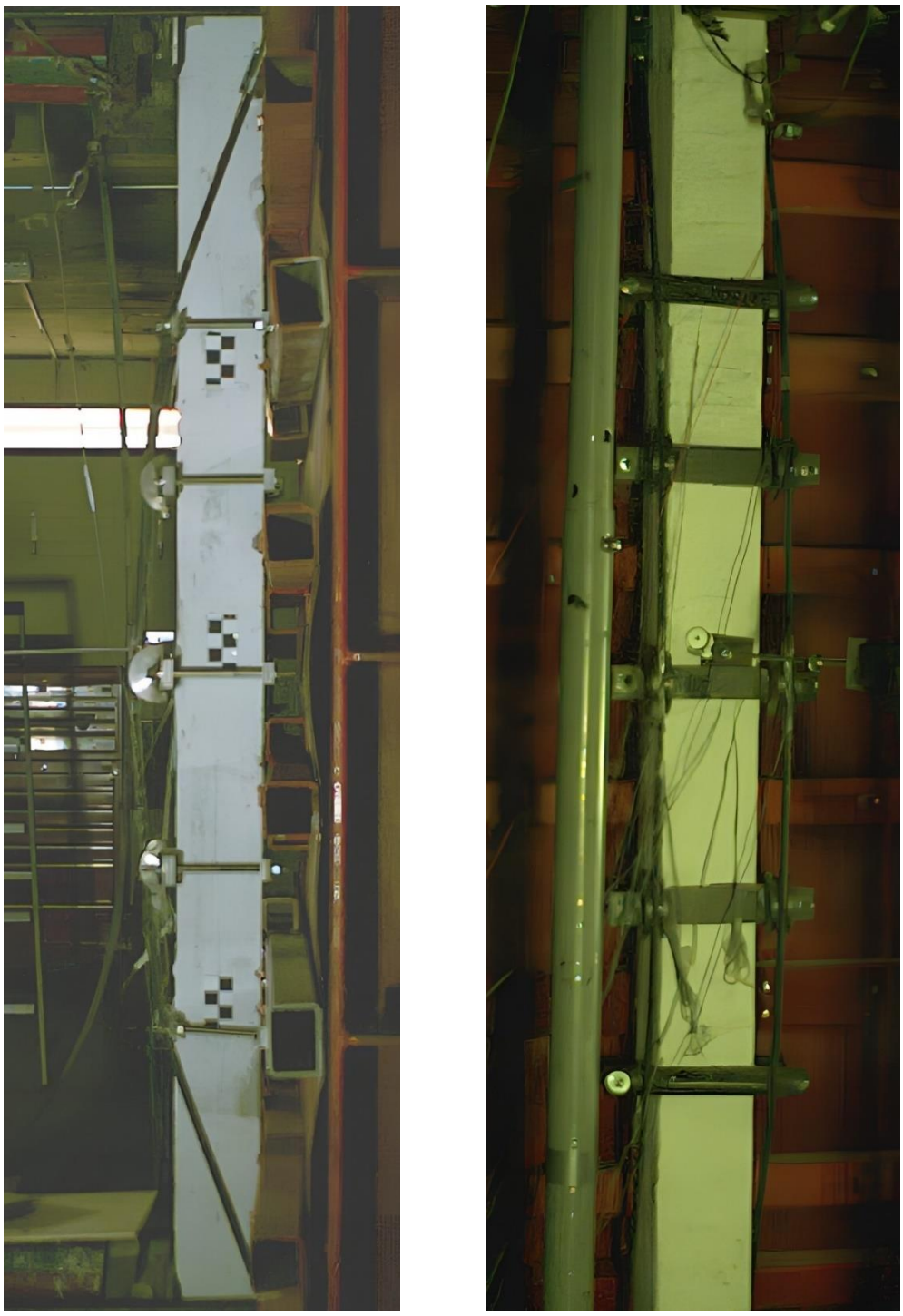

(a) (b)

Figure 4.34 –Photos of column P1-227e-0.09fpu-N1 after blast shot#2: a) side view, b) front view.

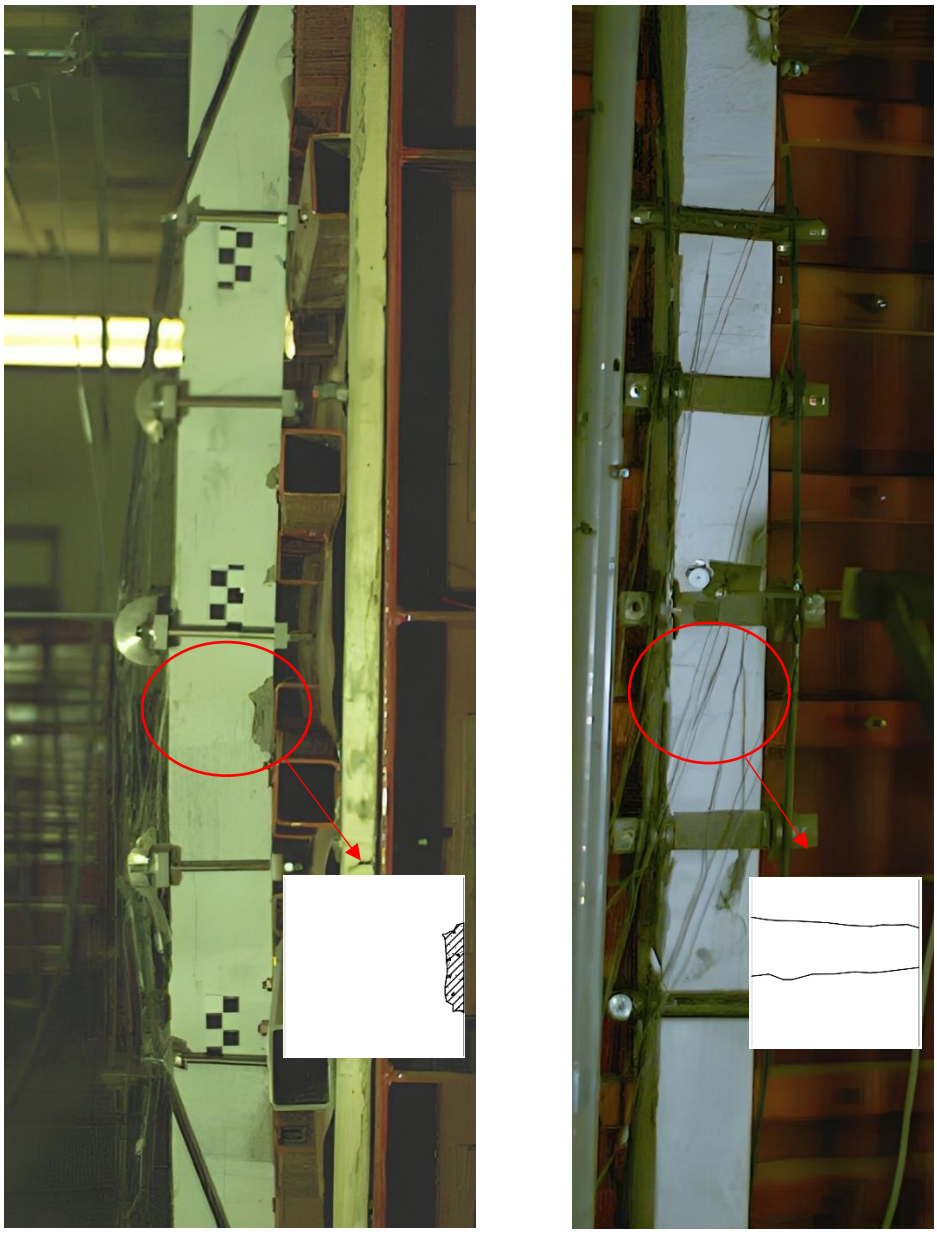

(a) (b)

Figure 4.35 – Photo of column P1-227e-0.09fpu-N1 with a sketch at the location of damage after blast shot#3; a) side view, b) front view.

(a) (b)

Figure 4.36 – Photos of column P1-227e-0.09fpu-N1 after blast shot#4: a) side view, b) front view.

(a) (b)

Figure 4.37 – Photos of column P1-227e-0.09fpu-N1 after blast shot#5: a) side view, b) front view.

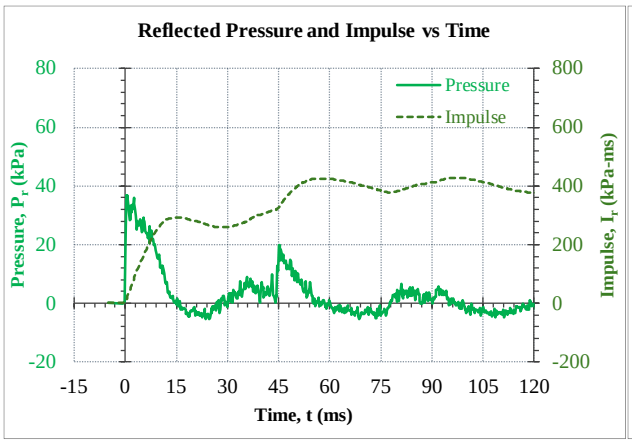

(a)

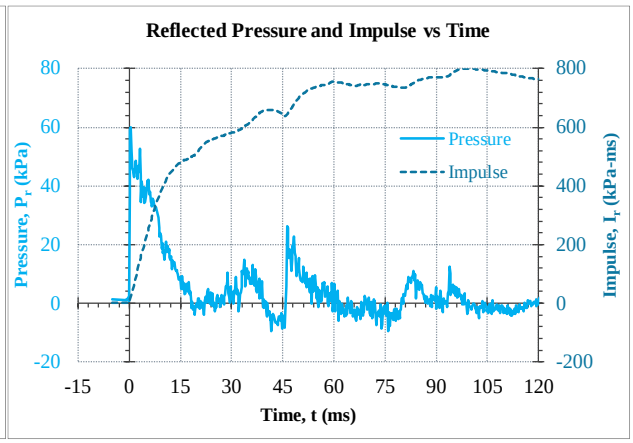

(b)

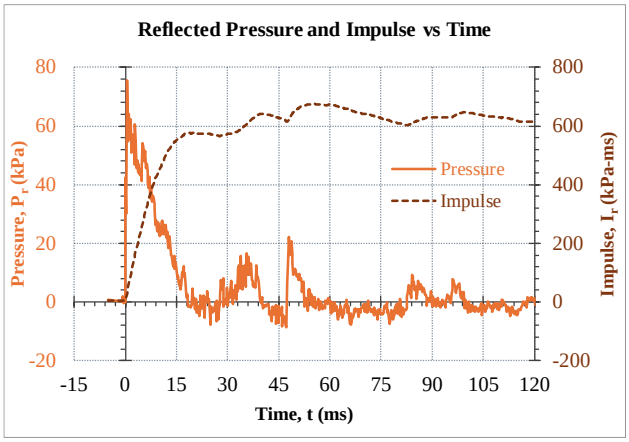

(c)

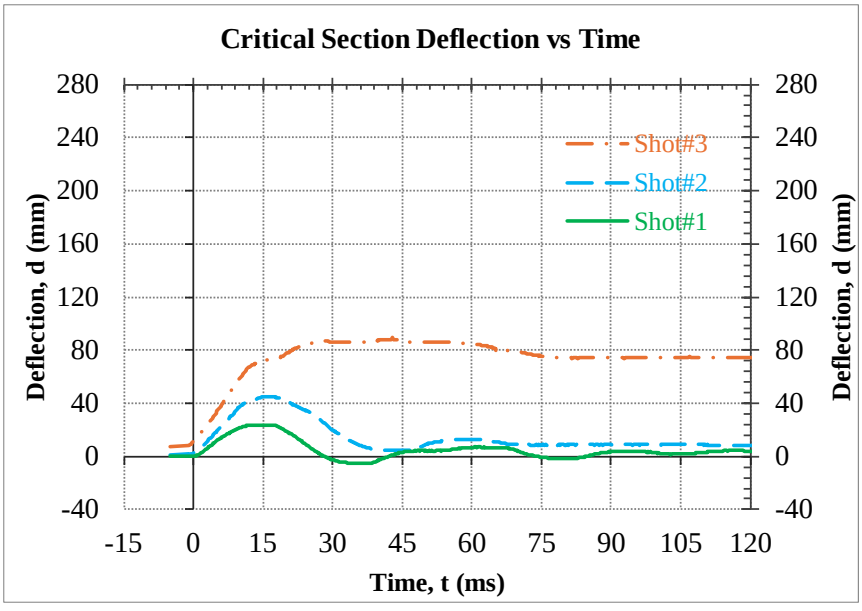

(d)

Figure 4.38 – Reflected pressure, impulse, and displacement time histories of column P2-227e-0.16fpu-N2; a) blast shot#1, b) blast shot#2, c) blast shot#3, and d) deflection at mid-height region.

(a) (b)

Figure 4.39 – Photos of column P2-227e-0.16fpu-N2 after blast shot#1: a) side view, b) front view.

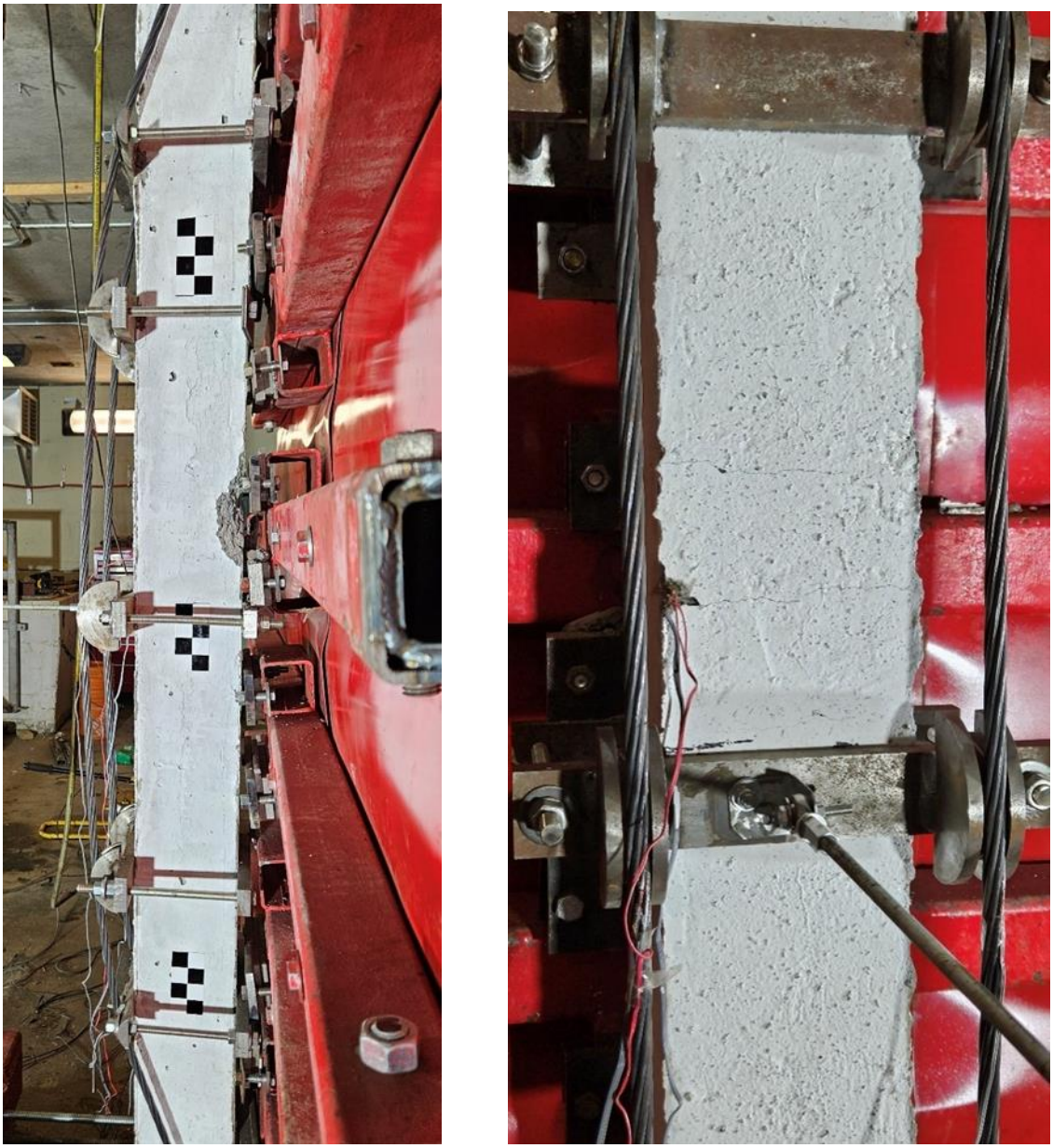

(a) (b)

Figure 4.40 – Photos of column P2-227e-0.16fpu-N2 after blast shot#2: a) side view, b) front view.

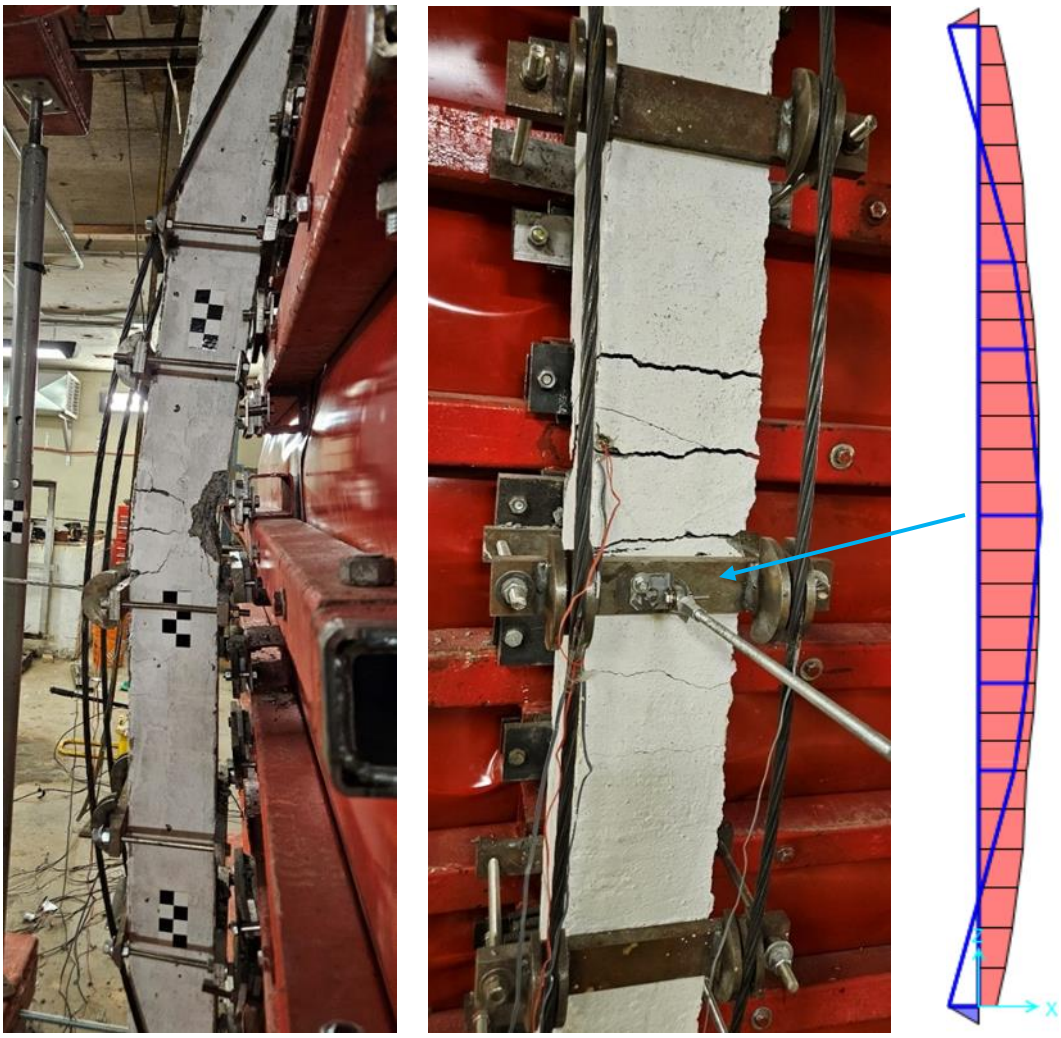

(a) (b) (c)

Figure 4.41 – Photos of column P2-227e-0.16fpu-N2 after blast shot#3: a) side view, b) front view, and c) resultant moment diagram.

Figure 4.42 – A close-up photo of connection failure during the third shot of column P2-227e-0.16fpu-N2.

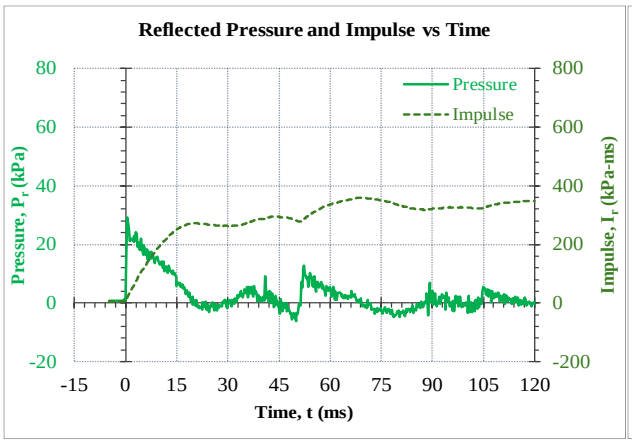

(a)

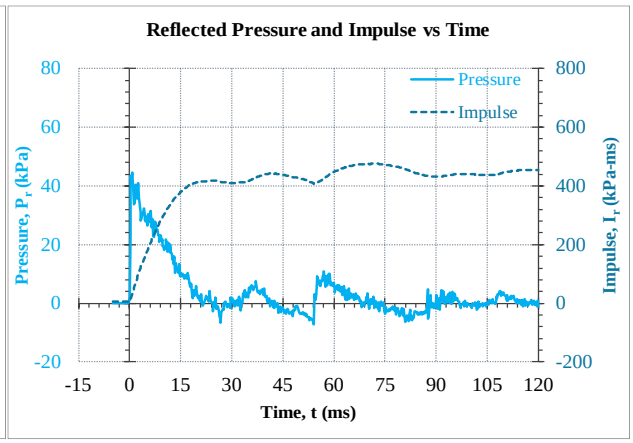

(b)

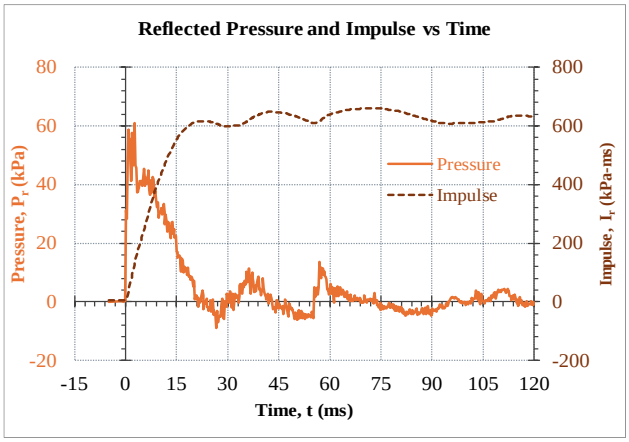

(c)

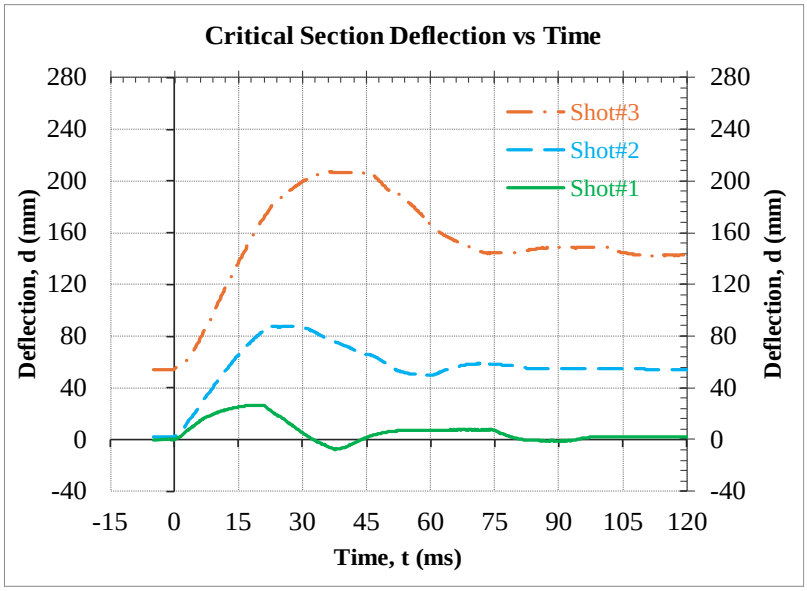

(d)

Figure 4.43 – Reflected pressure, impulse, and displacement time histories of column PT-SS-0.35fpu-S; a) blast shot#1, b) blast shot#2, c) blast shot#3, and d) deflection at mid-height region.

(a) (b)

Figure 4.44 – Photos of column PT-SS-0.35fpu-S after blast shot#1; a) side view, b) front view.

(a) (b)

Figure 4.45 – Photos of column PT-SS-0.35fpu-S after blast shot#2; a) side view, b) front view.

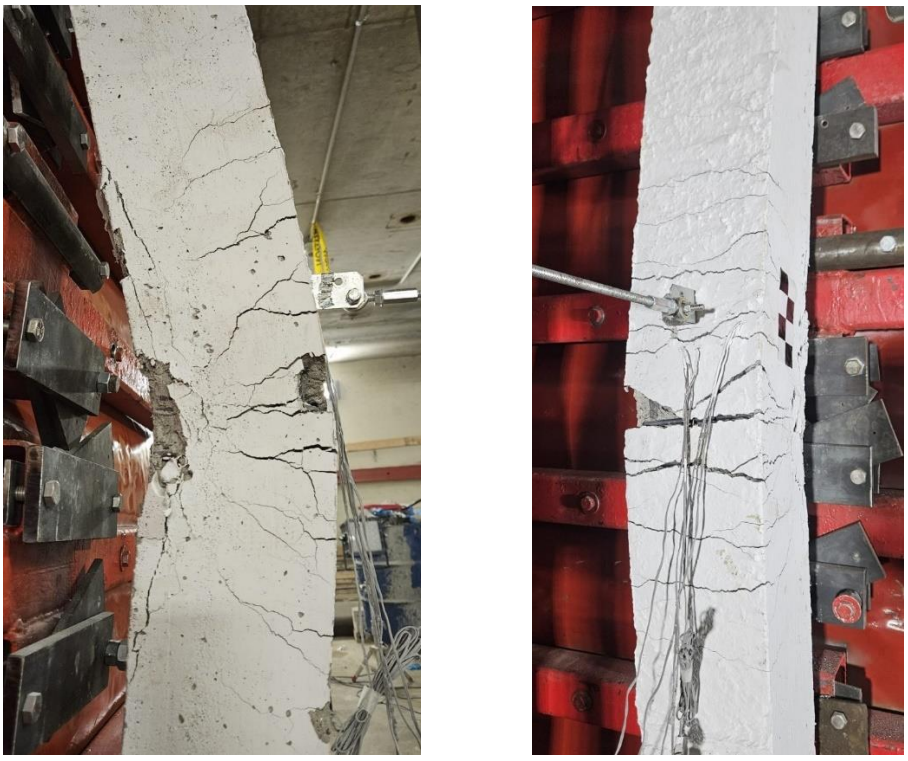

(a) (b)

Figure 4.46 – Photos of column PT-SS-0.35fpu-S after blast shot#3; a) side view, b) front view.

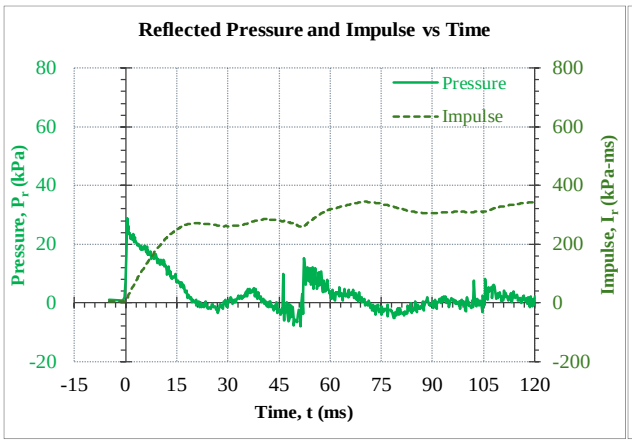

(a)

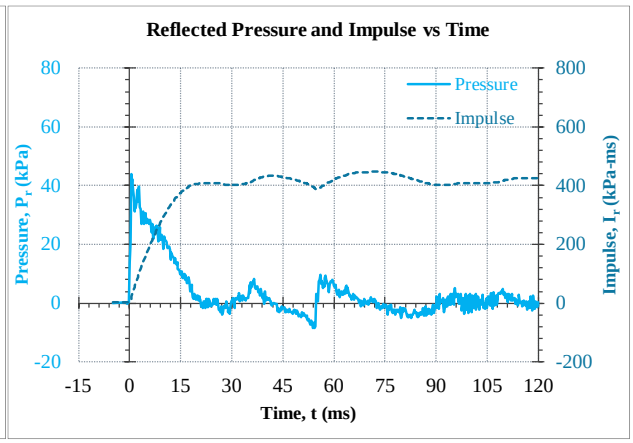

(b)

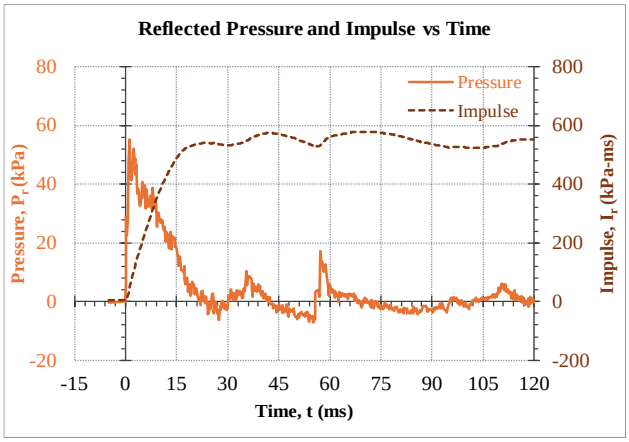

(c)

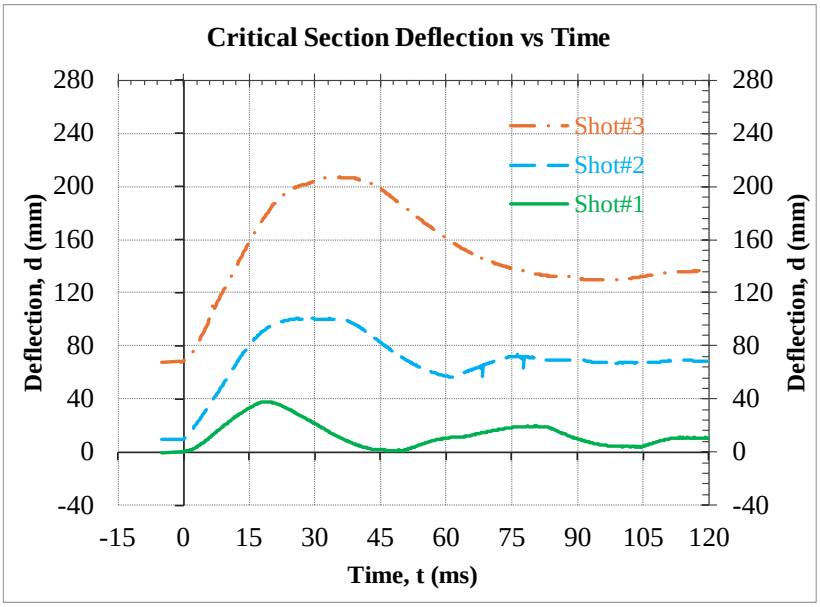

(d)

Figure 4.47 – Reflected pressure, impulse, and displacement time histories of column PT-DS-0.40fpu-S; a) blast shot#1, b) blast shot#2, c) blast shot#3, and d) deflection at mid-height region.

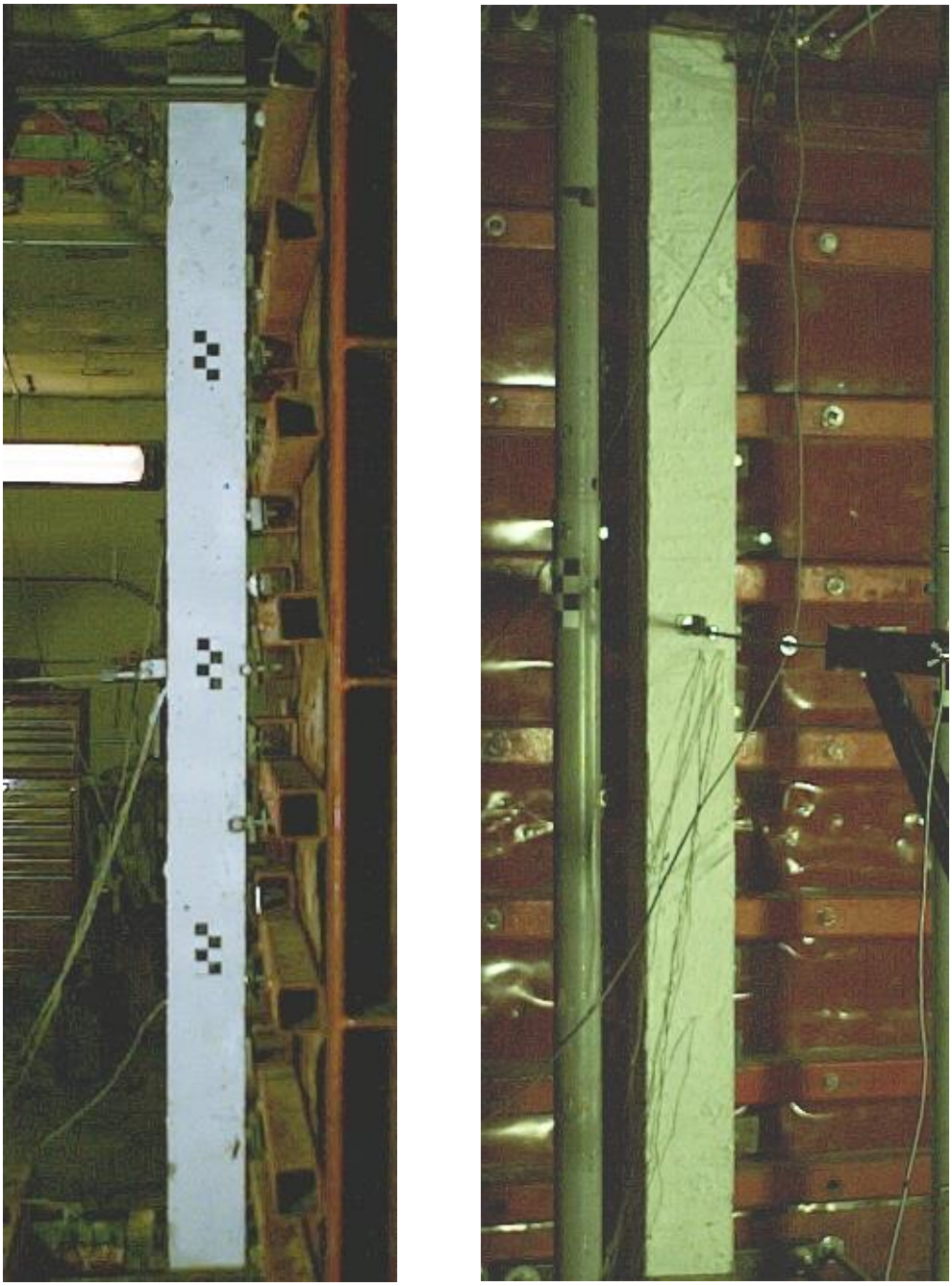

(a) (b)

Figure 4.48 – Photos of column PT-DS-0.40fpu-S after blast shot#1; a) side view, b) front view.

(a) (b)

Figure 4.49 - Photos of column PT-DS-0.40fpu-S after blast shot#2; a) side view, b) front view.

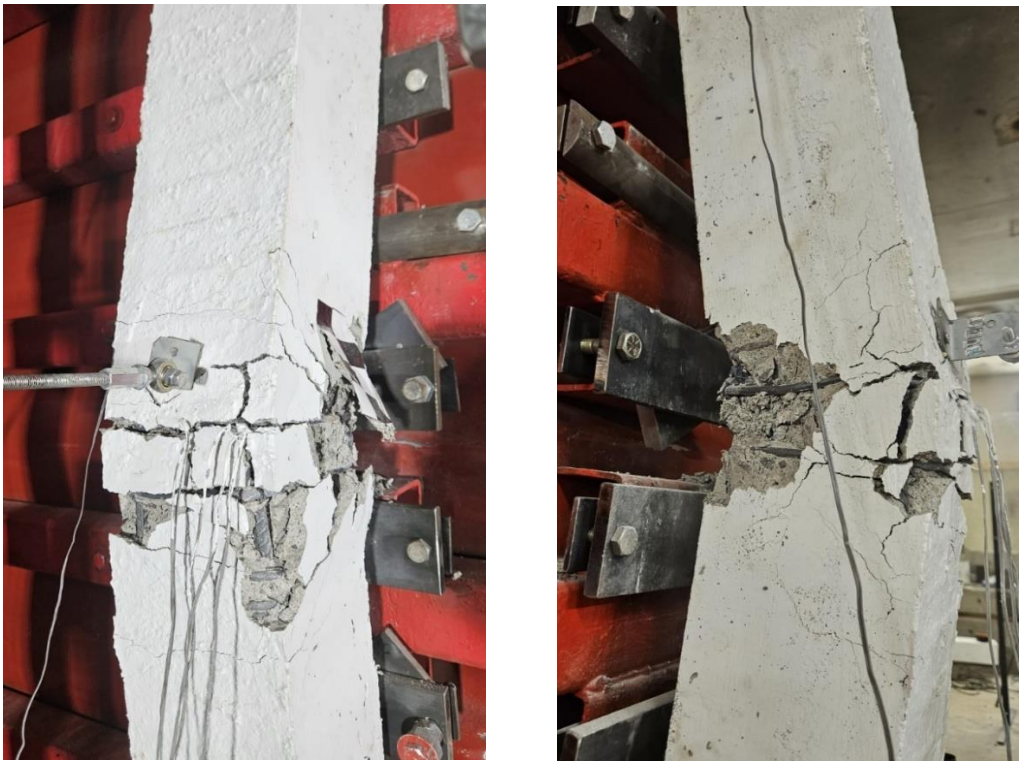

(a) (b)

Figure 4.50 – Photos of column PT-DS-0.40fpu-S after blast shot#3; a) side view, b) front view.

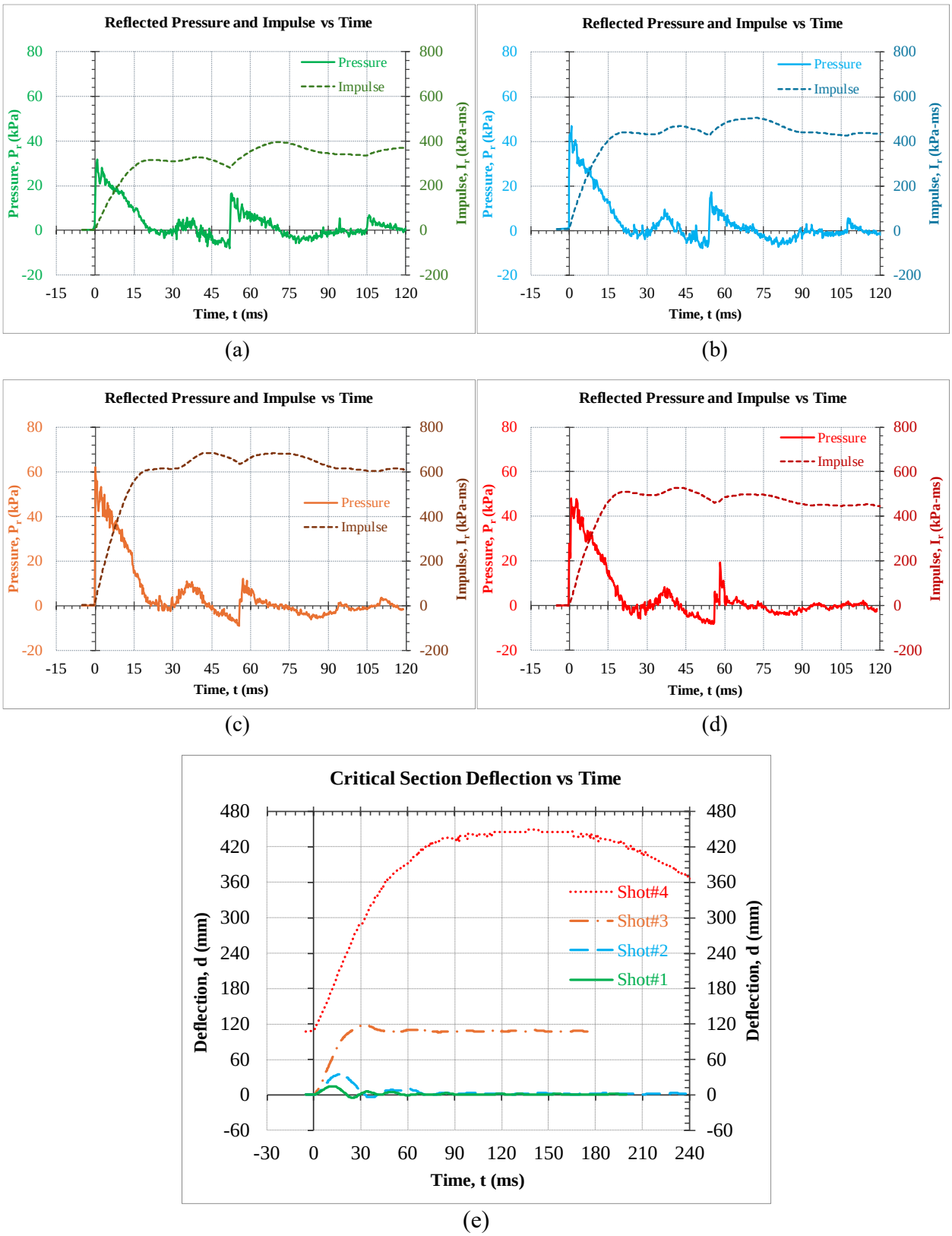

Figure 4.51 – Reflected pressure, impulse, and displacement time histories of column ECC-2.0%v_f-t30-N1; a) blast shot#1, b) blast shot#2, c) blast shot#3, d) blast shot#4, e) deflection at mid-height region.

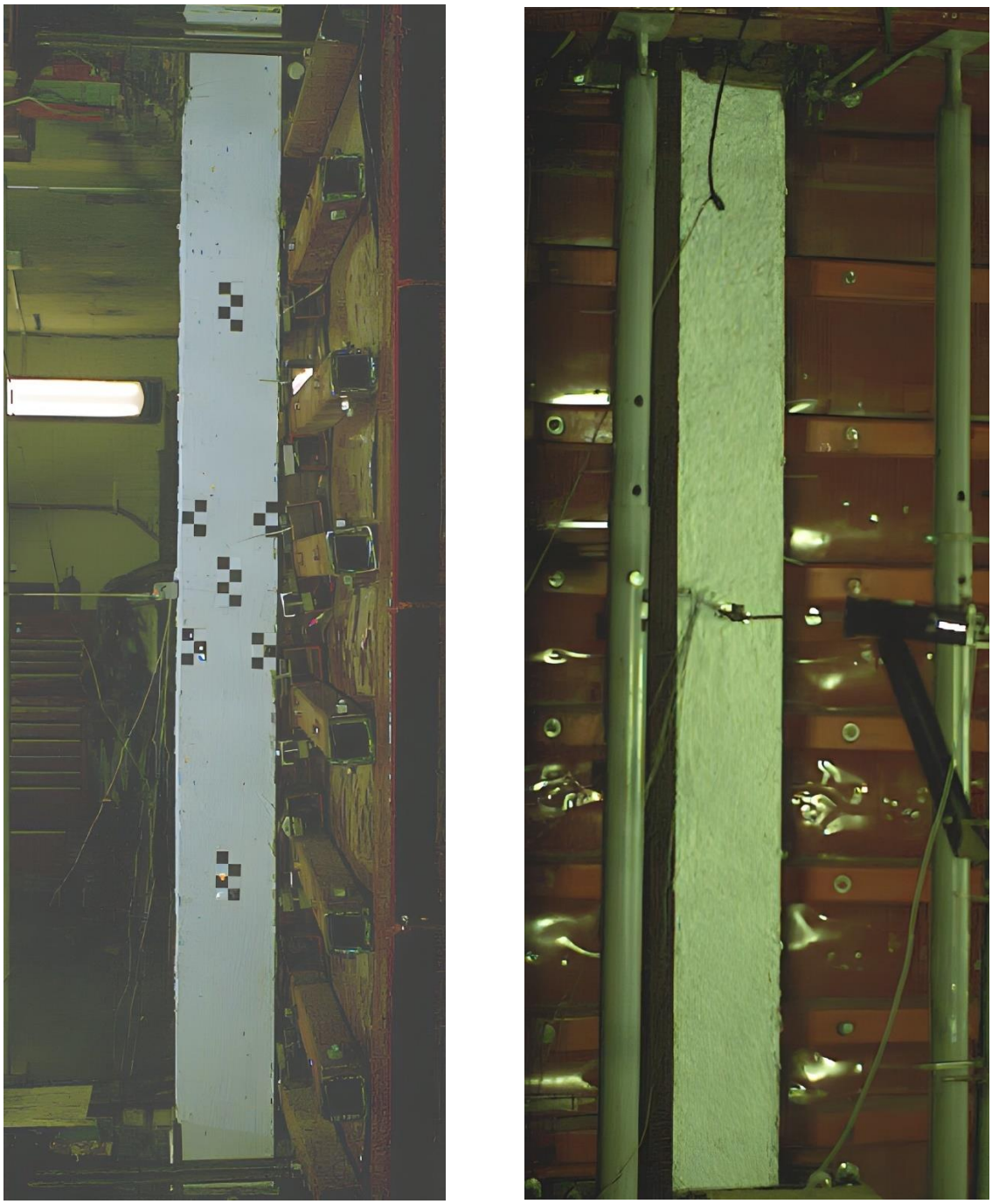

(a) (b)

Figure 4.52 – Photos of column ECC-2.0%v_f-t30-N1 after blast shot#1: a) side view, b) front view.

(a) (b)

Figure 4.53 – Photos of column ECC-2.0%v_f-t30-N1 after blast shot#2; a) side view, b) front view.

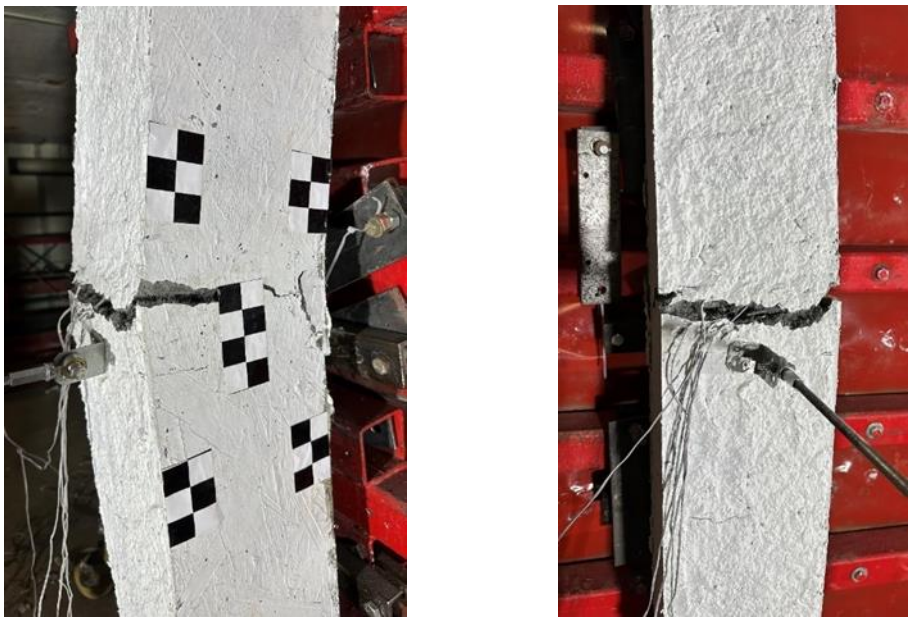

(a) (b)

Figure 4.54 – Photos of column ECC-2.0%vf-t30-N1 after blast shot#2; a) side view, b) front view.

(a) (b)

Figure 4.55 – Photos of column ECC-2.0%v_f-t30-N1 after blast shot#4; a) side view, b) front view.

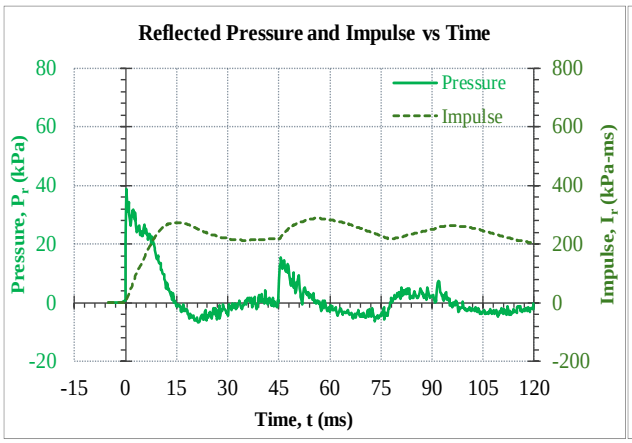

(a)

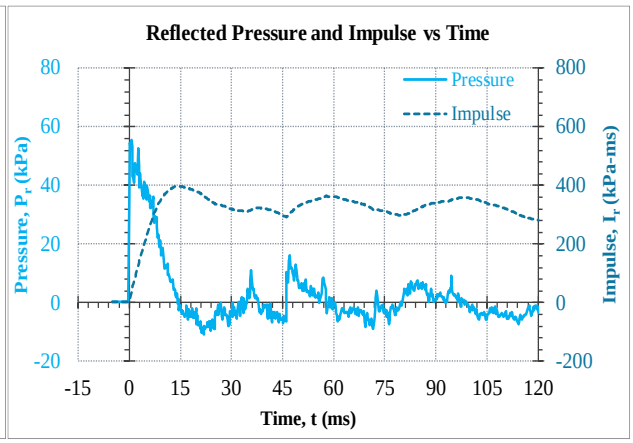

(b)

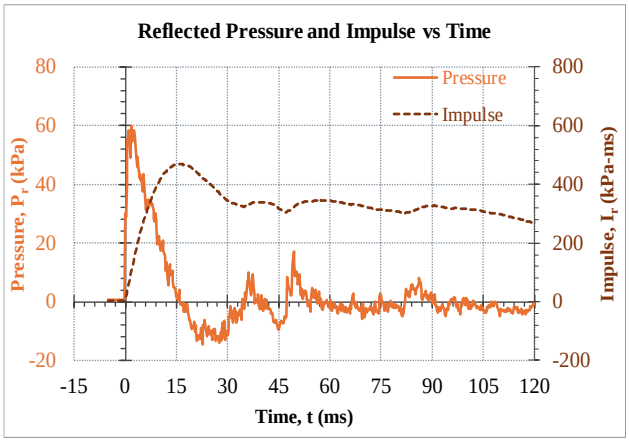

(c)

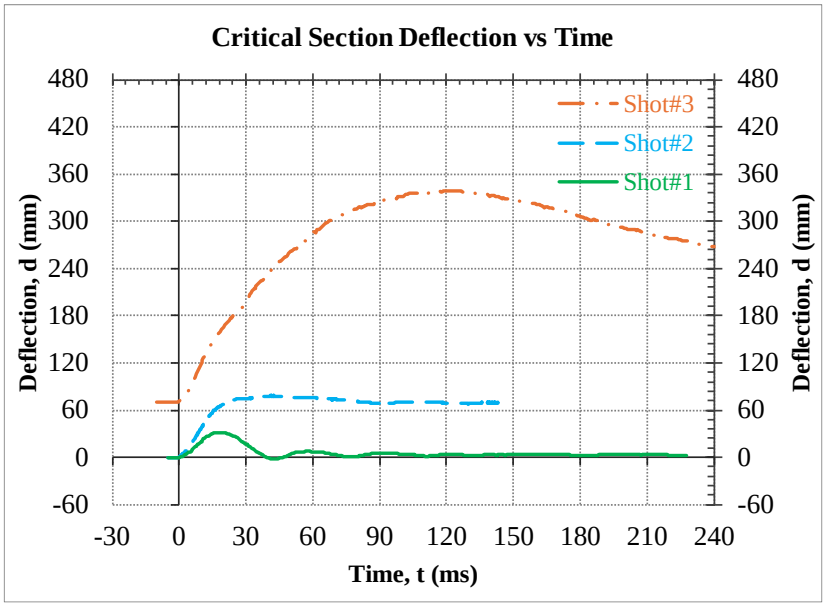

(d)

Figure 4.56 – Reflected pressure, impulse, and displacement time histories of column ECC-2.0%v_f-t20-N2; a) blast shot#1, b) blast shot#2, c) blast shot#3, and d) deflection at mid-height region.

(a) (b)

Figure 4.57 – Photos of column ECC-2.0%v_f-t20-N2 after blast shot#1: a) side view, b) front view.

(a) (b)

Figure 4.58 – Photos of column ECC-2.0%v_f-t20-N2 after blast shot#2; a) side view, b) front view.

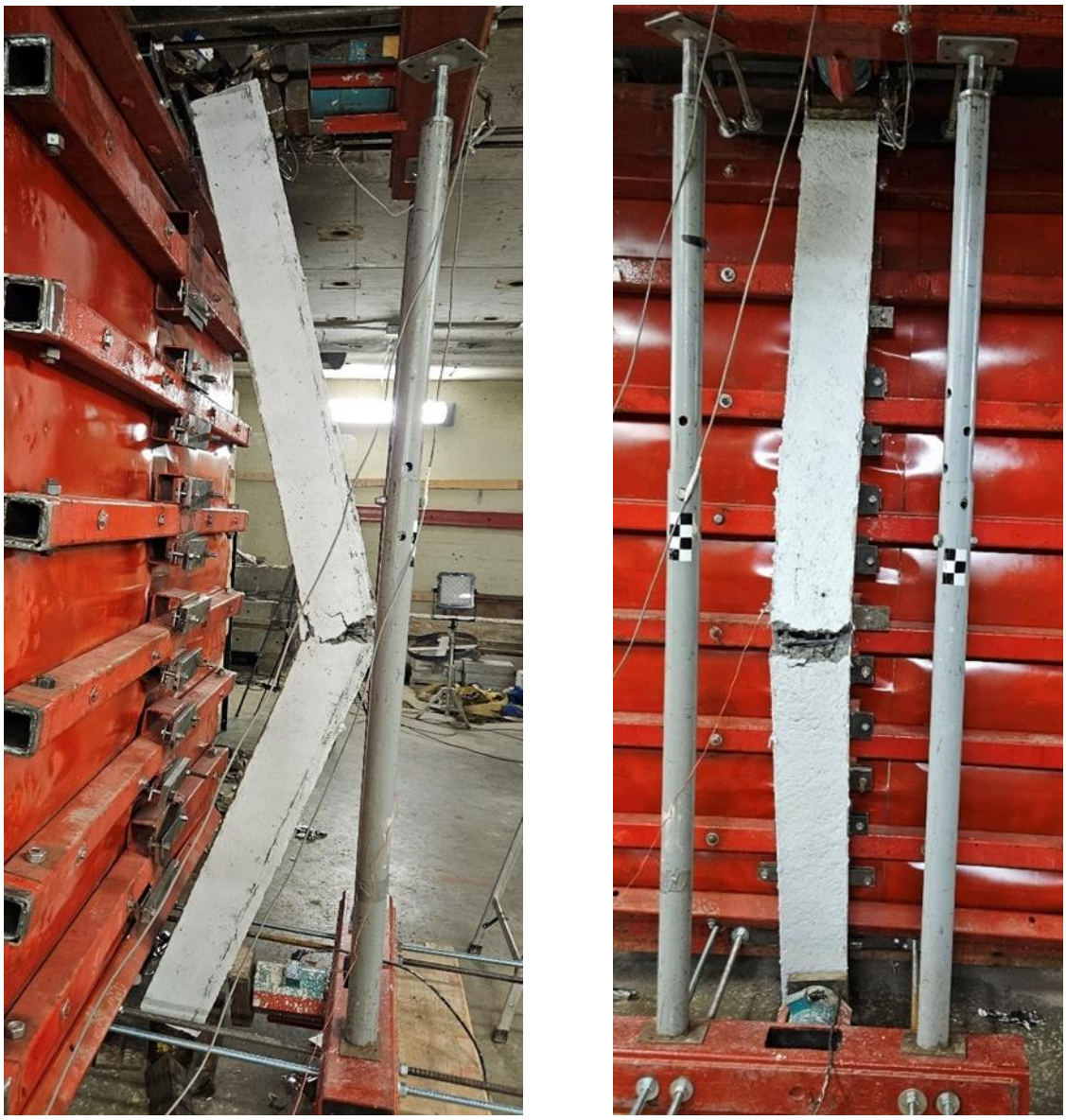

(a) (b)

Figure 4.59 – Photos of column ECC-2.0%v_f-t20-N2 after blast shot#3; a) side view, b) front view

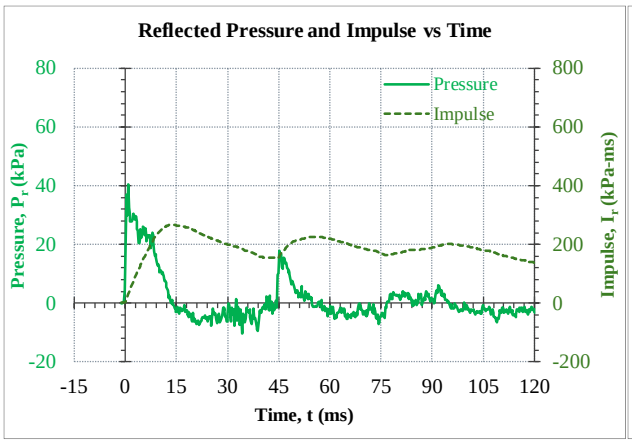

(a)

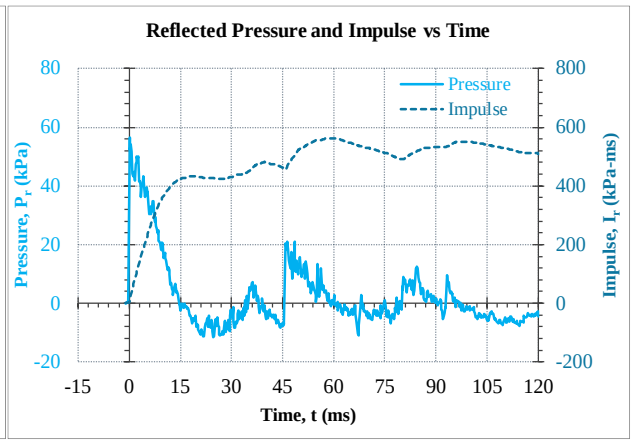

(b)

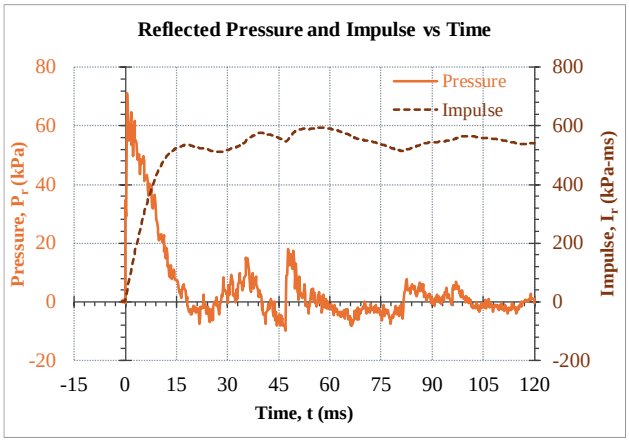

(c)

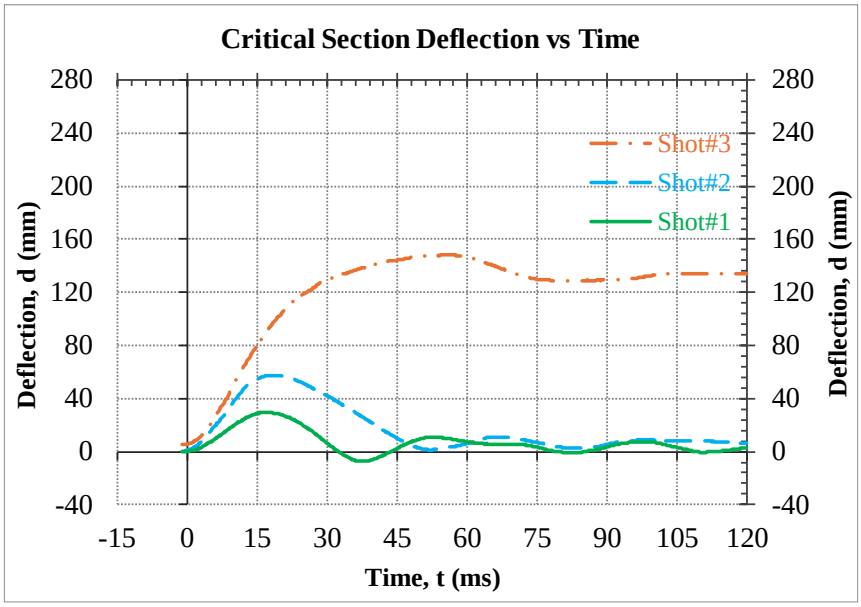

(d)

Figure 4.60 – Reflected pressure, impulse, and displacement time histories of column ECC-1.5%v_f-t25-N2; a) blast shot#1, b) blast shot#2, c) blast shot#3, and d) deflection at mid-height region.

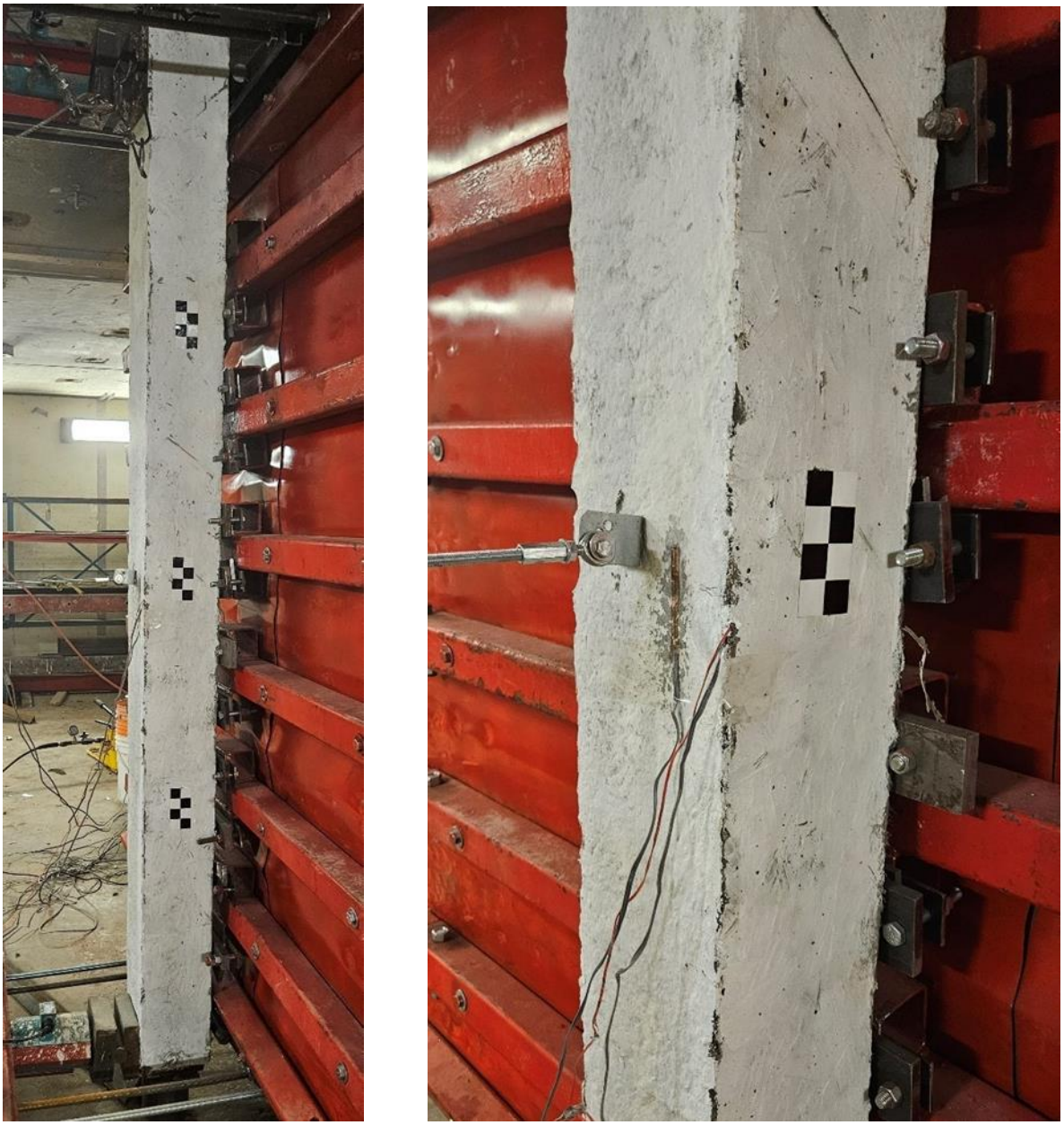

(a) (b)

Figure 4.61 – Photos of column ECC-1.5%v_f-t25-N2 after blast shot#1: a) side view, b) front view.

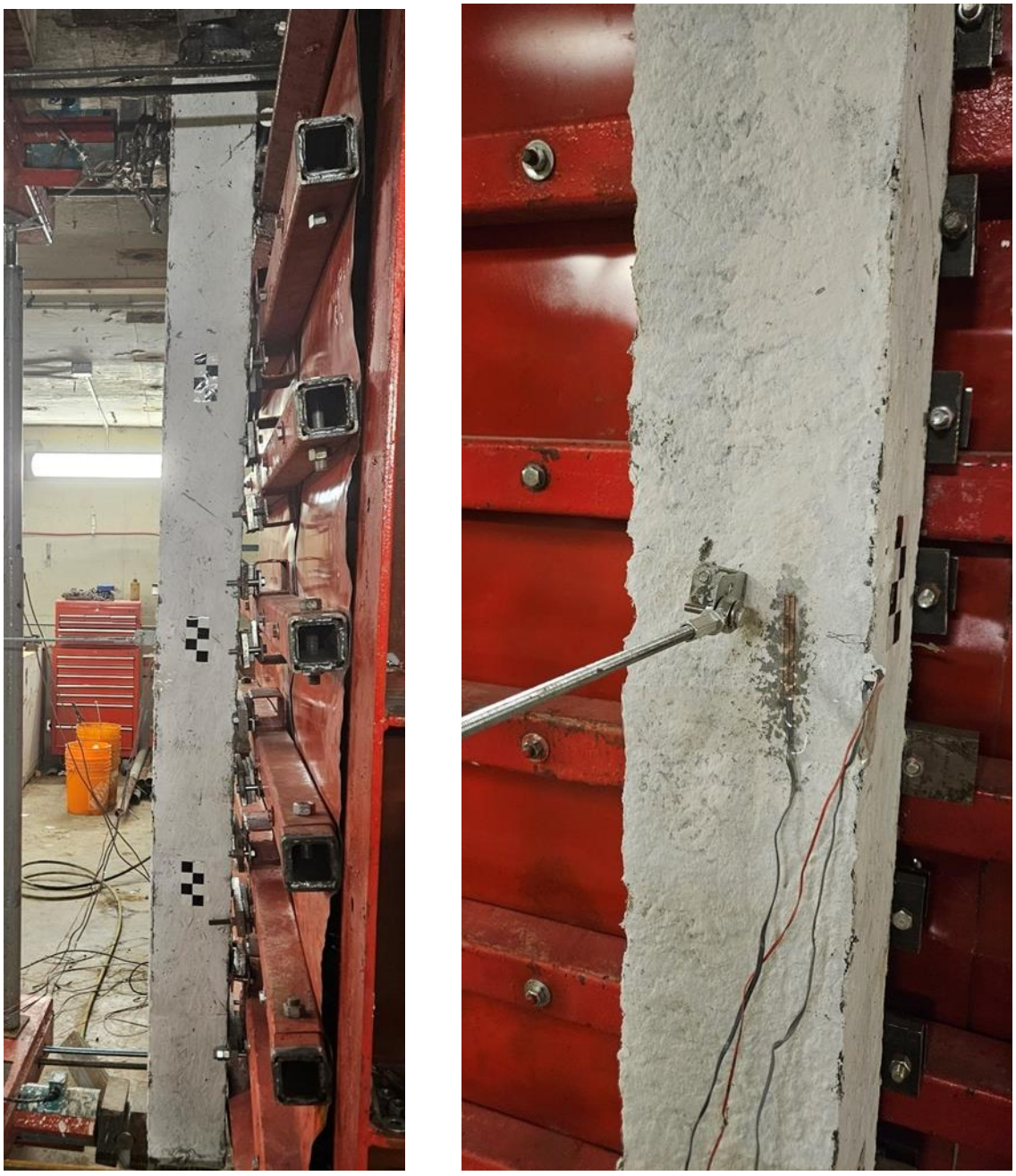

(a) (b)

Figure 4.62 – Photos of column ECC-1.5%v_f-t25-N2 after blast shot#2; a) side view, b) front view.

(a) (b)

Figure 4. 63 – Photos of column ECC-1.5%v_f-t25-N2 after blast shot#3; a) side view, b) front view

Chapter 5. Analysis and Discussion of Experimental Results

This chapter presents the assessment and analysis of the experimental results of column tests reported in Chapter 4. This is done for each of the four categories of columns: reference columns, columns hardened with external post-tensioning, internally post-tensioned columns, and ECC jacketed columns. The assessment of experimental parameters and the analysis of test data are first conducted within each group of columns, followed by the comparisons of columns between the categories.

The test results are compared based on the observed damage levels under similar loading conditions. The effects of each strengthening method, whether hardening of existing columns by providing external reactive forces through external prestressing strands or by providing ECC jackets, as well as the application of internal post-tensioning of new columns, are analyzed by comparing their performances relative to companion reference columns. The level of blast loads that could be sustained (pressure-impulse combinations) by the columns, along with maximum and residual column deflections as well as the maintained level of axial load, are used as quantitative data to assess column performance. For ease of comparison, a detailed data visualization technique is followed by plotting the data in various graphs and charts while also summarizing data in table formats. For better visualization of the combined effect of reflected pressure and impulse, three-dimensional (3D) graphs are generated for each group and each category and presented in figures. The impact of parameters such as the presence of closely spaced ties, compressive strength of concrete, and level of initial prestressing force in external post-tensioning is also displayed in the figures.

Applying the exact same load to each specimen during blast testing is not possible. However, an effort was made to apply blast loads of similar intensities (reflected pressure-impulse combinations) for fair comparisons of test results. A second approach is also adopted to get a better insight into the level of improvement achieved by normalizing blast loads and deflections to those of their companion reference column test results. In the loading protocol of this research, three shots are commonly used to assess elastic behavior, damaged state, and failure/residual capacity. Conducting multiple blast shots has pros and cons. More data can be collected during the experiments if multiple blast shots are applied. However, loading the same samples with back-to-back blast shots also causes some decay in the resistance of columns. This decay affects the stiffness and may have an impact on strength as well. A previous study conducted by a former

PhD student [82] at the University of Ottawa on the effect of multiple shots on columns indicated that the reduction in column resistance relative to a single shot was shown to be small, while following a similar loading protocol employed in current shock tube tests.

5.1 Reference Columns

Three columns were tested from this category: two gravity-designed (no seismic detailing, Ref-N1, and Ref-N2) columns and one seismic/blast designed (closely spaced ties over the entire length, Ref-S) column. The Ref-S column had 45 MPa concrete and a longitudinal duct along its height, designed to account for reduced concrete area when compared with columns internally post-tensioned with double strands (one on the tension side and one on the compression side). The non-seismic columns were tested against different pressure-impulse combinations. They also had slightly different concrete strengths, which were 45 MPa for Ref-N1 and 50 MPa for Ref-N2. Although comparisons of deflection response are made between the reference columns in the following paragraphs, the objective of testing them was to show the effects of primary test parameters included in post-tensioned and ECC jacketed columns relative to these reference columns.

The deflections recorded for Ref-N1 and Ref-S are compared in Figure 5.1 using a 3-dimensional plot (column labels in the figure are shortened as RN-1 and RS for clarity of the figure). The comparison indicates that the column with seismic detailing developed lower deflections. However, the companion column without the seismic detailing was subjected to 12% higher reflected pressure, which would contribute to the 12% higher deflection recorded for this column. It should be noted that the effect of seismic detailing cannot be decisively concluded by this limited comparison. The impact of seismic detailing on blast response was not included in the scope of the current research, and column Ref-S was included in the test matrix for comparison with internally post-tensioned columns, which also had seismic/blast detailing to simulate typical column designs for blast-resistant new construction.

The deflection results of columns Ref-N1 and Ref-N2 are compared in Figure 5.2. Both columns were subjected to almost identical blast loads. The mid-height deflection of Ref-N1 was higher than that of Ref-N2. This difference may be attributed to the slightly higher level of impulse imposed on Ref-N1, but more importantly, the difference can be attributed to the difference in compressive strength. Column Ref-N2 had higher compressive strength than column Ref-N1.

However, once again, this limited data is not intended to draw generalized conclusions on the effect of concrete strength, which was not included in the test program.

5.2 Columns Hardened by External Post-Tensioning

Five columns were hardened by externally post-tensioned strands to provide external resistance to applied blast loads in the first phase of testing (Phase I). These columns consisted of a single-harped, two double-harped, a triple-harped, and a parabolic profile (also referred to as draped in the prestressing industry). During the first shot applied to each column, the columns behaved elastically with no signs of concrete cracking on the tension side or crushing of concrete on the compression side. However, the columns exhibited yielding of the tension reinforcement as indicated by the strain gauges. At a similar blast shot, the reference column (Ref-N1) exhibited significant inelastic deflections while losing its axial load-carrying capacity due to excessive column deflection. Figure 5.3 shows the deflection time histories at the critical section of the reference column and those of the hardened columns resulting from the first shot reflected pressure plotted in the same figure. It can be seen that the hardened column significantly reduced the maximum deflection, resulting in almost zero residual deflection. The reference column could not survive a similar blast load and suffered a severe residual deflection of 55 mm. The result of the triple-harped column is not included in this figure because it was hit with a higher first blast shot that generated higher reflected pressure and impulse. Hence, it experienced higher maximum and residual deflections. However, this does not mean that the triple-harped column exhibited undesirable response because it outperformed the reference column even under a higher load.

The results of hardened column deflection response are compared among them in Figure 5.4 and Figure 5.5, under increased blast loads (shot#2), also shown in the same figures, that caused failure. It is worth mentioning that the deflections plotted in the figures are not necessarily the deflection at mid-height, since in some of the hardened columns, the locations of critical sections shifted from exact mid-height but still occurred within the mid-height region. The shift in the location of the critical section is due to the change in the resultant moment diagram under combined blast loads and the external resistance provided by the externally provided prestressing strands. The effect of restoring force that changed the shape of the moment diagram is illustrated in Chapter 4. It can be revealed from Figure 5.4 that even though there was a noticeable residual deflection, the level of deflection remains at almost half the value recorded for the reference column generated under a lower blast shot intensity (shot#1) shown in Figure 5.3. This was also

reflected in the axial load behavior of the hardened columns, which maintained their level of initially applied axial load after the blast shot under discussion. Comparing the level of deflections, it can be inferred from Figure 5.5 that columns labeled P1-227e-0.09fpu-N1 and DH2-227e-0.16fpu-N1 sustained the lowest residual deflection. In contrast, the column labeled SH-207e-0.15fpu-N1 had the highest residual deflection. This indicates that the parabolic-profile, despite having the lowest post-tensioning force, along with the double-harped column but with higher post-tensioning force, was more effective in restoring the blast-induced deflections.

In the second phase (Phase 2), two hardened columns, a triple-harped and a parabolic profile column, were tested using a different combination of reflected pressure and impulse than the first phase of testing. These columns test represented an explosion at a closer stand-off distance than the first phase testing of columns. Similar to their companion reference column (Ref-N2), both columns were subjected to three incrementally increasing blast shots, experiencing different reflected pressures and impulses at each shot. Figure 5.6 shows the test result of the hardened columns along with their companion reference column under similar blast loads. As can be noticed from the figure, the Ref-N2 was completely damaged, with a maximum deflection of 171 mm and a significant residual deflection of 124 mm. In contrast, the hardened columns could restore and minimize the maximum deflection, resulting in almost zero residual deflection. However, both hardened columns exhibited some localized concrete crushing on the compression side, but no drop was noticed in their axial loads. There were also two small cracks on the tension side of the column P2-227e-0.16fpu-N2, right above the column mid-height. For the TH2-247e-0.15fpu-N2 column, the localized concrete crushing location was between 1/3 and 1/2 of the loading span, and there was no cracking on the tension side.

To get an insight into the behavior of hardened columns (i.e., effectiveness of strand profile) under higher blast loads, the results of the last shot (shot#3 - also called the residual shot) are plotted in Figure 5.7. It can be observed from the figure that both columns experienced significant permanent deformations, resulting in residual deflections of 70 to 120 mm. The column with parabolic profile resulted in a lower residual deflection than the triple-harped column, once again indicating the effectiveness of the parabolic profile, as also observed from the first phase testing (Phase I) of hardened columns. On the other hand, the parabolic profile may be viewed as the less favorite option from an aesthetic perspective, as well as the possibility of an increase in cost due to more material and labor. It is worth mentioning that both hardened columns of this phase

experienced connection failure at end anchorage during the third shot (see Figure 4.31 and Figure 4.42). This indicates that even though the columns were subjected to almost similar impulses compared to the first phase of hardened columns, the higher reflected pressures imposed resulted in higher shear forces in the connecting bolts, the shear strength of which was exceeded. As emphasized in the strengthening procedure described in Chapter 3, proper considerations should be given to the design of end connections.

An essential factor in the design of the test matrix was the level of post-tensioning force in the prestressing strand. It was fixed at a level to meet the tensile and compressive stress limits specified in CSA A23.3 [79]. The two double-harped columns from the first phase were different only in the level of initial prestressing force. Figure 5.8 shows the behavior of both double-harped columns when subjected to a similar blast load. As can be deduced from the plot, the column labeled DH2-207e-0.16fpu-N1 developed less residual deflection compared to DH1-207e-0.13fpu-N1. This indicates that the slight increase in the level of prestressing force from 13% of ultimate capacity to 16% resulted in some improvement in restoring the blast-induced deflection. The effect can be further demonstrated by comparing the change in residual deflections with the applied impulse in Figure 5.9. It also indicates that the column with higher post-tensioning suffered less residual deflection while subjected to a higher impulse. However, this does not mean that the level of initial prestressing can be further increased for improved performance, as it may violate the code limits for extreme compression and tensile stresses. A similar comparison is made between columns of the triple-harped profile in Figure 5.10. As can be seen, the column with a higher level of post-tensioning (TH2-247e-0.15fpu-N2) exhibited less residual deflection even though it was subjected to a higher reflected pressure and impulse. It is worth mentioning that some of the improvement in behavior can also be attributed to the compressive strength of concrete in this column, which was 5 MPa greater than that of column TH1-247e-0.10fpu-N1.

5.3 Posttensioned Columns using Internal Prestressing Strands

Two columns strengthened by conventional post-tensioning using unbonded internal prestressing strands were tested along with their companion reference column. The first column had only one strand with constant eccentricity over the tension side, while the second had two constant eccentricity strands, one on the threat side (compression) and the other on the protected side (tension) of the column with equal eccentricity. Figure 5.11 shows the comparison of deflection

time histories of the post-tensioned columns (PT-SS-035fpu-S and PT-DS-0.40fpu-S) with their companion reference column (Ref-S) during the first blast shot (shot#1). As can be seen in the figure, both the reference column and double-strand column exhibited the same maximum deflection, while the single-strand column had a lower maximum deflection. In addition, the Ref-S column experienced a residual deflection of 13 mm, slightly more than the yield displacement, as evidenced by the tensile cracks and the crushing of concrete observed. However, neither of the post-tensioned columns showed tensile cracking or concrete crushing. The figure shows that the PT-DS-0.40fpu-S with double strands suffered some residual deflection of about 10 mm while the PT-SS-0.35fpu-S with a single strand had no residual deflection.

Figure 5.12 shows the test result of the reference and post-tensioned columns during the second blast shot (shot#2). It can be realized that both post-tensioned columns outperformed the reference column by reducing deflections significantly. The improved behavior of post-tensioned columns is attributed to the reactive moment created by prestressing. To get further understanding of the column behavior, 3-D diagrams of the test results are plotted in Figure 5.13 and Figure 5.14 where they present deflections versus blast loads expressed as the combination of reflected pressures and impulses. In addition, Figure 5.15 shows a bar chart of residual deflection at each shot of the post-tensioned columns and their companion reference column. It can be stated that the post-tensioning significantly enhanced the blast response of columns. It is worth noting that this series of columns represented members of new blast-resistant structures, which were detailed following seismic/blast resistant column requirements, having closely spaced ties for improved confinement and hence deformability. The posttensioning also improved the stiffness and stability of columns during high-displacement demands under blast loads. Improving stability is an important aspect of column survival under combined blast and axial compression, as stability failure may be the governing mode of failure, especially for slender columns.

5.4 Hardened Columns using ECC Jacketing

The displacement time history of an ECC jacketed column (ECC-2.0%v_f-t30-N1) is compared with those of its companion reference column (Ref-N1) and a column hardened by external prestressing strands having a parabolic profile (P1-227e-0.09fpu-N1) in Figure 5.16. The parabolic profile was the column that performed the best in the category of first-phase hardened columns by external post-tensioning. It can be seen from the plot that the jacketed column had the lowest

maximum deflection without any residual deflection. This indicates that the ECC shell significantly enhanced the column behavior under blast loading. In addition, it completely prevented the fragmentation of concrete debris at the location of failure after the third shot. However, it is worth mentioning that the thickness of the ECC shell was such that it resulted in a slightly larger column section with increased strength and stiffness. Because of the favorable response of the ECC jacketed column that was observed, it was decided to test more columns with ECC jackets having less thickness to assess the significance of jacket thickness, while investigating the bond characteristics of thin ECC jackets with the existing concrete core.

Two columns jacketed with either 20 mm or 25 mm ECC thickness, ECC-2.0%v_f-t20-N2 and ECC-1.5%v_f-t25-N2, respectively, were tested in the second phase of ECC tests. Both columns were subjected to three incrementally increasing blast shots. However, during the second shot, the ECC-2.0%v_f-t20-N2 column lost 10% of its initial axial load capacity. Figure 5.17 shows the reference column (Ref-N2) test results and those of ECC jacketed columns (ECC-2.0%v_f-t20-N2 and ECC-1.5%v_f-t25-N2) after the blast shot with a reflected pressure of almost 40 kPa. As can be seen in the figure, both jacketed columns behaved elastically under the blast load, which failed the reference column. This indicates that even a 20 mm ECC shell can improve column resistance during blast loading. However, when the blast load was increased, the column with 20 mm ECC thickness (the least thickness considered) could not survive the higher blast load, as shown in Figure 5.18. The same figure also shows that the second ECC column, which had a 25 mm ECC shell thickness, performed elastically as opposed to the reference column, which collapsed completely.

For further investigation of the ECC jacket effectiveness, column ECC-1.5%v_f-t25-N2 is compared with the triple-harped column (TH2-247e-0.15fpu-N2) from Phase II. Figure 5.19 illustrates displacement time histories of the columns. The figure shows that both columns performed almost equally the same. It can be deduced that ECC-1.5%v_f-t25-N2 could provide a similar improvement as those hardened with external strands, in this case, triple-harped.

Further comparisons of ECC jacketed columns are made in Figure 5.20 to assess the effectiveness of fiber dosage in the mix and the ECC layer thickness. The results show that the effect of increasing ECC thickness is better reflected in reducing residual deflection than in the maximum deflection. ECC-2.0%v_f-t20-N2, with the lowest ECC thickness, showed the least improvement in behavior. ECC-1.5%v_f-t25-N2 had 0.5% less fiber dosage than ECC-2.0%v_f-t20-

N2, but a 5 mm thicker ECC shell, performed better. Although subjected to higher impulse, the column with the lowest maximum and residual deflection was ECC-2.0%v_f-t30-N1 because it had the thickest ECC shell.

5.5 Summary of the Column Experimental Data Analysis

The experimental results obtained from column tests are summarized in this section in a tabular form for comparison. The data were normalized relative to those of the companion reference columns and presented in Table 5.1 to 5.6. The tables also include support rotations computed from experimentally recorded deflections with corresponding damage levels prescribed in CSA S850-2023.

Table 5.1 indicates that the columns hardened either by external strands or ECC jacketing showed reduced deflections and improved performance relative to the reference column. The statistics show that the decrease in maximum deflection ranged between 40% and 80%, and for residual deflection, it was more than 90%. The maximum support rotation of column RN1 was more than three degrees, whereas the residual rotation was more than two degrees. However, the hardened columns experienced less than two degrees of maximum support rotation and almost zero residual rotation, except for the triple-harped column, which developed higher rotations because of the higher pressure applied at the same stage of loading. The qualitative level of damage observed during testing is consistent with the support rotations. According to Cormie et al. [25], concrete is effective in resisting moment until support rotation reaches two degrees. This is consistent with the test observations, which showed that the concrete cover behaved without spalling or crushing at this level of deformation. Hardening the columns reduced support rotations, resulting in elastic behavior within the deformation range of less than two degrees of support rotation.

Table 5.2 shows the test data for the same columns as the previous table but subjected to higher blast loads, except for the reference column, which failed during the first shot (shot#1). It can be seen in the table that some damage was induced on hardened columns when the load was increased, but the level of damage was less than that of the reference column. The loads used in Table 5.2 were higher than the load that resulted in the failure of the reference column by at least 20% in reflected pressure and 40% in reflected impulse. However, the corresponding maximum deflections were about 10% less than that of the reference column. The residual deflections were

approximately 20% to 70% less than that of the reference column. The exception was the ECC jacketed column (E30), which exhibited 46% less maximum deflection and 96% less residual deflection than those of the reference column. The support rotation reported in the same table shows that the hardened columns, except the ECC jacketed column, exhibited a maximum support rotation in excess of two degrees. Assessment of qualitative damage observed during the tests, indicating concrete cracking and crushing in the critical mid-height region, also suggests that the columns developed higher deflections and higher support rotations. The ECC jacketed column with the lowest support rotation at maximum deflections did not exhibit any concrete cracking or crushing.

The test results summarized in the above tables are also plotted in Figure 5.21 and Figure 5.22 as 3-D graphs and bar charts for further insight into the hardened column performance. The figures show that all the hardened columns outperformed their companion reference column, suggesting that the proposed hardening techniques can significantly reduce the level of damage and increase the blast resistance of columns. As mentioned in Section 5.2, the triple-harped column deflection results from its first shot (shot#1) were not included in Figure 5.3. However, it is included in Figure 5.21 (TH1), and if the higher blast load is considered, then it can be assumed that the triple-harped column will fall at the level of a parabolic (P1) or double-harped (DH2) column in terms of its resistance to blast loading. This assumption is further consolidated in the next paragraph, where another triple-harped column behavior subject to a different combination of reflected pressure and impulse is discussed.

The results of the second phase (phase II) of hardened columns are summarized in Table 5.3. The hardened columns were subjected to blast loading similar to their companion reference column. The table shows that the maximum deflection decreased by 24% to 45%, and the residual deflection decreased by 88% to 100% due to hardening. The data for support rotations in Table 5.3 show that the reference column had a maximum rotation of 2 degrees while the hardened columns developed less than 2 degrees.

Table 5.4 includes test data for higher blast loads for the columns listed in the previous table. It can be concluded that the improvement attributed to the proposed hardening methods becomes more pronounced under higher loads. In this case, the decrease in maximum deflection associated with hardening was more than 50%. In residual deflections, the reduction was more than 90%,

except for column E20, which had the least thickness of the ECC shell and experienced less improvement. The table also shows that column RN2 had a significant support rotation of more than eight degrees, and column E20 exhibited a support rotation of more than three degrees. Both of these columns failed during this level of blast loading, resulting in the loss of their axial load-carrying capacity. For further visualization of column behavior, the test results are plotted in a 3-D graph in Figure 5.23 and Figure 5.24 and in the form of bar charts in Figure 5.25. It can be inferred from these figures that the hardened columns once again outperformed the reference column when subjected to a different combination of reflected pressure and impulse.

The data obtained from testing internally post-tensioned columns are tabulated in Table 5.5 and Table 5.6. The tables show the improvements achieved from internal post-tensioning of columns. It can be inferred from Table 5.5 that both post-tensioned columns had less residual deflection than their companion reference column, even though they were subjected to 12% higher reflected pressure. However, the decrease in maximum deflection was significant in column SS because of the initially introduced negative curvature to the column due to the post-tensioning applied on the protected side only. When double post-tensioning strands were used, the initially counteracting effects of the two strands did not result in a noticeable reduction in maximum deflection at this level of blast load, relative to the reference column. When the qualitative assessment was coupled with the statistics of residual deflections (23% decrease), an enhancement in column response can be noticed. Column SS developed a 30% reduction in maximum deflection (43% less support rotation) and an 85% reduction in residual deflection.

Table 5.6 shows the effect of the more intense second shot (shot#2). It can be seen that, despite being subjected to a similar load during the second shot, the decrease in maximum deflection of post-tensioned columns was 44% for column SS and 51% for column DS, with more than 50% reduction in the residual deflections. The support rotation data shows that post-tensioning reduced the maximum support rotation by almost one-half.

Table 5.1 – Comparisons of hardened and reference columns of Phase I tests using normalized blast loads under Shot#1.

Short name	P_r (kPa)	I_r (kPa-ms)	d_{max} (mm)	d_{rs} (mm)	Normalized P_r	Normalized I_r	% of decrease in d_{max}	% of the decline in d_{rs}	θ_{max}	θ_{rs}	Damage level	LOP*
RN1	35	303	66	55	1.00	1.00	0.0	0.0	3.15	2.62	Heavy	VL
SH	32	308	30	3	0.91	1.02	54.5	94.5	1.43	0.14	Superficial	M/H
DH1	33	310	35	0	0.94	1.02	47.0	100.0	1.67	0.00	Superficial	M/H
DH2	33	335	41	4	0.94	1.11	37.9	92.7	1.96	0.19	Superficial	M/H
TH1	40	361	57	13	1.14	1.19	13.6	76.4	2.72	0.62	Superficial	M/H
P1	32	301	40	0	0.91	0.99	39.4	100.0	1.91	0.00	Superficial	M/H
E30	32	315	13	0	0.91	1.04	80.3	100.0	0.62	0.00	Superficial	M/H

*Lop = Level of Protection, VL = very low, M = Medium, H = High, as per Table 4.1 of CSA S850-17 [83]

Table 5.2 – Comparisons of hardened and reference columns of Phase I tests using normalized loads under blast shot that caused damage.

Short name	P_r (kPa)	I_r (kPa-ms)	d_{max} (mm)	d_{rs} (mm)	Normalized P_r	Normalized I_r	% of d_{max} decrease	% of d_{rs} decrease	θ_{max}	θ_{rs}	Damage level	LOP*
RN1	35	303	66	55	1.00	1.00	0.0	0.0	3.15	2.62	Heavy	VL
SH	45	420	60	45	1.29	1.39	9.1	18.2	2.86	2.15	Moderate	L
DH1	43	418	59	32	1.23	1.38	10.6	41.8	2.81	1.53	Moderate	L
DH2	42	435	62	23	1.20	1.44	6.1	58.2	2.96	1.10	Moderate	L
TH1	40	435	57	13	1.14	1.44	13.6	76.4	2.72	0.62	Superficial	M/H
P1	46	440	60	18	1.31	1.45	9.1	67.3	2.86	0.86	Moderate	L
E30	47	441	36	2	1.34	1.46	45.5	96.4	1.72	0.10	Superficial	M/H

*Lop = Level of Protection, VL = very low, L = Low, M = Medium, H = High, and NA = Not available as per Table 4.1 of CSA S850-17 [83]

Table 5.3 – Comparison of hardened and reference columns of Phase II tests using normalized loads under blast shot that didn't cause any damage

Short name	P_r (kPa)	I_r (kPa-ms)	d_{max} (mm)	d_{rs} (mm)	Normalized P_r	Normalized I_r	% of decrease in d_{max}	% of the decline in d_{rs}	θ_{max}	θ_{rs}	Damage level	LOP*
RN2	37	290	42	25	1.00	1.00	0.0	0.0	2.00	1.19	Moderate	L
TH2	36	278	23	0	0.97	0.96	45.2	100.0	1.10	0.00	Superficial	M/H
P2	37	292	23	2	1.00	1.01	45.2	92.0	1.10	0.10	Superficial	M/H
E20	39	272	32	3	1.05	0.94	23.8	88.0	1.53	0.14	Superficial	M/H
E25	38	266	30	0	1.03	0.92	28.6	100.0	1.43	0.00	Superficial	M/H

*Lop = Level of Protection, L = Low, M = Medium, H = High, as per Table 4.1 of CSA S850-17 [83]

Table 5.4 – Comparison of hardened and reference columns of Phase II tests using normalized loads under blast shot that caused damage.

Short name	P_r (kPa)	I_r (kPa-ms)	d_{max_acm} (mm)	d_{rs_acm} (mm)	Normalized P_r	Normalized I_r	% of decrease in d_{max}	% of the decrease in d_{rs}	θ_{max_acm}	θ_{rs_acm}	Damage level	LOP*
RN2	55	384	171	124	1.00	1.00	0.0	0.0	8.11	5.90	Hazardous	NA
TH2	58	413	37	2	1.05	1.08	78.4	98.4	1.77	0.10	Moderate	L
P2	60	450	44	8	1.09	1.17	74.3	93.5	2.10	0.38	Moderate	L
E20	54	394	81	73	0.98	1.03	52.6	41.1	3.86	3.48	Heavy	VL
E25	56	410	57	6	1.02	1.07	66.7	95.2	2.72	0.29	Superficial	M/H

*Lop = Level of Protection, VL = very low, L = Low, M = Medium, H = High, and NA = Not available as per Table 4.1 of CSA S850-17 [83]

Table 5.5 – Comparison of post-tensioned and reference columns using normalized blast loads under Shot#1.

Short name	P_r (kPa)	I_r (kPa-ms)	d_{max} (mm)	d_{rs} (mm)	Normalized P_r	Normalized I_r	% of decrease in d_{max}	% of the decline in d_{rs}	θ_{max}	θ_{rs}	Damage level	LOP*
RS	26	272	37	13	1.00	1.00	0.0	0.0	1.77	0.62	Moderate	L
SS	29	268	26	2	1.12	0.99	29.7	84.6	1.24	0.10	Superficial	M/H
DS	29	267	37	10	1.12	0.98	0.0	23.1	1.77	0.48	Superficial	M/H

*Lop = Level of Protection, L = Low, M = Medium, H = High, as per Table 4.1 of CSA S850-17 [83]

Table 5.6 – Comparison of post-tensioned and reference columns using normalized loads under blast shot that caused damage.

Short name	P_r (kPa)	I_r (kPa-ms)	d_{max_acm} (mm)	d_{rs_acm} (mm)	Normalized P_r	Normalized I_r	% of decrease in d_{max}	% of the decrease in d_{rs}	θ_{max_acm}	θ_{rs_acm}	Damage level	LOP*
RS	43	415	179	153	1.00	1.00	0.0	0.0	8.48	7.27	Hazardous	NA
SS	44	415	87	54	1.02	1.00	51.4	64.7	4.15	2.58	Heavy	VL
DS	44	407	100	70	1.02	0.98	44.1	54.2	4.76	3.34	Heavy	VL

*Lop = Level of Protection, L = Low, M = Medium, H = High, as per Table 4.1 of CSA S850-17 [83]

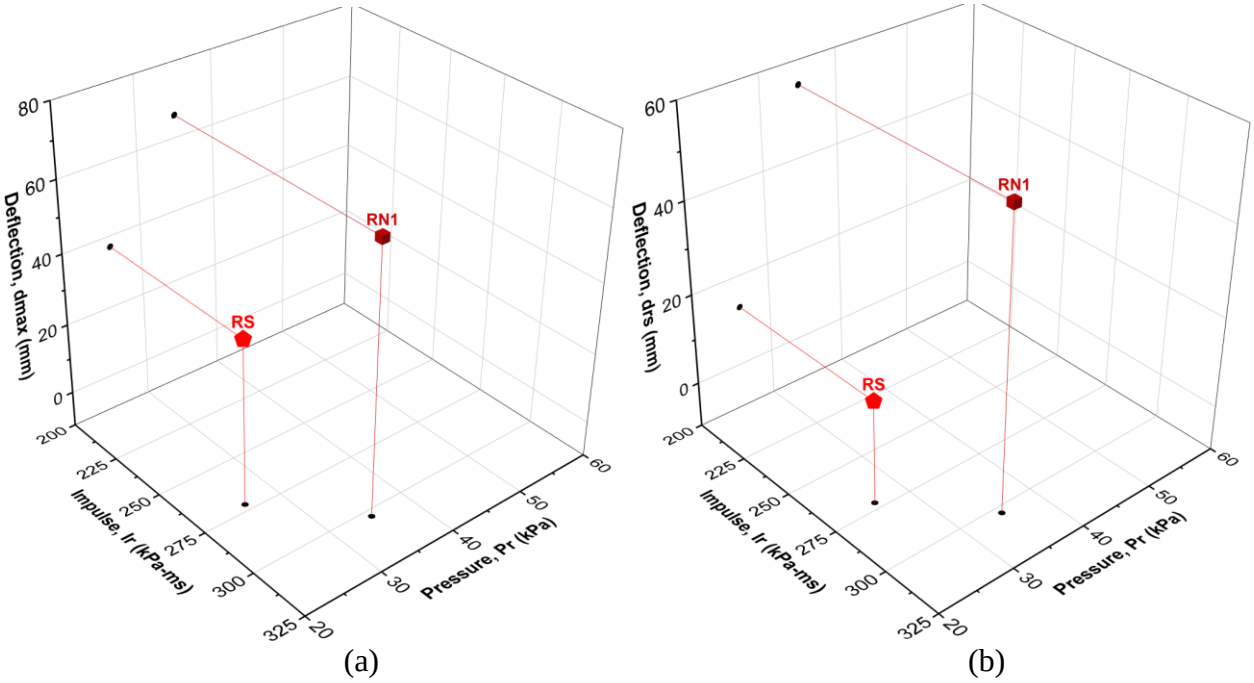

Figure 5.1 – Column deflections for Ref-N1 (RN1) and Ref-S (RS), a) maximum deflection, and b) residual deflection.

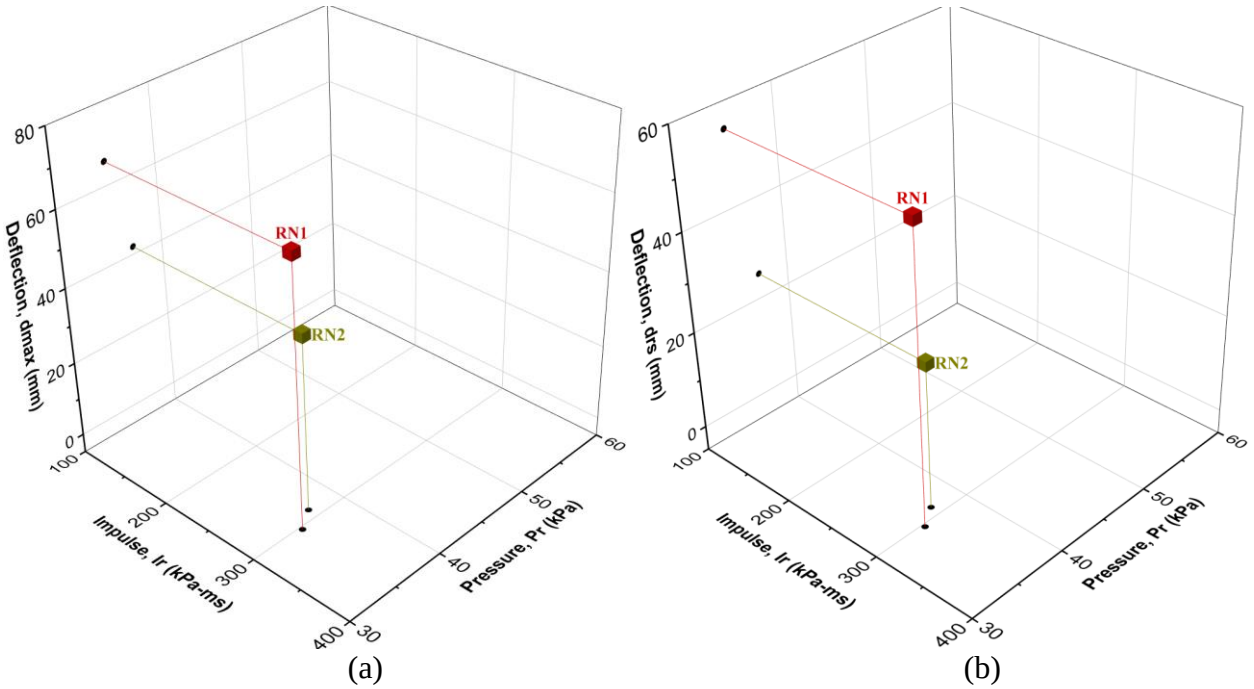

Figure 5.2 – Column deflections of Ref-N1(RN1) and Ref-N2 (RN2). a) maximum deflection, and b) residual deflection.

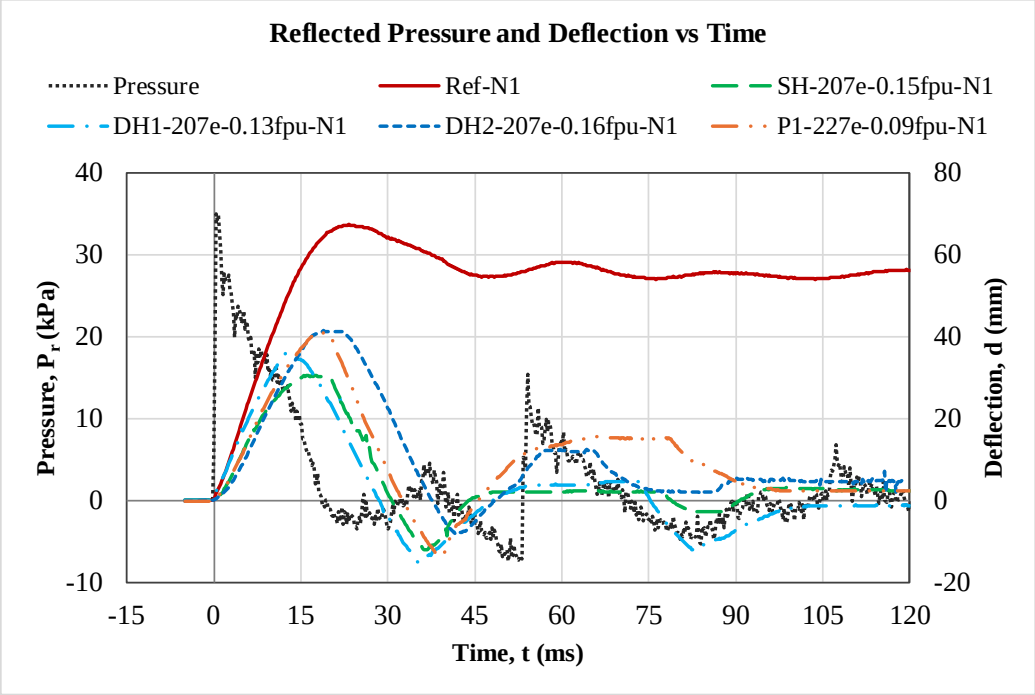

Figure 5.3 – Blast-load response of hardened columns versus companion reference column.

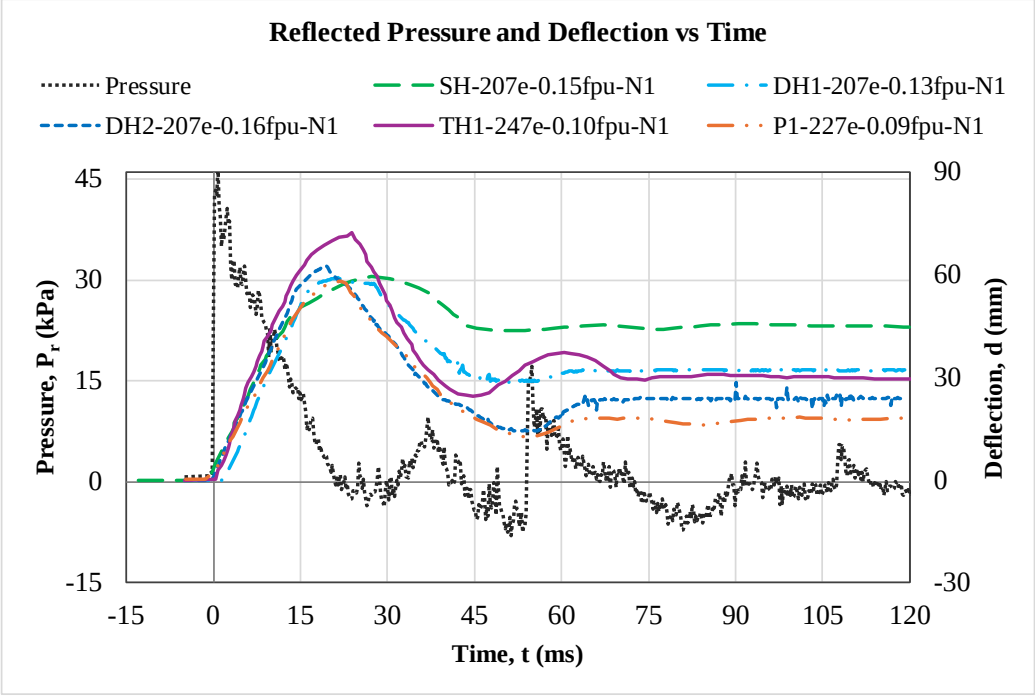

Figure 5.4 – Response of hardened columns subjected to a similar blast load.

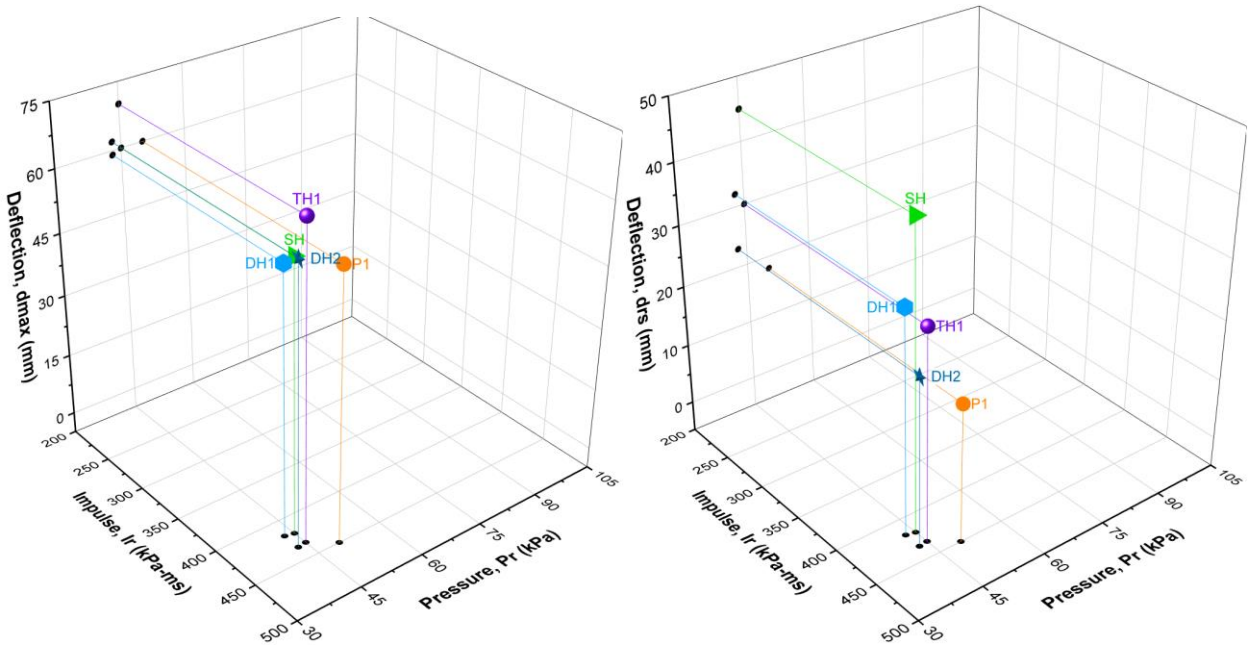

(a) (b)

Figure 5.5 – Column deflections of hardened columns from Phase I. a) maximum deflection, and b) residual deflection.

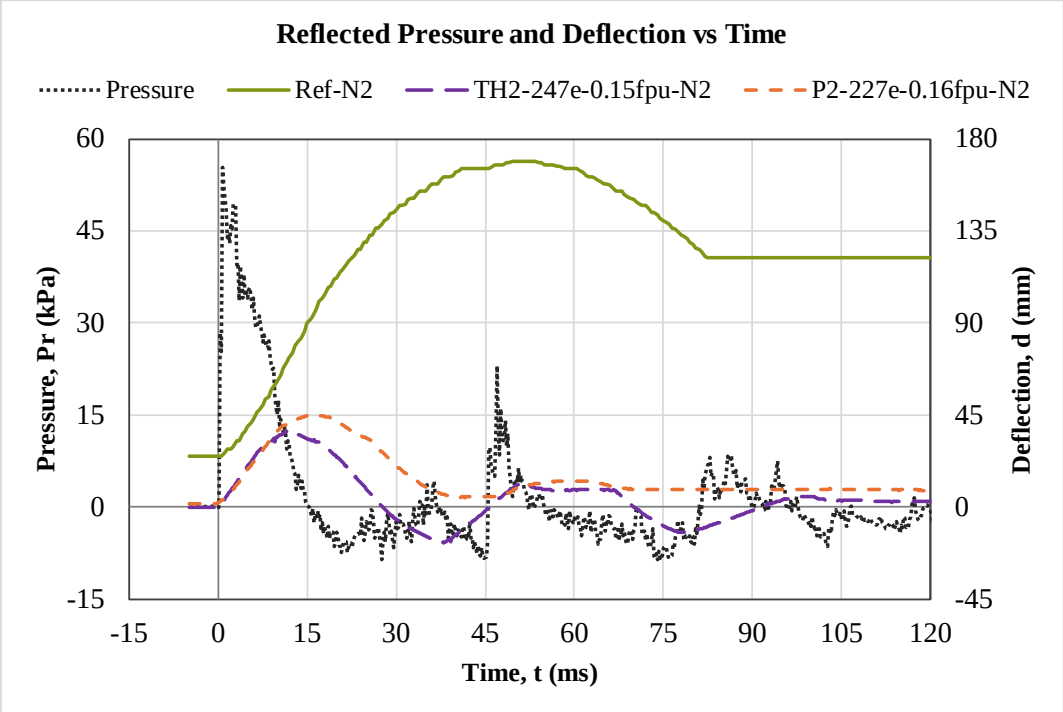

Figure 5.6 – Blast-load response of hardened columns from Phase II with companion reference column subjected to similar blast loads.

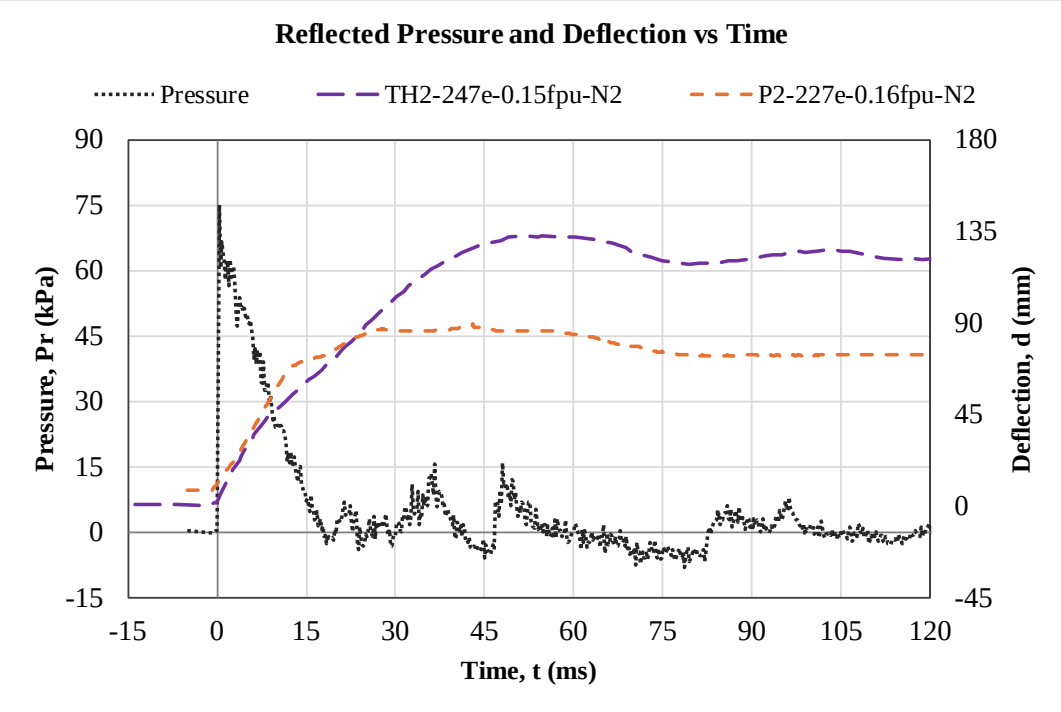

Figure 5.7 – Blast-load response of hardened columns from Phase II testing.

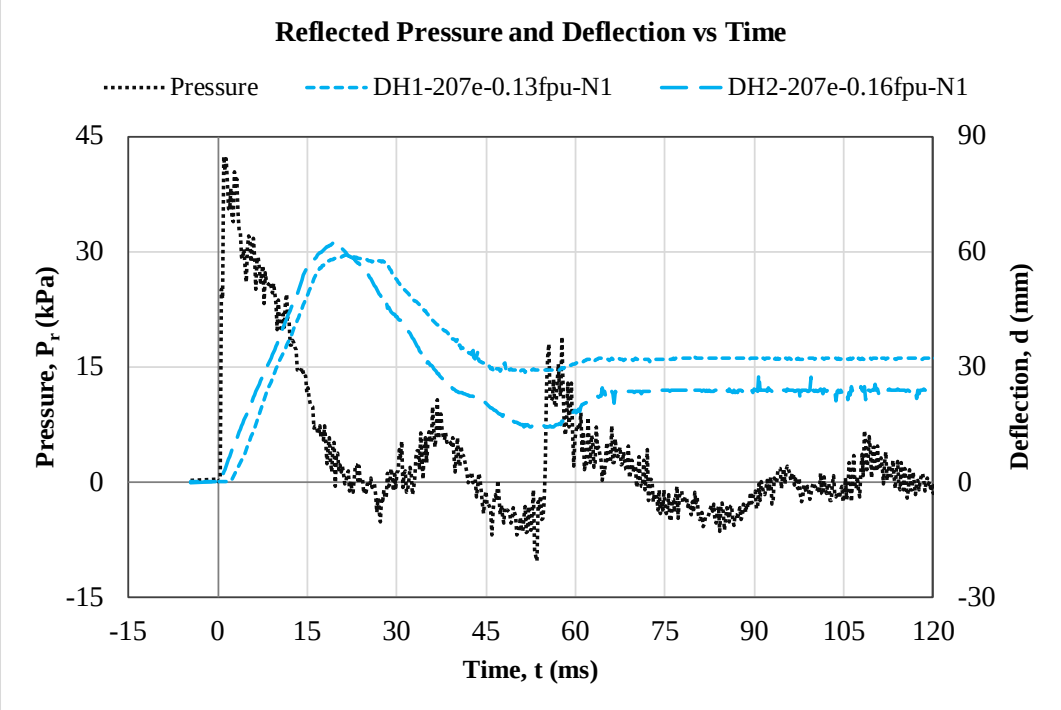

Figure 5.8 – Blast-load response of double-harped columns considering the effect of the level of initial prestressing force.

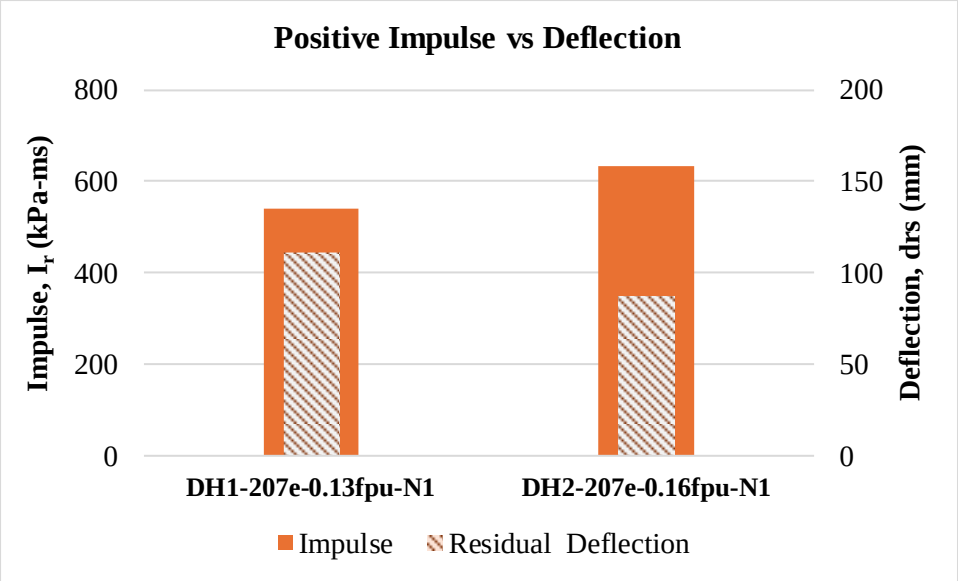

Figure 5.9- Effect of the level of initial prestressing force on blast-load response of double-harped columns.

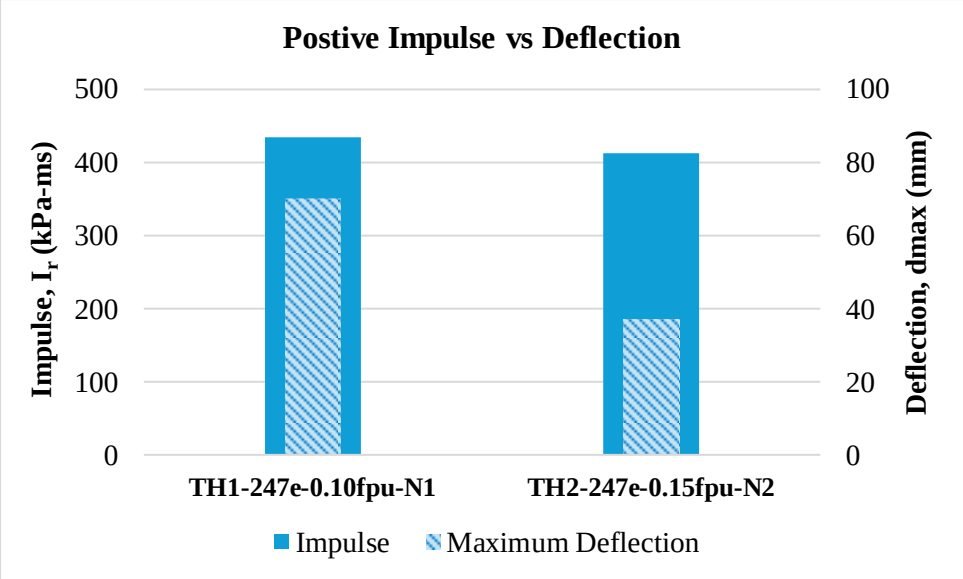

Figure 5.10 - Effect of the level of initial prestressing force on blast-load response of triple-harped columns..

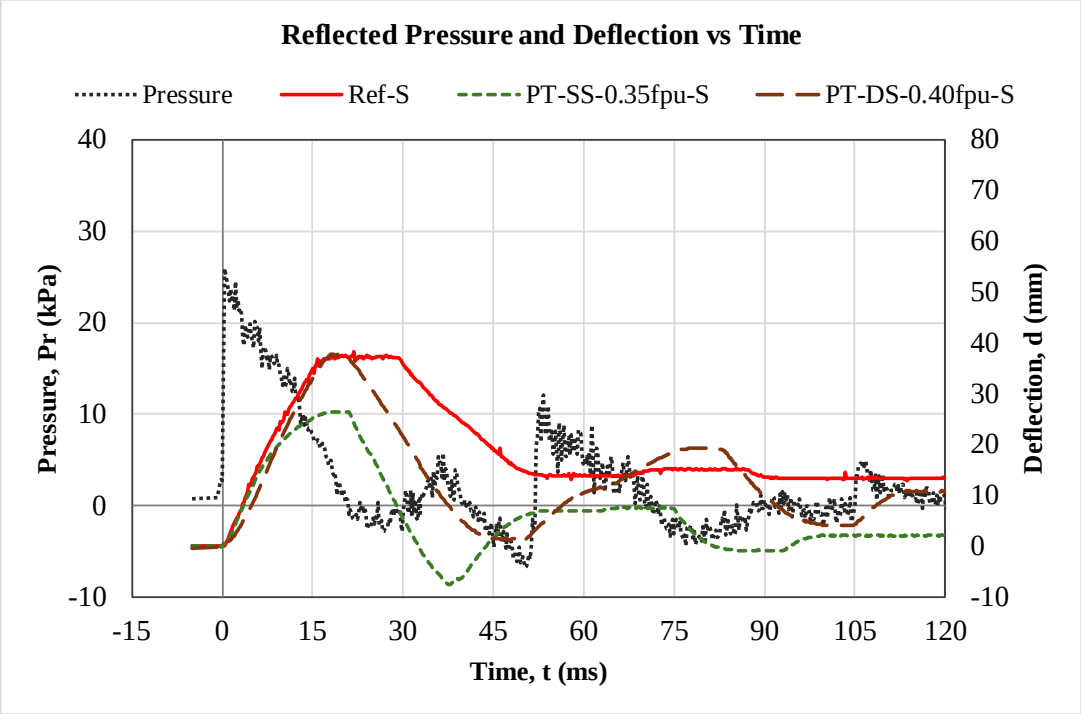

Figure 5.11 – Blast-load response of post-tensioned columns with their companion reference column when subjected to a reflected pressure of 27 kPa.

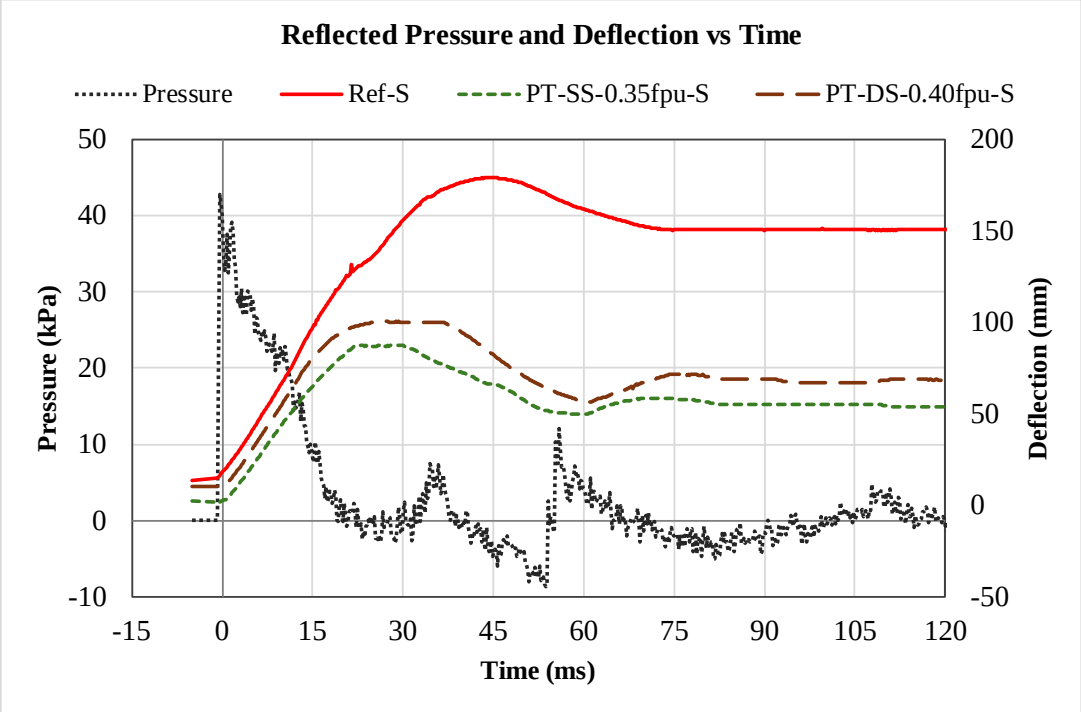

Figure 5.12 – Blast-load response of post-tensioned columns with their companion reference column when subjected to a reflected pressure of around 40 kPa.

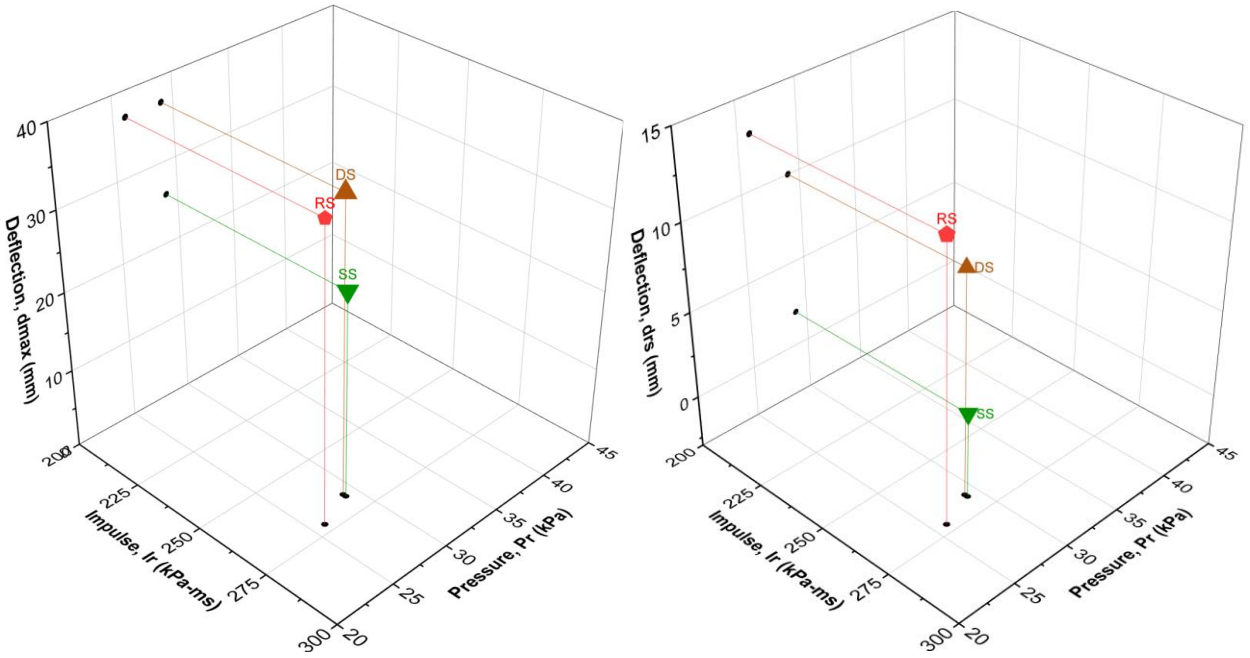

(a) (b)

Figure 5.13 – Mid-height deflections of post-tensioned columns with their companion reference column during the first blast shot: a) maximum mid-height deflection, and b) residual mid-height deflection.

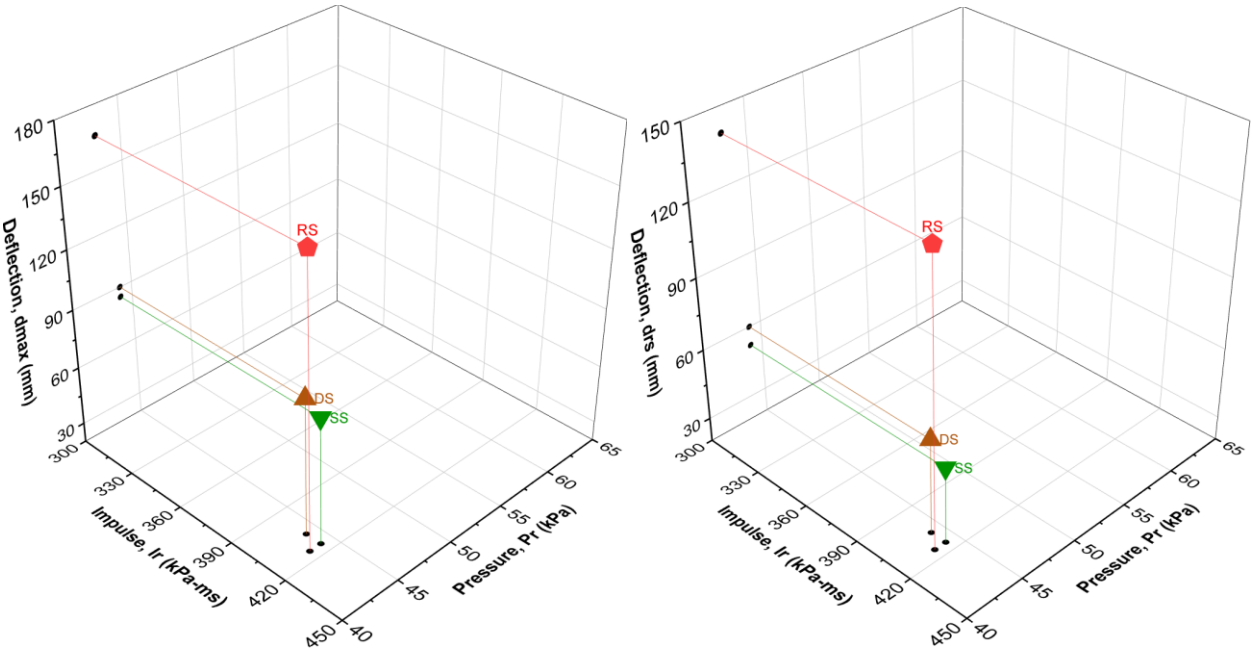

(a) (b)

Figure 5.14 – Mid-height deflections of post-tensioned columns with their companion reference column during the second blast shot: a) maximum mid-height deflection, and b) residual mid-height deflection.

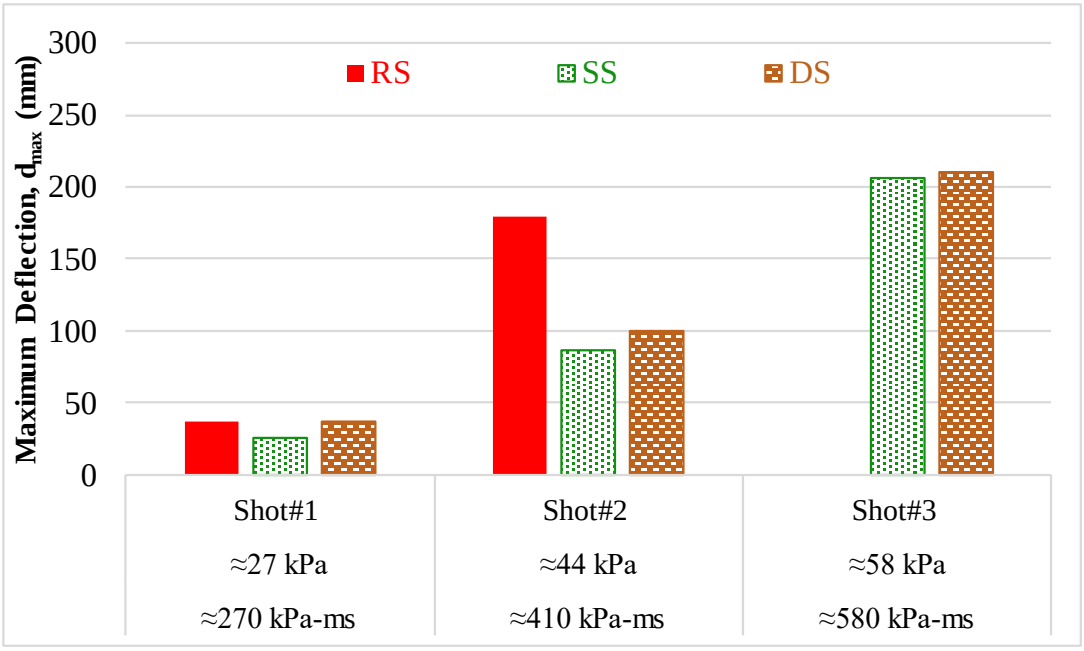

(a)

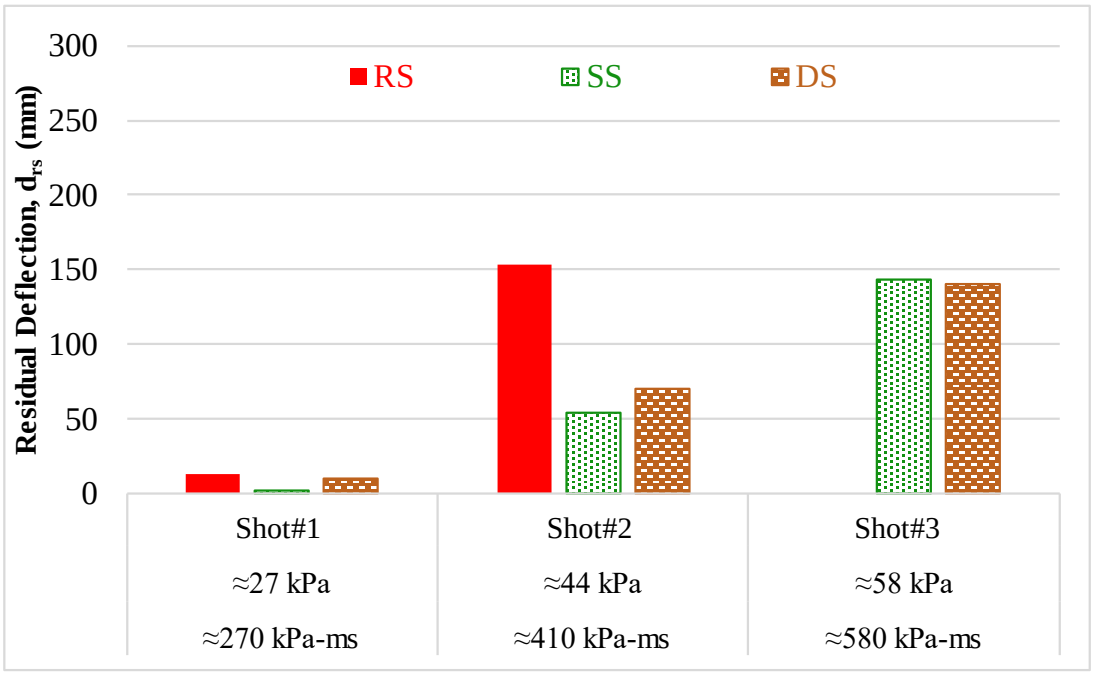

(b)

Figure 5.15 – Test results of post-tensioned columns: a) maximum deflection at mid-height region, and b) residual deflection at mid-height region.

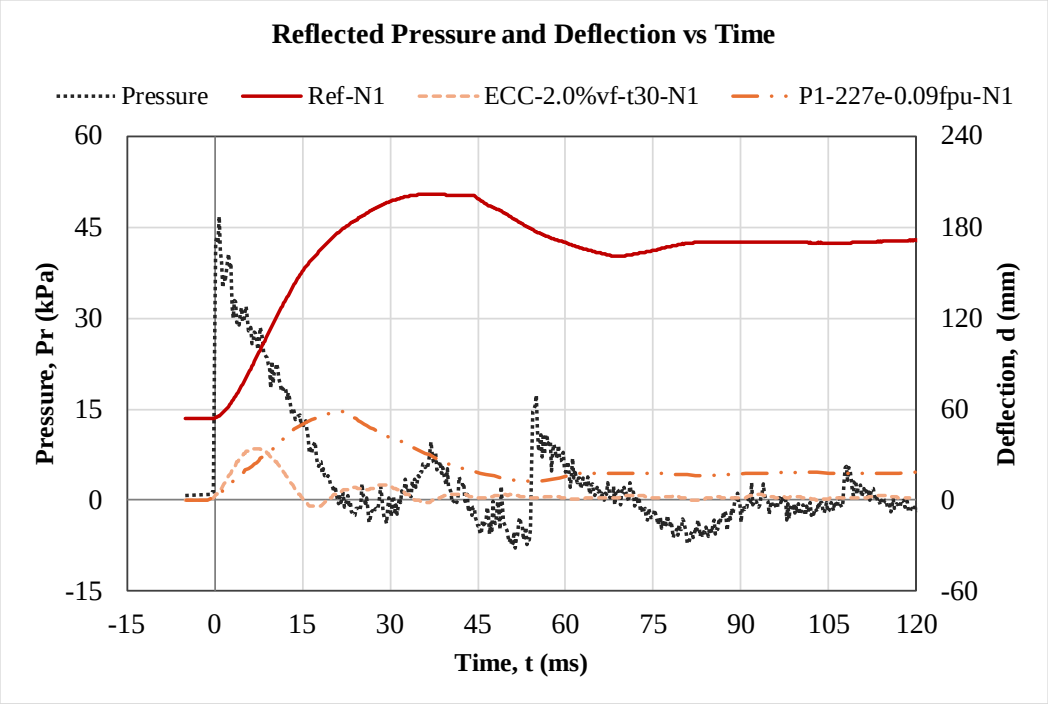

Figure 5.16 – Blast-load response of hardened columns together with their companion reference column when subjected to a reflected pressure of 45 kPa.

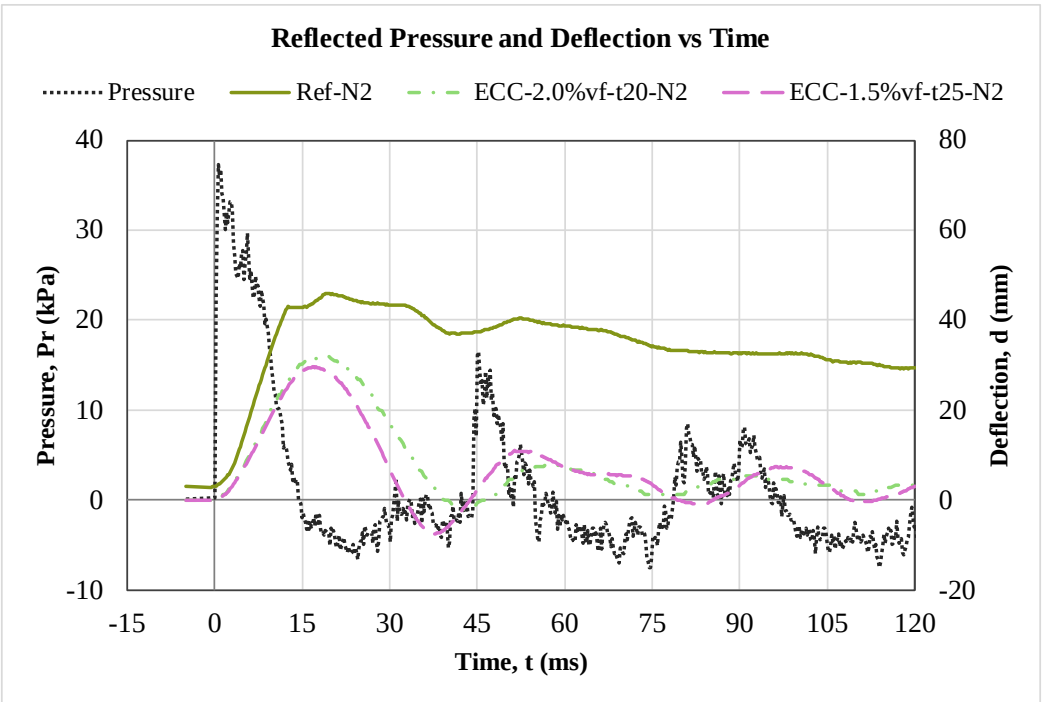

Figure 5.17 – Blast-load response of hardened columns by ECC jacketing from Phase II together with their companion reference column when subjected to a a reflected pressure of 37 kPa.

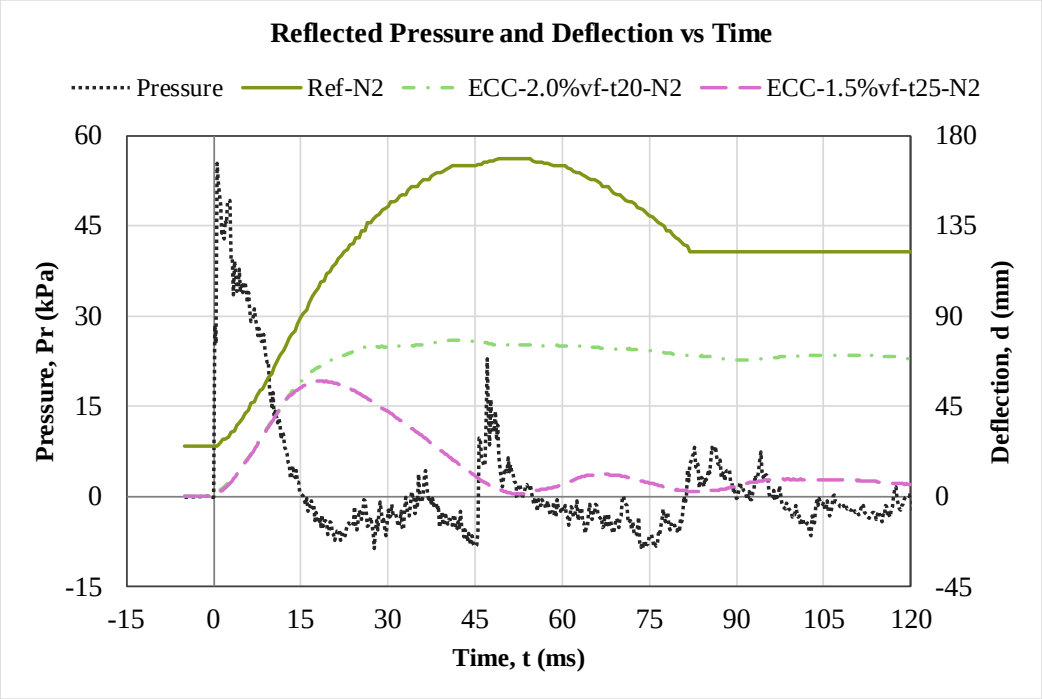

Figure 5.18 – Blast-load response of hardened columns by ECC jacketing from Phase II together with their companion reference column when subjected to a reflected pressure of 57 kPa.

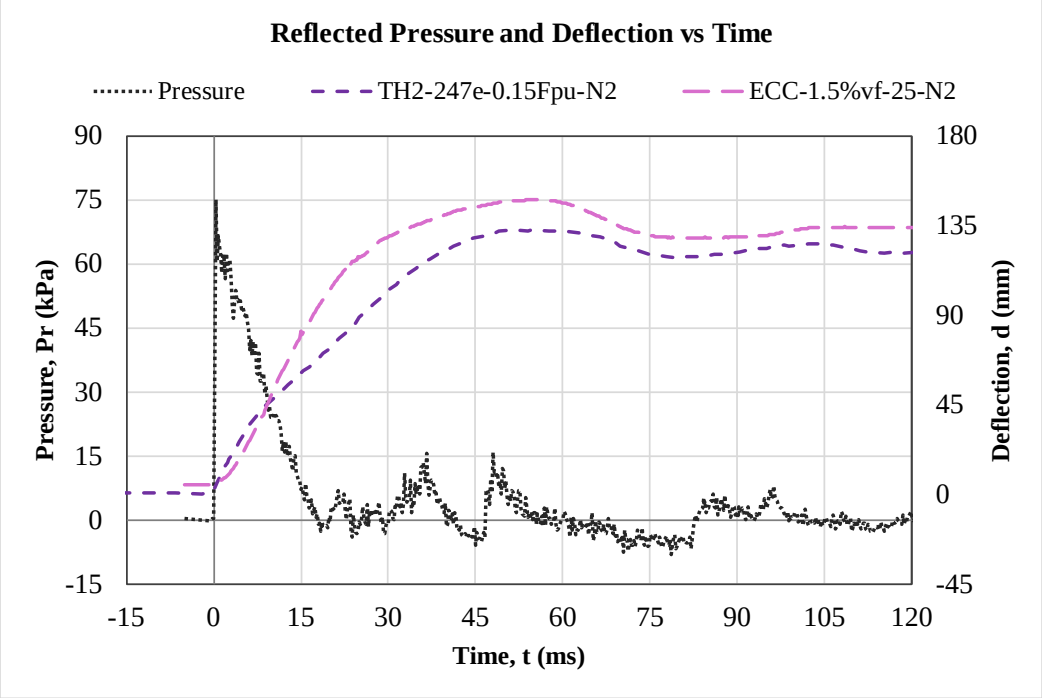

Figure 5.19 – Blast-load response of hardened columns when subjected to a reflected pressure of 75 kPa.

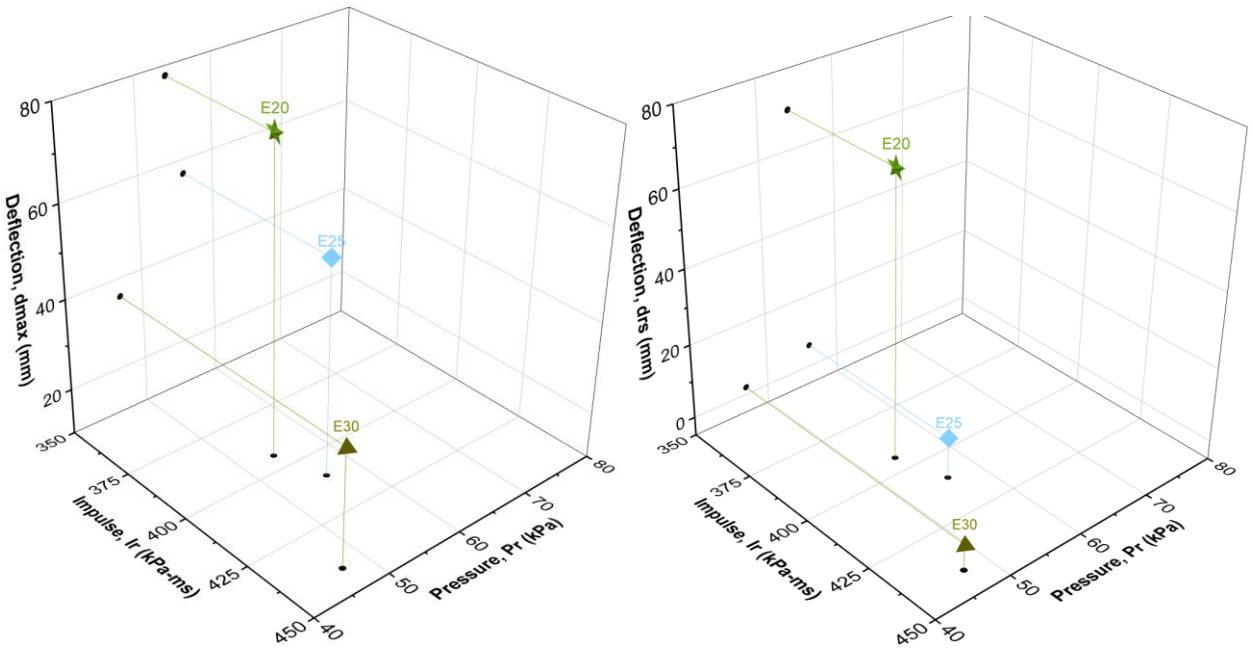

(a) (b)

Figure 5.20 – Column deflections during 2nd blast shot of hardened columns by ECC jacketing: a) maximum deflection at mid-height, and b) residual deflection at mid-height.

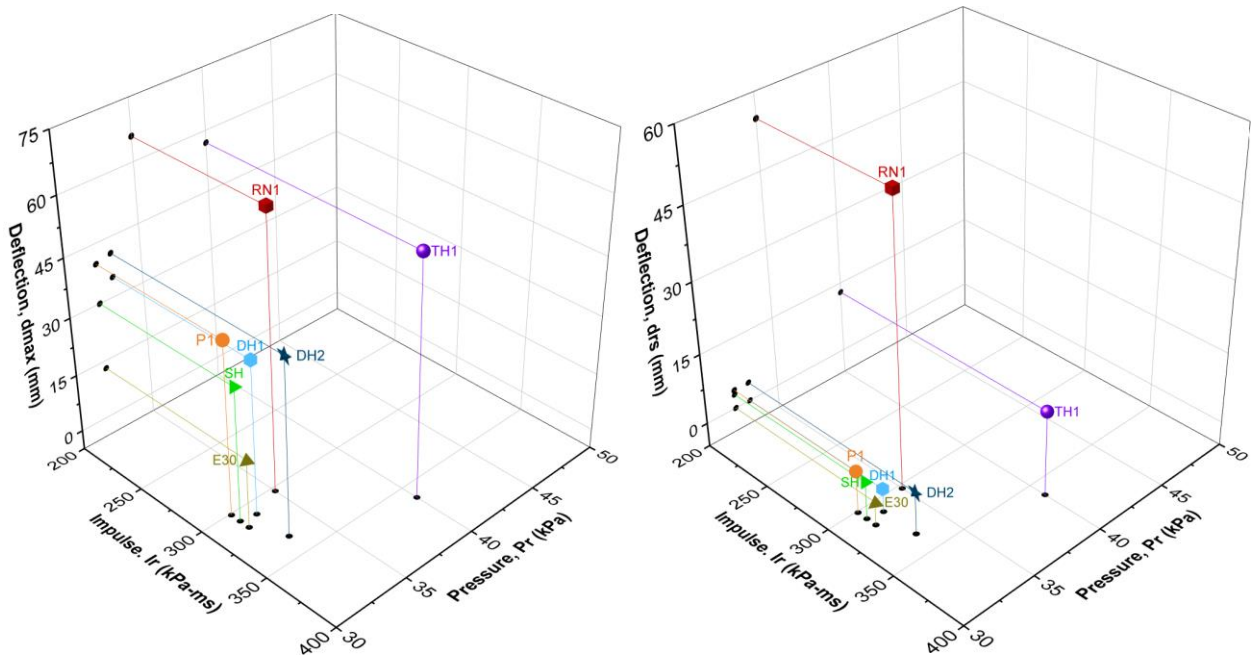

(a) (b)

Figure 5.21 – Column deflections from Phase I of testing: a) maximum deflection at mid-height region, and b) residual deflection at mid-height region.

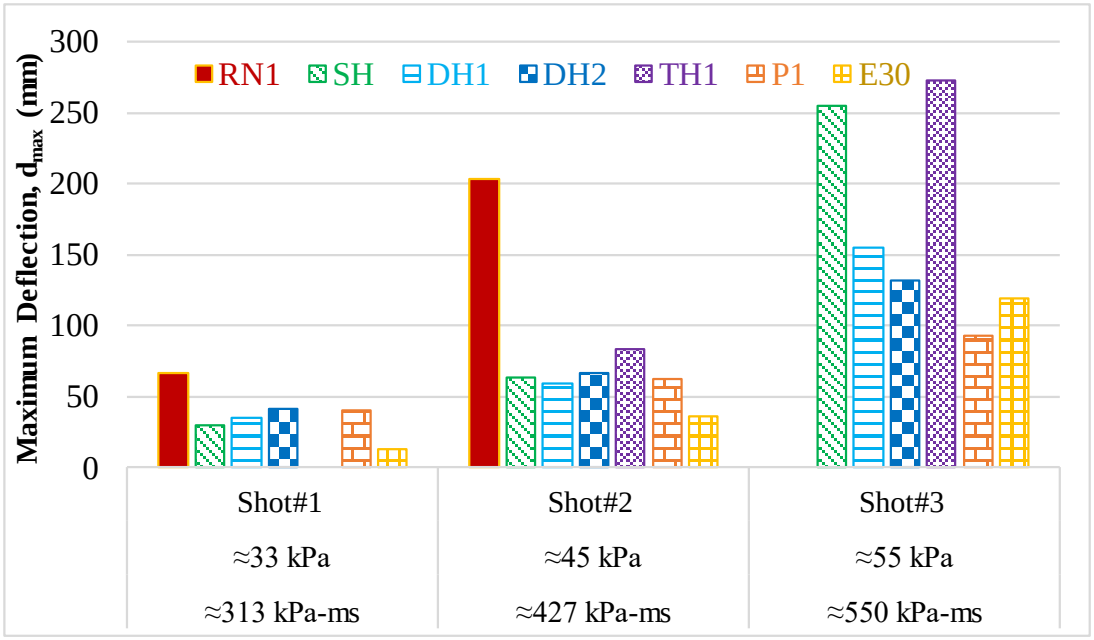

(a)

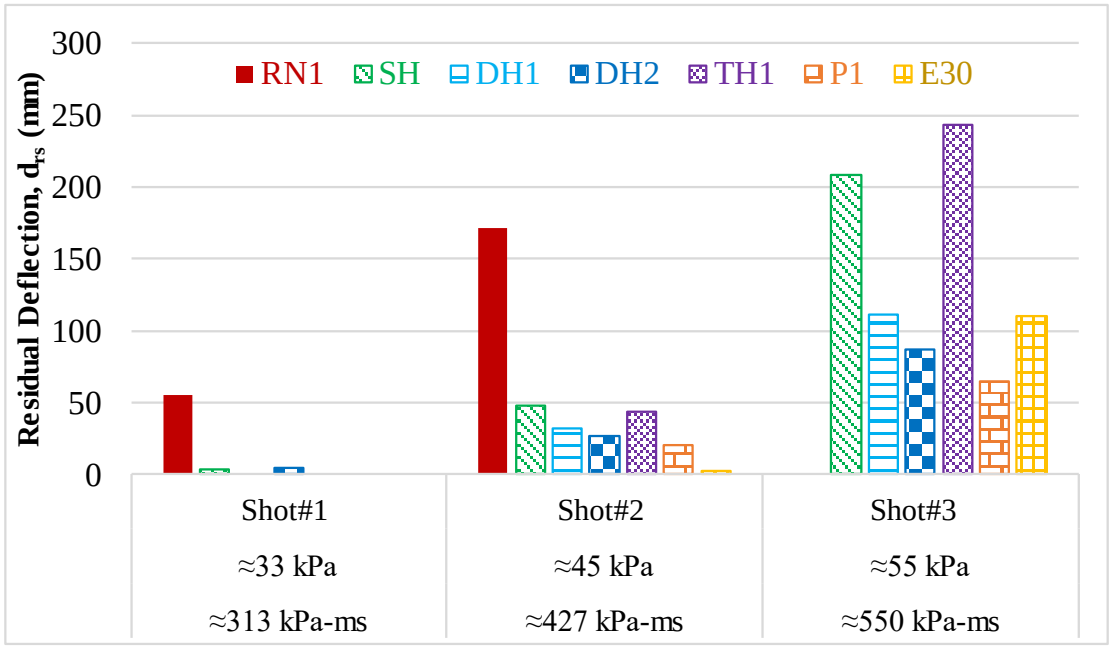

(b)

Figure 5.22– Test results of hardened columns from Phase I of testing: a) maximum deflection at mid-height region, and b) residual deflection at mid-height region.

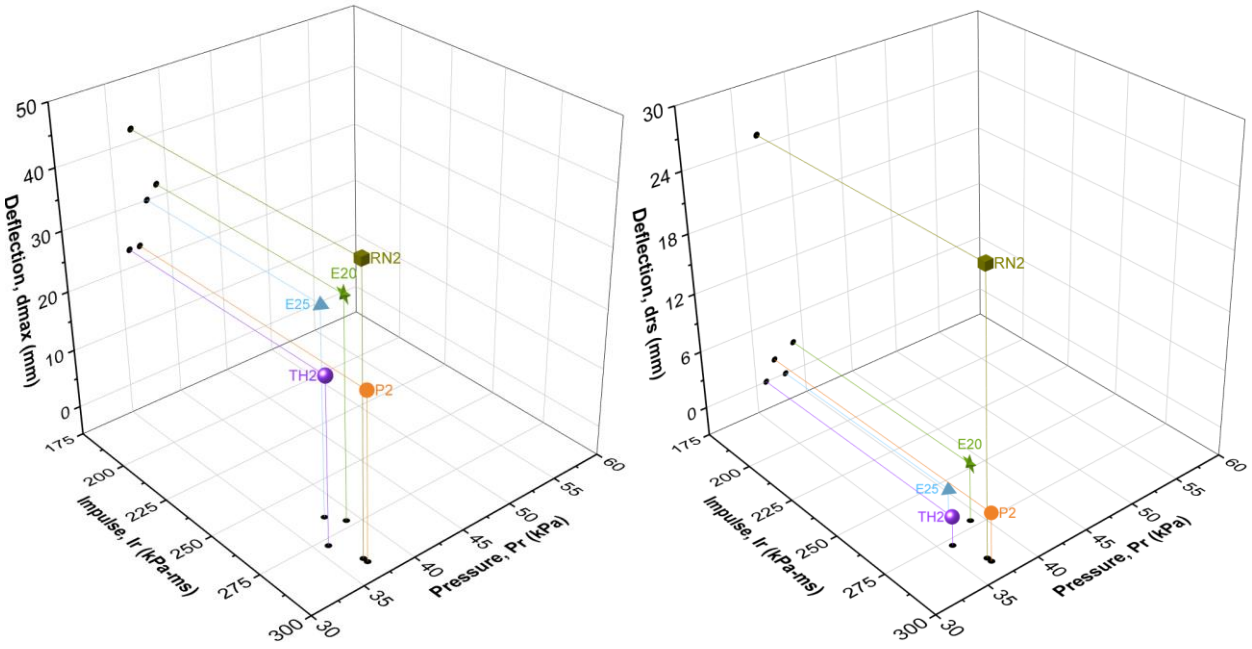

(a) (b)

Figure 5.23 – Column deflections from Phase II of testing: a) maximum deflection at mid-height region, and b) residual deflection at mid-height region.

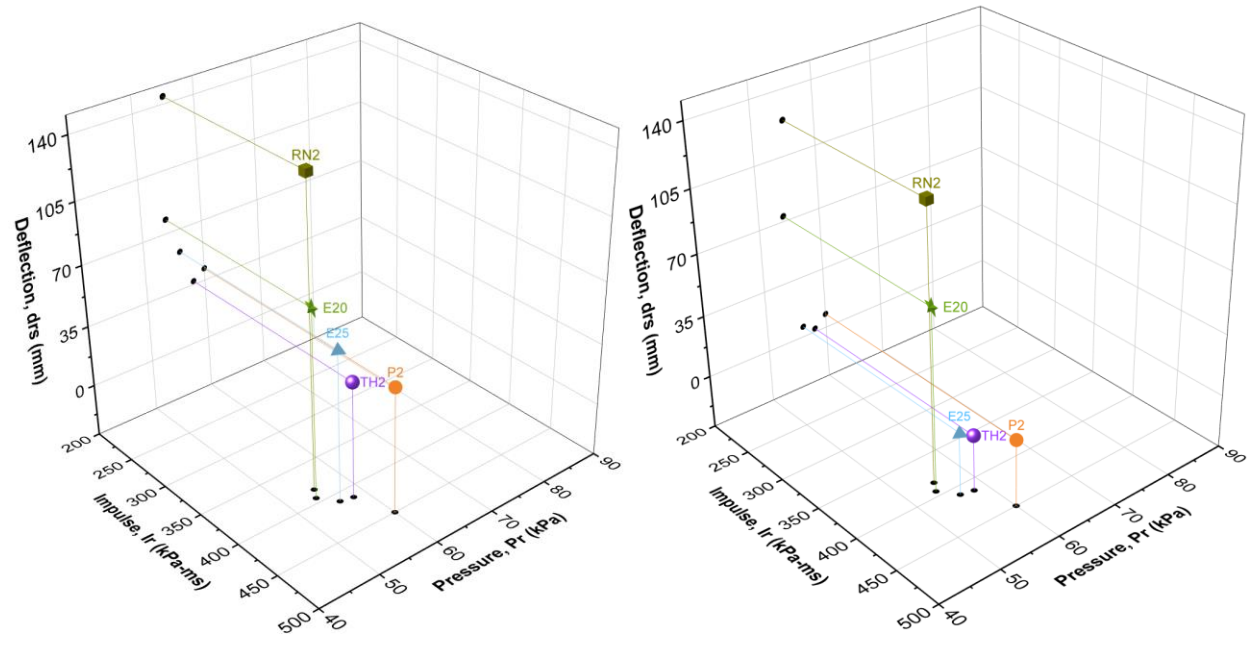

(a) (b)

Figure 5.24 – Column deflections from Phase II of testing when subjected to higher blast loads: a) maximum deflection at mid-height region, and b) residual deflection at mid-height region.

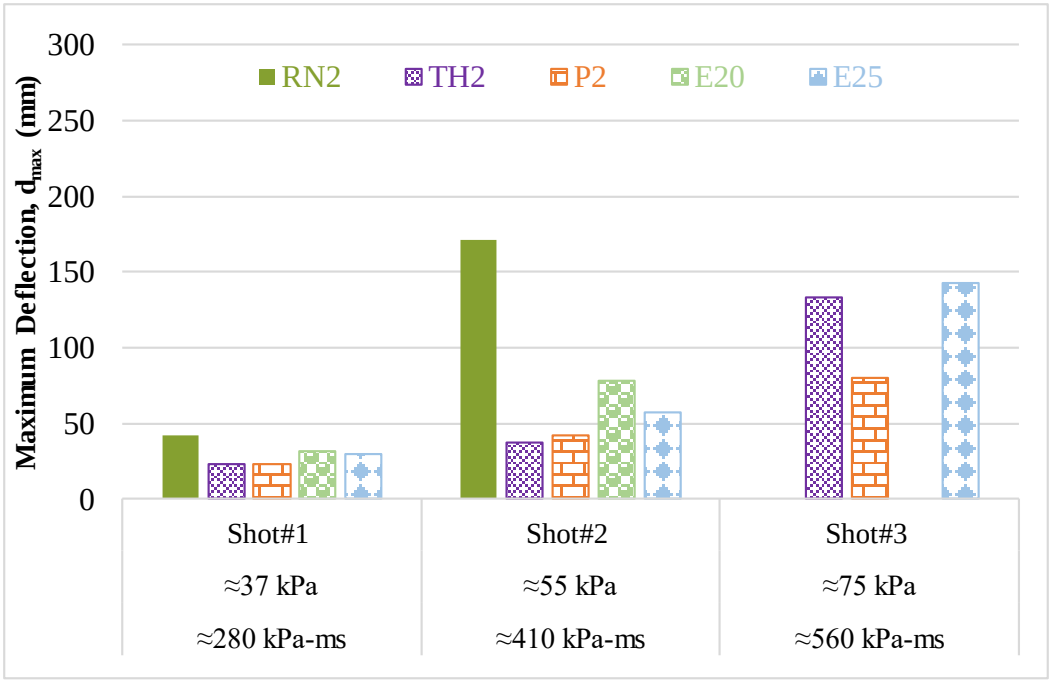

(a)

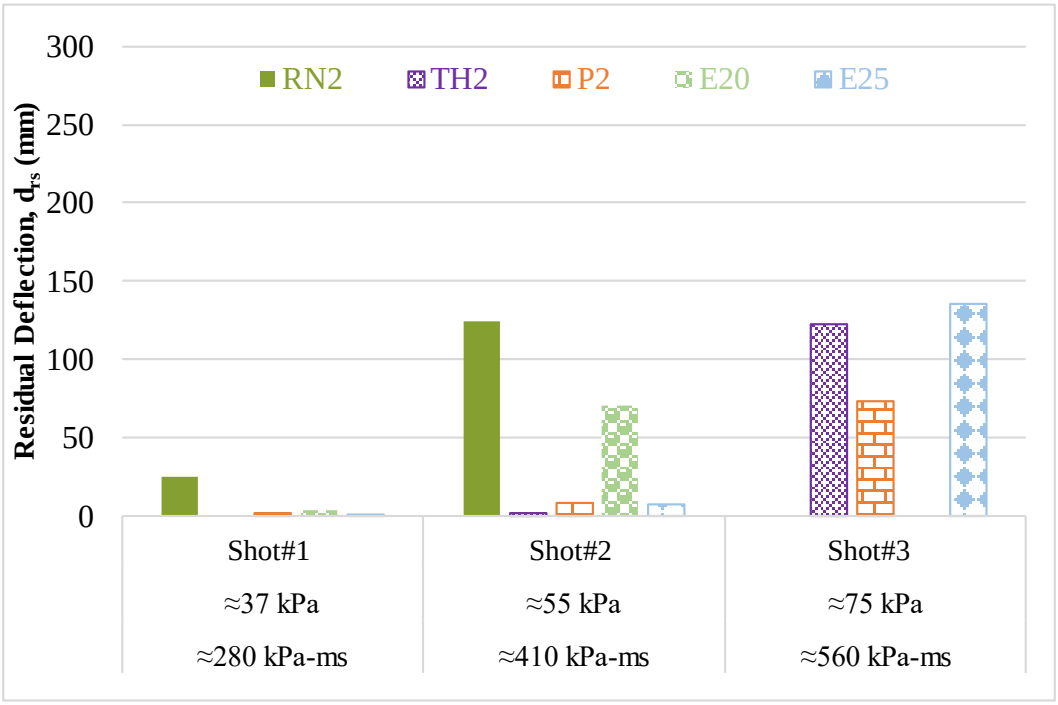

(b)

Figure 5.25 – Test results of hardened columns from Phase II of testing: a) maximum deflection at mid-height region, and b) residual deflection at mid-height.

Chapter 6. Analytical Research

Dynamic response of structures subjected to blast loading can be obtained using dynamic inelastic analysis of structural elements. Dynamic analysis is often conducted numerically because of the continuous change in loading, as well as the nonlinearity of materials and continuous change in structural and geometric characteristics during response. Dynamic response consists of contributions coming from different modes of response associated with different vibration frequencies and corresponding modes of structural response. This can be introduced through multiple-degree-of-freedom (MDOF) analysis and the use of finite element methods that require sophisticated modelling techniques. In blast analysis of structural elements, the response is often dominated by the first mode of response, making it possible to conduct single-degree-of-freedom (SDOF) analysis, especially for design purposes when maximum response is of concern. SDOF is commonly used in blast analysis of structural elements and has been adopted in current analytical research for the analysis of columns.

The columns tested in the experimental program, presented in Chapters 3 through 5, were modeled as SDOF elements to compute their response and compare it with experimentally recorded values. This chapter presents the steps followed and the analysis procedures implemented to conduct SDOF analysis by incorporating nonlinearity in materials and geometry. Material nonlinearity is introduced through constitutive material models in establishing force-deformation relations (resistance functions) used in the analysis. Geometric nonlinearity, as affected by P-delta effects generating secondary moments, is included in the analysis.

The first step in performing SDOF analysis involves generating a resistance function for the column considered. The resistance function provides strength and stiffness of the column and hence plays an important role in the accuracy of results. Having established the resistance function, the second step is to establish a mathematical model for SDOF analysis. This requires finding an equivalent lumped mass-spring system subjected to a time-varying concentrated force for the column, which has a uniformly distributed mass and a blast load that can be idealized as a uniformly distributed load. The equivalent SDOF system can be established by using transformation factors derived based on energy principles. The SDOF analysis can then be conducted using a numerical technique to solve the equation of motion. The specifics of the above steps are further discussed in the following subsections.

6.1 Resistance Functions

The resistance function relates the load-carrying capacity or load resistance to the deflection of the SDOF system, which is often taken as the maximum column mid-height deflection. In a statically applied load, the resisting (reactive) force is equal and opposite to the applied load. In blast loading, inertia forces develop, which interfere with the overall resistance of the dynamic system while member resistance continues to develop in proportion to its stiffness. Therefore, conventional procedures used for developing resistance function against static loading can also be used for blast loading and form part of the equation of motion governed by dynamic response. However, the change in material properties as affected by high strain rates, referred to as dynamic increase factor (DIF), may need to be considered.

The columns considered in current research have resistance provided either by reinforced concrete columns or internally post-tensioned columns with or without the effects of the hardening techniques developed. The columns were hardened either by introducing additional resistance generated through externally placed prestressing strands or by providing ECC jacketing. In the former case, the reactive forces generated by the strands develop a second component of resistance, which has to be incorporated in the resistance function. In the latter case, ECC is included in the column section as a material with different properties in the section while performing sectional analysis.

Sectional analysis forms the first step towards developing a resistance function. The moment-curvature relationship obtained from the sectional analysis helps establish member response, which leads to a resistance function in the form of a force-displacement relationship. This is done by selecting appropriate material constitutive models, as described in the following sections.

6.1.1 Concrete Models

The Hognestad model for unconfined concrete was used in the analysis of columns in this study unless the column core was confined. The confined concrete was modeled based on the model developed by Saatcioglu and Razvi [84]. Most of the columns tested in this study are considered unconfined because the core concrete is not confined by closely spaced ties (as required for seismic/blast detailing). The Hognestad model consists of parabolic ascending and linear descending branches. The parabolic branch for $0 \leq \varepsilon_c \leq \varepsilon_0$ is modeled using Equation 6.1a. The descending linear branch for $\varepsilon_c > \varepsilon_0$ is obtained by connecting the peak stress f'_c at $\varepsilon_0 = 0.002$ to

0.85 $f'c$ at a strain of ε_c = 0.0038 (Equation 6.1b). The linear segment extends to 0.2 f'_c beyond which it maintains a constant strength of 0.2 f'_c .

$$f_c = f'_c\left[\frac{2\varepsilon_c}{\varepsilon_0} - \left(\frac{\varepsilon_c}{\varepsilon_0}\right)^2\right] \quad for \quad \varepsilon_c \le \varepsilon_0 \tag{6.1a}$$

$$f_c = f'_c - (\varepsilon_c - \varepsilon_0)\left(\frac{0.15f'_c}{\varepsilon_{cu}-\varepsilon_0}\right) \quad for \quad \varepsilon_0 < \varepsilon_c \le \varepsilon_{cu} \tag{6.1b}$$

The strength of confined concrete is higher than that of unconfined concrete because of the lateral pressure provided by transverse reinforcement, which generates a biaxial state of stress. In addition, a significant effect of confinement is on the post-peak ductility of concrete, which is shown in the form of high strains beyond the peak. This results in a larger area under the stress-strain curve shown in Figure 6.1a, indicating increased toughness and energy absorption capacity. The lateral pressure provided by transverse reinforcement is adequate only when the ties are closely spaced, shortening the unsupported length of the longitudinal bar, which further improves the effects of confinement. The confined concrete model of Saatcioglu and Razvi presented below is based on equivalent uniform confinement pressure.

$$f'_{cc} = f'_c + k_1 f_{le} \tag{6.2}$$

Contribution of lateral pressure;

$$k_1 = 6.7\left(f_{le}\right)^{0.17} \tag{6.3}$$

Equivalent uniform lateral pressure;

$$f_{le} = k_2 f_l \tag{6.4}$$

The reinforcement arrangement factor k_2, which is a function of transverse reinforcement spacing (s), core dimensions (b_c) (it is the core width, center to center of perimeter hoop), and the distance between longitudinal bars (s_l), is given as follows:

$$k_2 = 0.26\sqrt{\frac{b_c}{s}\frac{b_c}{s_l}\frac{1}{f_l}} \tag{6.5}$$

Confining Lateral pressure, which is a function of transverse reinforcement spacing (s), area (A_s), yield strength (f_{yt}), and the hoop dimensions, is calculated as follows:

$$f_l = \frac{\sum A_s f_{yt}}{s b_c} \tag{6.6}$$

Nominal strength of confined core;

$$f'_{cc} = f'_{cc}\left[\frac{2\varepsilon_{cc}}{\varepsilon_1} - \left(\frac{\varepsilon_{cc}}{\varepsilon_1}\right)^2\right]^{1/(1+2K)} \quad for \quad \varepsilon_{cc} \le \varepsilon_1 \tag{6.7}$$

K is the ratio of equivalent uniform confinement pressure and unconfined concrete strength;

$$K = \frac{k_1 f_{le}}{f'_c} \tag{6.8}$$

Strain at peak confined concrete stress;

$$\varepsilon_1 = \varepsilon_0(1 + 5K) \tag{6.9}$$

Strain value corresponding to 85% of f'_{cc} where ρ is the area ratio of transverse reinforcement;

$$\varepsilon_{85} = 260\rho\varepsilon_1 + \varepsilon_{085} \tag{6.10}$$

$$\rho = \frac{\sum A_s}{s(b_{cx}+b_{cy})} \tag{6.11}$$

To find the strain value ε_{20} corresponding to 20% of f'_{cc}, a linear extrapolation can be conducted;

$$m = \frac{\partial f}{\partial \varepsilon} = \frac{f_{85} - f'_{cc}}{\varepsilon_{85} - \varepsilon_1} \qquad m = \frac{\partial f}{\partial \varepsilon} = \frac{f_{20} - f'_{cc}}{\varepsilon_{20} - \varepsilon_1} \qquad \rightarrow \qquad \varepsilon_{20} = \frac{0.20 * f'_{cc} - f'_{cc}}{m} + \varepsilon_1$$

It is assumed that the concrete will maintain a constant strength of $0.2 f'_{cc}$ for the strain values higher than ε_{20}.

6.1.2 Steel Reinforcement

Columns subjected to extreme loads, such as blasts, experience non-linear behavior. Therefore, contrary to traditional gravity load designs that do not consider the strain hardening of steel

reinforcement, the model used for steel reinforcement was the tension strain hardening model and bar buckling model by Yalcin and Saatcioglu [85]. The strain hardening model comprises three stages: elastic behavior until the onset of yield, yield plateau until the onset of strain hardening, and strain hardening until the rupturing of steel. Equation 6.12 describes all the stages of the stress-strain relationship with a parabolic strain hardening region.

$$f_s = E_s\varepsilon_s \quad for \quad \varepsilon_s \le \varepsilon_y \tag{6.12a}$$

$$f_s = f_y \quad for \quad \varepsilon_s = \varepsilon_y \tag{6.12b}$$

$$f_s = f_y + (\varepsilon_s - \varepsilon_y)\left(\frac{f_{sh}-f_y}{\varepsilon_{sh}-\varepsilon_y}\right) \quad for \quad \varepsilon_y < \varepsilon_s \le \varepsilon_{sh} \tag{6.12c}$$

$$f_s = f_y + (f_u - f_y)\left[\frac{2(\varepsilon_s-\varepsilon_{sh})}{\varepsilon_u-\varepsilon_{sh}} - \left(\frac{\varepsilon_s-\varepsilon_{sh}}{\varepsilon_u-\varepsilon_{sh}}\right)^2\right] \quad for \quad \varepsilon_{sh} < \varepsilon_s \le \varepsilon_u \tag{6.12d}$$

Steel in compression can exhibit a similar stress-strain relationship to that of tension, provided that the bar is restrained from buckling and maintains its stability. The restraining criterion for bar buckling can be expressed in terms of aspect ratio, which is the ratio of tie spacing over the diameter of the longitudinal bar (s/d_b). Generally, the compression bar is assumed to behave in a bilinear stress-strain relationship with a linear stage up to the yield and a constant post-yield stage by connecting a straight line from yield to ultimate. However, there are three expected behaviors of the compression bar for non-linear behavior depending on the aspect ratio based on the model by Yalcin and Saatcioglu [85] shown in Figure 6.1b. When the aspect ratio exceeds 8, the bar develops instability starting at the yield strain, with gradually diminishing force resistance. When the aspect ratio is less than 8 but greater than 4.5, the model considers the compression bar to exhibit strain hardening behavior. The compression bar exhibits identical behavior as tension reinforcement only when the unsupported bar length is reduced further to have an aspect ratio of less than 4.5. The stress-strain relationships for compression bars in these different stages are expressed with the following equations:

$$for \ \frac{s}{d_b} \ge 8, \quad f_s = f_y - (\varepsilon_s - \varepsilon_y)\left[-23000 + 11000\ln\left(\frac{s}{d_b}\right)\right] \quad for \quad \varepsilon_y < \varepsilon_s \le \varepsilon_{s/Du} \tag{6.13a}$$

$$for \ 8 > \frac{s}{d_b} \ge 4.5, \quad f_s = f_y + (f_{s/Du} - f_{sh})\left[\frac{2(\varepsilon_s-\varepsilon_{sh})}{\varepsilon_{s/Du}-\varepsilon_{sh}} - \left(\frac{\varepsilon_s-\varepsilon_{sh}}{\varepsilon_{s/Du}-\varepsilon_{sh}}\right)^2\right] \quad for \quad \varepsilon_s > \varepsilon_{sh} \tag{6.13b}$$

The limiting stress ($f_{s/Du}$) and strain ($\varepsilon_{s/Du}$) are given by the following equations:

$$for\ \frac{s}{d_b} \geq 8, \quad f_{s/Du} = 28\left(\frac{s}{d_b}\right)^{-1.7} f_y, \quad \varepsilon_{s/Du} = \left[40 - 6\ln\left(\frac{s}{d_b}\right)\right]\varepsilon_y \tag{6.14a}$$

$$for\ 8 > \frac{s}{d_b} \geq 4.5,\ f_{s/Du} = f_{sh} + (f_u - f_{sh})\left[48e^{-0.9\left(\frac{s}{d_b}\right)}\right],\ \varepsilon_{s/Du} = \varepsilon_{sh} + (\varepsilon_u - \varepsilon_{sh})\left[6e^{-0.9\left(\frac{s}{d_b}\right)}\right] \tag{6.14b}$$

6.1.3 Prestressing Strands

7-wire strands do not exhibit a well-defined yield plateau, unlike mild steel used in reinforcing bars. According to Collins and Mitchel [86], Yield strength for these strands is defined as stress on the ascending curved region corresponding to a strain of 0.01, and it is usually taken as 1650 MPa. The typical value for the low-relaxation strand yield strength ratio to its ultimate strength is 0.90. For a more accurate stress-strain relationship of strands (see Figure 6.1c), Mattock recommended using a modified Ramberg-Osgood equation [87]. Equation 6.15 provides an approximate formulation of the Ramberg-Osgood equation for a low relaxation strand with f_{pu} = 1860 MPa. The constants used in the equation are consistent with the minimum specified yield strength corresponding to 0.01 strain.

$$f_p = 200x10^3\varepsilon_{pf}\left\{0.025 + \frac{0.975}{\left[1+(118\varepsilon_{pf})^{10}\right]^{0.10}}\right\} \leq 1860\ MPa \tag{6.15}$$

6.1.4 Engineered Cementitious Composite (ECC)

Currently, there is no standard for characterizing the properties of ECC. However, many published articles about ECC properties and constitutive models for ECC exist. In this study, the stress-strain relationship of the ECC used was obtained experimentally. The experiments included a direct tensile strength test using dog-bone specimens, cylinder tests for stress-strain relationship in compression, and modulus of elasticity tests. The experimental results were used along with a constitutive model for ECC proposed by Chang Wu et al [88] shown in Figure 6.2. The model assumes that the tensile strength of ECC beyond cracking should not be ignored. This is because of the high tensile strain capacity of ECC, which is even higher than the yield strain of steel reinforcement. This strain capacity can reach 3% or higher. Therefore, the contribution of ECC in the tension region should be accounted for until the member fails in compression. The actual tensile stress-strain relationship of ECC can be described as a trilinear model consisting of three segments: linear up to cracking at the stress of f_{t0}, strain-hardening beyond cracking up to the maximum

strength of $f_{t1,}$ and strain-softening until the ultimate strain at a strain of ε_{tu}. However, for simplicity, ECC in tension can be modeled as a bilinear relationship that ignores increasing stress after cracking, thus changing the strain hardening to a flat line that extends from the cracking strain to the ultimate strain. Equation 6.16, proposed by Chang Wu et al [88], presents the bilinear relationship of ECC in tension. Since the cracking strain ε_{t0} of ECC is minimal, the distribution of tensile stress on the tension side of the neutral axis can be further simplified to a uniform rectangular stress block.

$$\sigma_{tens} = E\varepsilon \quad for \quad \varepsilon \leq \varepsilon_{to} \tag{6.16a}$$

$$\sigma_{tens} = f_{to} \quad for \quad \varepsilon_{to} < \varepsilon \leq \varepsilon_{tu} \tag{6.16b}$$

where E is the modulus of elasticity of ECC, ε_{t0} is the cracking strain of ECC, and ε_{tu} is the ultimate strain. The simplified stress-strain relationship of ECC under compression can be described with a parabola up to a strain of ε_c, followed by a linear segment with a constant stress up to the ultimate strain of ε_{cu}. Generally, the strains at peak stress, corresponding to the beginning and end of the straight portion, are approximately $\varepsilon_c = 5\%$ and $\varepsilon_{co} = 6\%$. Equation 6.17 presents the stress-strain relationship of ECC in compression proposed by Chang Wu et al [88].

$$\sigma_{comp} = f_c \left[\zeta \left(\frac{\varepsilon}{\varepsilon_c} \right) + (1 - \zeta) \left(\frac{\varepsilon}{\varepsilon_c} \right)^2 \right] \quad for \quad \varepsilon \leq \varepsilon_c \tag{6.17a}$$

$$\sigma_{comp} = f_c \quad for\ \varepsilon_c < \varepsilon \leq \varepsilon_{cu} \tag{6.17b}$$

where f_c is the peak stress, ε_c is the strain at peak stress, ε_{cu} is the ultimate compressive strain, and ζ is the initial stiffness parameter approximated to be 1.5.

To consider the confinement effect of the ECC shell on the column core, the compressive strength model for confined concrete by Richart et al [89] was used. The model is presented in the following equations:

$$\frac{f'_{cc}}{f'_c} = 1 + 4.1 \cdot \frac{f'_l}{f'_c} \tag{6.18}$$

$$f'_l = k_e \rho_h f_{cy} \tag{6.19}$$

$$\rho_h = 2 \cdot \frac{t}{b} \tag{6.20}$$

$$k_e = 1 - \left[\frac{(b^2+h^2)}{6(1-\rho_{sc})bh}\right] \quad (6.21)$$

where f'_{cc} is the confined compressive strength of concrete, f_l' is the effective passive confining pressure by the material (ECC jacket in this investigation), f'_c is the unconfined compressive strength of concrete, k_e is the shape factor for square and rectangular columns, ρ_h is the ratio of jacket confinement (ECC) having a thickness of t, f_{cy} is the tensile strength of confining material (ECC), ρ_{sc} is the longitudinal reinforcement ratio, b and h are the cross-sectional dimensions of the column core concrete.

6.1.5 Effects of High Strain Rate on Material Properties

It is widely accepted that strain rates, particularly in the high-strain range, significantly impact material characteristics. The strength of materials may increase under high strain rates associated with blast loads, which can be introduced by the dynamic increase factor (DIF). In other words, the DIF is the ratio of dynamic to static strength of the material. DIFs for blast loading are given in design guidelines and tables such as the "United Facilities Criteria" (UFC 3-340-02) [19] and CSA S850 "Design and Assessment of Buildings Subjected to Blast Loads." [83]. DIFs for materials subjected to close-range detonations are higher than those for far-range detonations. In addition, DIFs differ with the state of stress in the material (flexure dominant, diagonal tension, compression, etc.). For instance, in RC members under bending, DIFs are obtained assuming the strain rate in the material is 0.0001 mm/mm/msec and 0.0003 mm/mm/msec for far-range and close-range detonations, respectively. The blast loads generated by the shock tube used in current research are considered to be a far-range detonation [90] Hence, the DIFs from Table 4.1 of UFC 3-340-02 extracted from the PCI Design Handbook [91], for concrete, steel reinforcement, and prestressing strands under flexure are reported in Table 6.1.

6.1.6 Development of Analytical Resistance Functions

The columns included in the scope of this research fall into four categories in terms of developing their resistance functions for use in dynamic analysis. They consist of: i) reference reinforced concrete columns, ii) reinforced concrete columns jacketed with ECC, iii) reinforced concrete columns hardened with external prestressed strands, and iv) post-tensioned columns. For columns in the first and second categories, resistance functions were established by constructing force-displacement relationships starting with sectional analysis, followed by member analysis using

computer software RC-Blast, which is software developed at the University of Ottawa [26]. For columns in the third category, the resistance function consisted of two components, provided by the reinforced concrete column and the externally placed prestressed strands. The last category of columns were post-tensioned columns for which computer software RESPONSE-2000 [92] with capabilities of analyzing prestressed members was used to establish the resistance function. The details are provided in the following paragraphs. All the resistance functions were developed for columns under constant axial compression.

The software RC-Blast used for generating the force-displacement relationship of reinforced concrete columns includes a built-in module that can generate the resistance functions. The software needs input from the user, such as material properties, cross-section dimensions, equivalent plastic hinge length (assumed equal to column depth in this study), and the level of applied axial load, including any variation in axial load if applicable. The resistance functions for reference columns (Ref-N1 and Ref-N2) are presented in Figure 6.3.

ECC jacketed columns had a column core, the same as the reference columns, and an ECC jacket in place of the cover. The software RC-Blast was used to develop the resistance function with data consisting of ordinary concrete specified for the column core and ECC material properties specified for the column cover. The software has an option for unconfined and confined concrete material models. The unconfined material model was customized for the ECC layer, which was introduced as a cover for the column. The confined model was customized for the column core by considering the confinement effect provided by the ECC jacket (shell). Figure 6.4 shows the resistance function for the jacketed columns.

The resistance of columns hardened with external prestressing strands had two components, one provided by the column and the other provided by the external strands, applying concentrated forces along the column height in the opposite direction to the applied blast loads. The force-displacement relationship of the column is the same as the one developed for the reference columns using software RC-Blast. The contribution of external prestressing strands to blast resistance was computed as perpendicular components of the prestressing force at locations of change in the slope of the strand profile. The two components of resistance (provided by the column and the prestressing strands) are merged based on the compatibility of column mid-height deflection. The force in the strands is initially equal to the prestressing force applied, which causes a camber in the column (negative deflection of the column). As the column deflects under blast

loads, the column camber is first offset and starts developing positive deflections. The strands are stretched as the column develops progressively increasing positive deflections and increasing prestressing force further. The resulting elongation of the strands can be calculated by considering the change in geometry. This translates into an incremental increase in the strand force. Figure 6.5 and 6.6 show lateral force-displacement relationships for the column as well as the strands. Superposition of these two components is done based on displacement response to establish the composite resistance function.

The resistance functions for internally post-tensioned columns were developed using software Response-2000 because the RC-Blast software was developed for reinforced concrete elements and could not analyze prestressed concrete columns. Response-2000 is a non-linear analysis software designed for reinforced concrete members with and without prestressing based on the Modified Compression Field Theory [93]. The resistance function for the companion reference column to post-tensioned columns (Ref-S) was also generated using software Response-2000 for consistency. Unlike RC-Blast, Response 2000 does not have a built-in confinement model for RC material; however, it allows the user to enter material stress-strain relationships manually. The effect of confinement is especially important for this series of columns, as they represent columns designed following the requirements of seismic/blast resistant buildings with closely spaced column ties. The resulting resistance curves are presented in Figure 6.7.

6.1.7 Derivation of Experimental Resistance Function

In addition to the resistance functions constructed analytically, as explained in the preceding sections, the resistance functions were also computed from experimental data. Experimental resistance functions can be calculated if the applied load and inertia force time histories are available. Applied force-time history was recorded as reflected pressure-time histories in the experimental program. Inertia force-time histories were calculated from mass and accelerations. Accelerations were not recorded directly using an accelerometer. They were obtained from the second derivatives of experimentally recorded displacement-time histories based on Equation 6.22. First, the velocity-time profile of each column was obtained using MATLAB. Velocity at mid-height of a column is the rate of change in displacement at that location. The acceleration (the rate of change in velocity at column mid-height) was also obtained using MATLAB. An attempt was initially made to get the velocity and acceleration time histories using Microsoft Excel;

however, due to the high frequency of data, the profiles were noisy. A filtering code was used in MATLAB to eliminate the noise, and a smooth profile was obtained.

$$a(t) = y''(t) = \frac{\partial^2 y(t)}{\partial t^2} = \frac{\partial v(t)}{\partial t} \quad (6.22)$$

where *a(t), v(t)* and *y(t)* are acceleration, velocity and displacement functions, and *y''(t)* is the second derivative of displacement over time.

The pressure-time history recorded during each experiment was converted to a force-time history by multiplying the reflected pressure and the tributary area (i.e., the area of the LTD). Inertia force-time history was calculated from the total mass (i.e., the mass of the LTD and column) multiplied by acceleration and Load-Mass Factor (K_{LM}). The experimental resistance *R(t)* was then calculated using the equation of motion given in Equation 6.23 as the difference between the applied and inertia forces:

$$K_{LM} M[y''(t)] + R(y(t)) = F(t) \quad (6.23)$$

The experimental resistance functions for selected columns are plotted in Figure 6.8 to 6.10. For the remaining columns, the method of obtaining accelerations through double differentiation of displacement data was not reliable.

An alternative to obtaining the experimental resistance function is to use the dynamic reaction equation (i.e., rearrange the terms of equation 6.24) presented in Introduction to Structural Dynamics by Biggs [12], expressed as:

$$V(t) = c_1 R(t) + c_2 F(t) \quad (6.24)$$

Where *V(t)* is the reaction as a function of time (can be recorded using load cells during the experiment), *R(t)* is the column resistance-time history, *F(t)* is the applied force-time history, and c_1 and c_2 are the constant that varies for elastic and plastic behavior.

6.2 Single Degree-of-Freedom (SDOF) Analysis

6.2.1 Equation of Motion and Transformation Factors

SDOF analyses of the columns tested in the experimental program were conducted using software RC-Blast, which incorporates the step-by-step constant acceleration method of analysis in solving the dynamic equation of motion. The software conducts non-linear analysis following the

resistance function, either input into the software or computed internally through the built-in module for reinforced concrete elements. The solution is based on a spring-lumped mass mathematical model obtained from the actual member properties using transformation factors. The equation of motion given in Equation 6.25 is solved for an equivalent spring-mass system. This equation also has a term for damping, but damping has not been considered in the current analysis, as it is generally neglected in blast analysis due to the very short duration of loading.

$$K_{LM}M\ddot{u} + ku = F \tag{6.25}$$

One of the terms in Equation 6.24 represents the load-mass transformation factor (K_{LM}), a function of the deflected shape (mode shape) and the distribution of mass and applied load, which converts a continuous system into an equivalent single-degree-of-freedom (SDOF) model. K_{LM} is the ratio of mass factor (K_M) over the load factor (K_L) that can be calculated using equations 6.26 to 6.28 [12]. For the columns tested in this study, the K_{LM} factors are reported in Table 6.2.

$$K_M = \frac{\int_0^L m\varphi^2(x)dx}{mL} \tag{6.26}$$

$$K_L = \frac{\int_0^L p\varphi(x)dx}{pL} \tag{6.27}$$

$$K_{LM} = \frac{K_M}{K_L} \tag{6.28}$$

The other terms in Equation 6.24 are lumped mass (M), acceleration, or the second derivative of the displacement ($\ddot{u}$) as a function of time, resistance of the member expressed as ku, u is the displacement, k is the stiffness, and the forcing function (F) as a function of time. The forcing function can be calculated from the tributary area (A) times the reflected pressure (P_r(t)).

6.2.2 Displacement-Time History Predictions

Mid-height displacement response of the test columns was established through non-linear SDOF analysis. The tributary area and the mass during testing had to be considered carefully. Furthermore, the P-Δ effects due to the applied axial load and the effects of end eccentricities due to external prestressing had to be incorporated into the analysis. These aspects of the analysis are discussed in the following subsections prior to presenting the analysis results.

6.2.2.1 Tributary Area and Total Mass

During the shock tube testing, the columns were loaded through a load transfer device (LTD), as discussed in Chapter 3. Since the columns were not directly loaded with applied pressure, the loaded area was different than the surface area of the loaded side of the column. The actual loaded area was the area of the LTD, which was 4.3 m^2. This tributary area was specified as input in RC-Blast. Similarly, the loaded mass was different than the column mass. The loaded mass included the mass of the LTD because it moved together with the column when the pressure was applied. The total mass used as input in RC-Blast for reference and post-tensioned columns was 383 kg (i.e., 133 kg of column plus 250 kg of LTD). The total mass for the columns hardened by external strands included the mass added due to the presence of external prestressing strands, deviators, and end anchorage fixtures. Therefore, their total mass was 407 kg, 412 kg, 418 kg, and 428 kg for the column with single-harped, double-harped, triple-harped, and parabolic profiles, respectively. The jacketed column also had a different total mass because the cross-section dimension changed with the addition of the ECC jacket. The total mass for columns having 30 mm, 25 mm, and 20 mm ECC thickness was 480 kg, 430 kg, and 411 kg, respectively.

6.2.2.2 Secondary Moments due to P-Δ Effects

Columns tested in this study were subjected to a combined loading scenario where a constant axial load was first applied using a hydraulic jack, followed by blast shockwaves using a shock tube. The applied axial load was approximately 35% of the column concentric capacity. However, the displacements caused by applied pressure create secondary moments in the form of the product of axial load and mid-height displacement (P-delta effect). For an accurate and realistic SDOF analysis, the P-delta effect should be considered because of the relatively high displacements expected during blast loading, where P-delta moments can be quite substantial.

The current version of RC-Blast does not have an option to include the effects of P-delta moments in the analysis. However, an alternative approach suggested by Oswald [32] can be adopted to add the P-delta effects conveniently as an additional equivalent dynamic lateral load to be superimposed on the reflected pressure from blast loading. Oswald's method uses an equivalent lateral dynamic load that can approximately simulate an additional moment of similar magnitude to secondary moments generated by P-delta effects at each time step of the analysis. This method is called the Equivalent Lateral Load (ELL) method and uses the following equation. :

$$p'(t) = P(t)[\Delta(t) + e]\left(\frac{C}{L^2}\right) \quad (6.29)$$

where *p'(t)* is the equivalent dynamic lateral load in (kPa), *P(t)* is the total axial load divided by the supported width of the element over which the blast pressure is applied (kN/mm) (2m in this study because it is the curtain width that is supported), *Δ(t)* is the flexural deflection in (mm), *e* is the eccentricity of the axial load relative to the centroid of column cross-section in the direction of bending caused by the lateral load in (mm), *L* is the span of the column in the direction of axial load in (m), *C* is the constant corresponding to the distribution of blast load and supports location and can be found by the following equation:

$$C = K_1 K_2 \quad (6.30)$$

where K_1 is a factor for the location of supports in the direction of axial load and can be found from Table 6.3 for one-way spanning members. K_2 is taken as 1 for one-way spanning members and 0.64 for two-way spanning members.

To apply Equation 6.29, the user needs the input values of *P(t)* and *Δ(t)* as well as the other known parameters. Because the deflection quantity *Δ(t)* is not known prior to the analysis, a SDOF analysis (without the P-delta effect) is performed under a known *P(t)* using the RC-Blast software to obtain an initial value of *Δ(t)* for use in the equation. Next, the value of ELL is obtained using Equation 6.29, and the computed time-varying pressure is added to the blast pressure for the subsequent analysis to obtain results under the P-Δ effect. This is shown in Table 6.4. The second SDOF analysis with a modified applied pressure incorporates the effect of P-delta in ELL.

6.2.2.3 Applied Loads and Displacement Time Histories

After specifying the correct mass, the total loaded area, and additional reflected pressure to account for the secondary moment, displacement time histories of all the tested columns were obtained under all the shots. The blast loads were applied as reflected pressure-duration relationships, idealized to have triangular forcing functions. The reflected pressure used for each load was the same as that recorded during the test, and the equivalent duration was computed from the maximum impulse recorded, such that the distribution was triangular. The software RC-Blast was used to conduct SDOF dynamic inelastic analysis to generate displacement time histories. RC-Blast allows the user to consider the accumulated damage of a column when multiple shots are applied. Appendix C presents the results of the analysis in the form of mid-height deflection time histories up to the peak displacements. During the tests, the load transfer device (LTD), which

accumulated the blast pressure applied over the shock tube test area and transferred it onto the columns, moved together with the columns until the maximum positive displacements were attained. It was observed during the tests that the LTD separated from the column beyond the peak positive displacement and was detached from the column entirely. Therefore, the column-LTD system no longer responded together at this response stage. In the analysis, the mass used for the SDOF model was the combined mass of the column and the LTD. Hence, the analysis results beyond the peak were considered to be inaccurate and not included in the plots of Appendix C.

The numerical results are compared with experimentally recorded displacement histories in Appendix C. The software was able to generate displacement time histories up to the peak displacement reasonably well for all the columns, especially for the first two shots. The third shots, and the second shots of columns RN1, RS, and DS, developed higher displacements than the maximum displacement considered in generating resistance functions used in the analysis. Therefore, the analysis stopped when the displacement exceeded the maximum displacement capacity of the column based on the computed resistance function in the software.

6.3 Computed Support Reaction of Columns

During the experiments, applied forces (i.e., blast and axial loads) on the column and the resulting reactions of the columns were recorded using pressure sensors and load cells. The recorded reaction forces, along with applied forces, are presented in Appendix B figures, which present the time history of applied forces (blast and axial load), reaction, and deflections at the mid-height region. As can be seen in these figures, the support reactions increase, reaching their peak values when the blast load drops to near-zero values. The axial loads also show variations. Initial axial loads develop a slight increase due to arching action as the deflecting column exerts axial force on the hydraulic jack, which then decreases gradually as the column deflection increases. The drop in axial load is usually very small during the first two shots when the column essentially remains elastic with little damage. However, at later stages of loading, a substantial drop in axial load is observed. The support reactions were also computed analytically (presented by bar charts in Figure 6.11) using the equations proposed by Biggs [12], which are given below. Equation 6.31a is for a simply supported column subjected to a distributed blast load in the elastic range, while Equation 6.31b is for a similar condition in the plastic range.

$$V(t) = 0.38 \cdot R(t) + 0.10 \cdot F(t) \qquad (6.31a)$$

$$V(t) = 0.39 \cdot R(t) + 0.11 \cdot F(t) \quad (6.31b)$$

where *V(t)* is the reaction as a function of time, *R(t)* is the column resistance, and *F(t)* is the applied force.

Generally, the resistance of the column, *R(t)*, under dynamic loading is obtained by applying the maximum dynamic load factor (DLF_{max}) to the resistance under static loading. DLF_{max} is found from Figure 2.16, which is reproduced in this Chapter as Figure 6.12. The applied force *F(t)* at the time of maximum response should be found and substituted into the same equations. The time to maximum response (t_m) can also be obtained from Figure 6.12.

6.4 Experimental vs Analytical Results

Comparisons of experimental and analytical resistance functions are conducted with reference to the resistance curves presented earlier in Figure 6.8 to 6.10. As can be seen in Figure 6.8, the experimental and analytical relationships for columns RN1 and RS follow a similar stiffness pattern, with some discrepancies in maximum resistance. Figure 6.9 shows the force-displacement relationships of columns hardened by external strands as well as those internally post-tensioned. The agreement between the analytical and experimental results is fairly good. However, the experimental force-displacement relationship of column E30 is higher than that computed analytically, as shown in Figure 6.10a. Figure 6.10b shows the comparison for column E25, with a good agreement in maximum resistance. It should be mentioned that the accelerations obtained through double differentiation of experimental displacements for columns E30 and E25 resulted in excessive noise in the high deformation range and, hence, were discontinued in the plots.

Deflection-time histories were recorded during the experimental program, as reported in Chapter 4. Analytical SDOF deflection-time histories were computed using the RC-blast software as discussed earlier in this Chapter and plotted in Figure C.1 to C.5 of Appendix C. They are also compared in Appendix C. The numerical values for the comparisons are summarized in Table 6.5 to 6.8. The tables present the analytical results with and without the P-delta effects, indicating good agreement when the P-delta effects are considered. Similar observations can be made in Appendix C, where the time history plots are presented.

The bar charts in Figure 6.11 show comparisons of experimental versus analytical support reactions in the elastic and inelastic stages of response. In addition, Table 6.9 to 6.12 present the applied forces and the associated support reactions (experimental and analytical) corresponding to

each blast shot for all the columns, along with the ratio of predicted over experimental support reactions. It can be inferred from the bar charts and tables that the prediction of support reactions in the elastic range was overall conservative, except for one ECC jacketed column. The analytical results provided better agreement during the inelastic response. Any inaccuracy in the agreement of experimental and analytical values can be attributed to the way the support reactions were measured. The support reactions were measured with two load cells, one at each end, and the value reported here is the average of the two measurements. Since the column deflected shape was not always symmetric and the failure did not always occur right at mid-height, the recorded support reactions were not identical and showed some variations.

Table 6.1 – Dynamic increase factor for steel and concrete.

Stress Type	Dynamic Increase Factor, *DIF*		
	Reinforcing bars*		Concrete
	f_{dy}/f_y	f_{du}/f_u	f'_{dc}/f'_c
Flexure	1.17	1.05	1.19
Compression	1.10	1.00	1.12
Diagonal Tension	1.00	1.00	1.00
Direct Shear	1.10	1.00	1.10
Bond	1.17	1.05	1.00

*Applicable for Grade 40 and Grade 60 reinforcing steel only.

Note: *DIF* for all prestressing steel is equal to 1. f_{dy} is the dynamic yield strength of steel reinforcement, f_y is the specified yield strength of steel reinforcement, f_{du} is the dynamic tensile strength of steel reinforcement, fu is the specified tensile strength of steel reinforcement, f'_{dc} is dynamic concrete compressive strength, and f'_c is specified concrete compressive strength

Table 6.2 – Load-mass factors for one-way simply supported members.

Load Distribution	Response Range	Load Factor K_L	Mass Factor K_M	Load-Mass Factor K_{LM}*
Single point load at midspan	Elastic	1.0	0.49	0.49
	Plastic	1.0	0.33	0.33
Two point-loads at third points	Elastic	0.87	0.52	0.60
	Plastic	1.0	0.56	0.56
Uniformly distributed load	Elastic	0.64	0.50	0.78
	Plastic	0.50	0.33	0.66

*For members with uniformly distributed mass

Table 6.3 – K_1 values from Oswald [35].

Case	Boundary or support locations	Blast load Distribution	K_1	Example
1	At both ends of the member in the direction of the axial load	uniform	8	Uniformly loaded column or one-way spanning wall with top and bottom supports. Supports may be fixed and/or simple.
2	At both ends of the member in the direction of the axial load	Concentrated at midspan	4	Column with beam applying blast load as concentrated load at midspan. Supports may be fixed and/or simple.
3	At one end of the member in the direction of the axial load	Uniform	2	Cantilevered column or wall that is not supported at the top where the axial load is applied (i.e., supported on two or three sides, not including the top of the wall). Uniform blast load in both cases.
4	At one end of the member in the direction of axial load (unloaded end)	Concentrated at the free end	1	A cantilevered column with a blast load applied by a supported beam as concentrated load at a free end.

Table 6.4 – Sample of Additional pressure from the ELL method to account for the P-delta effect.

Column ID	SDOF analysis without P- Δ			Modified Reflected Pressure with P-Δ				
	Shot #	t (ms)	Δ(t) (mm)	P_{axial}(t) (kN)	P_{strand}(t) (kN)	ELL p'(t) (kPa)	Pr (recorded) (kPa)	Pr (total) (kPa)
RN1	1	18	28	300	0	6.9	2.0	8.9
	2	4	53	250	0	11.0	31.0	42.0
RN2	1	15	17	300	0	4.2	2.0	6.2
	2	15	29	300	0	7.2	2.3	9.5
RS	1	20	19	300	0	4.7	1.2	5.9
	2	5	20	270	0	4.5	32.3	36.8
SH	1	15	15	300	102	10.1	6.7	16.8
	2	15	37	300	190	18.5	9.5	28.0
DH1	1	15	16	300	120	11.4	6.9	18.3
	2	15	34	300	220	22.1	10.8	32.9
DH2	1	15	16	300	130	12.0	9.4	21.4
	2	10	25	300	178	17.2	21.5	38.7
TH1	1	15	20	300	114	12.0	8.4	20.4
	2	10	33	300	170	18.7	21.3	40.0
TH2	1	10	11	300	95	8.6	12.0	20.6
	2	10	23	300	140	14.4	16.6	31.0
P1	1	10	15	300	82	8.8	16.0	24.8
	2	10	25	300	118	13.5	22.2	35.7
P2	1	10	12	300	98	9.0	13.9	22.9
	2	10	26	300	143	15.3	20	35.3
SS	1	15	15	300	91	3.7	6.1	9.8
	2	15	37	250	91	7.3	9.3	16.6
DS	1	15	16	300	204	5.3	6.1	11.4
	2	10	32	300	204	10.7	20.8	31.5
E30	1	15	16	365	0	4.8	8.0	12.8

Column ID	SDOF analysis without P- Δ			Modified Reflected Pressure with P-Δ				
	Shot #	t (ms)	Δ(t) (mm)	$P_{axial}(t)$ (kN)	$P_{strand}(t)$ (kN)	ELL p'(t) (kPa)	Pr (recorded) (kPa)	Pr (total) (kPa)
	2	15	25	365	0	7.5	9.9	17.4
E20	1	10	16	300	0	4.0	11.1	15.1
	2	10	27	300	0	6.7	18.0	24.7
E25	1	10	14	300	0	3.5	10.9	14.3
	2	10	24	300	0	6.0	18.7	24.7

Table 6.5 – Comparison of experimental and analytical maximum displacement of reference columns.

Column ID	Shot #	Experimental Results	SDOF Results		w/o P-Δ $Disp_{SDOF}$ / $Disp_{Exp}$	w/ P-Δ $Disp_{SDOF}$ / $Disp_{Exp}$
		Max Displacement $Disp_{Exp}$ (mm)	Max Displacement without P-Δ $Disp_{SDOF}$ (mm)	Max Displacement with P-Δ $Disp_{SDOF}$ (mm)		
RN1	1	66	28	39	0.42	0.59
	2	203	Failed	Failed	NA	NA
RN2	1	21	17	20	0.81	0.95
	2	44	31	41	0.70	0.93
	3	171	Failed	Failed	NA	NA
RS	1	37	19	24	0.51	0.65
	2	179	72	Failed	0.40	NA
				Average	0.57	0.78

Table 6.6 – Comparison of experimental and analytical maximum displacement of hardened columns.

Column ID	Shot #	Experimental Results	SDOF Results		w/o P-Δ	w/ P-Δ
		Displacement $Disp_{Exp}$ (mm)	Max Displacement without P-Δ $Disp_{SDOF}$ (mm)	Max Displacement with P-Δ $Disp_{SDOF}$ (mm)	Max $Disp_{SDOF}$ / $Disp_{Exp}$	$Disp_{SDOF}$ / $Disp_{Exp}$
SH	1	30	15	23	0.50	0.77
	2	63	40	69	0.63	1.10
	3	255	Failed	Failed	NA	NA
DH1	1	35	16	23	0.46	0.66
	2	59	37	62	0.63	1.05
	3	155	Failed	Failed	NA	NA
DH2	1	41	16	24	0.39	0.59
	2	66	43	73	0.65	1.10
	3	132	Failed	Failed	NA	NA
TH1	1	57	20	30	0.35	0.53
	2	83	50	75	0.60	0.90
	3	273	Failed	Failed	NA	NA
TH2	1	23	14	19	0.61	0.83
	2	37	30	42	0.81	1.13
	3	135	54	Failed	0.40	NA
P1	0	31	15	21	0.48	0.68
	1	40	25	37	0.63	0.93
	2	62	51	74	0.82	1.19
	3	93	Failed	Failed	NA	NA
P2	1	23	15	22	0.65	0.96
	2	44	36	54	0.82	1.23
	3	88	68	Failed	0.77	NA
				Average	0.60	0.91

Table 6.7 – Comparison of experimental and analytical maximum displacement of post-tensioned columns.

Column ID	Shot #	Experimental Results	SDOF Results		w/o P-Δ $Disp_{SDOF}$ / $Disp_{Exp}$	w/ P-Δ $Disp_{SDOF}$ / $Disp_{Exp}$
		Max Displacement $Disp_{Exp}$ (mm)	Max Displacement without P-Δ $Disp_{SDOF}$ (mm)	Max Displacement with P-Δ $Disp_{SDOF}$ (mm)		
SS	1	26	15	19	0.58	0.73
	2	87	40	51	0.46	0.59
	3	206	Failed	Failed	NA	NA
DS	1	37	16	20	0.43	0.54
	2	100	51	75	0.51	0.75
	3	210	Failed	Failed	NA	NA
				Average	0.50	0.65

Table 6.8 – Comparison of experimental and analytical maximum displacement of jacketed columns.

Column ID	Shot #	Experimental Results	SDOF Results		w/o P-Δ $Disp_{SDOF}$ / $Disp_{Exp}$	w/ P-Δ $Disp_{SDOF}$ / $Disp_{Exp}$
		Max Displacement $Disp_{Exp}$ (mm)	Max Displacement without P-Δ $Disp_{SDOF}$ (mm)	Max Displacement with P-Δ $Disp_{SDOF}$ (mm)		
E30	1	13	16	18	1.23	1.38
	2	36	27	32	0.75	0.89
	3	119	62	Failed	0.52	NA
E20	1	32	23	26	0.72	0.81
	2	81	49	61	0.60	0.75
	3	338	Failed	Failed	NA	NA
E25	1	30	20	23	0.67	0.77
	2	57	46	54	0.81	0.95
	3	149	Failed	Failed	NA	NA
				Average	0.76	0.93

Table 6.9 – Applied loads and support reactions of reference columns.

ID	Shot #	F_B (kN)	F_{A-i} (kN)	F_{A-rs} (kN)	$V_{R-max/exp}$ (kN)	$V_{R-max/pre}$ (kN)	$V_{R,pre}/V_{R,exp}$
Ref-N1	1	150	300	250	53	50	0.94
	2	181	250	0	24	21	0.89
Ref-N2	1	125	300	300	29	42	1.46
	2	159	300	300	47	41	0.87
	3	236	300	20	53	39	0.74
Ref-S	1	108	300	280	43	52	1.20
	2	184	300	0	72	44	0.61
						Average	0.96

Table 6.10 – Applied load and support reaction forces of post-tensioned columns.

ID	Shot#	F_B (kN)	F_{A-i} (kN)	F_{A-rs} (kN)	$V_{R-max/exp}$ (kN)	$V_{R-max/pre}$ (kN)	$V_{R,pre}/V_{R,exp}$
PT-SS-0.35f_{pu}-S	1	125	300	285	55	60	1.09
	2	189	300	160	78	66	0.85
	3	258	300	0	66	54	0.81
PT-DS-0.40f_{pu}-S	1	125	300	270	56	60	1.07
	2	189	300	140	79	60	0.76
	3	236	280	0	53	48	0.90
						Average	0.92

Table 6.11 – Applied load and support reaction forces of hardened columns.

ID	Shot #	F_B (kN)	F_{A-i} (kN)	F_{A-rs} (kN)	$V_{R-max/exp}$ (kN)	$V_{R-max/pre}$ (kN)	$V_{R,pre}/V_{R,exp}$
SH-207e-0.15f_{pu}-N1	1	138	300	300	53	80	1.52
	2	194	300	250	88	84	0.95
	3	237	300	0	78	86	1.10
DH1-207e-0.13f_{pu}-N1	1	142	300	300	51	88	1.73
	2	185	300	300	83	88	1.06
	3	237	300	0	85	90	1.06
DH2-207e-0.16f_{pu}-N1	1	141	300	300	61	96	1.57
	2	185	300	290	85	93	1.09
	3	258	300	25	87	101	1.16
TH1-247e-0.10f_{pu}-N1	1	172	300	300	59	90	1.52
	2	193	300	200	89	85	0.95
	3	237	300	0	76	93	1.23
TH2-247e-0.15f_{pu}-N2	1	155	300	300	33	76	2.31
	2	250	300	300	68	83	1.23
	3	322	300	90	96	87	0.90
P1-227e-0.09f_{pu}-N1	0	125	300	300	50	70	1.39
	1	138	300	300	67	80	1.20
	2	194	300	300	NR	73	NA
	3	260	300	130	107	81	0.76
	4	237	200	0	75	74	0.99
P2-227e-0.16f_{pu}-N2	1	159	300	300	48	71	1.49
	2	258	300	300	79	73	0.93
	3	322	300	140	92	74	0.81
						Average	1.18

Table 6.12 – Applied load and support reaction forces of ECC jacketed columns.

ID	Shot #	F_B (kN)	F_{A-i} (kN)	F_{A-rs} (kN)	$V_{R-max/exp}$ (kN)	$V_{R-max/pre}$ (kN)	$V_{R, pre}$ /$V_{R,exp}$
ECC-2.0%v_f-t30-N1	1	138	365	365	42	76	1.82
	2	201	365	365	71	95	1.34
	3	268	365	150	95	100	1.06
	4	206	200	0	NR	NA	NA
ECC-2.0%v_f-t20-N2	1	166	300	300	53	48	0.90
	2	235	300	270	77	52	0.68
	3	240	270	0	32	25	0.79
ECC-1.5%v_f-t25-N2	1	163	300	300	43	54	1.26
	2	243	300	300	75	55	0.73
	3	305	300	50	87	60	0.69
						Average	1.03

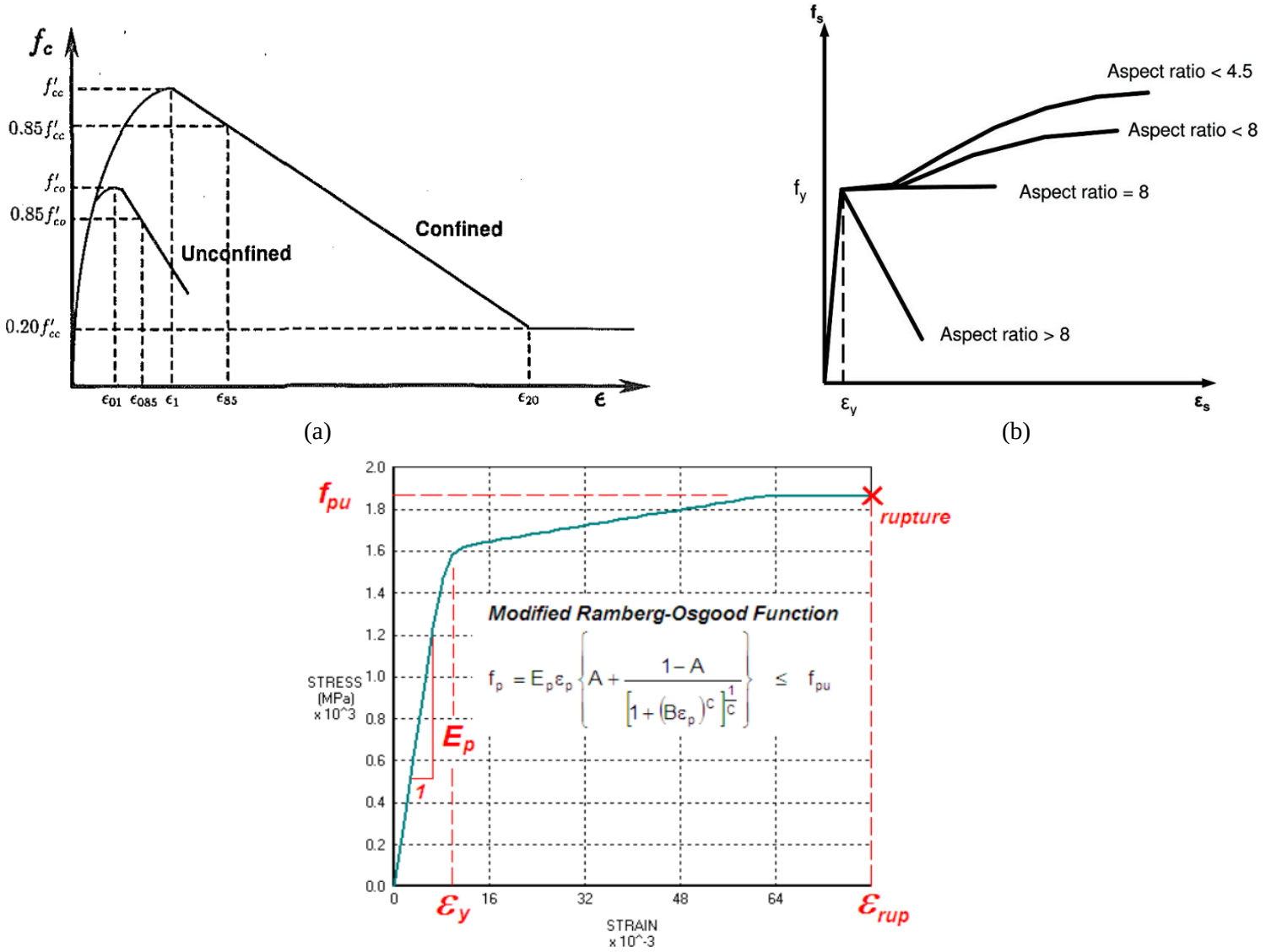

Figure 6.1 – Stress-strain relationship of materials used in this study, a) concrete model, b) steel compression model, and c) low-relaxation strand model [94].

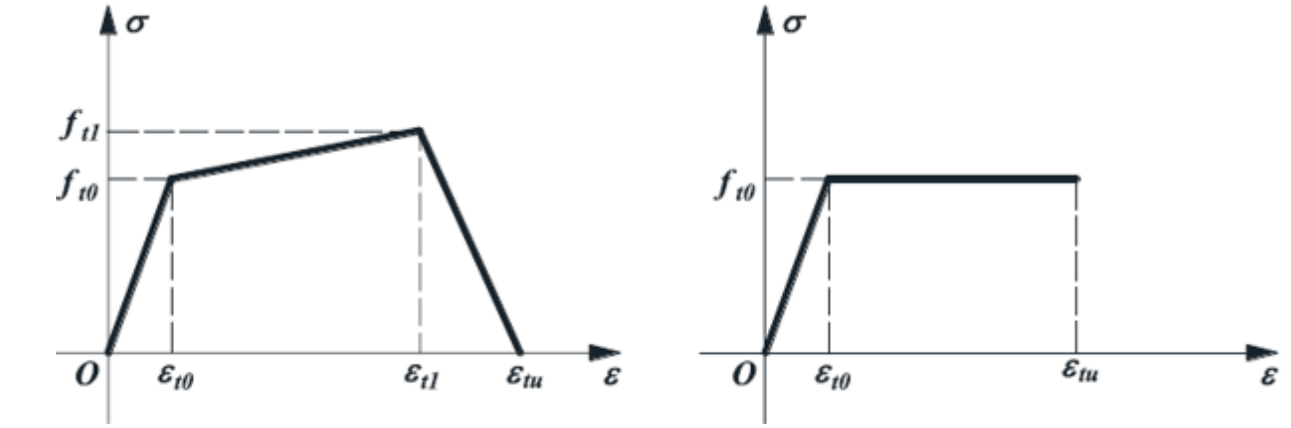

(a)

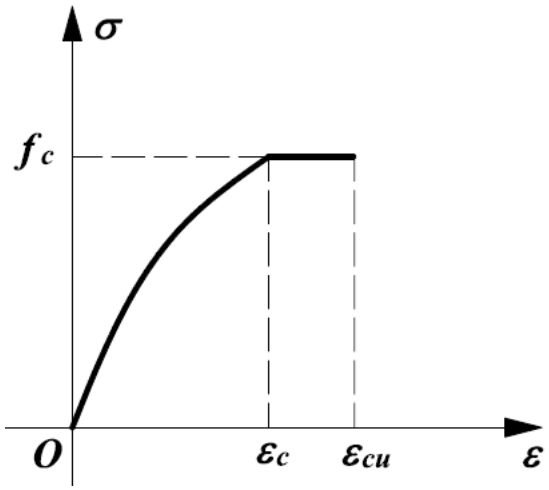

(b)

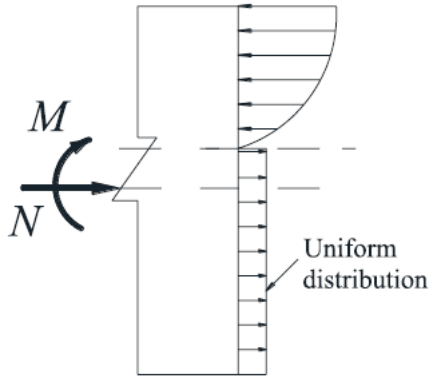

(c)

Figure 6.2 – The simplified stress-strain relationship of ECC used in sectional analysis of jacketed columns, a) the tensile model, b) the compressive model, and c) the stress distribution in sectional analysis.

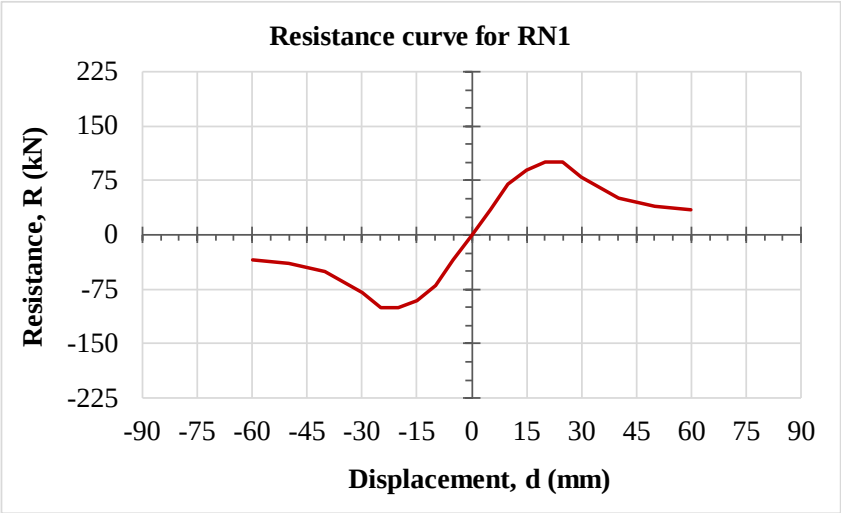

(a)

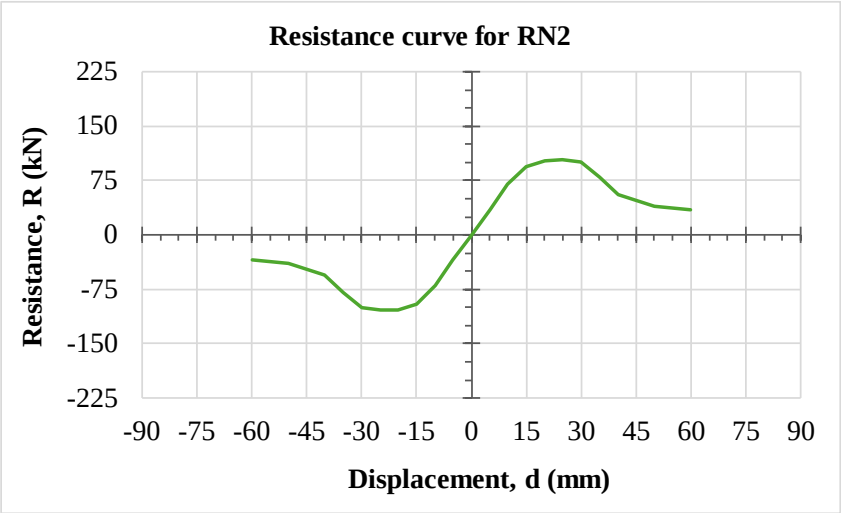

(b)

Figure 6.3 – Resistance function of reference columns, a) Ref-N1 and b) Ref-N2.

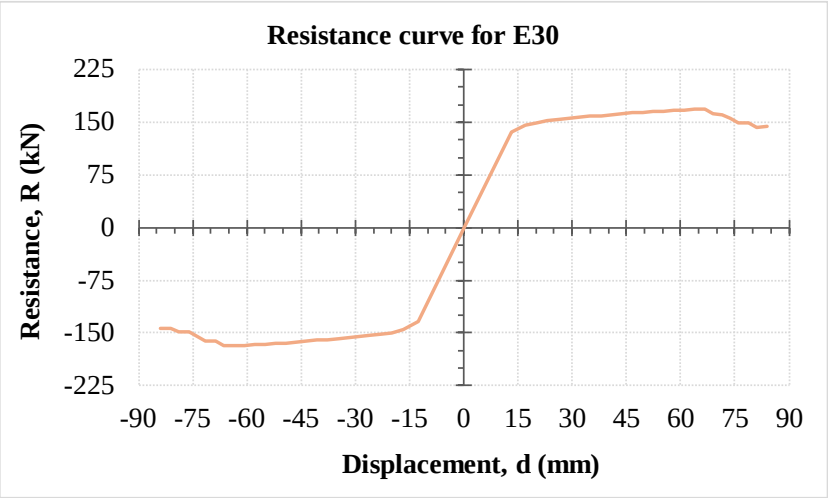

(a)

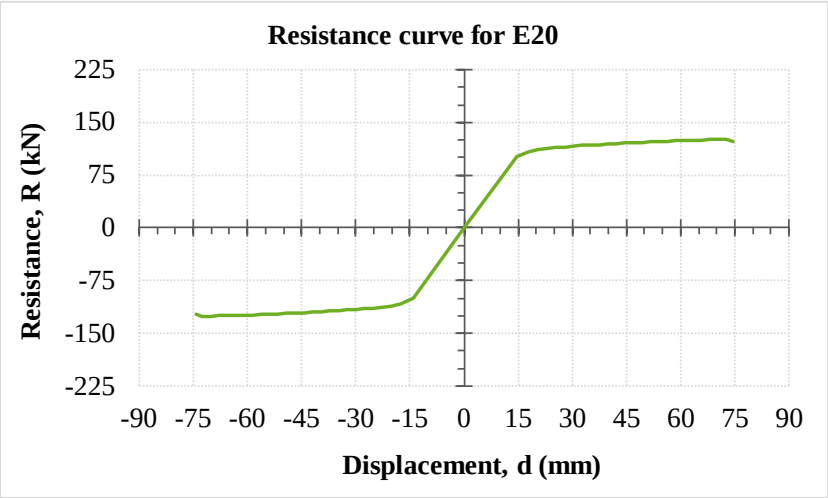

(b)

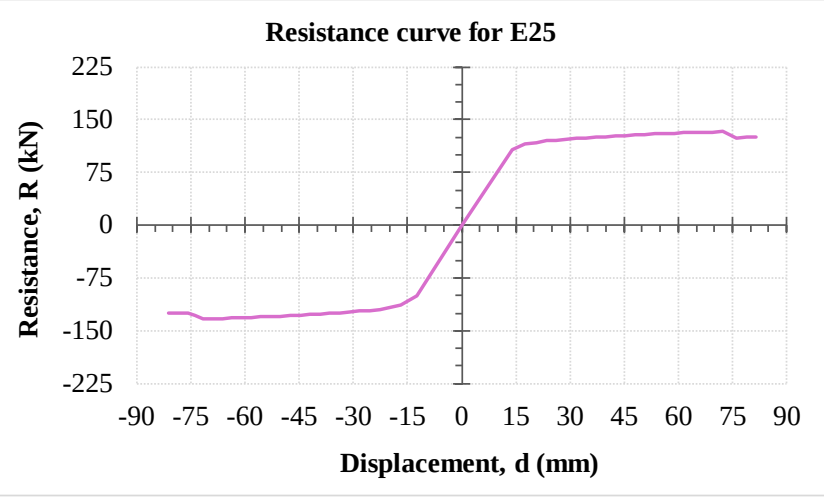

(c)

Figure 6.4 – Resistance function of jacketed columns, a) ECC-2.0%v_f-t30-N1, b) ECC-2.0%v_f-t20-N2, and c) ECC-1.5%v_f-t25-N2.

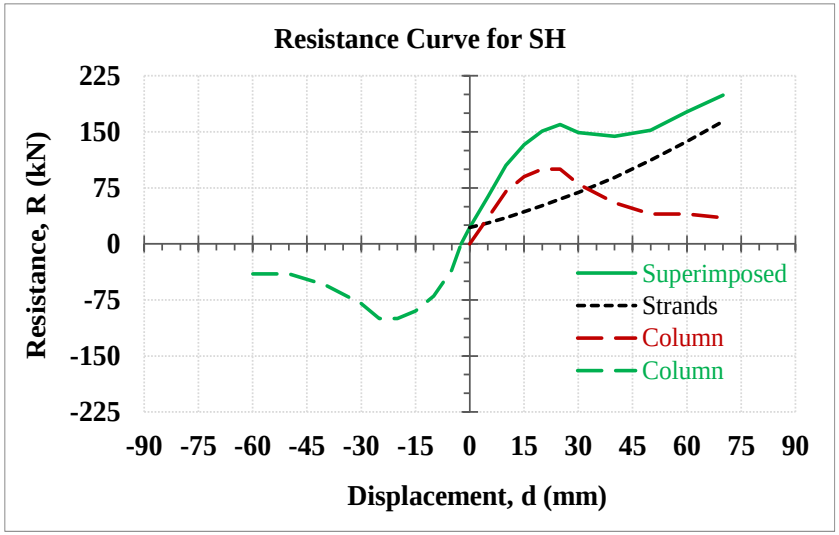

(a)

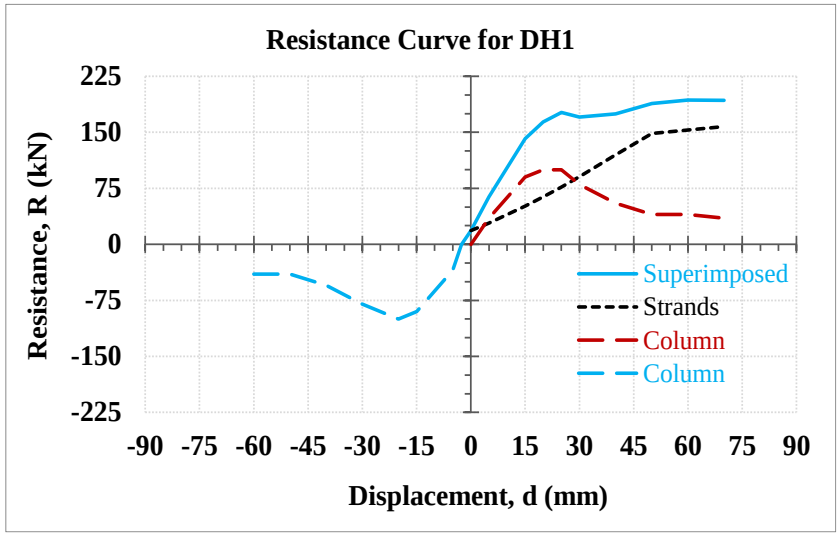

(b)

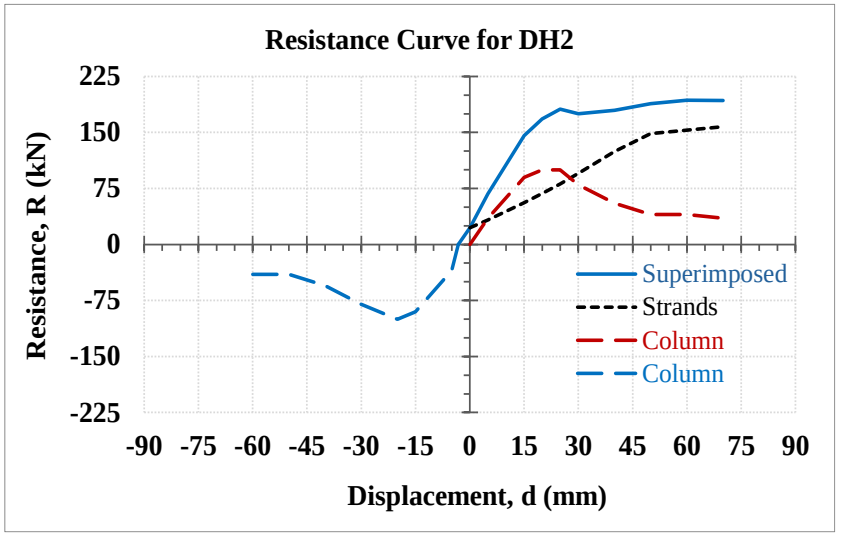

(c)

Figure 6.5 – Resistance function of hardened columns, a) SH-207e-0.15fpu-N1, b) DH1-207e-0.13fpu-N1, and c) DH2-207e-0.15fpu-N1.

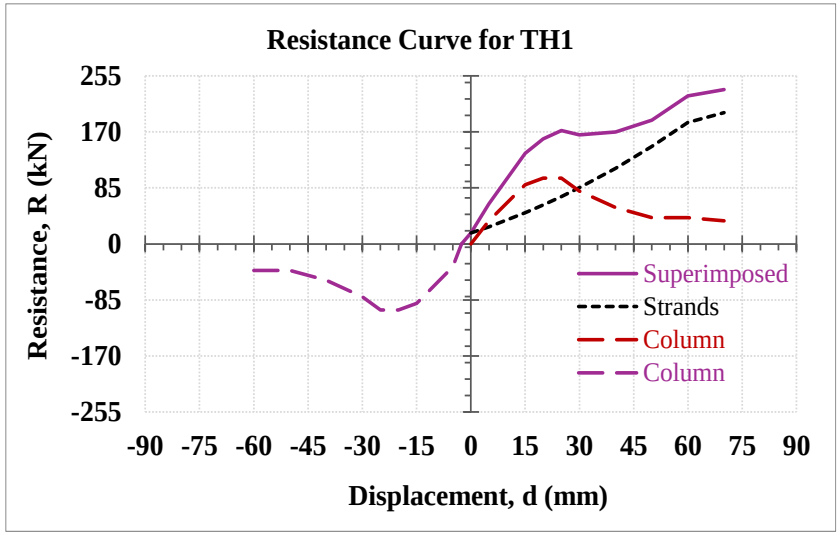

(a)

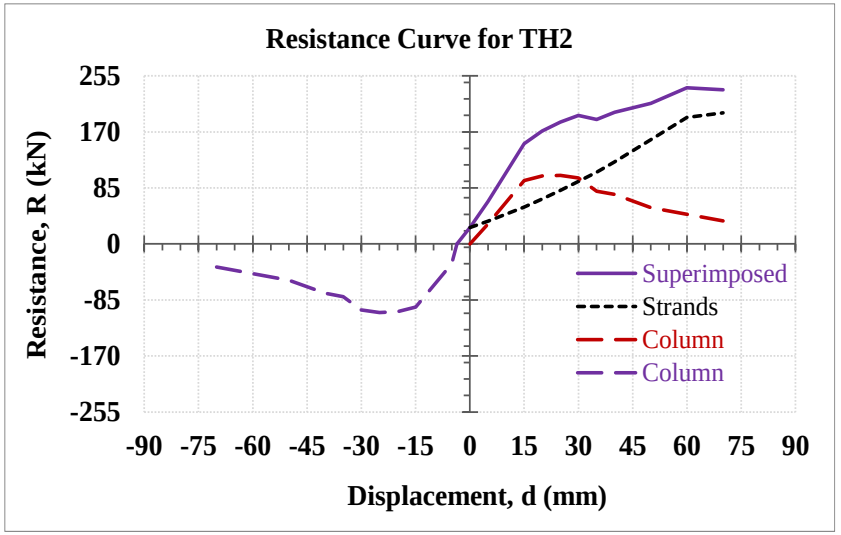

(b)

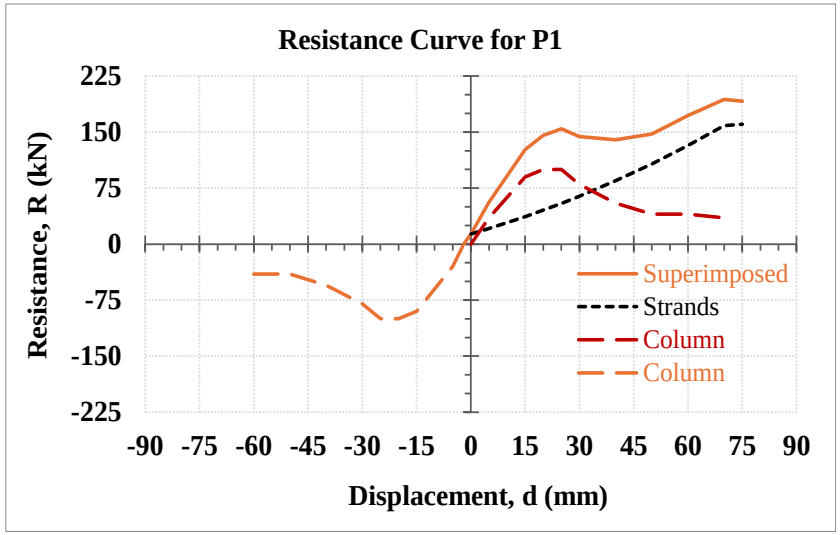

(c)

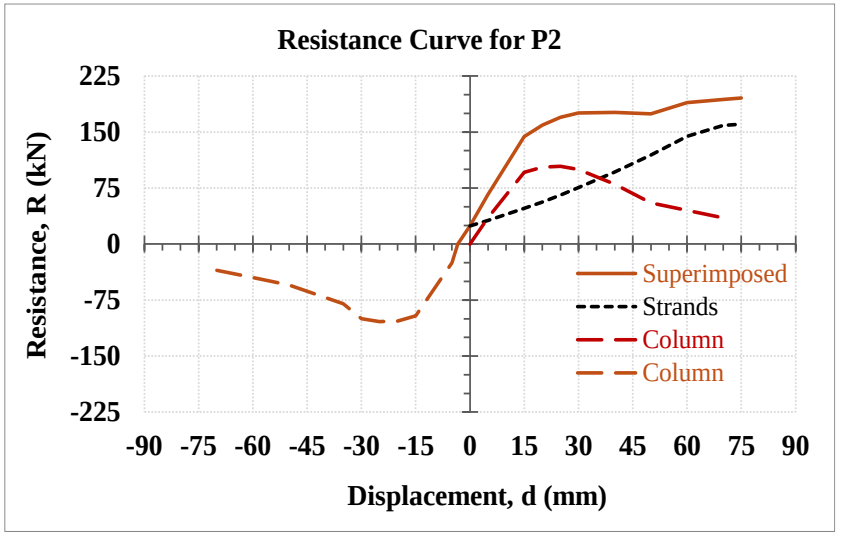

(d)

Figure 6.6 – Resistance function of hardened columns, a) TH1-247e-0.10fpu-N1, b) TH2-247e-0.15fpu-N2, c) P1-227e-0.09fpu-N1 and c) P2-227e-0.16fpu-N2.

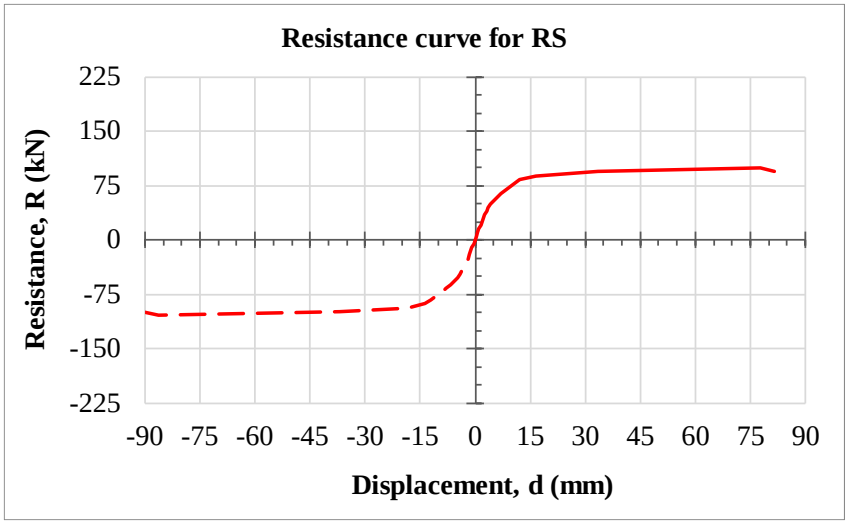

(a)

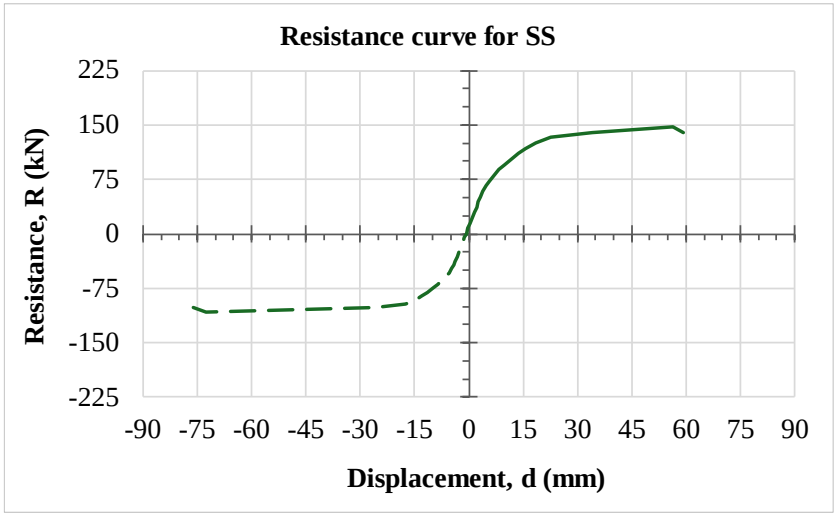

(b)

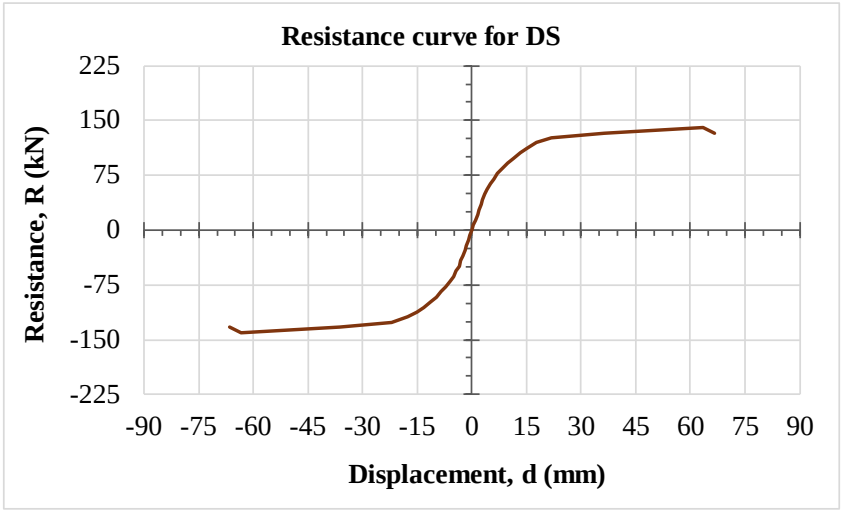

(c)

Figure 6.7 – Resistance functions of post-tensioned columns, a) Ref-S, b) PT-SS-0.35fpu-S, and c) PT-DS-0.40fpu-S.

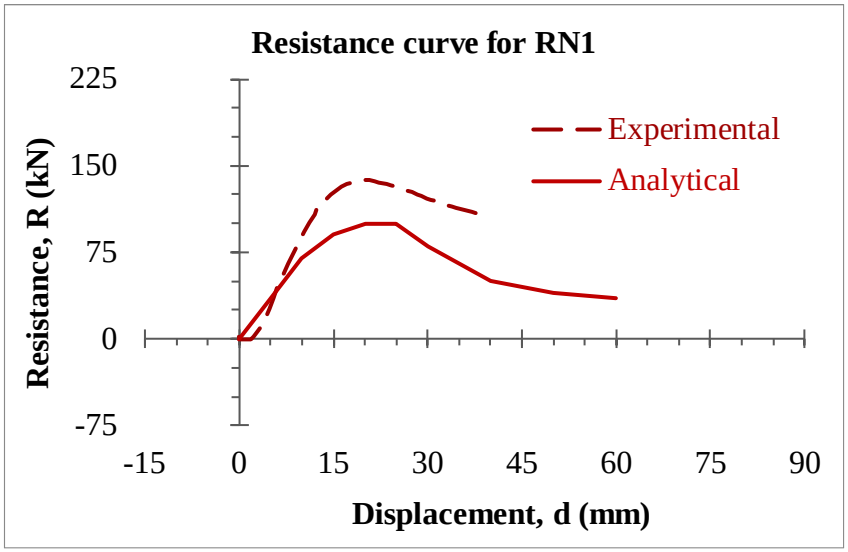

(a)

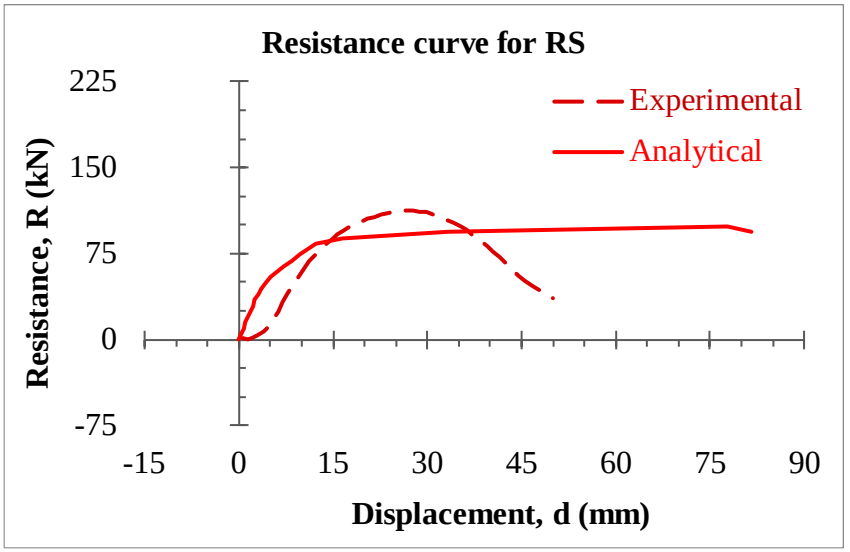

(b)

Figure 6.8 – Comparison of experimental and analytical force-displacement relationships for reference columns, a) Ref-N1, and b) Ref-S.

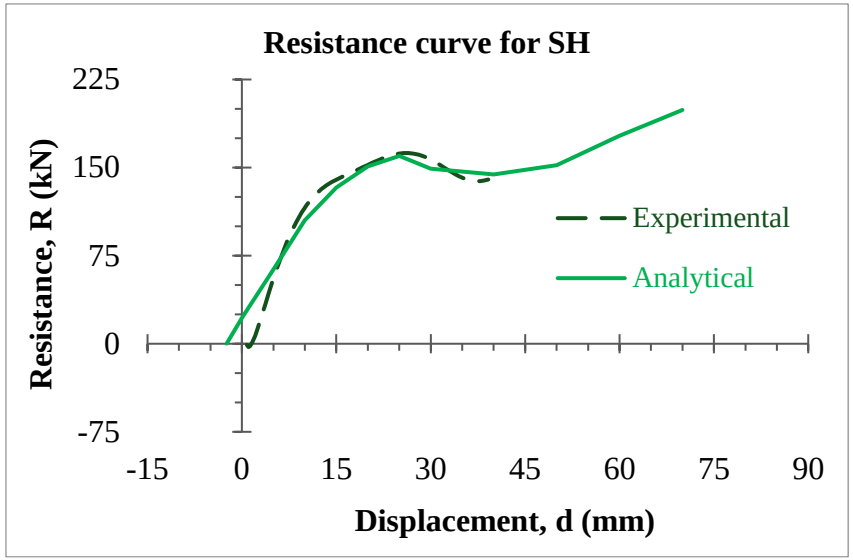

(a)

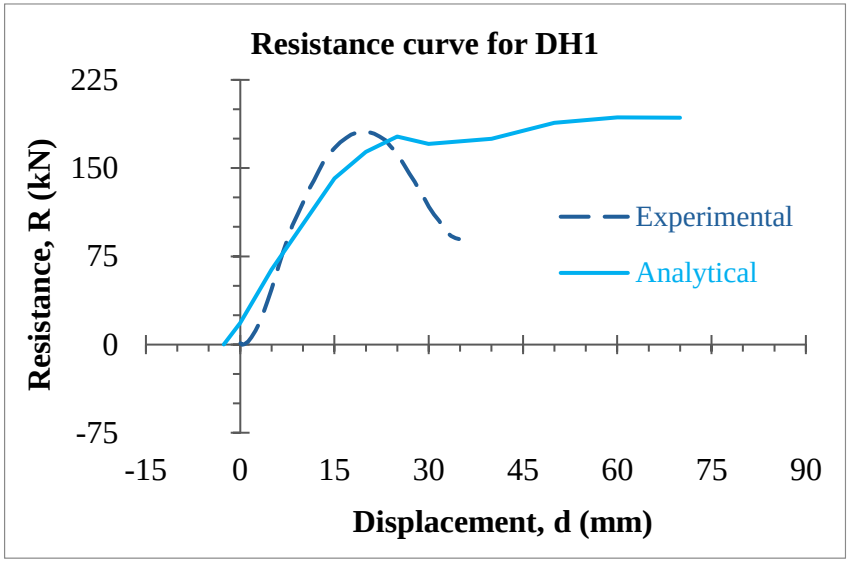

(b)

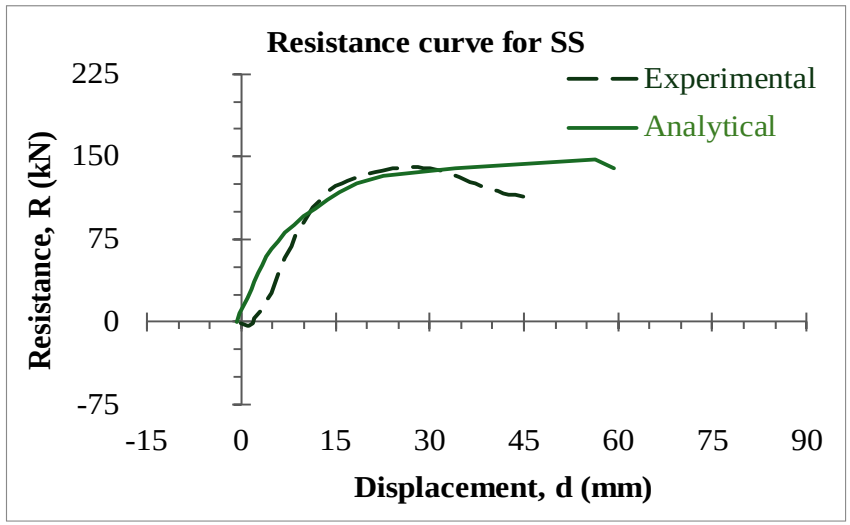

(c)

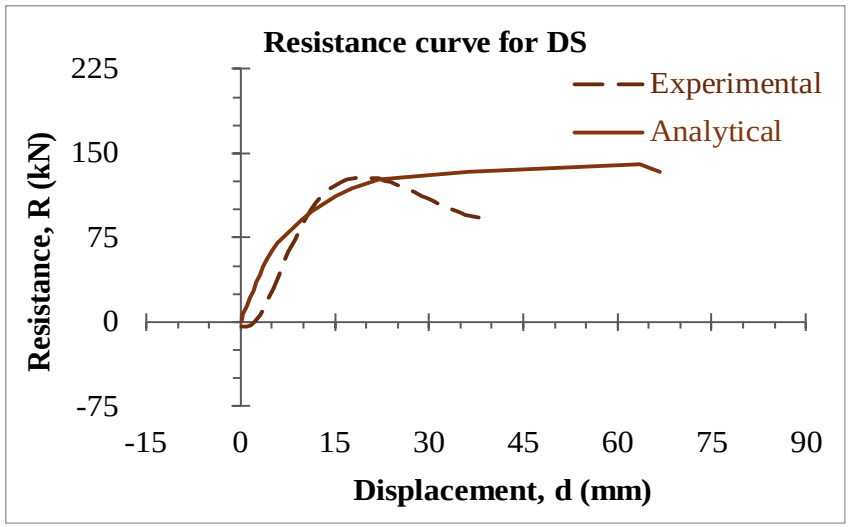

(d)

Figure 6.9 – Comparison of the experimental and analytical force-displacement relationship of hardened and post-tensioned columns, a) SH-207e-0.15fpu-N1, b) DH1-207e-0.13fpu-N1, c) PT-SS-0.35fpu-S, and d) PT-DS-0.40fpu-S.

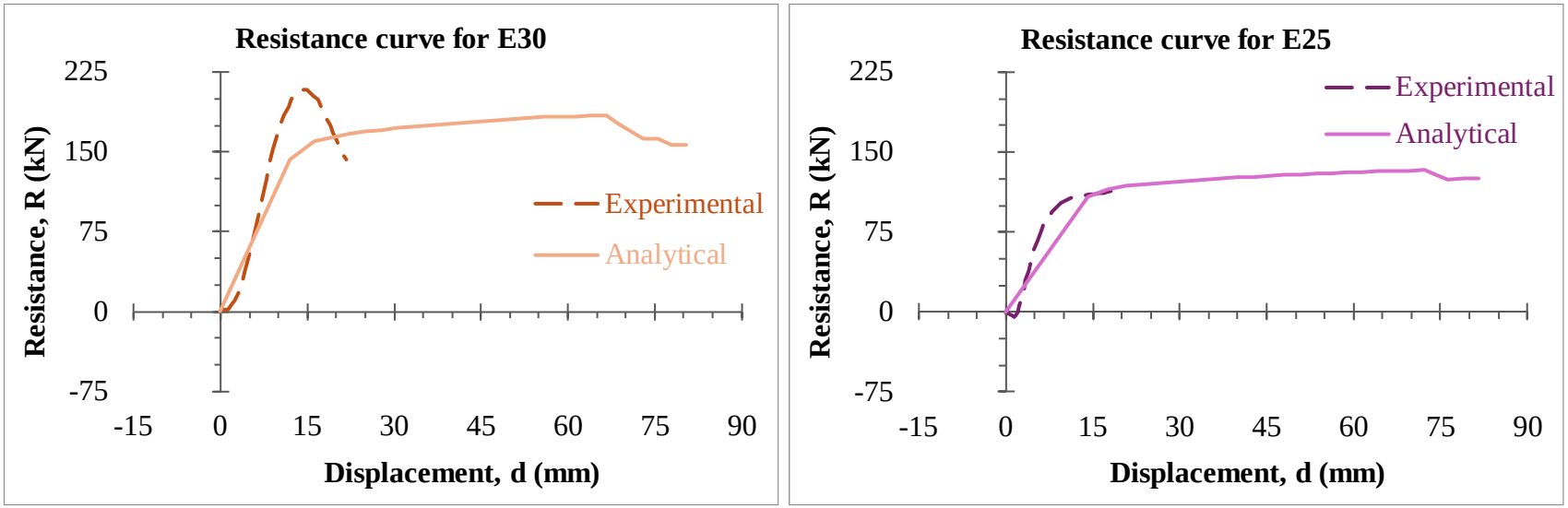

(a) (b)

Figure 6.10 – Comparison of the experimental and analytical force-displacement relationship of jacketed columns, a) ECC-2.0%v_f-t30-N1, and b) ECC-1.5%v_f-t25-N2.

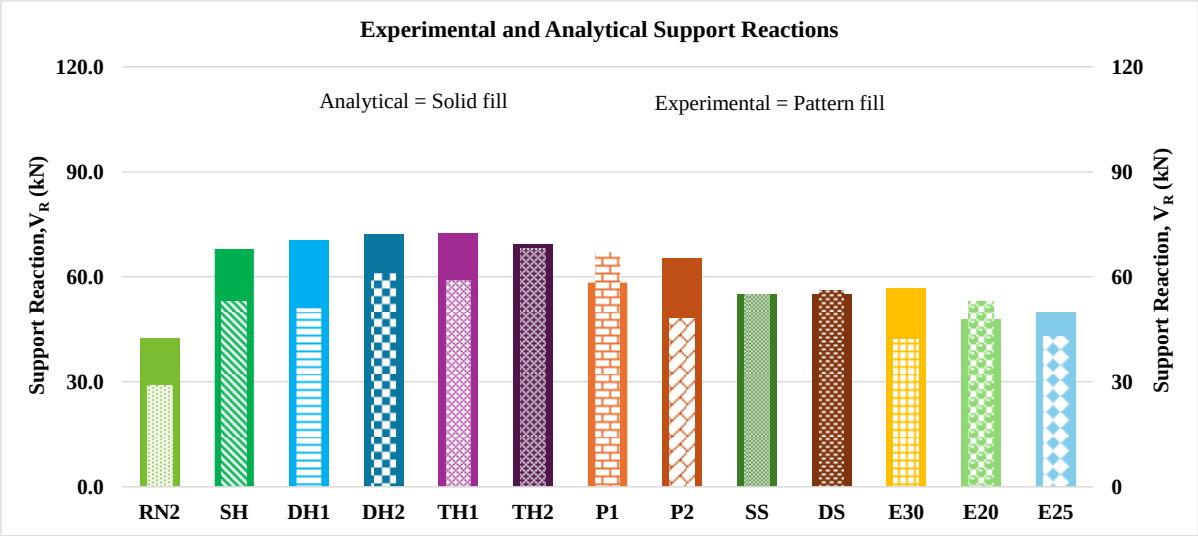

(a)

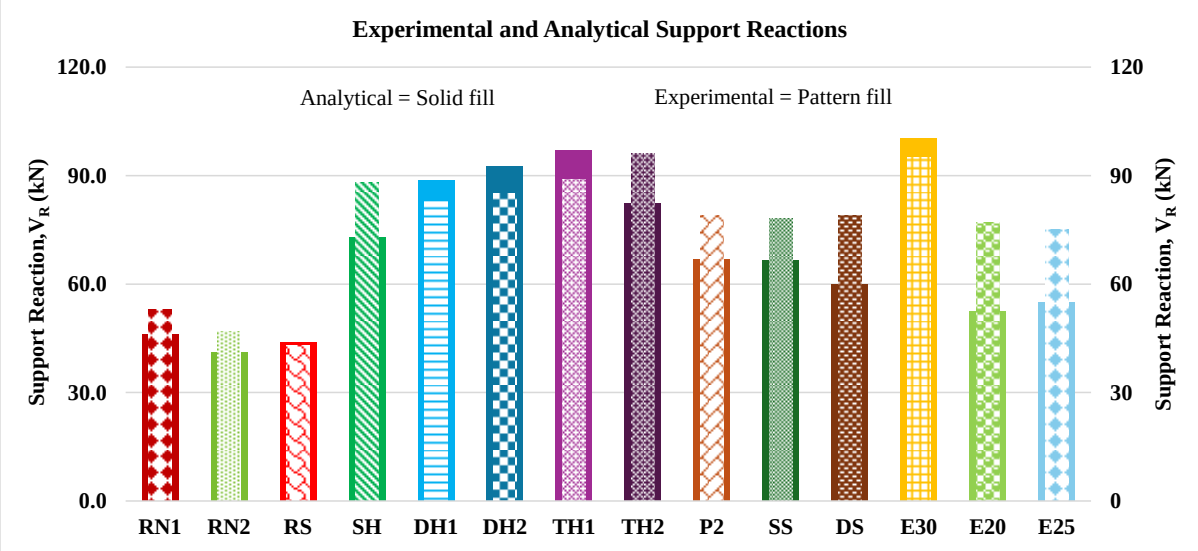

(b)

Figure 6.11 – Comparison of predicted versus experimentally measured support reactions: a) elastic behavior, b) inelastic behavior.

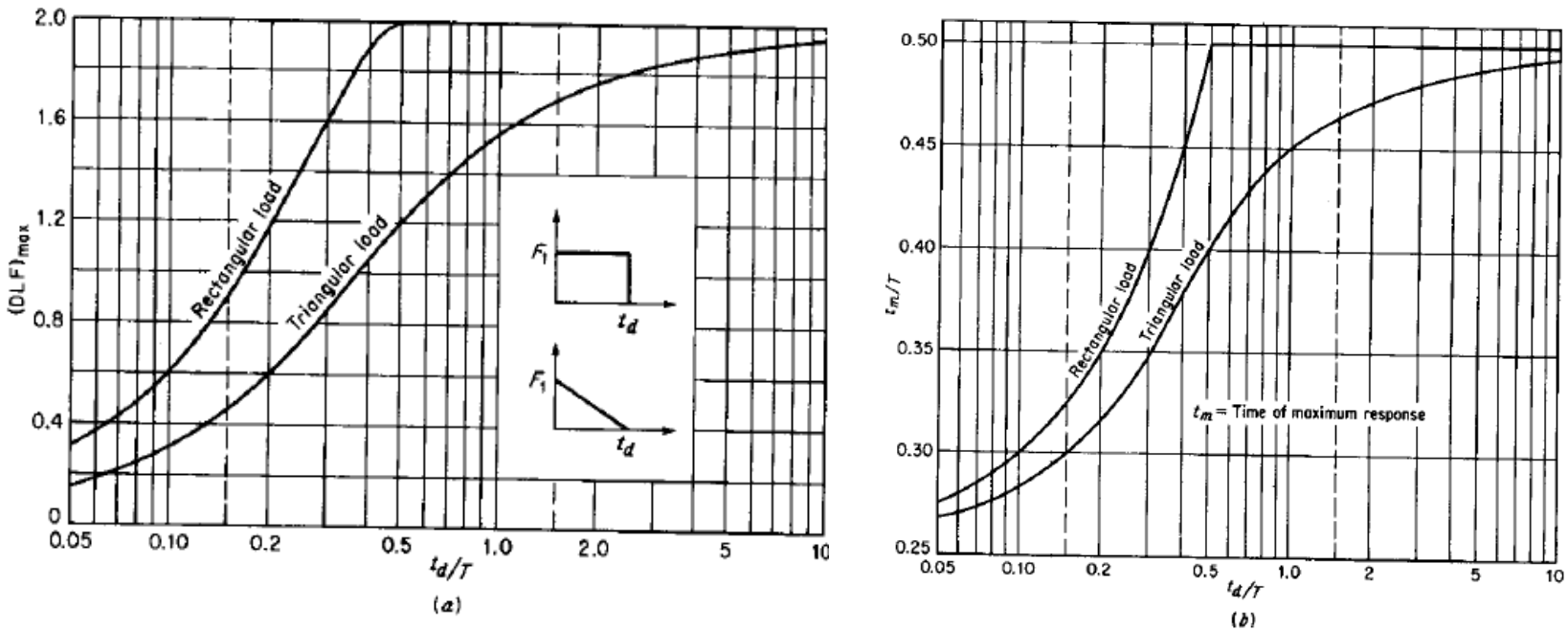

Figure 6.12 – Relationship of DLF maximum and time to maximum response with the ratio of blast duration over the natural period of a structure (source: [12]).

Chapter 7. Summary, Design Recommendations, and Conclusions

7.1 Summary

Columns of existing or new buildings designed and built without the implementation of blast standards and guidelines lack adequate resistance to blast shock waves, suffering from deficiencies in strength and deformability. Critical infrastructures with vulnerabilities against blast risk require strengthening/hardening for improved performance. The current research study comprises experimental and analytical investigations to develop innovative hardening technologies for RC columns to resist blast loads. A total of 15 columns were designed, constructed, and tested to develop the techniques. The test columns had a square cross-section with dimensions of 152 x 152 mm, a height of 2400 mm, and a clear span of 2200 mm. The columns were reinforced with four 10M longitudinal reinforcements, one in each corner. Transverse reinforcement (column ties) was in the form of closed hoops having a diameter of 6.3 mm, spaced either at half or one-quarter of the cross-sectional dimension (h/2 and h/4). Twelve columns having h/2 tie spacing were categorized as gravity/non-seismic columns. Three columns with ties of h/4 spacing along the entire column height were classified as blast-resistant columns.

The methods investigated in the current research project involve hardening of existing columns either by providing externally placed prestressing strands to generate reactive forces during blast response of a column or a jacket using an emerging cementitious high-performance material, i.e., engineered cementitious composite (ECC). The first method is based on the principles of prestressing by externally placed longitudinal 7-wire strands. Seven RC columns designed as gravity/non-blast columns were externally post-tensioned and then tested using a shock tube at the Blast Research Laboratory of the University of Ottawa. The second method involved the use of an ECC jacket with strain-hardening and high-toughness characteristics. Three gravity/non-blast columns were jacketed with a thin layer of ECC with different jacket thicknesses and fiber dosages in the ECC mix. The third technique developed is intended for newly designed blast-resistant columns. The technique involves post-tensioning of columns having blast-resistant transverse reinforcement detailing for improved strength and stability. Two columns were post-tensioned by inserting 7-wire strands through ducts provided during concrete casting. One of the columns had a single strand with a constant eccentricity on the protected side, and the other column had two strands with a constant eccentricity, one on either side. The second strand profile was

introduced to assess the significance of this type of posttensioning during rebound, as well as addressing the possibility of having a threat on either side of the column.

The columns were tested under combined axial and blast loading with simple supports at both ends. The columns were subjected to multiple blast shots generated by a shock tube capable of reproducing shock waves that are representative of high-explosive blast loads. Proper instrumentations, such as pressure sensors, strain gauges, linear variable differential transducers (LVDTs), and load cells, were used for data acquisition. In addition, high-speed cameras (one at the front and one on the side) were used to complement the recorded data. A detailed presentation and discussion of experimental research was provided, along with companion analytical research and comparisons between the two.

The analytical research consisted of an equivalent single degree of freedom (SDOF) modeling and analysis under dynamic blast loading. An essential component of analytical research was the development of resistance functions. Because of the uniqueness of the techniques developed, new procedures had to be developed and implemented for establishing the resistance functions prior to undertaking the SDOF analyses. Software RC-Blast was employed to conduct a nonlinear dynamic analysis.

7.2 Design Recommendations

7.2.1 Hardening by External Prestressing Strands

The primary purpose of providing external strands with eccentricity is to activate reactive forces against blast loads along the height of the column. The reactive forces are distributed along the height based on the strand profile. While a single-harped strand results in a single concentrated force at the location of change in the slope (typically at mid-height), strands with multiple harped profiles, especially when they approach a parabolic profile, result in well-distributed reactive forces, improving the effectiveness of the hardening techniques. Well-distributed reactive forces balance the uniformly applied blast pressure, thereby generating an effective restoring mechanism. The selection of the strand profile is also affected by the end eccentricity of the strands, which must be anchored at or near the column ends. The anchorage location and design vary depending on the geometry of the beam-column or slab-column connections and should be done carefully so as to maximize the effectiveness of the system.

Step-by-step design guidelines are provided below:

- For a given column geometry, estimate the required prestressing force and strand profile with associated eccentricities such that the stress limits in the concrete standard for the initial posttensioning load stage are not exceeded. An upper limit of the prestressing force can be selected based on the state of stress on the extreme compression and tension fibers, following the recommendation of CSA A23.3-19 (Clause 18.3.2). Equations 7.1 and 7.2 can be used to find the governing upper limit force for the case of the triple-harped and parabolic profiles, respectively, noting that the total eccentricity (e) and the end eccentricity (e') are established based on the prevailing conditions (i.e., space limitation, aesthetic concerns, accessibility, etc.). The total strand eccentricity at column mid-height is measured relative to the anchorage point, whereas the end eccentricity is measured from the anchorage point to the section centroid. Similarly, Equations 7.3 and 7.4 can be used for single and double-harped strand profiles.

$$-\frac{P}{A}-\frac{My}{I}-\frac{F_{p1}}{A}+\frac{F_{p1}ey}{I}-\frac{F_{p1}e'y}{I}=-0.6f_c'$$

$$\rightarrow\ F_{p1}=(0.6f_c'-\tfrac{P}{A}-\tfrac{My}{I})(\tfrac{AI}{I-Aey+Ae'y}) \quad (7.1)$$

$$-\tfrac{P}{A}+\tfrac{My}{I}-\tfrac{F_{p2}}{A}-\tfrac{F_{p2}ey}{I}+\tfrac{F_{p1}e'y}{I}=0.5\sqrt{f_c'}$$

$$\rightarrow\ F_{p2}=(-0.5\sqrt{f_c'}-\tfrac{P}{A}+\tfrac{My}{I})(\tfrac{AI}{I+Aey-Ae'y}) \quad (7.2)$$

$$-\frac{P}{A}-\frac{My}{I}-\frac{F_{p1,y}}{A}+\frac{F_{p1,x}\,L/_{l'}\,y}{I}-\frac{F_{p1,y}e'y}{I}=-0.6f_c'$$

$$\rightarrow\ F_{p1}=\left(0.6f_c'-\tfrac{P}{A}-\tfrac{My}{I}\right)\left(\tfrac{AI}{Isin\alpha-Acos\alpha\,L/_{l'}\,y+Asin\alpha e'y}\right) \quad (7.3)$$

$$-\frac{P}{A}+\frac{My}{I}-\frac{F_{p2,y}}{A}-\frac{F_{p2,x}\,L/_{l'}\,y}{I}+\frac{F_{p2,y}e'y}{I}=0.5\sqrt{f_c'}$$

$$\rightarrow\ F_{p1}=(-0.5\sqrt{f_c'}-\tfrac{P}{A}+\tfrac{My}{I})(\tfrac{AI}{Isin\alpha+Acos\alpha\,L/_{l'}\,y-Asin\alpha e'y}) \quad (7.4)$$

where P is the axial load from the service loads, M is the bending moment due to service loads, y is the distance from the column centroid to the extreme tension or compression fibers, A is the column cross-sectional area, I is the column moment of inertia, and F_{p1} and

F_{p2} are the upper limits of the post-tensioning force as governed by compressive and tensile stress limits, respectively. The angle α and ℓ' in Equations 7.3 and 7.4 are the angle that the strands make with the horizontal and the location of the deviator(s) from the support, respectively. The smaller of the two post-tensioning forces, F_{p1} and F_{p2}, governs the design. The level of initial prestressing force may be reduced if the initial camber is of concern.

- The governing post-tensioning force can then be used to determine the size, the number of strands, and the strand profile. Strand profiles that result in uniform or near-uniform external resisting forces provide effective levels of hardening, balancing the uniformly applied blast loads. While these profiles provide optimum load resistance, other profiles may also have sufficient effectiveness for the column geometry under consideration.
- The initial prestressing force and the strand profile established above facilitate the development of the composite resistance function (combined effects of column resistance and the additional resistance provided by external strands).
- Once the resistance function is obtained, non-linear SDOF analysis of the column is performed under the Design Basis Threat (DBT) for which the hardening system is designed. The analysis can be conducted using any applicable software. The applicability of Software RC-Blast has been validated in the current research project. If the analysis results meet the desired performance level, the analysis can be terminated. Otherwise, a second iteration can be conducted by considering different combinations of prestressing forces and eccentricities.
- The strand eccentricity determined as described in the preceding steps can be implemented during construction with the use of properly designed deviators. Deviators should be made of high-strength material to remain rigid and maintain their integrity during blast loading. If deviators deform and bend, they will result in prestress losses. In addition, they should be secured on the column to prevent their movement. The available space and aesthetic limitations may play additional roles during the selection of the deviators.
- Anchorage of the prestressing strands should be designed to have sufficient strength and rigidity to prevent any prestress loss both during the initial prestressing phase and under blast loading. Any connection or shear pins used for the end fixture should be made of high-strength material to avoid shear failure and dismantling of the anchorage assembly.

- Post tensioning of strands can be done using traditional jacking techniques or manually by means of splice tensioner chucks, which are ideal for post-tensioning of the strands used in the proposed hardening procedure. They provide easy manual stressing by wrenches and allow for future re-stressing if necessary.
- The strands, deviators, and end fixtures must be protected against environmental factors, such as corrosion, chemical attack, and vandalism. The use of sleeved strands, galvanized or stainless steel fixtures, or sacrificial corrosion elements can help reduce the risk of corrosion. In addition, the use of false column covers adds to the protection of the hardware while improving aesthetic appearance.

7.2.2 Posttensioning by Internal Prestressing

Prestressing axially loaded members, such as columns, is not a common practice. However, prestressing enhances column stability and shear resistance. In the event of blast loading, columns can fail due to loss of stability. Therefore, prestressing can be a possible solution, particularly for internal post-tensioning of newly designed columns as opposed to the hardening of existing columns addressed in the previous section. Prestressing provides an additional reinforcement for columns while providing internal resistance to blast loads. The design procedure for internal posttensioning will follow the conventional prestressed concrete design procedures. The steps outlined in the previous section for hardening of columns by means of external strands will also apply to the design for internal posttensioning. The prestressing forces and eccentricities will have to be established such that the stress limits specified in CSA A23.3- 19 will not be exceeded. One significant difference is in establishing the eccentricity and the strand profile, as in this case, the maximum eccentricity is governed by the section size. Another difference may be the location of the threat; internal post-tensioning may be done on one side of the column if the threat is known to be on one side or on both sides if there is the possibility of threat location changing, and/or if the rebound effects need to be considered. Additional factors that need to be considered in the design include the relatively higher levels of prestressing forces (due to the limited eccentricity of strands), which may increase axial compression caused by external loads. Lastly, the difference in anchorage design should also be taken into account.

The analysis of columns for design follows the steps as those discussed for external post-tensioned as hardening methodology, except for the manner in which the resistance function is developed. The computation of the resistance function for internally post-tensioned columns

requires conventional methods of developing the column force-displacement relationship, starting with sectional analysis with due considerations given to the effects of prestressing. In the current research project, this was done by employing Software Response-2000, which has the capability of analyzing prestressed concrete elements. Once the resistance function is established, conducting nonlinear dynamic analysis can be done in much the same manner as for hardened columns by external prestressing using appropriate software that employs a numerical technique. The software RC-Blast used in the current research project provides a convenient tool to compute dynamic displacements, which can be linked to response limits and damage levels, leading to levels of protection to be checked and verified.

7.2.3 Hardening using ECC Jacketing

Jacketing is a known technique for improving the strength and deformability of columns. Often, steel or reinforced concrete jackets are used with significant structural interference and construction efforts on existing columns. ECC jacketing was investigated in current research with proven improvements in blast resistance. ECC is an emerging construction material with strain-hardening and toughness, unlike other conventional cementitious materials. It can be applied as a thin layer without requiring steel reinforcement.

A primary consideration in design is the superior toughness and deformability of ECC, and hence, the mix design for the material is of paramount importance. While 2% polyethylene discrete macro fibers (approximately 12 mm or 6 mm lengths) mixed with cement paste can be considered a standard mix, there are variations in mix design that may be considered. Careful consideration should be given to the workability of the mix to ensure proper consolidation of ECC, especially when a very thin layer is designed. The jacket thickness can be established through an iterative procedure. For existing columns, either removing the cover concrete and replacing it with ECC or enlarging the section by adding an ECC layer with an equivalent thickness to the concrete cover may form the initial trial thickness. Depending on the additional demand-capacity ratio, the ECC layer can be customized in terms of the layer thickness and/or fiber dosage to obtain the desired result. The iterations of the thickness layer can begin with an initial guess, followed by a sectional analysis. The new section is then analyzed with stress-strain relationships for existing concrete and ECC to establish the moment-curvature relationship, which can then be used to construct force-displacement relations as the resistance function. The resistance function is used to establish the column stiffness during numerical dynamic analysis. As before for the previous design procedures,

SDOF analysis of the ECC jacketed column can be conducted to assess its dynamic response and associated damage level, and the level of protection. The toughness of the material ensures enhanced deformability during response. Once the desired level of protection is obtained, the final design is achieved.

The design should ensure a perfect bond between ECC and the existing substrate, which is not difficult to achieve if appropriate surface preparation is done. Bond should not be a concern in this application since ECC is a cement-based material that is compatible with existing concrete surfaces. Providing a rough surface as required by ICRI (International Concrete Repair Institute) is a feasible approach to improve the bond during blast loading. A minimum effort for surface preparation will be to perform dust removal and spray water on the surface. Sided or full jacketing options can be implemented depending on the intended increase in the blast resistance of the jacketed column, with due consideration given to physical constraints. Shotcreting is a viable option for the application of ECC.

7.3 Conclusions

A combined experimental and analytical research was conducted to develop new and innovative column hardening and strengthening methodologies to resist blast-induced shock waves. The results are summarized below:

- The new techniques developed for hardening of existing concrete columns by providing external resisting forces via prestressing strands or jacketing with ECC prove to be effective in resisting blast loads. Post-tensioning of columns designed for new construction is equally effective in strengthening columns. The new technologies were validated through shock tube tests of the columns considered in the current investigation with blast loads of up to 75 kPa and 630 kPa-ms, developing superficial to moderate damage, in comparison with companion unhardened columns that showed heavy to hazardous damage at a lower pressure-impulse combination. In general, the hardened columns resisted between 20% and 40 % higher blast loads as compared to their companion reference columns. The hardened columns behaved elastically during a load stage at which the reference columns experienced moderate to heavy damage.
- Reference columns without hardening or strengthening suffered premature failures and developed plastic deformations in their critical regions near mid-column height. The

observed column failures were in flexural mode, resulting in the crushing of concrete. The columns developed heavy damage at a pressure-impulse combination of 35 kPa – 303 kPa-ms with support rotations in excess of 3-degrees and hazardous failure at 55 kPa – 384 kPa-ms at a support rotation in excess of 8-degrees. The column with blast detailing in the form of closely spaced hoops showed improved behavior and well-distributed cracks prior to failure at a higher pressure-impulse combination of 43 kPa–415 kPa-ms with a support rotation in excess of 8 degrees.

- The enhancement observed in columns hardened by external prestressing was due to the restoring force provided by the prestressing strands acting against the applied blast forces. All the strand profiles considered in the test program showed good performance under pressure impulse combinations ranging between 45 kPa – 430 kPa-ms and 58 kPa – 420 kPa-ms (during second shots) developing less than 3 degrees of support rotation with 1-degree of rotation at the residual deformation stage, showing moderate damage prior to the last shot (shot#3) that caused heavy damage. All the columns in this group failed near the critical mid-height region except for the column that had a double-harped strand profile, which failed exactly at the mid-height. In the former case, one of the restoring force components was located at exactly the mid-height location, thereby forcing the failure region to occur either slightly above or below the mid-height region.
- The post-tensioned columns with internal prestressing strands outperformed their companion reference column without the post-tensioning, as expected. The improved performance was due to the additional flexural resistance and stability provided by the strands. These columns exhibited more damage than the columns hardened by external strands because of the smaller internal eccentricity, which was limited by the column dimension and the inefficiency of the constant eccentricity strand profile used. The columns developed superficial damage when subjected to a reflected pressure impulse combination of 29 kPa – 268 kPa-ms and heavy damage under an increased blast load of 44 kPa- 415 kPa-ms, showing up to 3-degree support rotation. When the impulse reached around 600 kPa-ms at the final blast shot, the columns were fully damaged to a hazardous level. The column with a single prestressing strand (placed only over the protected side) performed slightly better than that with double strands. This can be explained by the initial camber introduced by the single strand toward the threat side.

- The ECC jacketed columns performed significantly better than their companion reference columns, developing superficial damage at 39 kPa-272 kPa-ms in comparison to unhardened columns, which showed moderate to heavy damage at the same load stage. The better performance of these columns was mainly due to strain hardening and toughness of the ECC shell with considerable effect of layer thickness changing the cross section dimensions. The column with a 30 mm thick ECC jacket showed the best performance when compared with columns having 20 mm or 25 mm jacket thickness, developing 0.6-degree support rotation in comparison with jackets having reduced thickness, which developed 1.5-degree rotation at the same level of blast load. The column with 30 mm ECC jacket was able to resist more than 600 kPa-ms before it showed hazardous failure, which was one of the highest blast loads reported in this research project. With the reduction in ECC jacket thickness, the enhancement in blast resistance gradually diminished. The column with a 25 mm thick ECC shell exhibited heavy damage at an impulse of 536 kPa-ms, while the column with a 20 mm thick ECC jacket experienced heavy damage at an impulse of 394 kPa-ms.
- A careful comparison of the behavior of the two methods developed for hardening existing columns (external prestressing and ECC jacketing) suggests that both methods have their advantages. External prestressing may look more appropriate for occasions where the direction of a threat from an explosion can be determined. However, when protection is needed along any axis of the column, ECC jacketing should be considered. ECC jacketing is also an option when a proper anchorage platform is not available in the vicinity of the column under consideration.
- The methodology employed in the current research project for generating resistance functions to conduct SDOF nonlinear dynamic analysis while considering secondary moments due to P-delta effects results in good correlations with test data. Hence, the approach followed can be used as a design tool for the analysis and design of columns in implementing the techniques developed.
- The design procedure outlined in this Chapter can be followed in practice for hardening/strengthening of reinforced concrete columns for blast risk mitigation.

7.4 Future Work Recommendations

The current research project included extensive experimental and analytical research for hardening/strengthening of reinforced concrete columns against blast threats utilizing new and innovative technologies. Further research to expand the scope of this project can enhance the knowledge gained and the techniques developed. In particular, the following are recommended for future research.

- Behavior of the columns when subjected to a single blast shot compared to multiple shots performed in this study.
- The effects of initial prestressing force level and the use of different size deviators on column performance.
- Variations in end anchorage characteristics, including the location and configuration of end fixtures and consideration of anchoring the strands to adjacent members rather than the column itself.
- Placing the external prestressing strands on both sides of the columns for protection against possible threats from either direction.
- Tests of columns with different internal post-tensioning strand profiles for improved blast load resistance to be used in new construction.
- Tests of columns with different configurations of ECC layers, involving one-sided or two-sided applications to improve column resistance on the tension side or tension and compression sides, which reduces the use of ECC while providing a practical solution when accessibility becomes a challenge.
- Research on the effects of ECC mix characteristics and jacket thickness on column performance.

References

[1] T. Roy and V. Matsagar, "Probabilistic framework for failure investigation of reinforced concrete wall panel under dynamic blast loads," *Eng Fail Anal*, vol. 125, Jul. 2021, doi: 10.1016/j.engfailanal.2021.105368.

[2] "Wikipedia," https://en.wikipedia.org/wiki/Car_bomb.

[3] A. Meena, A. Singh Jethoo, and P. V. Ramana, "Impact of blast loading over reinforced concrete without infill structure," in *Materials Today: Proceedings*, Elsevier Ltd, 2021, pp. 8783–8789. doi: 10.1016/j.matpr.2021.04.139.

[4] A. Goswami and S. Das Adhikary, "Retrofitting materials for enhanced blast performance of Structures: Recent advancement and challenges ahead," Apr. 20, 2019, *Elsevier Ltd*. doi: 10.1016/j.conbuildmat.2019.01.188.

[5] L. J. Malvar, J. E. Crawford, and K. B. Morrill, "Use of Composites to Resist Blast," *Journal of Composites for Construction ASCE*, 2007, doi: 10.1061/ASCE1090-0268200711:6601.

[6] Y. Liu, J. Yan, Z. Li, and F. Huang, "Improved SDOF and numerical approach to study the dynamic response of reinforced concrete columns subjected to close-in blast loading," *Structures*, vol. 22, pp. 341–365, Dec. 2019, doi: 10.1016/j.istruc.2019.08.014.

[7] D. Lange, "A review of blast loading and explosions in the context of multifunctional buildings," in *SP Technical Research Institute of Sweden*, 2013.

[8] M. Y. H. Bangash and · T Bangash, *Explosion-Resistant Buildings*. Springer, 2006.

[9] A. Lloyd, "Blast Retrofit of Reinforced Concrete Columns," in *Ph.D. Dissertation, University of Ottawa*, 2014.

[10] Federal Emergency Management Agency (FEMA), "Risk Management Series Primer for Design of Commercial Buildings to Mitigate Terrorist Attacks," in *Department of Homeland Security US*, 2003. [Online]. Available: www.fema.gov

[11] Army Corps U.S., Naval Facilities Engineering Comman, and Air Force Civil Engineer Support Agency, *Structures to Resist the Effects of Accidental Explosions, TM5-1300*. 1990.

[12] J. M. Biggs, *Introduction to Structural Dynamics*. McGraw-Hill, 1964.

[13] S. Marjanishvili and I. Alsharkawi, "Blast and Impact Effects on Structures," in *Structural Engineering and Geomechanics*, 2012. Accessed: May 20, 2023. [Online]. Available: https://www.eolss.net/outlinecomponents/structural-engineering-geomechanics.aspx

[14] P. A. Shirbhate and M. D. Goel, "A Critical Review of Blast Wave Parameters and Approaches for Blast Load Mitigation," *Archives of Computational Methods in Engineering*, vol. 28, no. 3, pp. 1713–1730, May 2021, doi: 10.1007/s11831-020-09436-y.

[15] C. M. Harris and A. G. Piersol, *Harris' Shock and Vibration Handbook*, Fifth. McGraw-Hill, 2002.

[16] G. F. Kinney and K. J. Graham, *Explosive Shocks in Air*, Second Edition. Springer Science+Business Media, LLC, 1985.

[17] H. L. Brode, "Numerical solutions of spherical blast waves," *J Appl Phys*, vol. 26, no. 6, pp. 766–775, 1955, doi: 10.1063/1.1722085.

[18] Smith P.D. and Hetherington J.G., *Blast and Ballistic Loading of Structures*. Routledge Taylor & Francis Group, 1994.

[19] A. C. of E. U.S., Naval Facilities Engineering Comman, and Air Force Civil Engineer Support Agency, "Unified Facilities Criteria (UFC): Structures to Resist the Effects of Accidental Explosions," 2005. [Online]. Available: http://dod.wbdg.org/.

[20] W. E. Baker, *Explosion hazards and evaluation*. Elsevier Scientific Pub. Co, 1983.

[21] M. V Dharaneepathy, M. N. Keshava Raot, and A. R. Santhakumar, "Critical Distance for Blast-Resistant Design," *Compurrrs & Srrucrures*, vol. 54, no. 4, pp. 587–595, 1995.

[22] "Fundamentals of Protective Design for conventional Weapons, TM 5-855-1," 1986.

[23] Philip. Miller, "Towards the modelling of blast loads on structures.," in *Master Thesis, University of Toronto*, 2004.

[24] Applied Research Associates (ARA), "A.T. Blast," https://www.ara.com/at-blast/.

[25] D. Cormie, G. Mays, and P. Smith, *Blast Effects on Buildings*. Thomas Telford, 2022.

[26] E. Jacques, A. Lloyd, and M. Saatcioglu, "Predicting reinforced concrete response to blast loads," *Canadian Journal of Civil Engineering*, vol. 40, no. 5, pp. 427–444, Jan. 2013, doi: 10.1139/L2012-014.

[27] U.S. Army Corps of Engineers Protective Design Center, "Single Degree of Freedom Blast Effects Design Spreadsheets."

[28] "Column Blast Analysis Retrofit Design (CBARD)," https://www.kcse.com/column-blast-analysis-retrofit-design/.

[29] A. K. Chopra, *Dynamics of Structures*, Fourth Edition. Prentice Hall Pearson, 2012.

[30] Task Commitee on Blast Resistant Design of the Petrochemical Committee of the Energy Division of the ASCE, *Design of Blast Resistant Buildings in Petrochemical Facilities*. ASCE, 1999.

[31] Y. Liu, J. bo Yan, and F. lei Huang, "Behavior of reinforced concrete beams and columns subjected to blast loading," *Defence Technology*, vol. 14, no. 5, pp. 550–559, Oct. 2018, doi: 10.1016/j.dt.2018.07.026.

[32] C. J. Oswald, “Comparison of Response from Combined Axial and Blast Loads Calculated with SDOF and Finite Element Methods,” 2010.

[33] H. Al-Thairy, “A modified single degree of freedom method for the analysis of building steel columns subjected to explosion induced blast load,” *Int J Impact Eng*, vol. 94, pp. 120–133, Aug. 2016, doi: 10.1016/j.ijimpeng.2016.04.007.

[34] S. Astarlioglu, T. Krauthammer, D. Morency, and T. P. Tran, “Behavior of reinforced concrete columns under combined effects of axial and blast-induced transverse loads,” *Eng Struct*, vol. 55, pp. 26–34, Oct. 2013, doi: 10.1016/j.engstruct.2012.12.040.

[35] M. D. Goel and V. A. Matsagar, “Blast-Resistant Design of Structures,” *Practice Periodical on Structural Design and Construction*, vol. 19, no. 2, May 2014, doi: 10.1061/(asce)sc.1943-5576.0000188.

[36] J. Sakula, “The design of building facades for blast resistance,” in *Building Envelope Technology (ICBEST’97)*, S. Ledbetter and R. Harris, Eds., 1997.

[37] N. Torunbalci, Z. Koccaz, and F. Sutcu, “Architectural and Structural Design for Blast Resistant Buildings,” in *The 14th World Conference on Earthquake Engineering*, Beijing, China, Oct. 2008. [Online]. Available: https://www.researchgate.net/publication/228698492

[38] “Polyurea Coatings: The Basics ,” https://www.waterproofmag.com/2014/10/polyurea-coatings-the-basics/.

[39] N. Iqbal, M. Tripathi, S. Parthasarathy, D. Kumar, and P. K. Roy, “Polyurea coatings for enhanced blast-mitigation: A review,” 2016, *Royal Society of Chemistry*. doi: 10.1039/c6ra23866a.

[40] S. Vavilala, P. Shirbhate, J. Mandal, and M. D. Goel, “Blast mitigation of RC column using polymeric foam,” in *Materials Today: Proceedings*, Elsevier Ltd, 2019, pp. 1347–1351. doi: 10.1016/j.matpr.2020.02.273.

[41] M. Saatcioglu, A. Lloyd, E. Jacques, A. Braimah, and G. Doudak, “Focused research for the development of a CSA standard on design and assessment of buildings subjected to blast loads,” 2011.

[42] R. Tahzeeb, M. Alam, and S. M. Muddassir, “Effect of transverse circular and helical reinforcements on the performance of circular RC column under high explosive loading,” *Mater Today Proc*, vol. 64, pp. 315–324, Jan. 2022, doi: 10.1016/j.matpr.2022.04.676.

[43] C. Kyei and A. Braimah, “Effects of transverse reinforcement spacing on the response of reinforced concrete columns subjected to blast loading,” *Eng Struct*, vol. 142, pp. 148–164, Jul. 2017, doi: 10.1016/j.engstruct.2017.03.044.

[44] F. Siba, “Near-Field Explosion Effects on Reinforced Concrete Columns: An Experimental Investigation,” 2014.

[45] B. Kadhom, H. Almansour, and M. Saatcioglu, “Structural Performance of Seismically Versus Non-Seismically RC Columns Subjected to Simulated Blast Loads,” in *The 2nd International Conference of Buildings, Construction and Environmental Engineering (BCEE-2015)* , 2015.

[46] X. Bao and B. Li, “Residual strength of blast damaged reinforced concrete columns,” *Int J Impact Eng*, vol. 37, no. 3, pp. 295–308, Mar. 2010, doi: 10.1016/j.ijimpeng.2009.04.003.

[47] E. B. Williamson, O. Bayrak, C. Davis, and G. D. Williams, “Performance of Bridge Columns Subjected to Blast Loads. I: Experimental Program,” *Journal of Bridge Engineering*, vol. 16, no. 6, pp. 693–702, Nov. 2011, doi: 10.1061/(asce)be.1943-5592.0000220.

[48] E. B. Williamson, O. Bayrak, C. Davis, and G. Daniel Williams, “Performance of Bridge Columns Subjected to Blast Loads. II: Results and Recommendations,” *Journal of Bridge Engineering*, vol. 16, no. 6, pp. 703–710, Nov. 2011, doi: 10.1061/(asce)be.1943-5592.0000221.

[49] G. D. Williams, E. B. Williamson, K. A. Marchand, A. E. McKay, S. Antonio, and O. Bayrak, “Design and Detailing Guidelines for Bridge Columns Subjected to Blast and other Extreme Loads,” *Structures Congress ASCE*, 2009.

[50] A. Lloyd, “Performance of Reinforced Concrete Columns Under Shock Tube Induced Shock Wave Loading,” in *Master of Science Thesis, University of Ottawa*, Ottawa, 2010.

[51] N. H. Yi, J. H. J. Kim, T. S. Han, Y. G. Cho, and J. H. Lee, “Blast-resistant characteristics of ultra-high strength concrete and reactive powder concrete,” *Constr Build Mater*, vol. 28, no. 1, pp. 694–707, Mar. 2012, doi: 10.1016/j.conbuildmat.2011.09.014.

[52] D. Y. Yoo and N. Banthia, “Mechanical and structural behaviors of ultra-high-performance fiber-reinforced concrete subjected to impact and blast,” Sep. 15, 2017, *Elsevier Ltd*. doi: 10.1016/j.conbuildmat.2017.05.136.

[53] A. Hammoud, J. Yan, Y. Li, and H. Aoude, “Blast behavior of columns built with high-strength concrete and grade 690 mpa high-strength reinforcement,” *Canadian Journal of Civil Engineering*, vol. 48, no. 11, pp. 1422–1439, 2021, doi: 10.1139/cjce-2019-0554.

[54] J. Xu *et al.*, “Behaviour of ultra high performance fibre reinforced concrete columns subjected to blast loading,” *Eng Struct*, vol. 118, pp. 97–107, Jul. 2016, doi: 10.1016/j.engstruct.2016.03.048.

[55] H. Aoude, F. P. Dagenais, R. P. Burrell, and M. Saatcioglu, “Behavior of ultra-high performance fiber reinforced concrete columns under blast loading,” *Int J Impact Eng*, vol. 80, pp. 185–202, 2015, doi: 10.1016/j.ijimpeng.2015.02.006.

[56] R. P. Burrell, H. Aoude, and M. Saatcioglu, “Response of SFRC Columns under Blast Loads,” *Journal of Structural Engineering*, vol. 141, no. 9, Sep. 2015, doi: 10.1061/(asce)st.1943-541x.0001186.

[57] S. Astarlioglu and T. Krauthammer, “Response of normal-strength and ultra-high-performance fiber-reinforced concrete columns to idealized blast loads,” *Eng Struct*, vol. 61, pp. 1–12, Mar. 2014, doi: 10.1016/j.engstruct.2014.01.015.

[58] Y. Cui, M. Song, Z. Qu, S. Sun, and J. Zhao, “Research on damage assessment of concrete-filled steel tubular column subjected to near-field blast loading,” *Shock and Vibration*, vol. 2020, 2020, doi: 10.1155/2020/8883711.

[59] M. Li, Z. Zong, H. Hao, X. Zhang, J. Lin, and G. Xie, “Experimental and numerical study on the behaviour of CFDST columns subjected to close-in blast loading,” *Eng Struct*, vol. 185, pp. 203–220, Apr. 2019, doi: 10.1016/j.engstruct.2019.01.116.

[60] F. Zhang, C. Wu, X. L. Zhao, A. Heidarpour, and Z. Li, “Experimental and numerical study of blast resistance of square CFDST columns with steel-fibre reinforced concrete,” *Eng Struct*, vol. 149, pp. 50–63, Oct. 2017, doi: 10.1016/j.engstruct.2016.06.022.

[61] H. Wang *et al.*, “Experimental study of large-sized concrete filled steel tube columns under blast load,” *Constr Build Mater*, vol. 134, pp. 131–141, Mar. 2017, doi: 10.1016/j.conbuildmat.2016.12.096.

[62] S. Fujikura, M. Asce, M. Bruneau, and D. Lopez-Garcia, “Experimental Investigation of Multihazard Resistant Bridge Piers Having Concrete-Filled Steel Tube under Blast Loading,” *Journal of Bridge Engineering ASCE*, vol. 13, no. 6, 2008, doi: 10.1061/ASCE1084-0702200813:6586.

[63] S. Fujikura and M. Bruneau, “Experimental Investigation of Seismically Resistant Bridge Piers under Blast Loading,” *Journal of Bridge Engineering*, vol. 16, no. 1, pp. 63–71, Jan. 2011, doi: 10.1061/(asce)be.1943-5592.0000124.

[64] D. K. Thai, T. H. Pham, and D. L. Nguyen, “Damage assessment of reinforced concrete columns retrofitted by steel jacket under blast loading,” *Structural Design of Tall and Special Buildings*, vol. 29, no. 1, Jan. 2020, doi: 10.1002/tal.1676.

[65] M. Esmaeilnia Omran and S. Mollaei, “Investigation of Axial Strengthened Reinforced Concrete Columns under Lateral Blast Loading,” *Shock and Vibration*, vol. 2017, 2017, doi: 10.1155/2017/3252543.

[66] P. Fouché, M. Bruneau, and V. P. Chiarito, “Modified Steel-Jacketed Columns for Combined Blast and Seismic Retrofit of Existing Bridge Columns,” *Journal of Bridge Engineering*, vol. 21, no. 7, Jul. 2016, doi: 10.1061/(asce)be.1943-5592.0000882.

[67] Y. Hu, L. Chen, Q. Fang, X. Kong, Y. Shi, and J. Cui, “Study of CFRP retrofitted RC column under close-in explosion,” *Eng Struct*, vol. 227, Jan. 2021, doi: 10.1016/j.engstruct.2020.111431.

[68] B. Kadhom, H. Almansour, and M. Saatcioglu, “Effect of CFRP Laminate Design on Blast Behavior of RC Columns,” in *The 2nd International Conference of Buildings, Construction and Environmental Engineering (BCEE2-2015)*, 2015.

[69] J. O. Berger, P. J. Heffernan, and R. G. Wight, “Blast testing of CFRP and SRP strengthened RC columns,” in *WIT Transactions on State of the Art in Science and Engineering*, 2012, pp. 189–198. doi: 10.2495/978-1-84564-750-6/18.

[70] H. M. Elsanadedy, T. H. Almusallam, H. Abbas, Y. A. Al-Salloum, and S. H. Alsayed, “Effect of blast loading on CFRP-Retrofitted RC columns-a numerical study,” *Latin American Journal of Solids and Structures*, vol. 8, pp. 55–81, 2011.

[71] T. Rodriguez-Nikl *et al.*, “Carbon Fiber Composite Jackets to Protect Reinforced Concrete Columns against Blast Damage,” *Structures Congress ASCE*, 2009.

[72] J. E. Crawford, L. J. Malvar, B. W. Dunn, and D. J. Gee, “Retrofit of Reinforced Concrete Columns Using Composite Wraps to Resist Blast Effects,” in *Karagozian & Case, Structural Engineers and Hexcel Fyfe Company*, 1996.

[73] J. Wang, W. Yuan, R. Feng, J. Guo, and X. Dang, “Dynamic performances of ultra-high-performance fiber-reinforced concrete–strengthened concrete columns subjected to blast impacts,” *Advances in Structural Engineering*, vol. 23, no. 14, pp. 3009–3023, Oct. 2020, doi: 10.1177/1369433220924797.

[74] R. Codina, D. Ambrosini, and F. de Borbón, “Alternatives to prevent the failure of RC members under close-in blast loadings,” *Eng Fail Anal*, vol. 60, pp. 96–106, Feb. 2016, doi: 10.1016/j.engfailanal.2015.11.038.

[75] Y. Qasrawi, P. J. Heffernan, and A. Fam, “Performance of Concrete-Filled FRP Tubes under Field Close-in Blast Loading,” *Journal of Composites for Construction*, vol. 19, no. 4, Aug. 2015, doi: 10.1061/(asce)cc.1943-5614.0000502.

[76] “Global Terrorism Index,” 2023. [Online]. Available: http://visionofhumanity.org/resources

[77] V. Karlos, G. Solomos, and M. Larcher, “Analysis of blast parameters in the near-field for spherical free-air explosions 2016 EUR 27823,” 2016.

[78] J. Y. Lee, H. Aoude, Y. S. Yoon, and D. Mitchell, “Impact and blast behavior of seismically-detailed RC and UHPFRC-Strengthened columns,” *Int J Impact Eng*, vol. 143, Sep. 2020, doi: 10.1016/j.ijimpeng.2020.103628.

[79] CSA Standard A23.3, “Design of concrete structures,” 2019. [Online]. Available: www.ShopCSA.ca

[80] ICRI, “ICRI standard 310.2 selecting and specifying Concrete surface preparation for sealers, coatings, polymer overlays, and concrete repair with CSP chips,” 2013.

[81] Canadian Precast/Prestressed Concrete Institute., *Design manual : precast and prestressed concrete.* 2017.

[82] B. Kadhom, “Blast Performance of Reinforced Concrete Columns Protected by FRP Laminates,” PhD Dissertation, University of Ottawa, 2016.

[83] CSA S850, “Design and Assessment of Buildings Subjected to Blast Loads,” 2017.

[84] M. Saatcioglu and S. R. Razvi, “Strength and Ductility of Confined Concrete,” *Journal of Structural Engineering*, vol. 118, no. 6, pp. 1590–1607, Jun. 1992, doi: 10.1061/(asce)0733-9445(1992)118:6(1590).

[85] C. Yalcin and M. Saatcioglu, “Inelastic analysis of reinforced concrete columns.” [Online]. Available: www.elsevier.com/locate/compstruc

[86] Michael P. Collins and Denis Mitchell, *Prestressed Concrete Structures*. 1997.

[87] A. H. Mattock, “Flexural Strength of Prestressed Concrete Sections by Programmable Calculator,” *PCI Journal*, 1979.

[88] C. Wu, Y. Su, Y. Sun, C. Jin, and Z. Pan, “Sectional Analysis of Reinforced Engineered Cementitious Composite Columns Subjected to Combined Lateral Load and Axial Compression,” *Front Mater*, vol. 9, Apr. 2022, doi: 10.3389/fmats.2022.869835.

[89] K. M. Anwar Hossain, S. Parajuli, and T. Manzur, “Axial Behavior of Columns Confined with Engineered Cementitious Composite,” *ACI Struct J*, vol. 119, no. 1, pp. 67–76, 2022, doi: 10.14359/51734217.

[90] A. Lloyd, E. Jacques, M. Saatcioglu, D. Palermo, I. Nistor, and T. Tikka, “Capabilities of a Shock Tube to Simulate Blast Loading on Structures,” *ACI Symposium Paper*, 2011.

[91] PCI, “PCI Design Handbook: Appendix A: Blast-resistant design of Precast, Prestressed Concrete Components,” 2014.

[92] E. C. Bentz, “Sectional Analysis of Reinforced Concrete Members,” University of Toronto, Torronto, 2000. [Online]. Available: http://www.ecf.utoronto.ca/~bentz/t2k.htm

[93] Denis. Mitchell and Abdeldjelil. Belarbi, *Shear in structural concrete :* American Concrete Institute, 2018.

[94] ALTAIR, “ALTAIR S-Concrete Moment-Curvature Tool (M vs Phi Diagram),” 2021.

Appendix A – Strain and Deflection Time Histories of Flexural Reinforcement and Strands

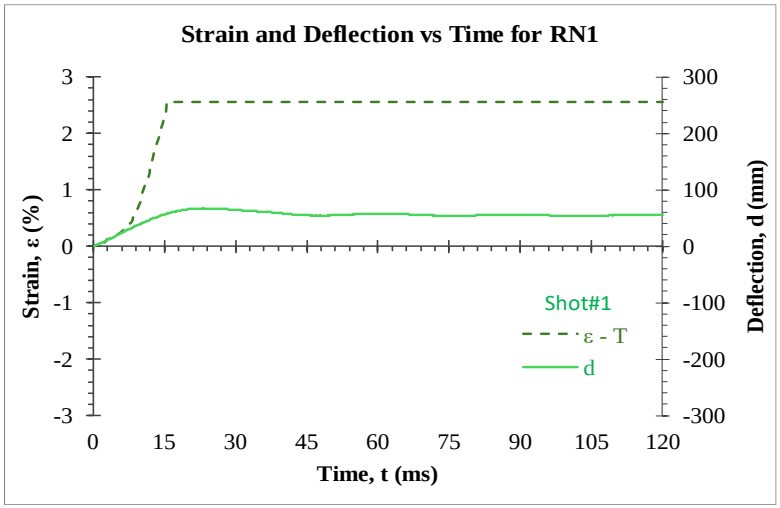

(a)

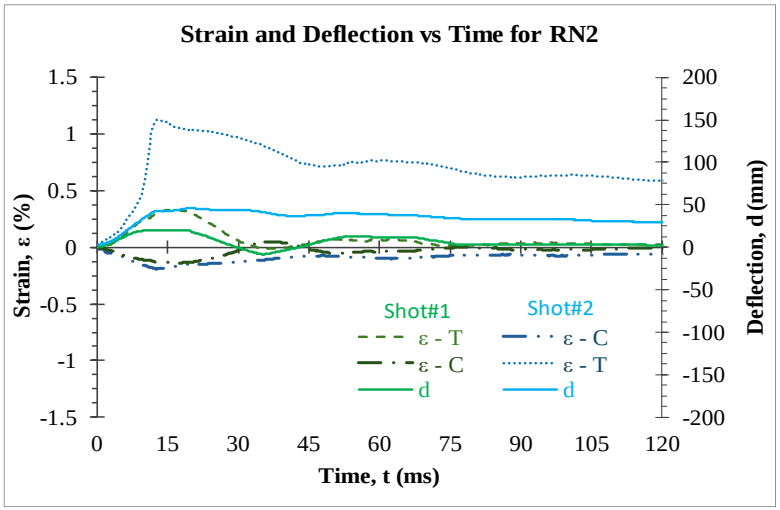

(b)

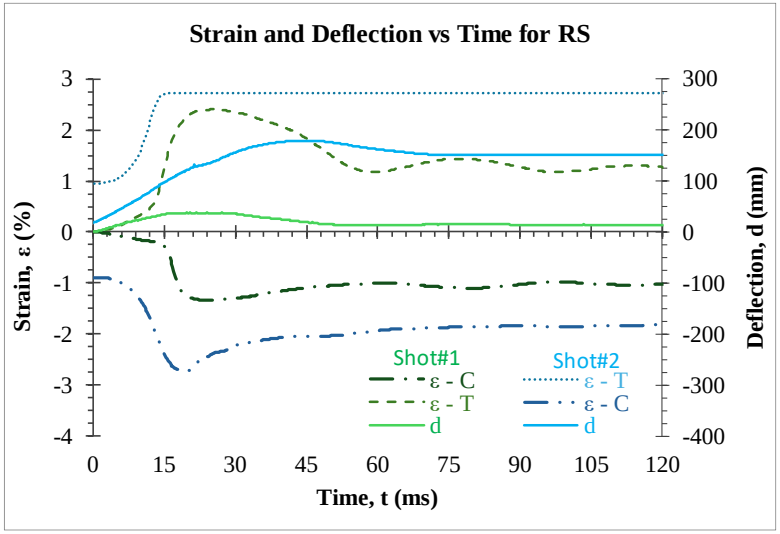

(c)

Figure A.1 – Reference columns, a) Ref-N1, b) Ref-N2, and c) Ref-S.

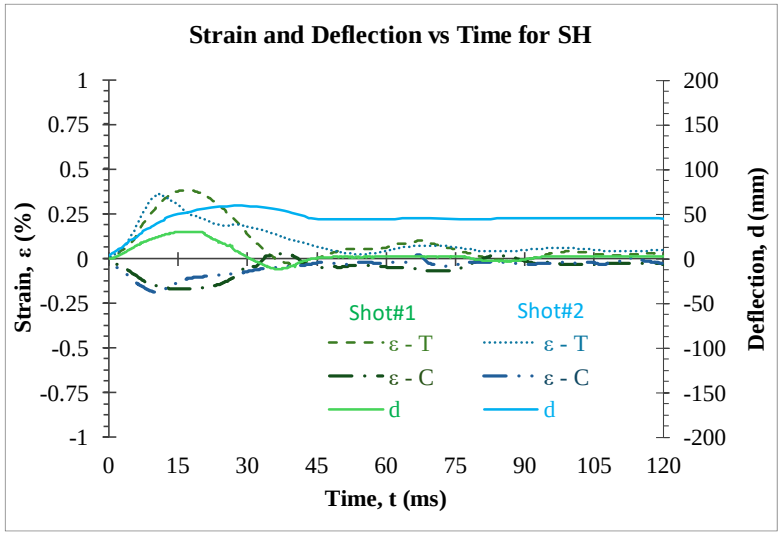

(a)

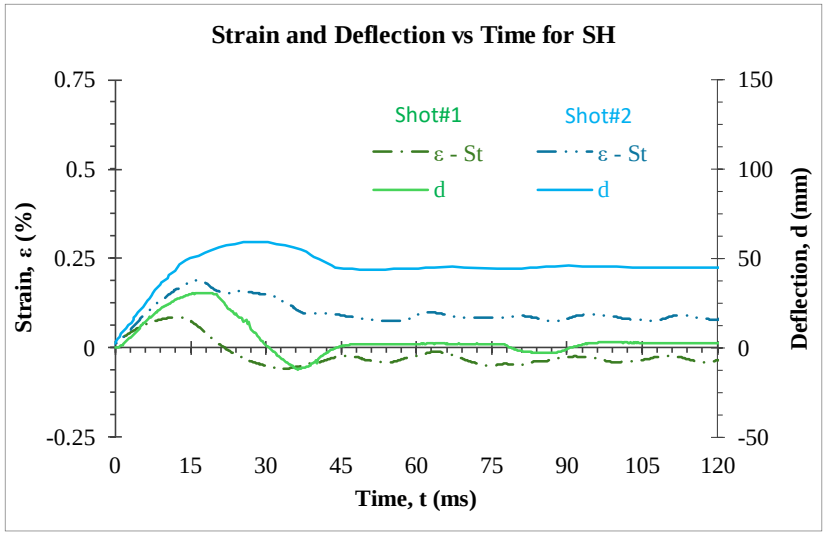

(b)

Figure A.2 – Single-harped column, a)flexural reinforcement, and b) External strands.

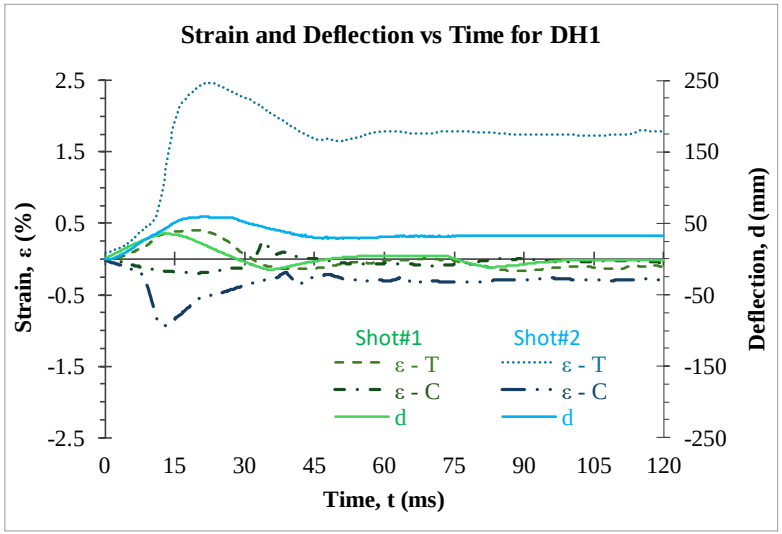

(a)

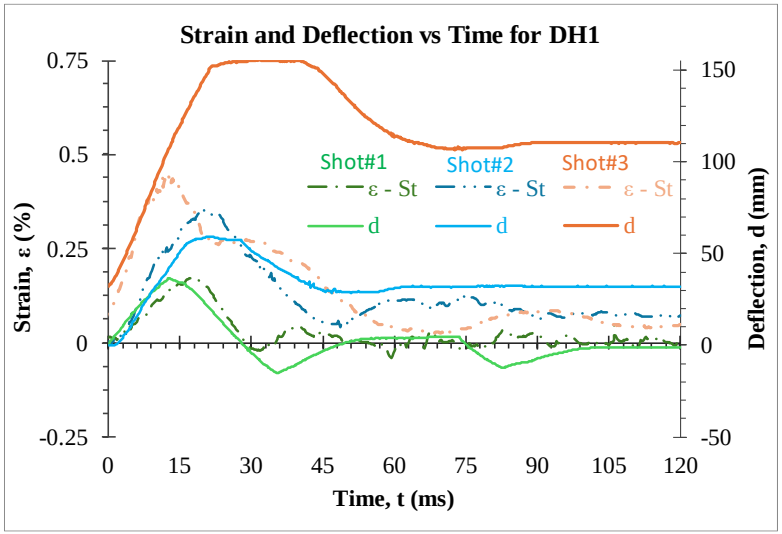

(b)

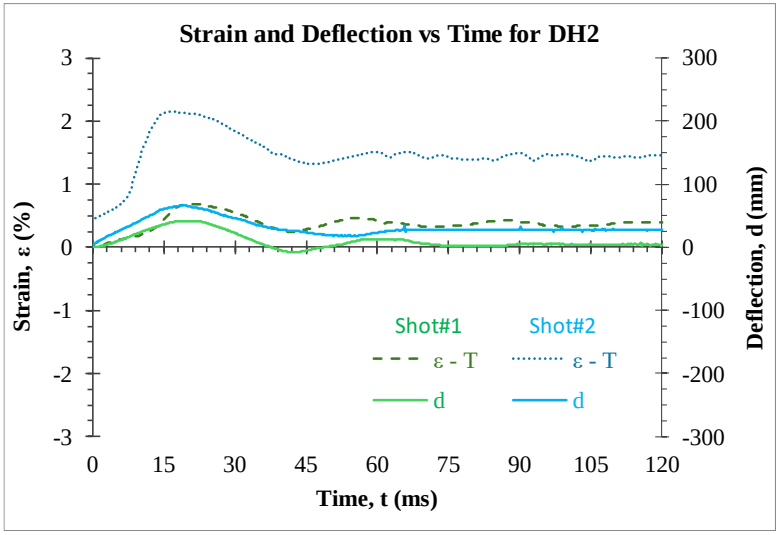

(c)

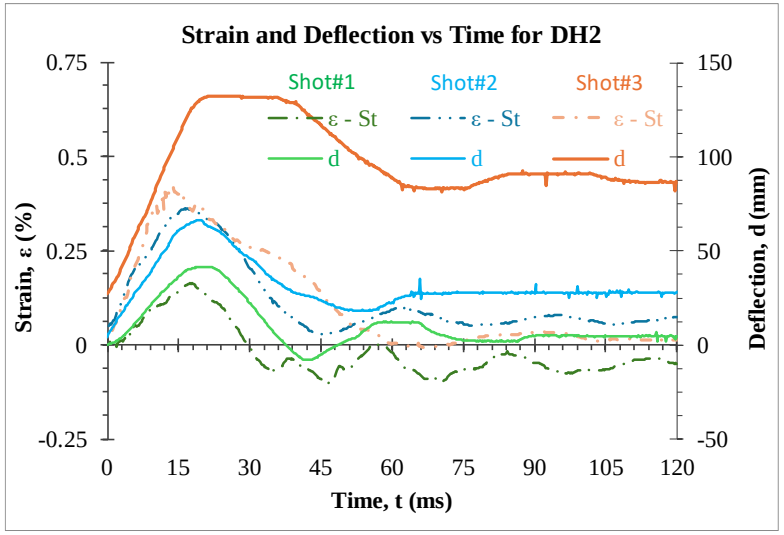

(d)

Figure A.3 – Double-harped columns, a) flexural reinforcement of DH1, b) External strands of DH1, c) flexural reinforcement of DH2, and d) External strands of DH2.

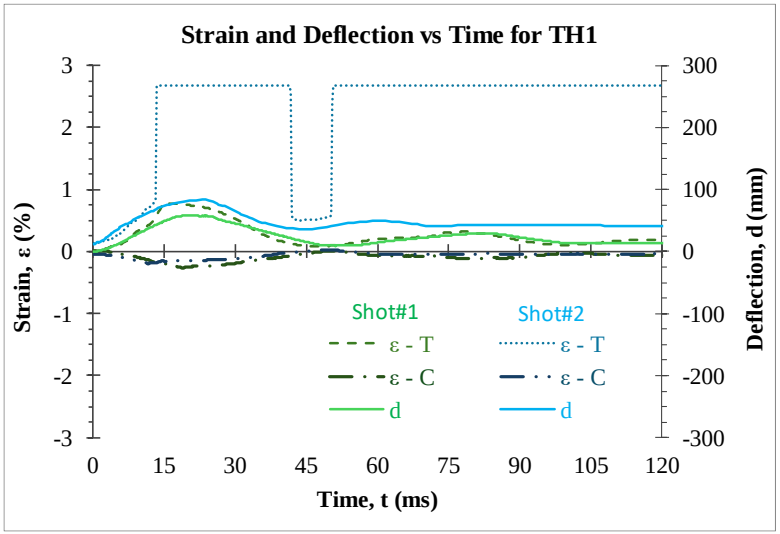

(a)

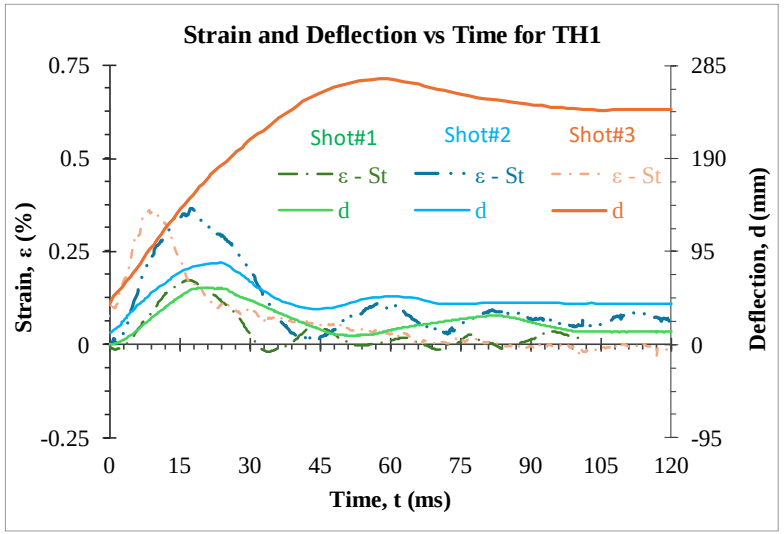

(b)

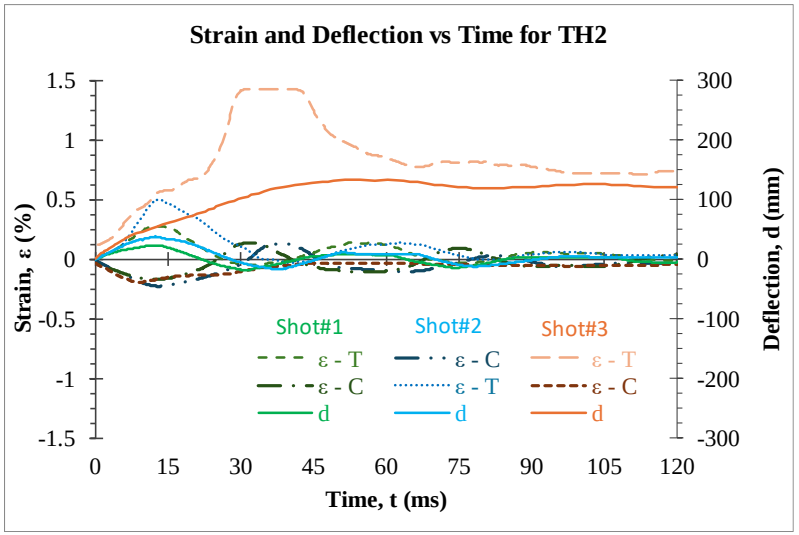

(c)

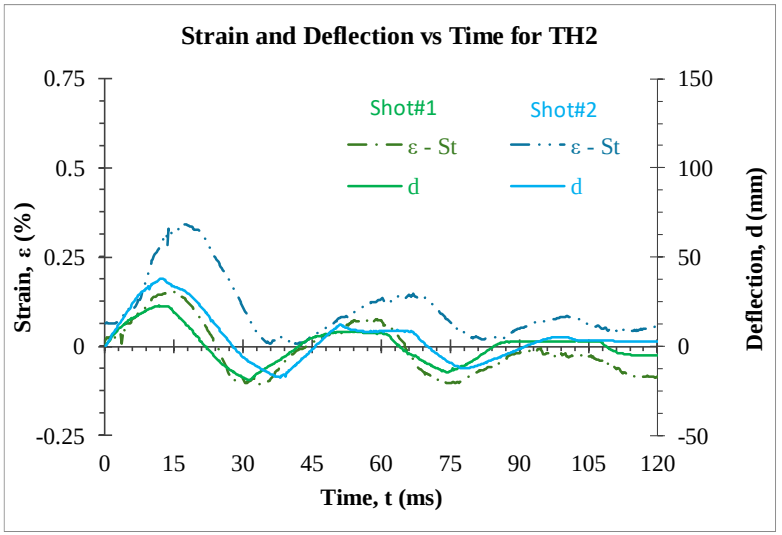

(d)

Figure A.4 – Triple-harped columns, a) flexural reinforcement of TH1, b) External strands of TH1, c) flexural reinforcement of TH2, and d) External strands of TH2.

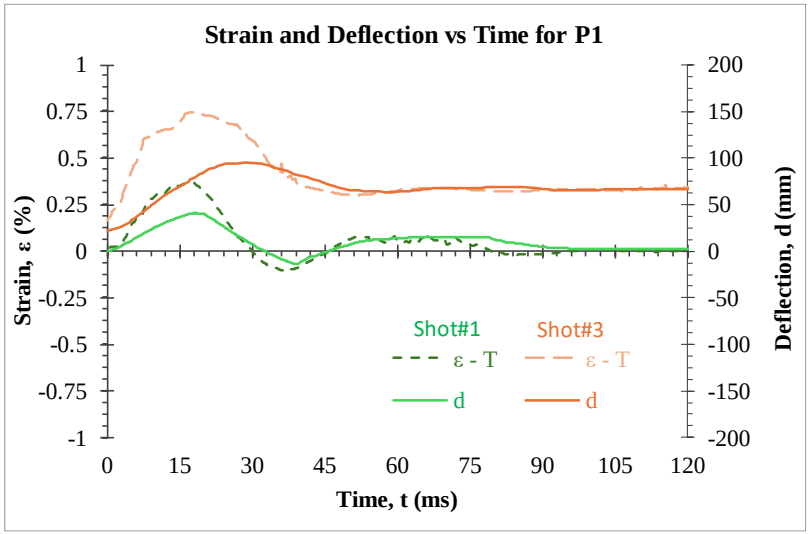

(a)

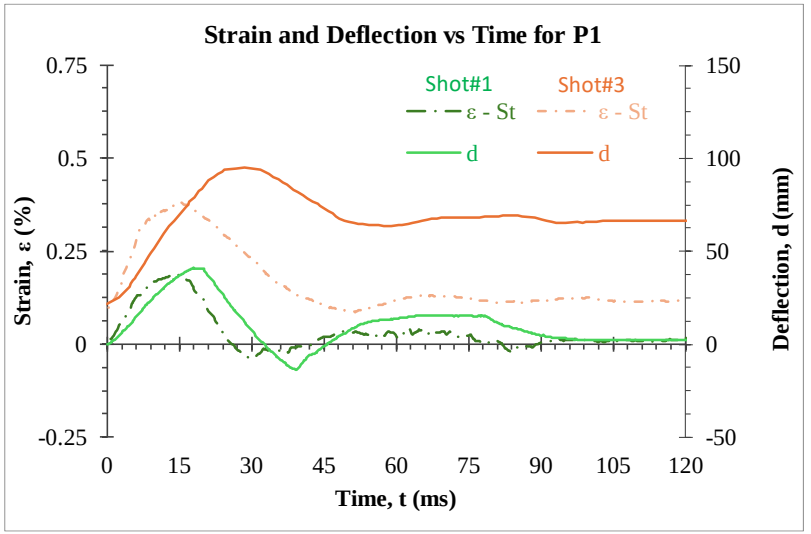

(b)

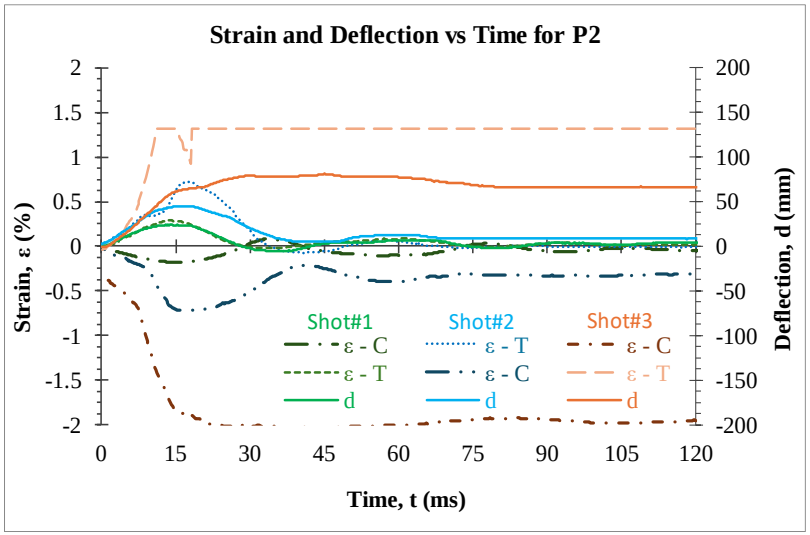

(c)

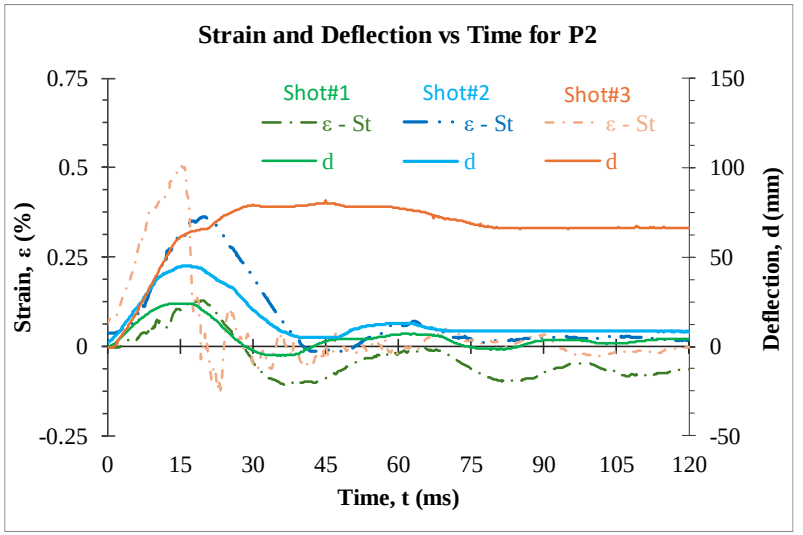

(d)

Figure A.5 – Parabolic profile columns, a) flexural reinforcement of P1, b) External strands of P1, c) flexural reinforcement of P2, and d) External strands of P2.

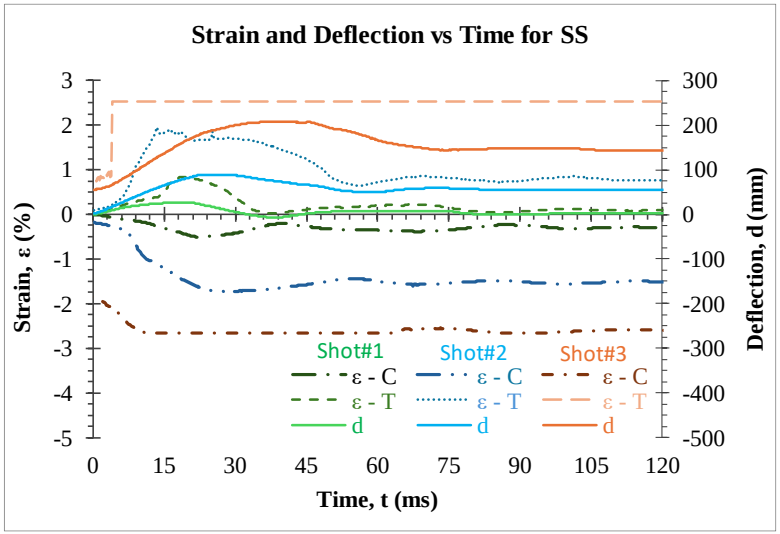

(a)

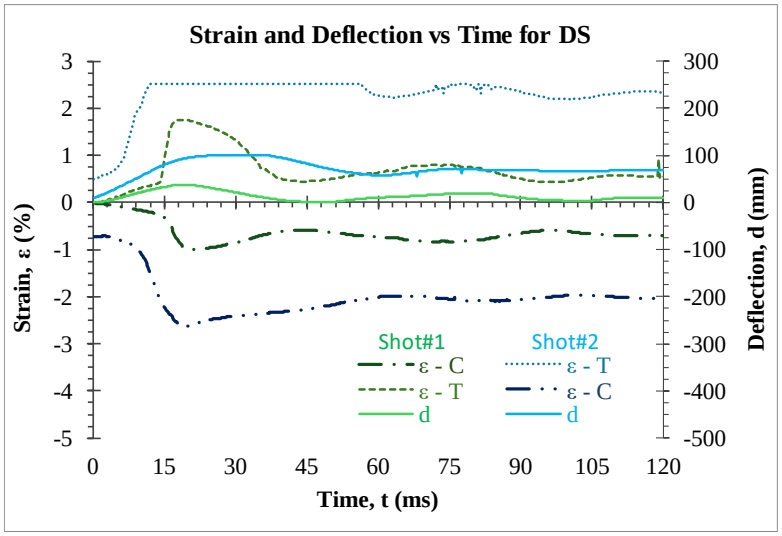

(b)

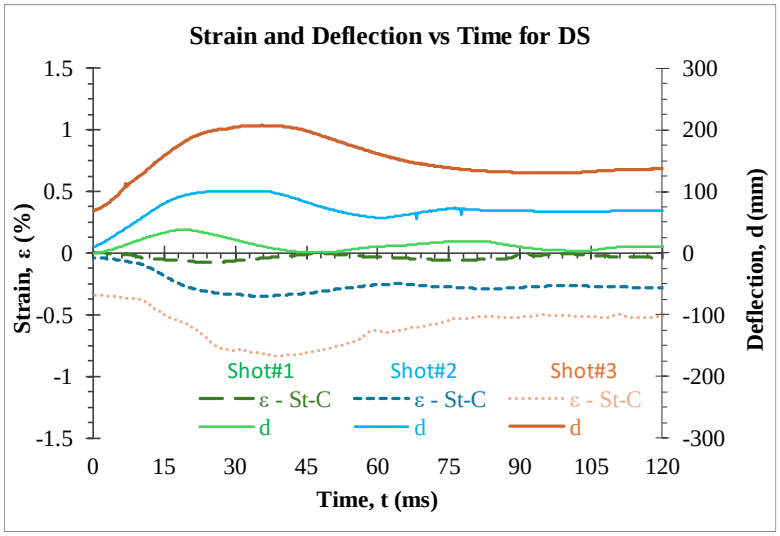

(c)

Figure A.6 – Post-tensioned columns, a) flexural reinforcement of SS, b) flexural reinforcement of DS, and c) Internal compression strand of DS.

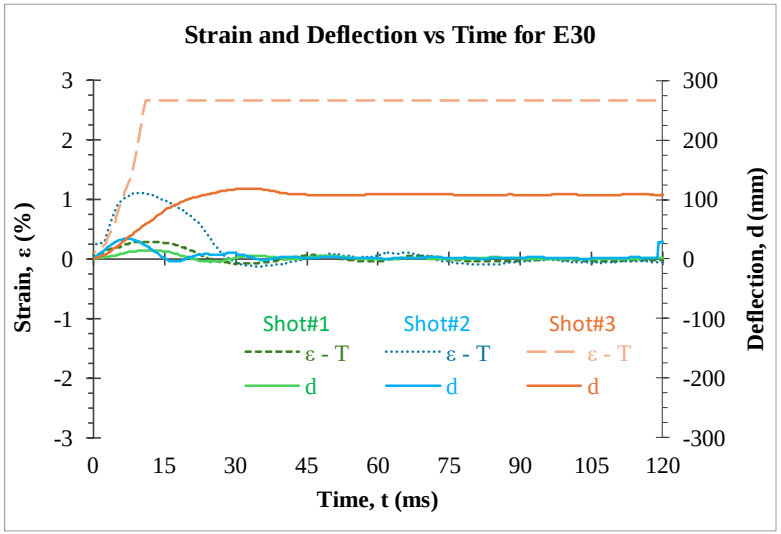

(a)

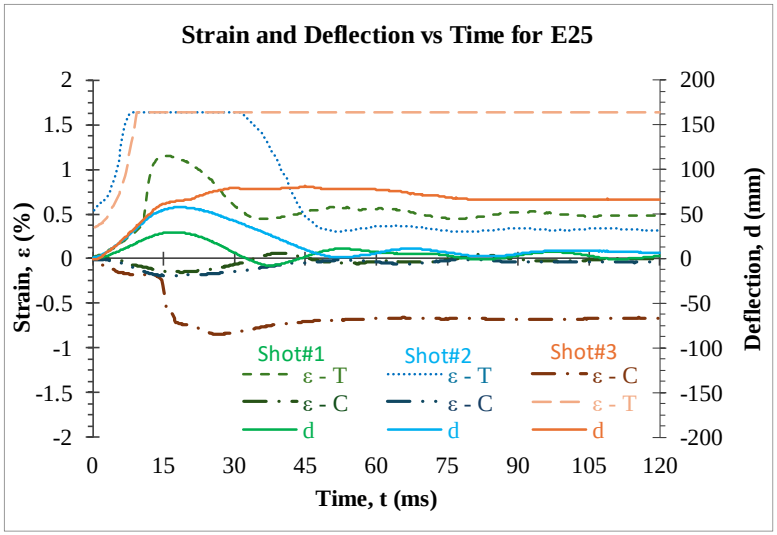

(b)

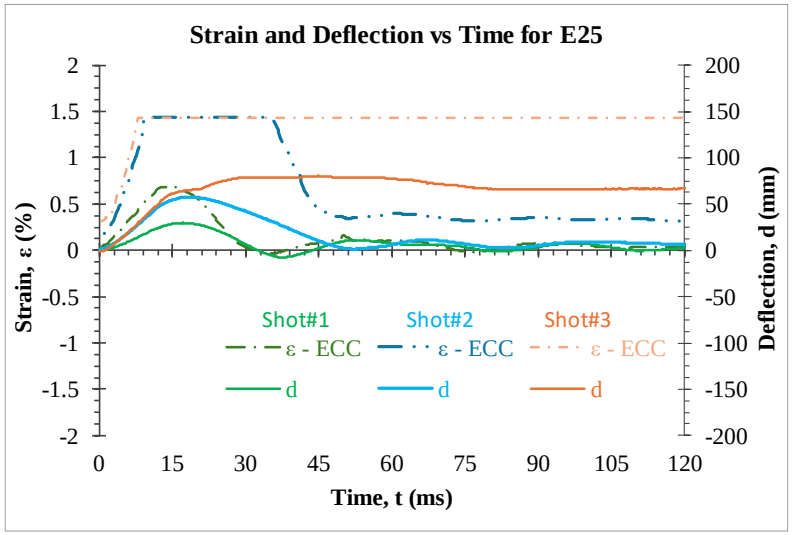

(c)

Figure A.7 – Jacketed columns, a) flexural reinforcement of E30, b) flexural reinforcement of E25, and c) ECC tensile strain of E25.

Appendix B – Time Histories of Forces and Mid-height displacement

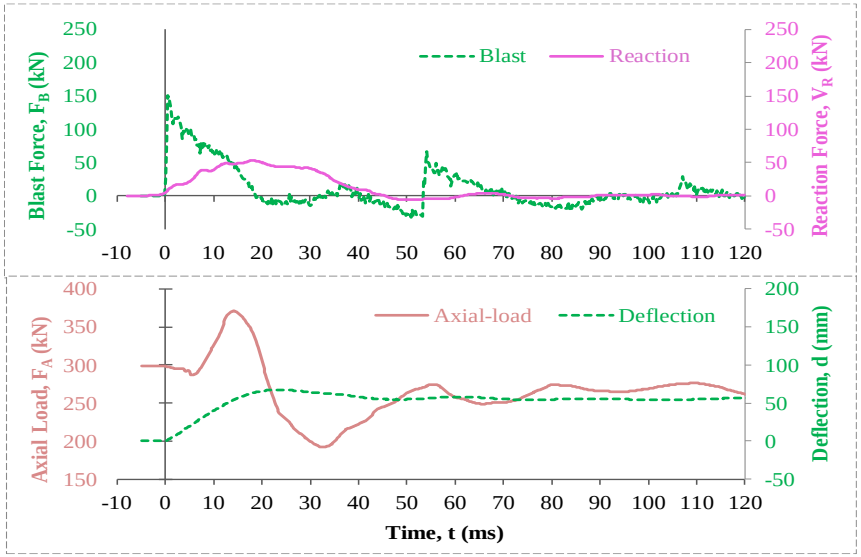

(a)

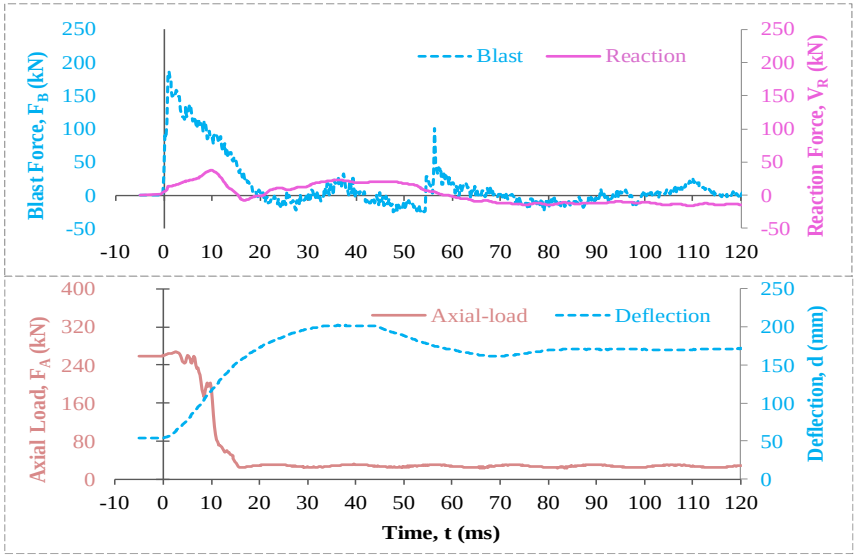

(b)

Figure B.1 – Ref-N1, a) shot#1, and b) shot#2.

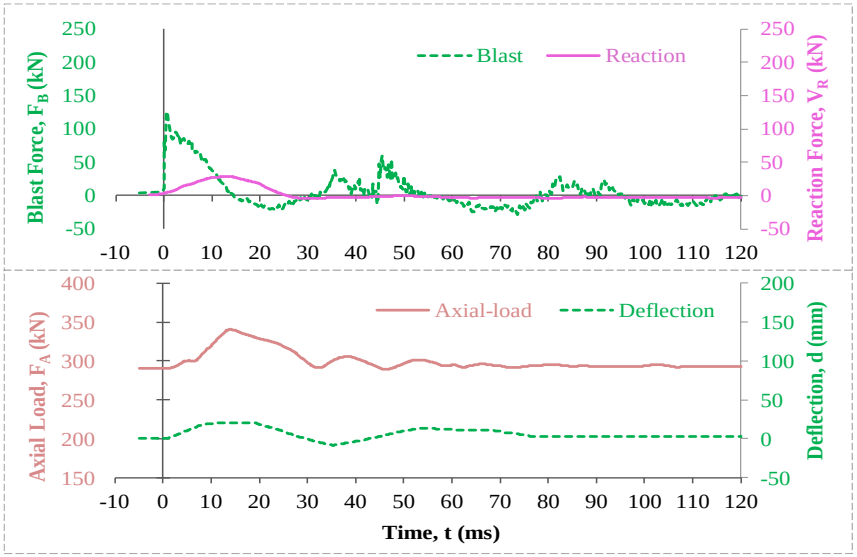

(a)

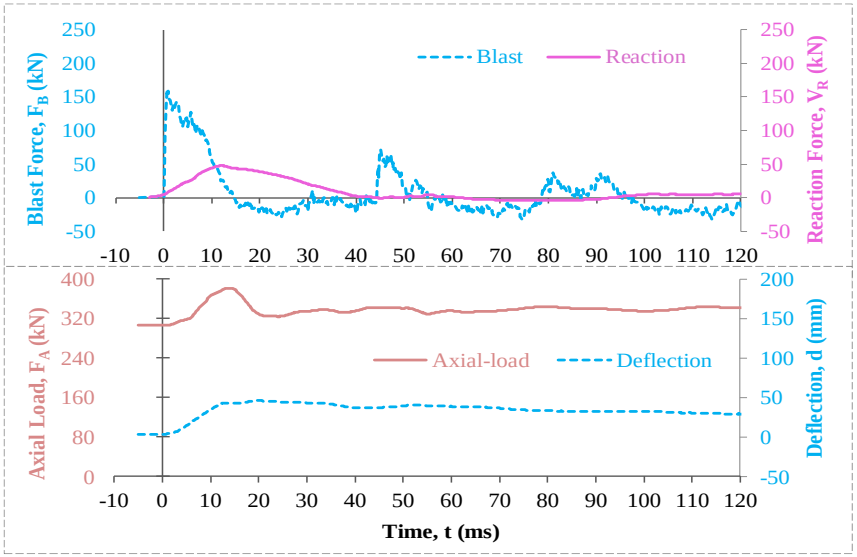

(b)

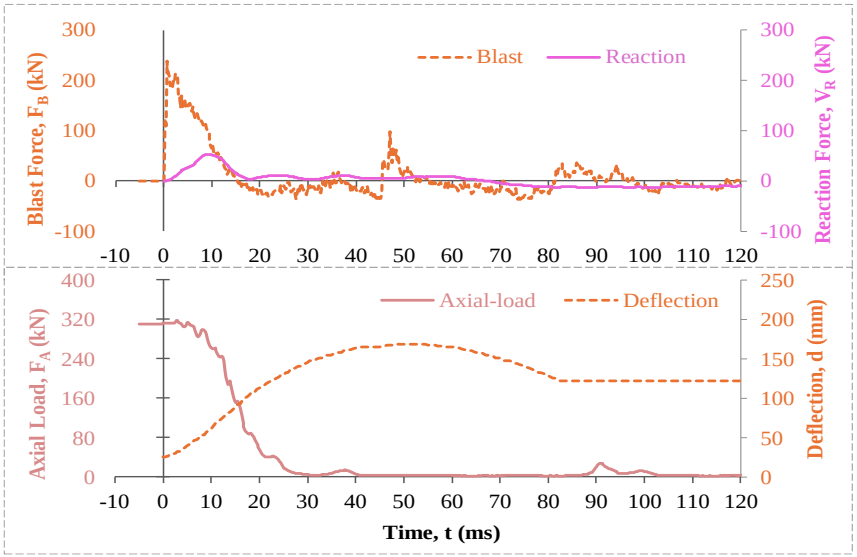

(c)

Figure B.2 – Ref-N2, a) shot#1, b) shot#2, and c) shot#3.

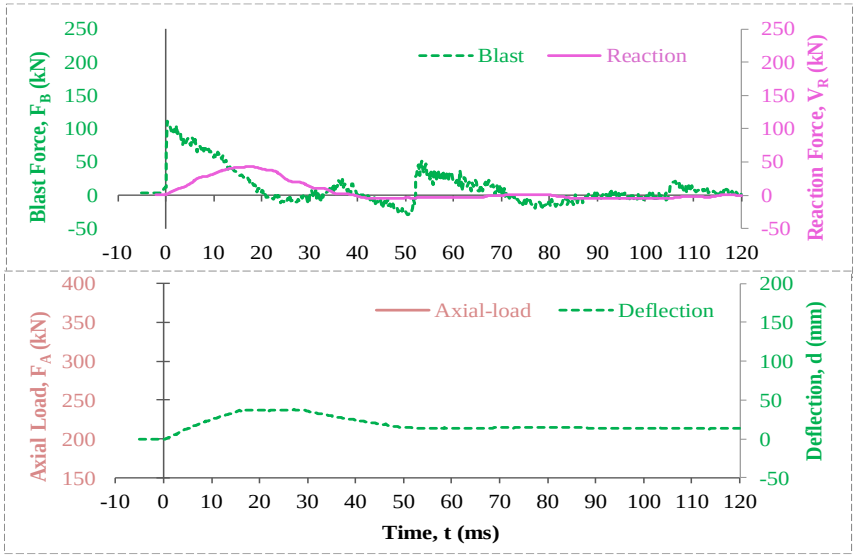

(a)

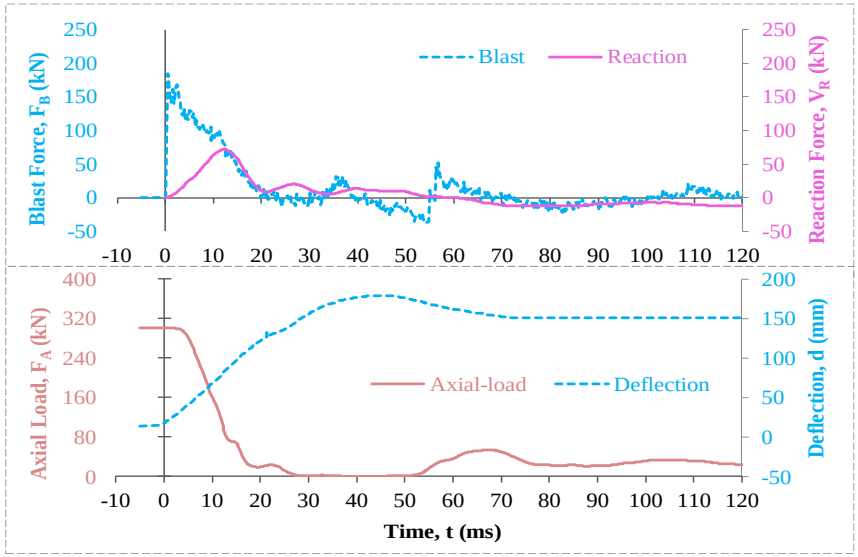

(b)

Figure B.3 – Ref-S, a) shot#1, and b) shot#2.

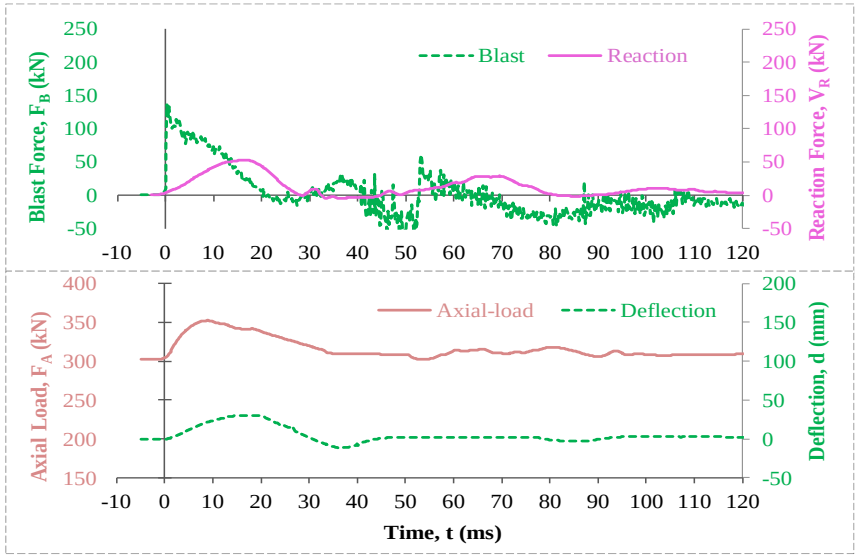

(a)

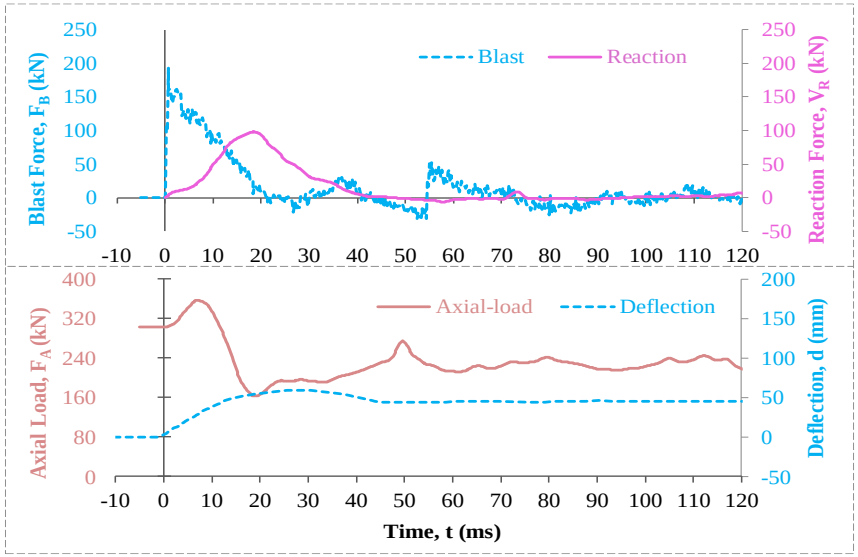

(b)

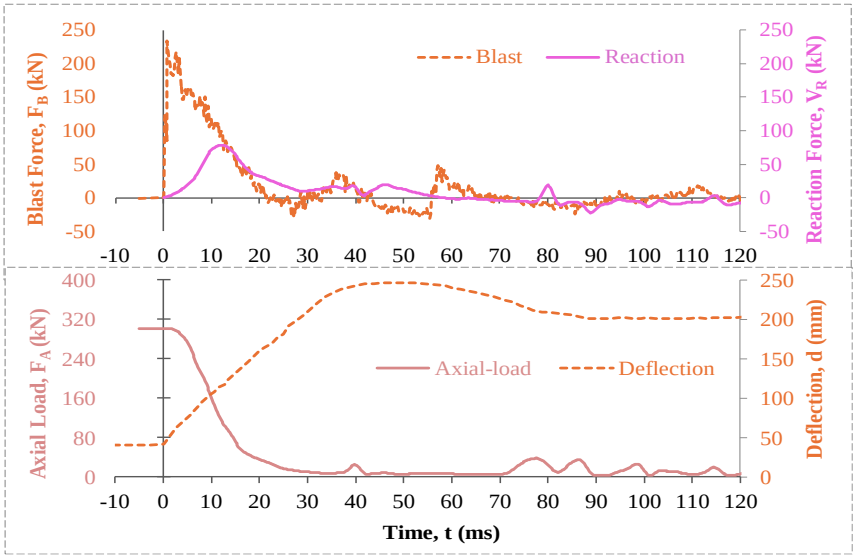

(c)

Figure B.4 – SH-207e-0.15fpu-N1, a) shot#1, b) shot#2, and c) shot#3.

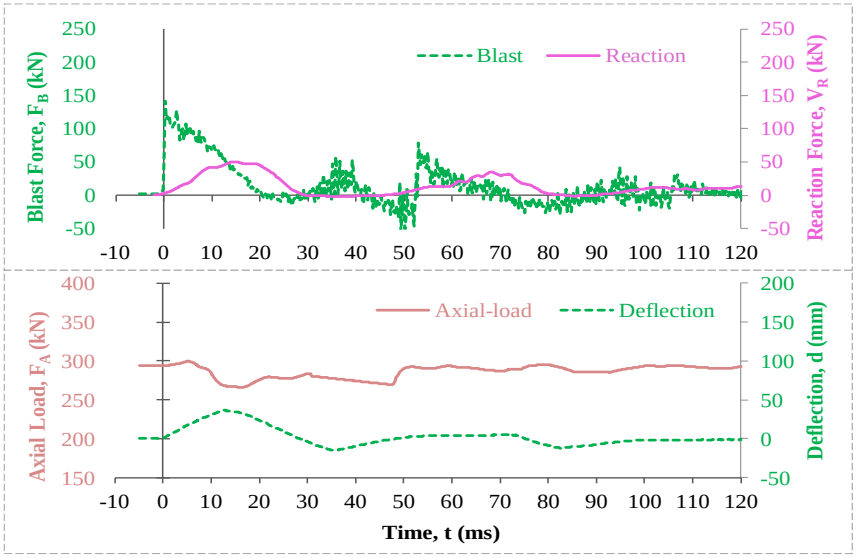

(a)

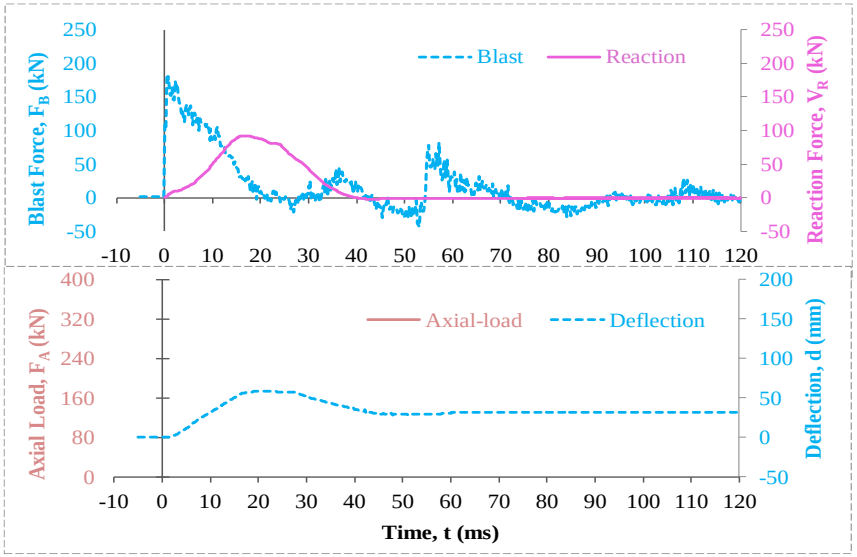

(b)

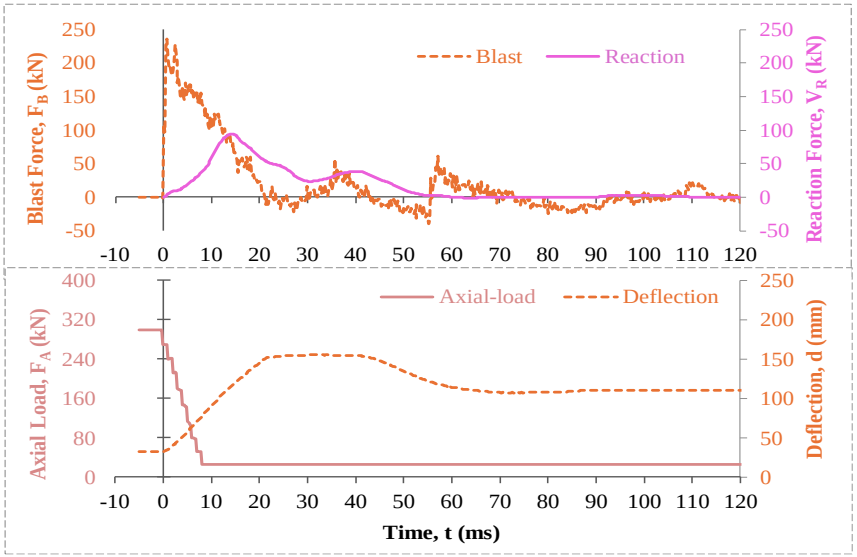

(c)

Figure B.5 – DH1-207e-0.13fpu-N1, a) shot#1, b) shot#2, and c) shot#3.

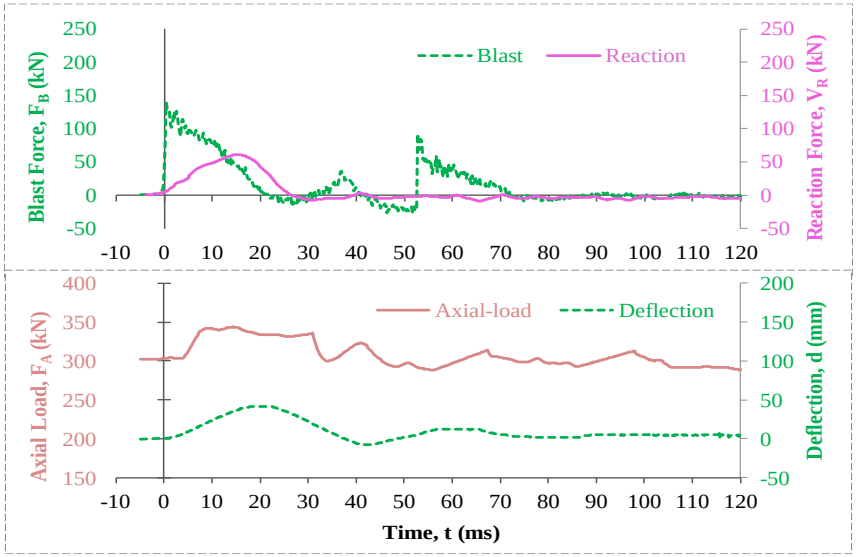

(a)

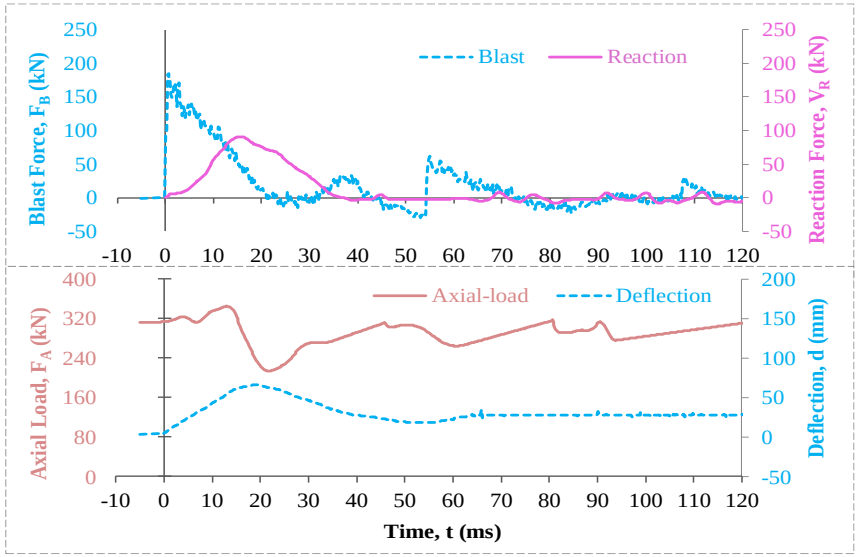

(b)

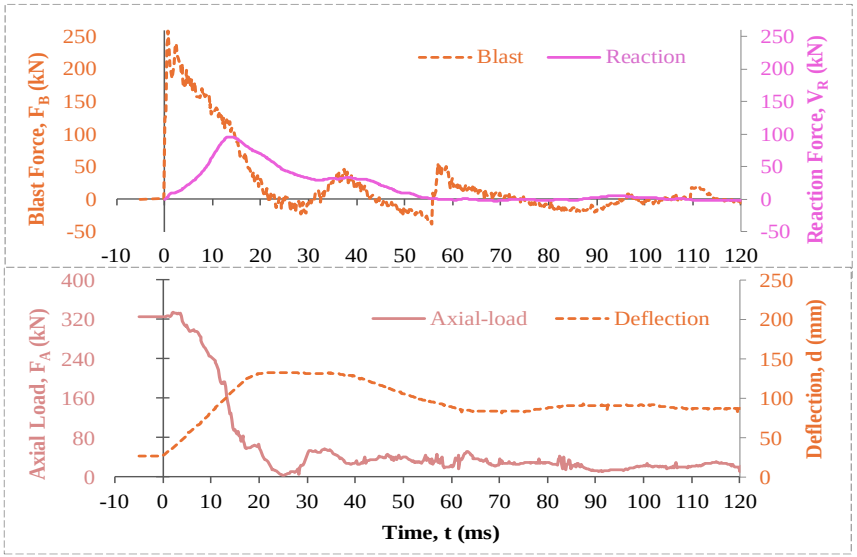

(c)

Figure B.6 – DH2-207e-0.15fpu-N1, a) shot#1, b) shot#2, and c) shot#3.

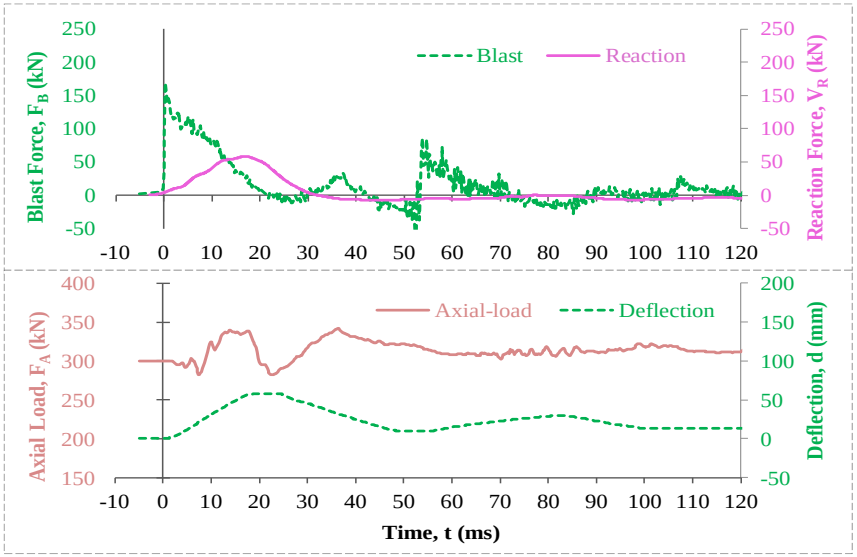

(a)

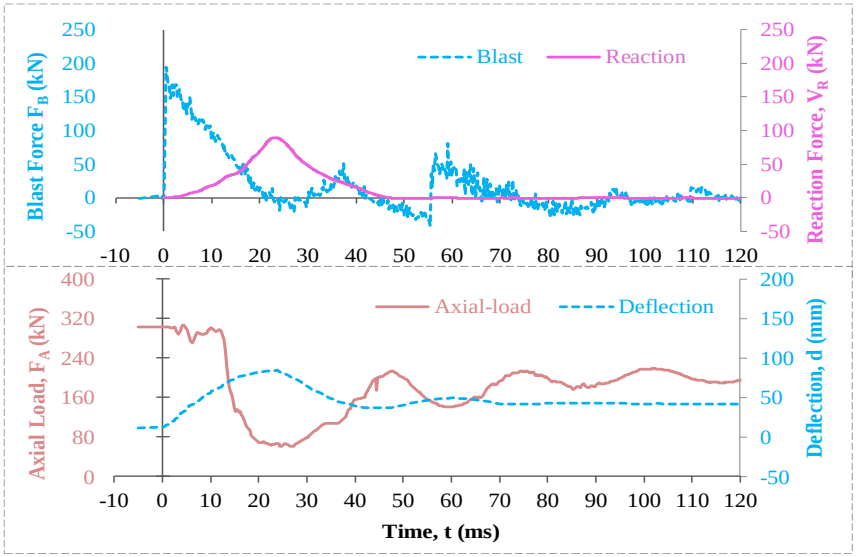

(b)

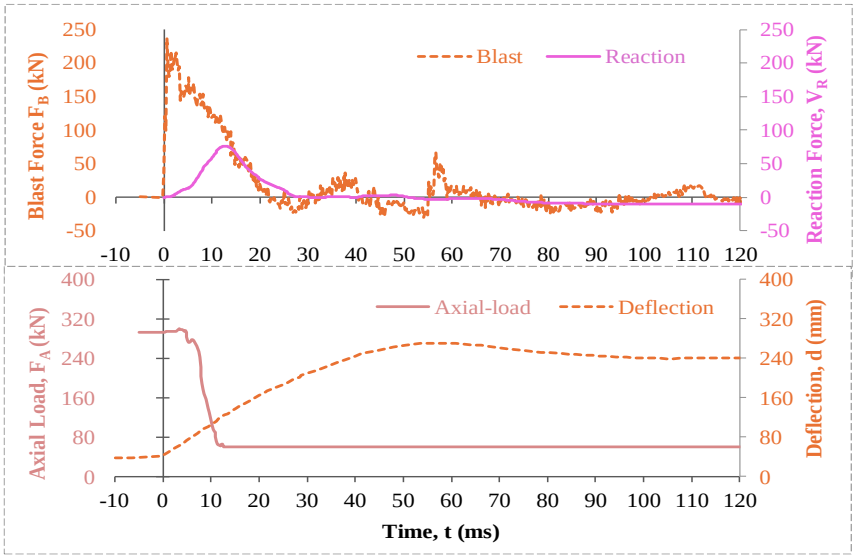

(c)

Figure B.7 – TH1-247e-0.10fpu-N1, a) shot#1, b) shot#2, and c) shot#3.

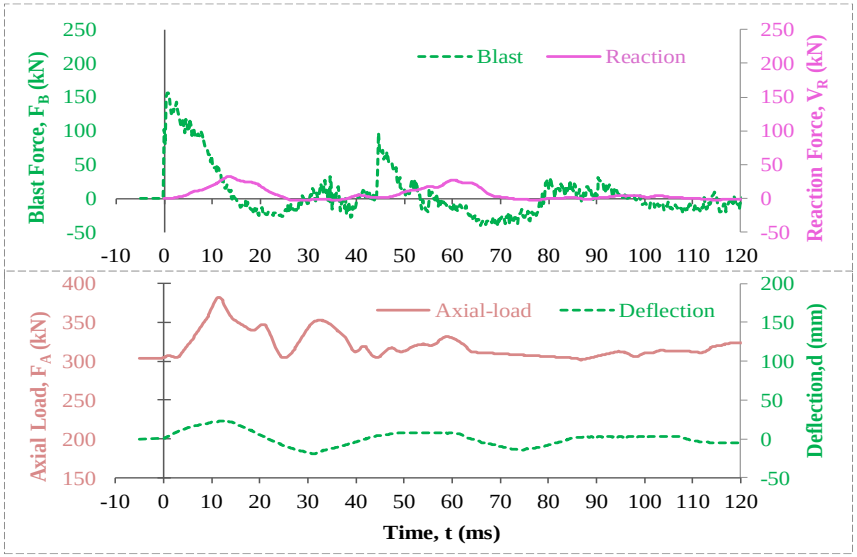

(a)

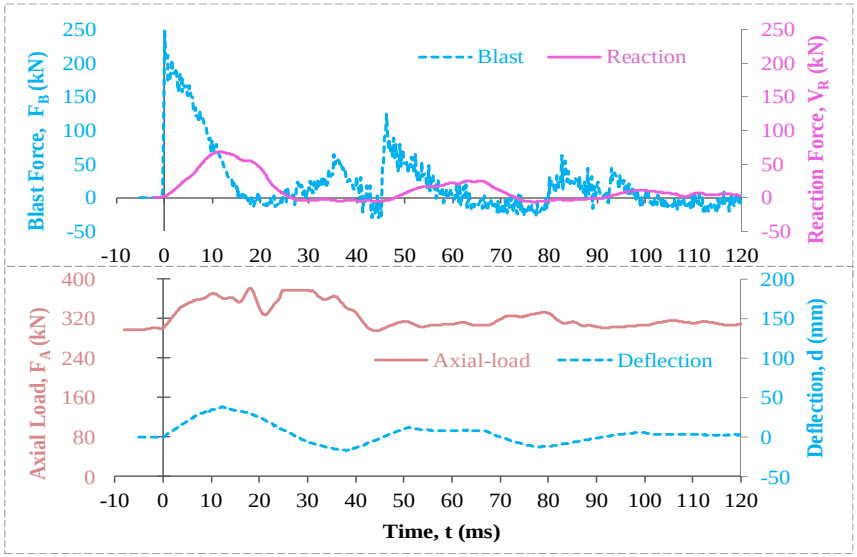

(b)

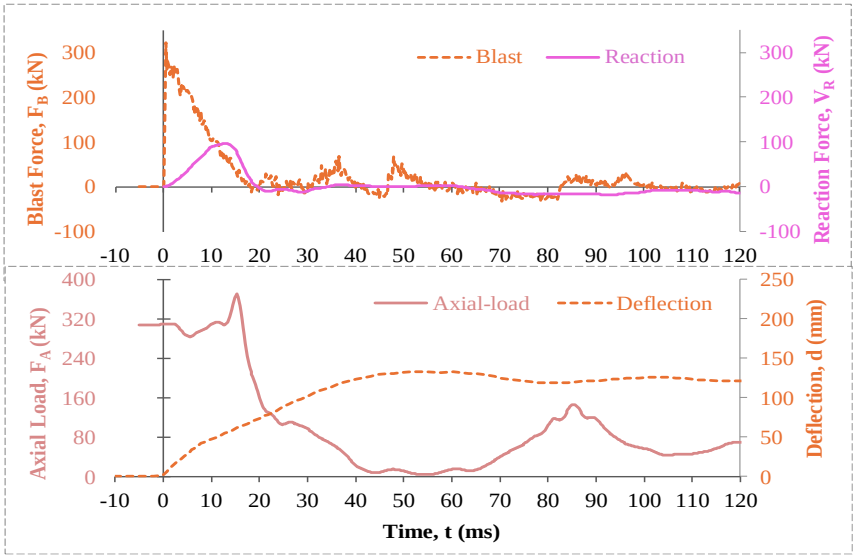

(c)

Figure B.8 – TH2-247e-0.15fpu-N2, a) shot#1, b) shot#2, and c) shot#3.

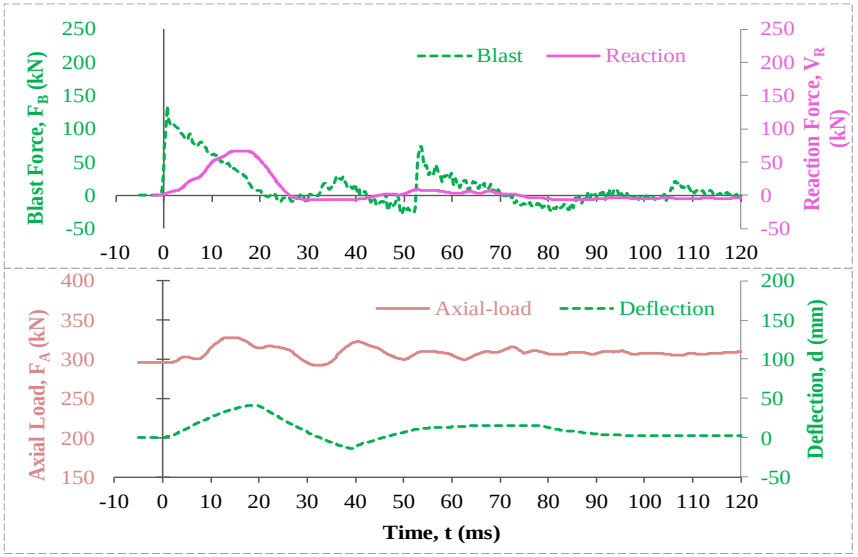

(a)

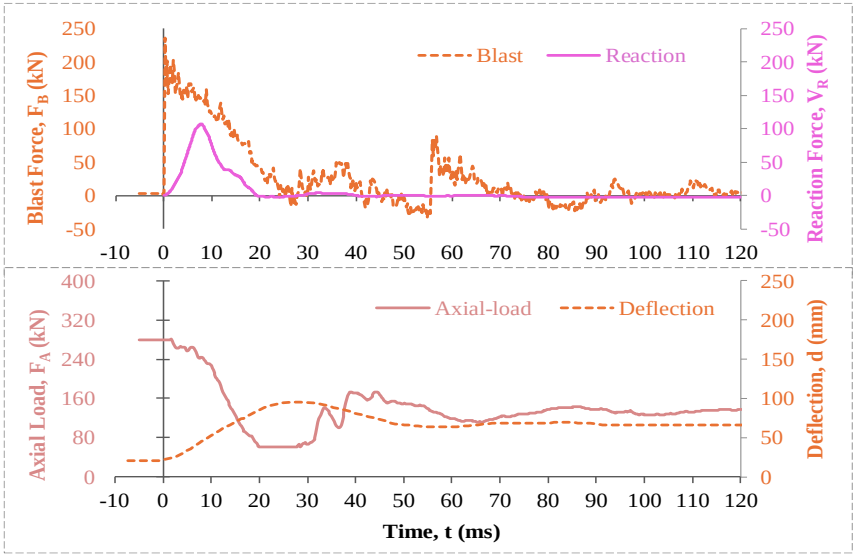

(b)

Figure B.9 – P1-227e-0.09fpu-N1, a) shot#1, and b) shot#3.

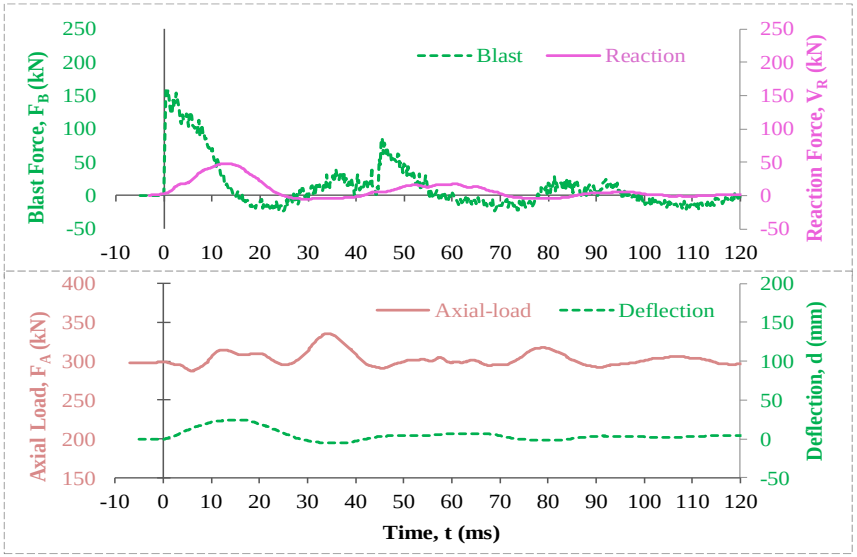

(a)

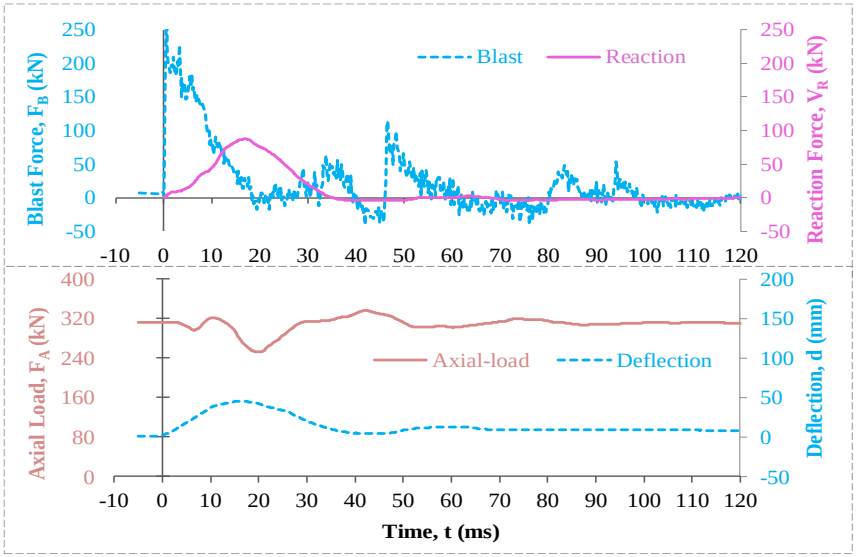

(b)

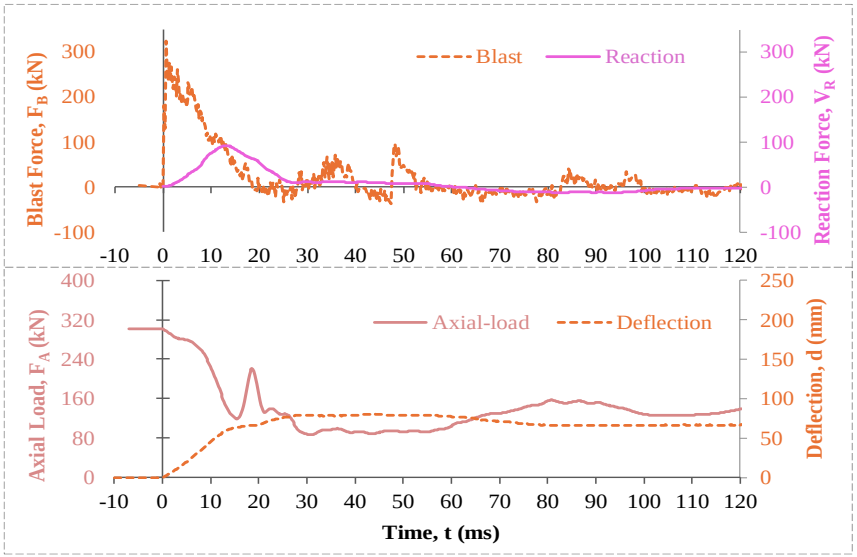

(c)

Figure B.10 – P2-227e-0.16fpu-N2, a) shot#1, b) shot#2, and c) shot#3.

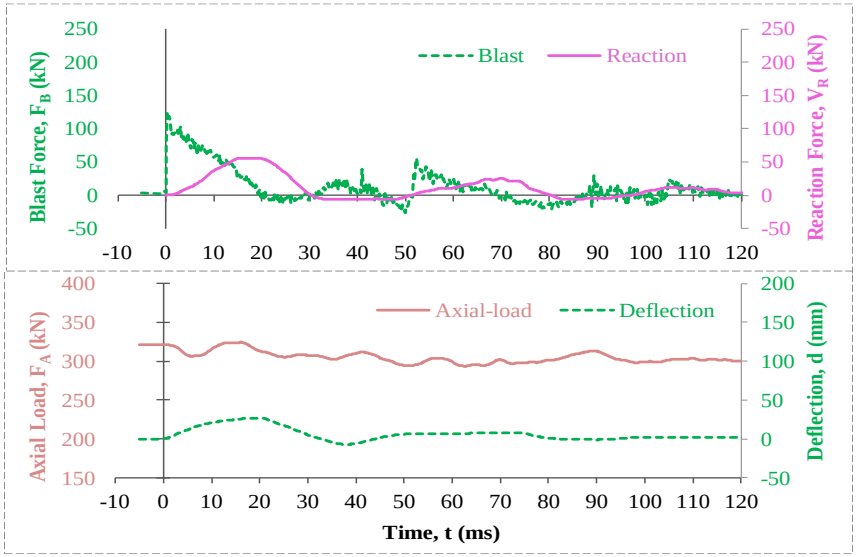

(a)

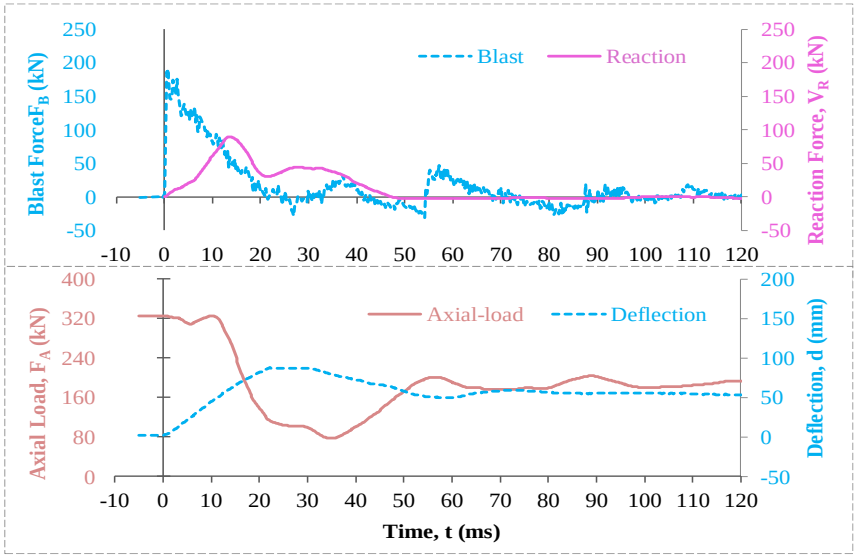

(b)

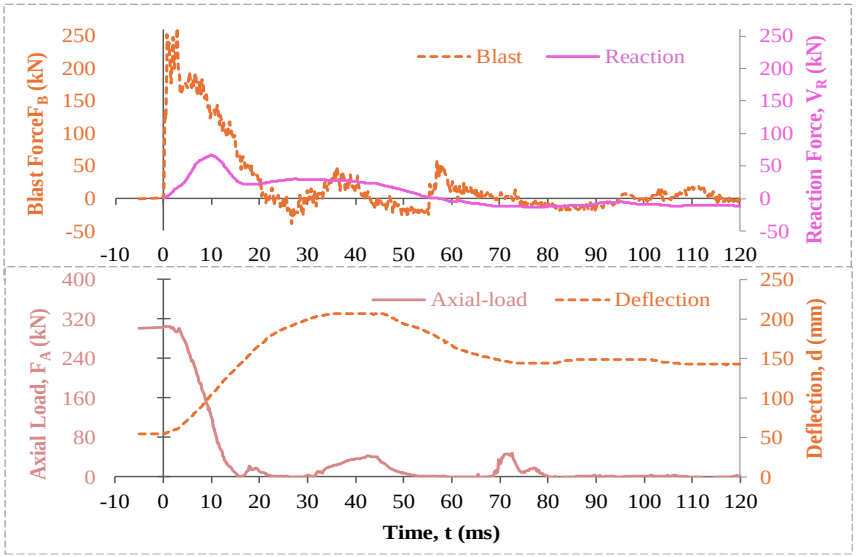

(c)

Figure B.11 – PT-SS-0.35fpu-S, a) shot#1, b) shot#2, and c) shot#3.

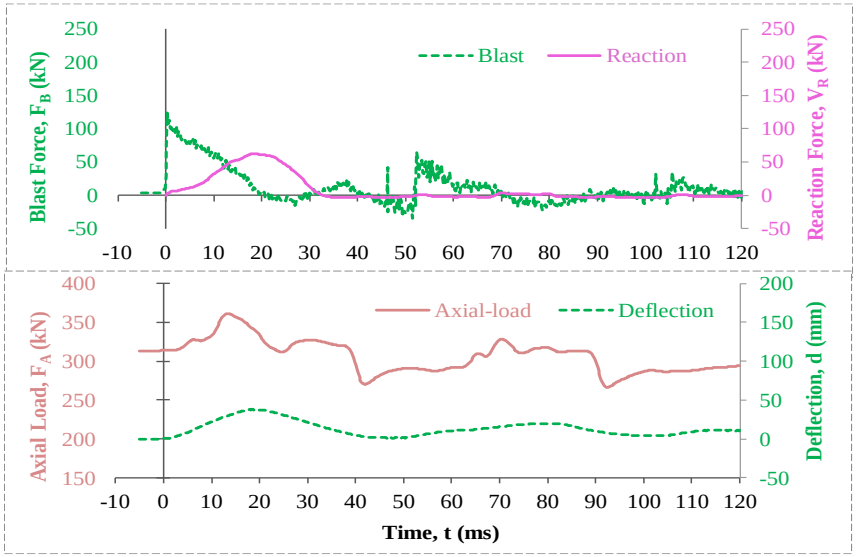

(a)

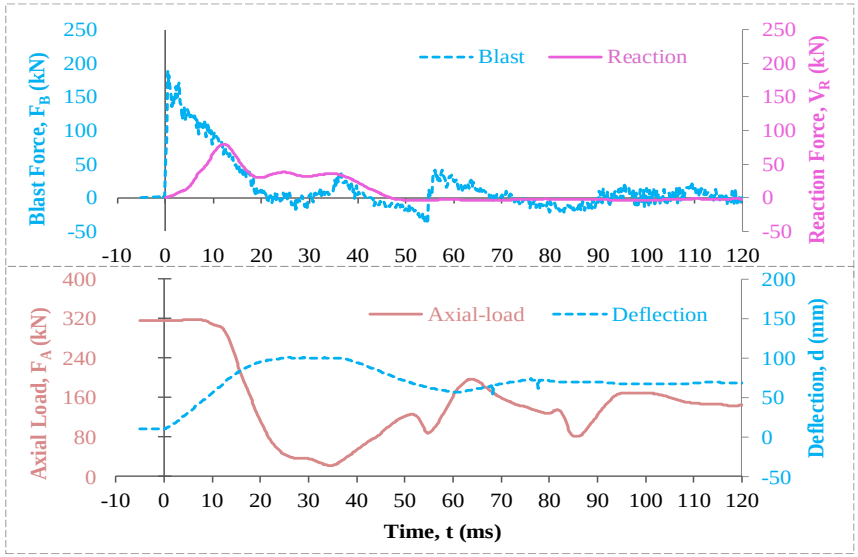

(b)

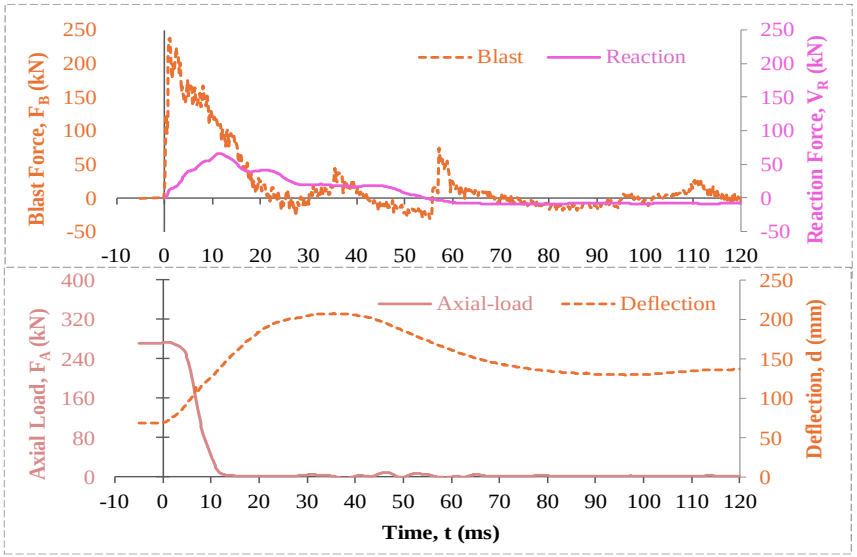

(c)

Figure B.12 – PT-DS-0.40fpu-S, a) shot#1, b) shot#2, and c) shot#3.

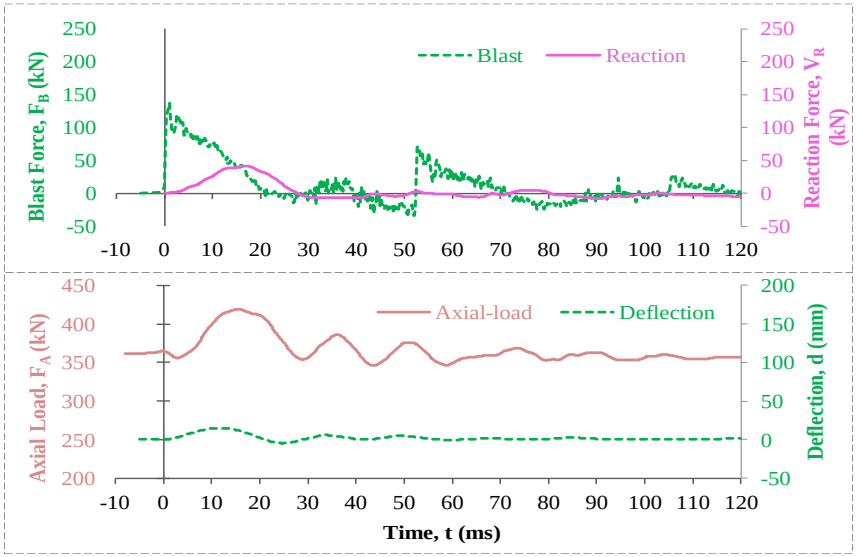

(a)

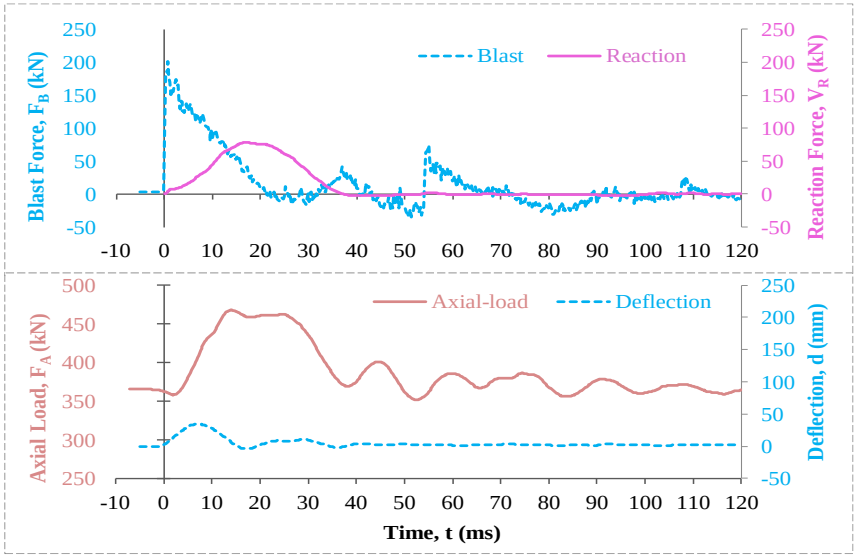

(b)

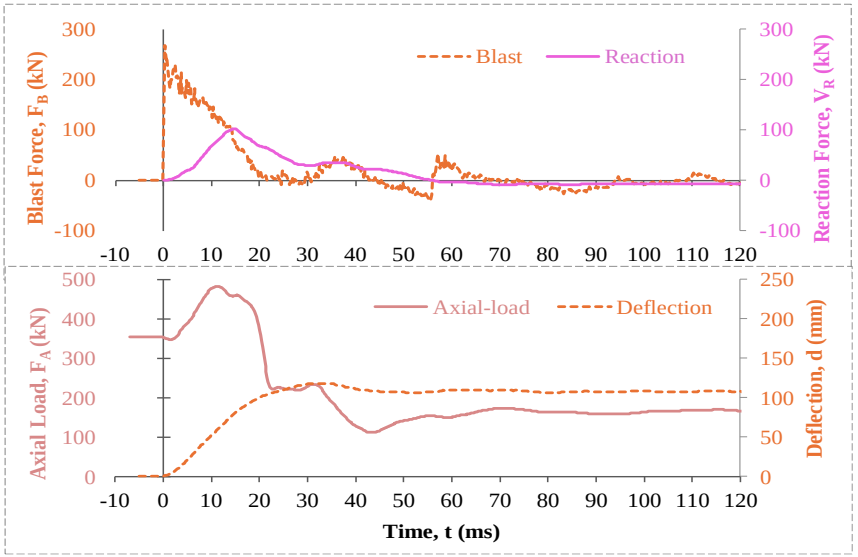

(c)

Figure B.13 – ECC-2.0%v_f-t30-N1, a) shot#1, b) shot#2, and c) shot#3.

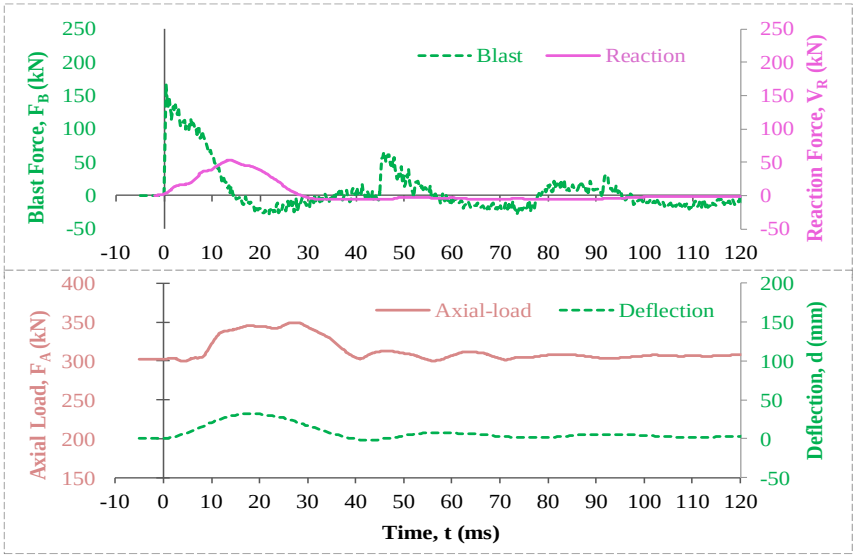

(a)

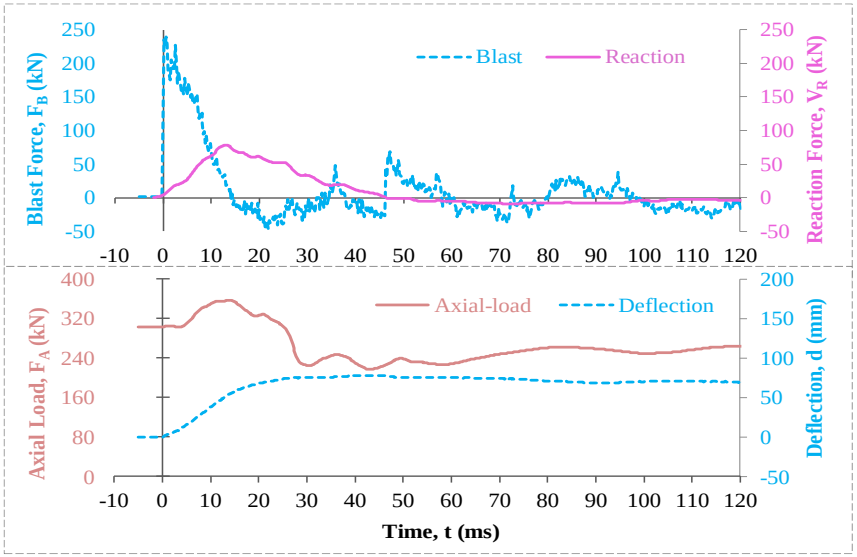

(b)

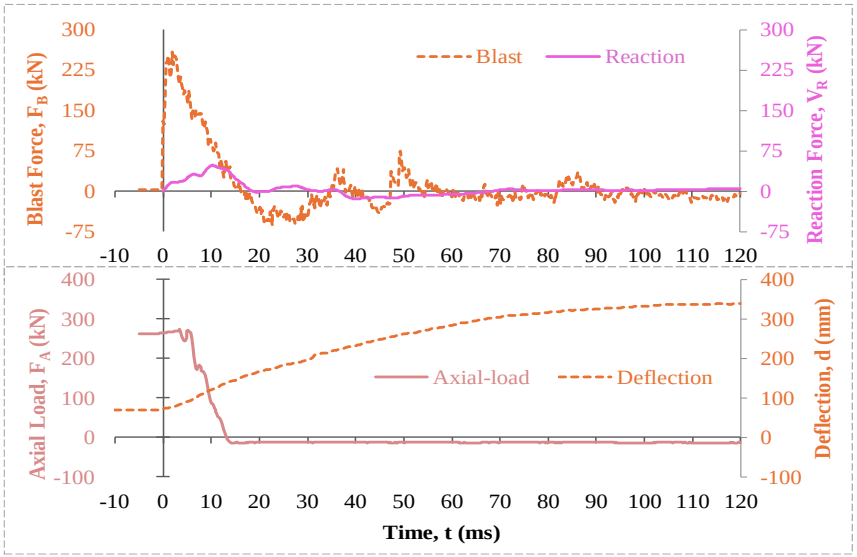

(c)

Figure B.14 – ECC-2.0%v_f-t20-N2, a) shot#1, b) shot#2, and c) shot#3.

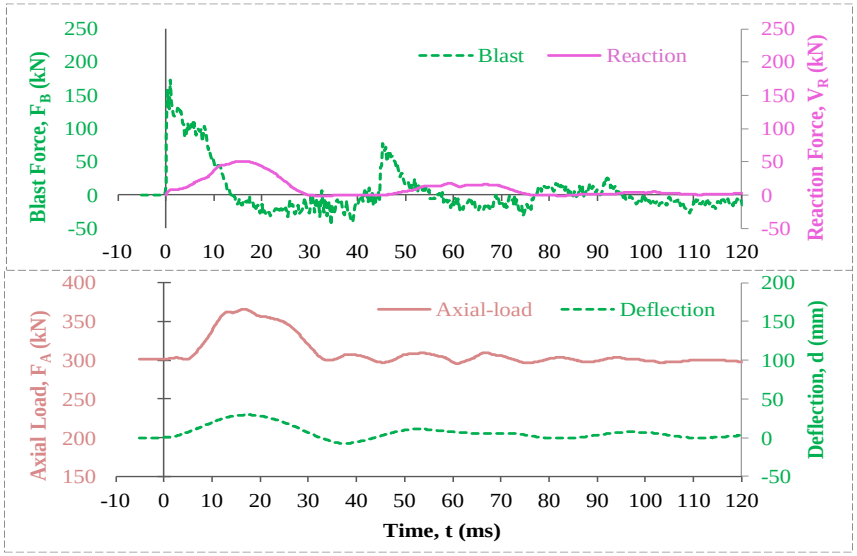

(a)

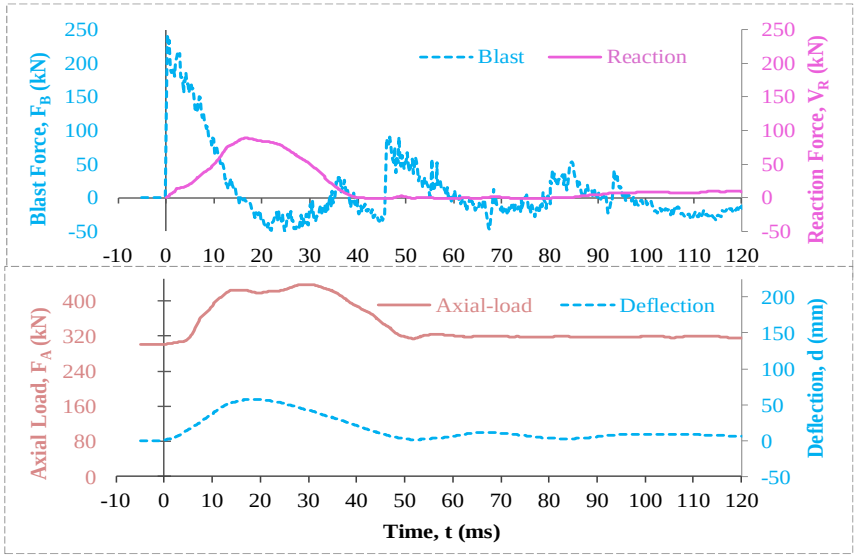

(b)

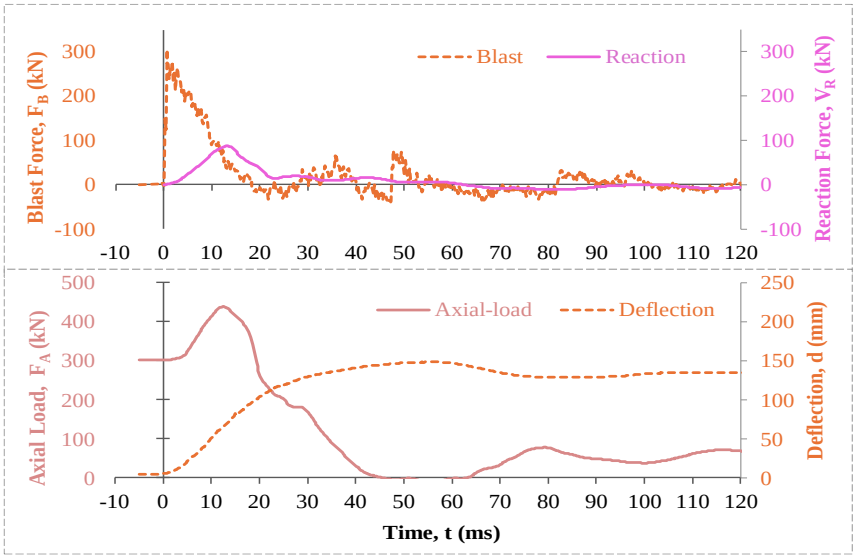

(c)

Figure B.15 – ECC-1.5%v_f-t25-N2, a) shot#1, b) shot#2, and c) shot#3.

Appendix C – Experimental vs Analytical Displacement Time Histories

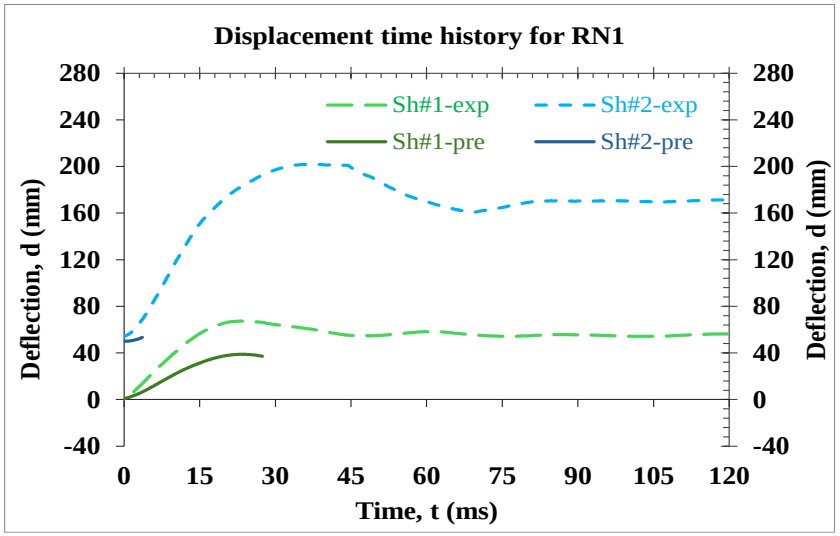

(a)

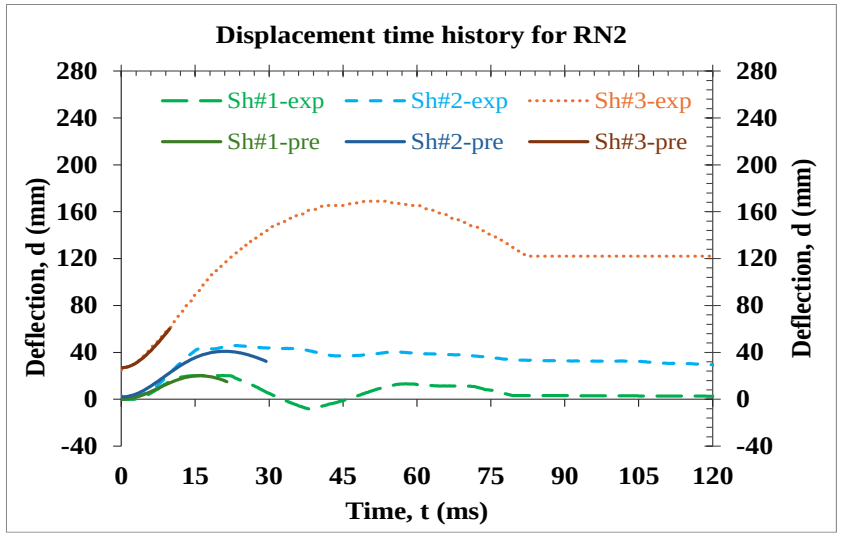

(b)

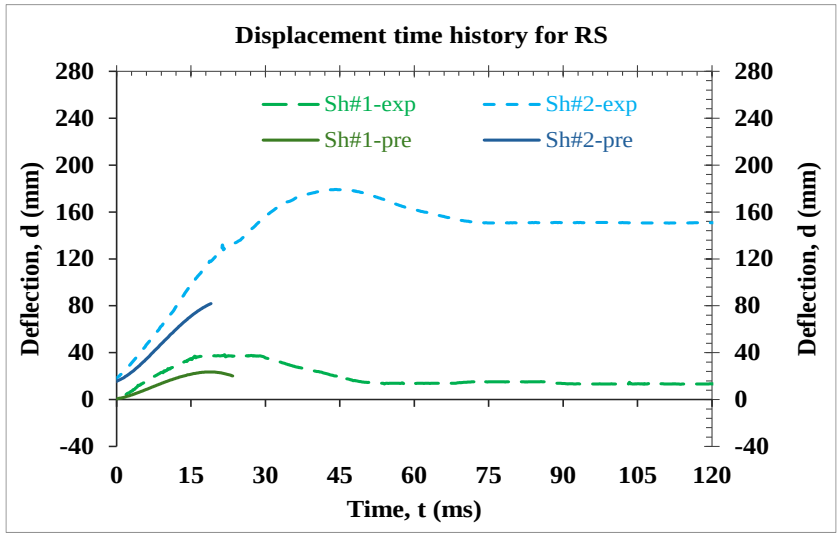

(c)

Figure C.1 – Reference columns, a) Ref-N1, b) Ref-N2, and c) Ref-S.

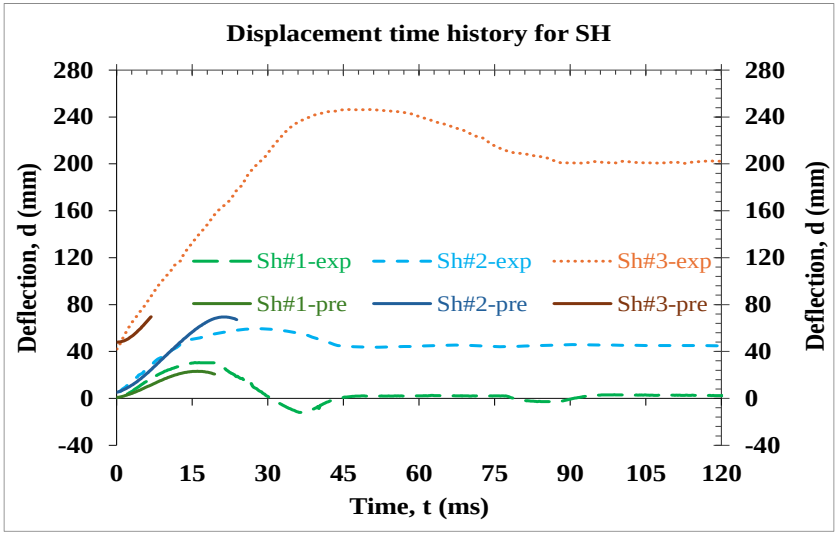

(a)

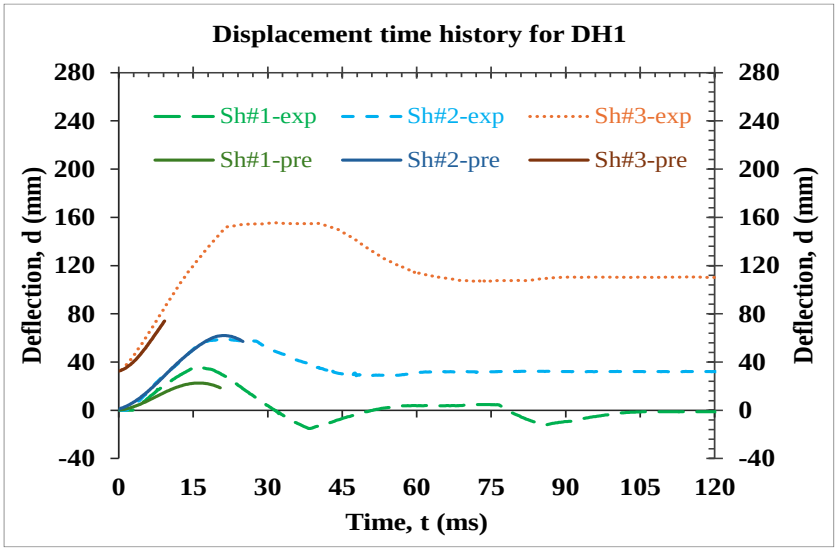

(a)

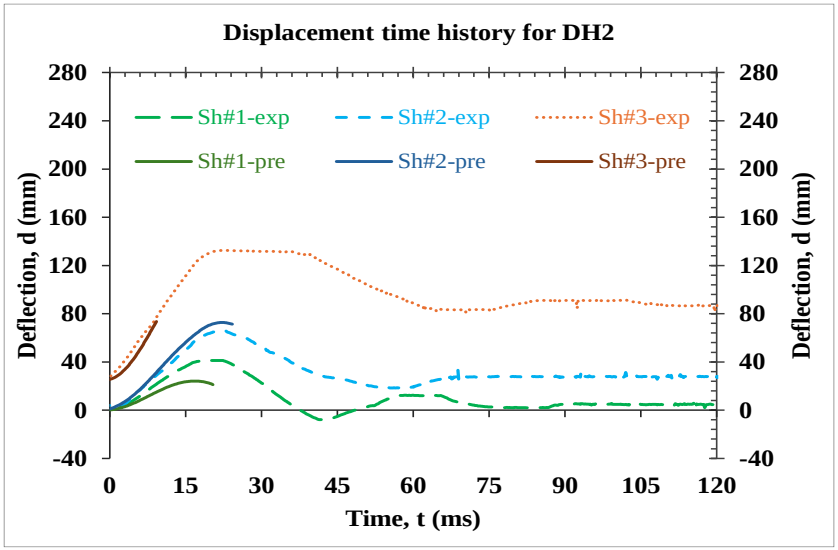

(c)

Figure C.2 – Hardened columns by external post-tensioning, a) SH-207e-0.15fpu-N1, b) DH1-207e-0.13fpu-N1, and c) DH2-207e-0.15fpu-N1.

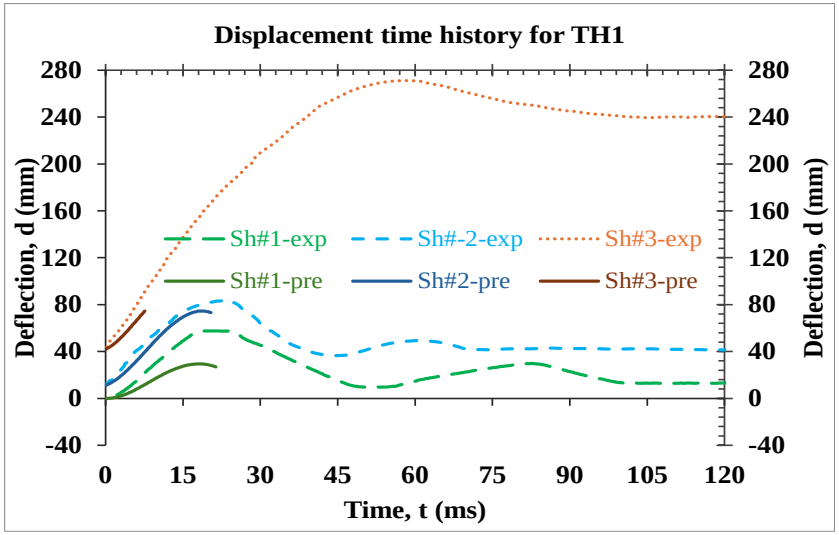

(a)

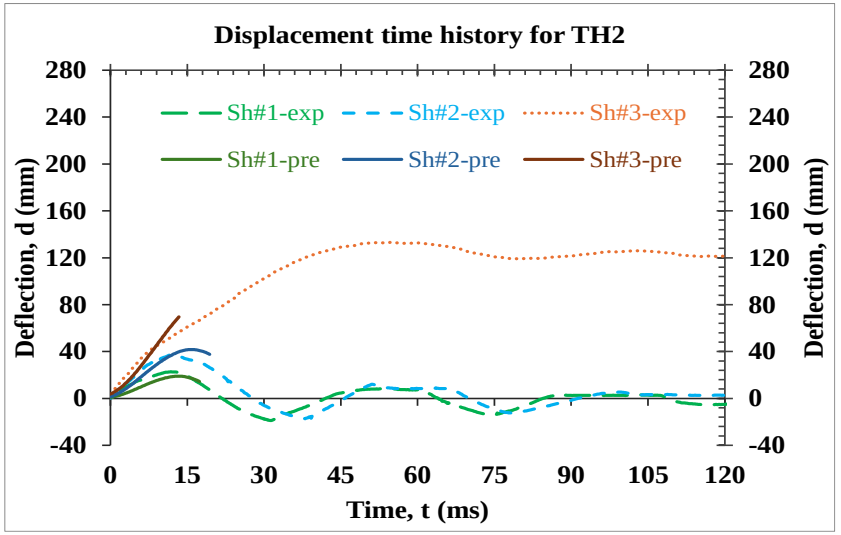

(b)

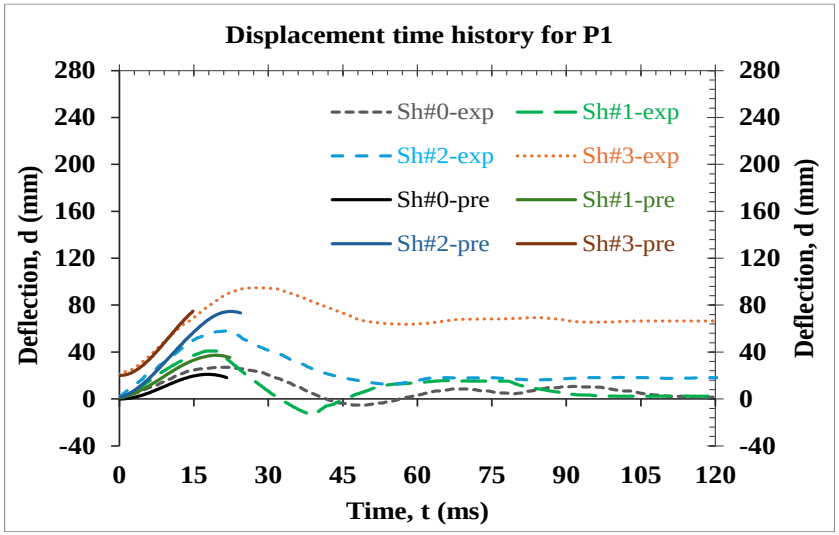

(c)

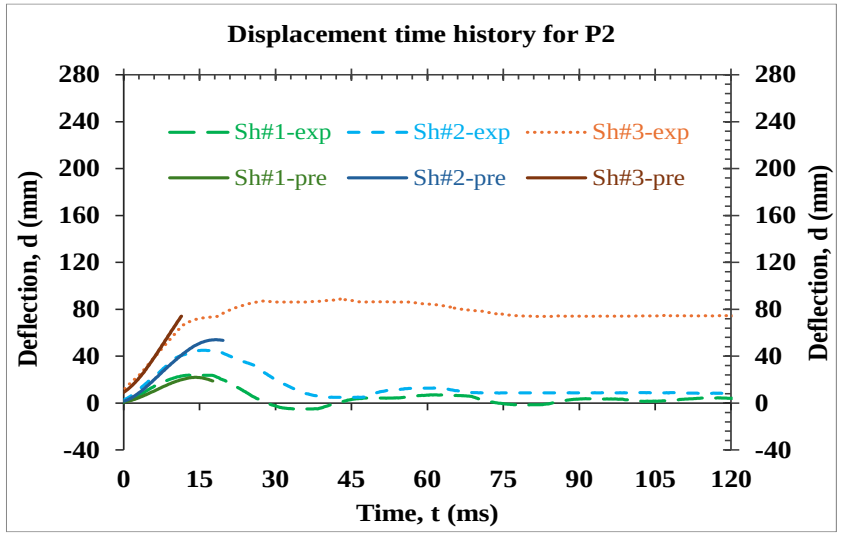

(d)

Figure C.3 – Hardened columns by external post-tensioning, a) TH1-247e-0.10fpu-N1, b) TH2-247e-0.15fpu-N2, c) P1-227e-0.09fpu-N1, and d) P2-227e-0.16fpu-N2.

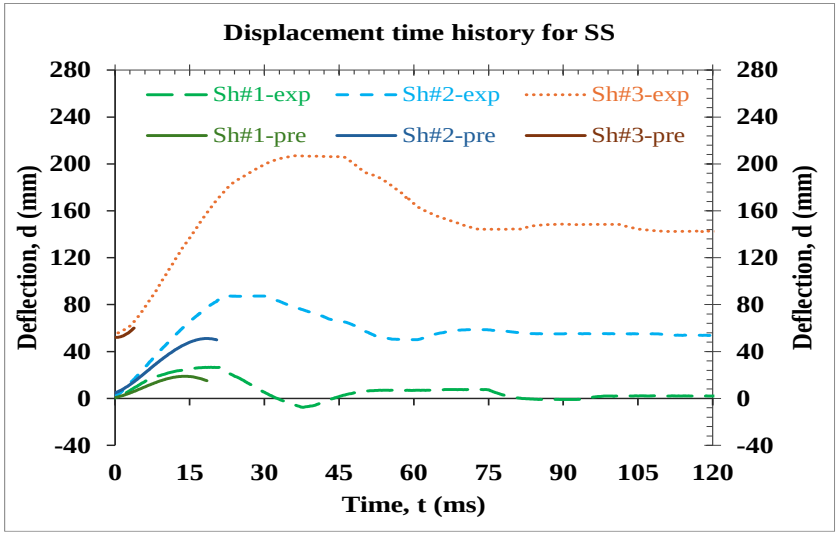

(a)

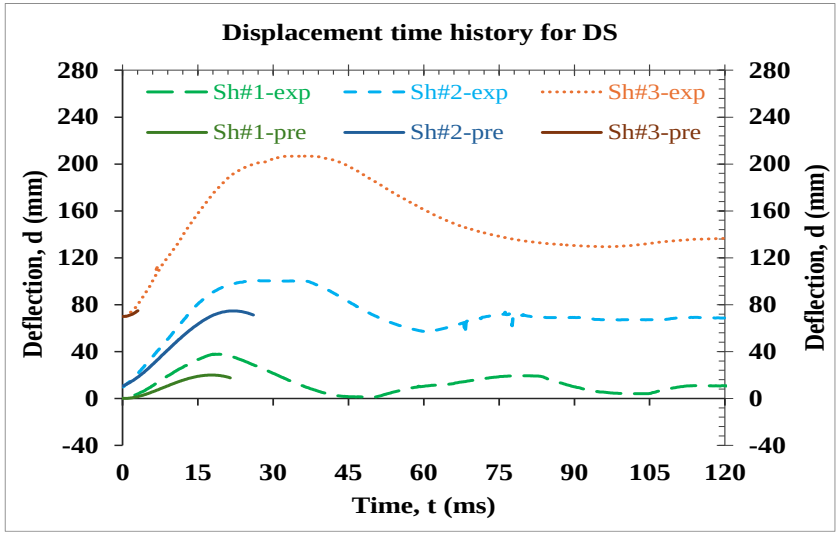

(b)

Figure C.4 – Post-tensioned columns, a) PT-SS-0.35fpu-S, and b) PT-DS-0.40fpu-S.

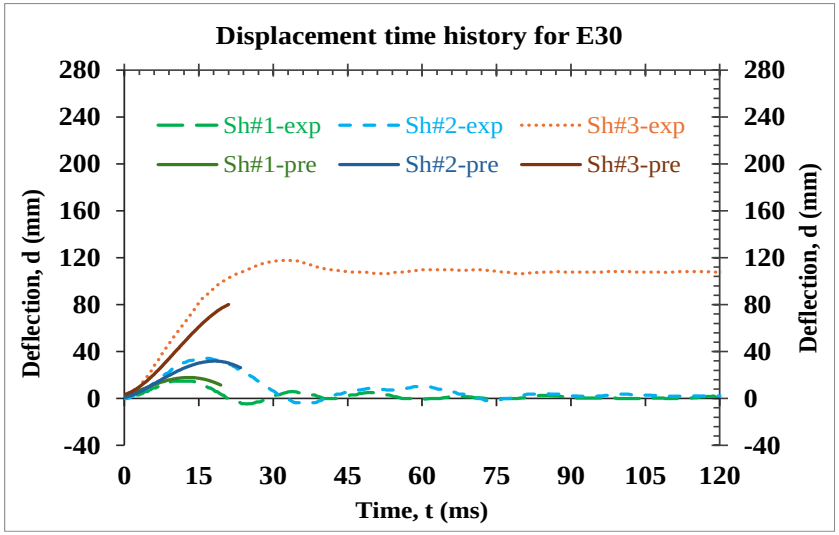

(a)

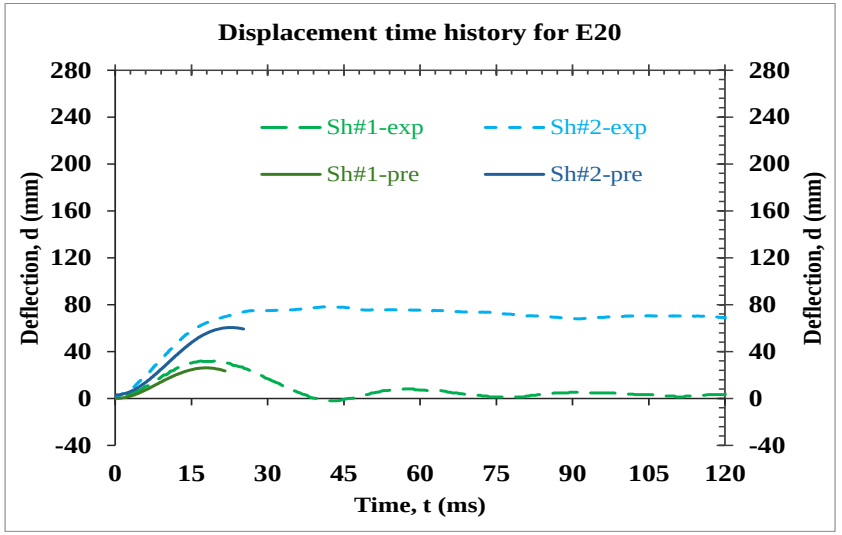

(b)

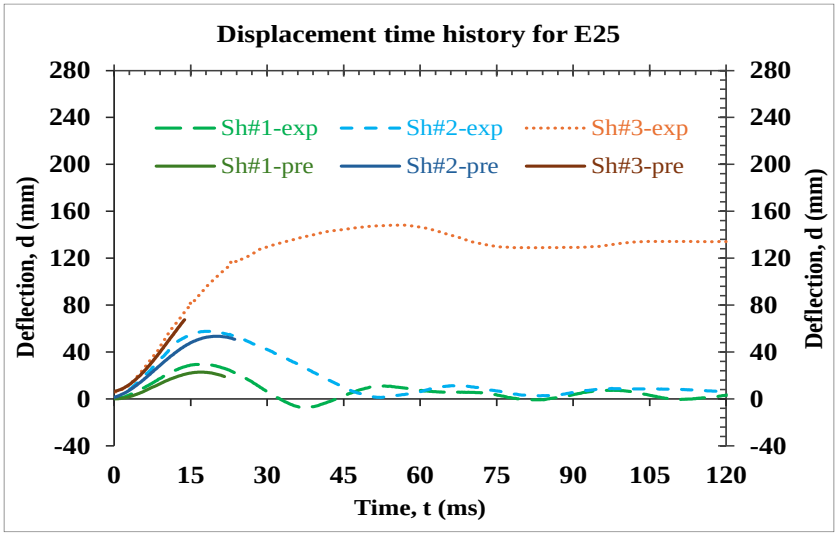

(c)

Figure C.5 – Hardened columns by ECC jacketing, a) ECC-2.0%vf-t30-N1, b) ECC-2.0%vf-t20-N2, and c) ECC-1.5%vf-t25-N2.